

Fatigue debonding resistance of wrapped composite X-joints

Feng, W.

DOI

[10.4233/uuid:609be108-6fd4-4a24-8677-7d76bbec3515](https://doi.org/10.4233/uuid:609be108-6fd4-4a24-8677-7d76bbec3515)

Publication date

2024

Document Version

Final published version

Citation (APA)

Feng, W. (2024). *Fatigue debonding resistance of wrapped composite X-joints*. [Dissertation (TU Delft), Delft University of Technology]. <https://doi.org/10.4233/uuid:609be108-6fd4-4a24-8677-7d76bbec3515>

Important note

To cite this publication, please use the final published version (if applicable). Please check the document version above.

Copyright

Other than for strictly personal use, it is not permitted to download, forward or distribute the text or part of it, without the consent of the author(s) and/or copyright holder(s), unless the work is under an open content license such as Creative Commons.

Takedown policy

Please contact us and provide details if you believe this document breaches copyrights. We will remove access to the work immediately and investigate your claim.

**FATIGUE DEBONDING RESISTANCE OF CHS
WRAPPED COMPOSITE X-JOINTS**

FATIGUE DEBONDING RESISTANCE OF CHS WRAPPED COMPOSITE X-JOINTS

Dissertation

for the purpose of obtaining the degree of doctor
at Delft University of Technology
by the authority of the Rector Magnificus prof.dr.ir. T.H.J.J. van der Hagen
chair of the Board for Doctorates
to be defended publicly on
Monday 15th April 2024 at 10:00 am

by

Weikang FENG

Master of Engineering in Architectural and Civil Engineering
Tongji University, China
born in Zaozhuang, China

This dissertation has been approved by the promotor.

Composition of the doctoral committee:

Rector Magnificus,	Chairperson
Prof. dr. M. Veljkovic	Delft University of Technology, promotor
Dr. M. Pavlovic	Delft University of Technology, copromotor

Independent members:

Prof. dr. ir. L. J. Sluys	Delft University of Technology
Prof. dr. D. Fernando	University of Edinburgh
Prof. dr. E. Ghafoori	Leibniz University Hannover
Dr. X. Jiang	Delft University of Technology
Dr. J. Sena Cruz	University of Minho
Prof. dr. ir. M.A.N. Hendriks	Delft University of Technology, reserve member



Key words: CHS, wrapped composite joints, composite-to-steel interface, fatigue debonding, finite element modelling, DIC

Printed by: Ipskamp Printing, The Netherlands

Cover design: Weikang Feng

Copy right @ 2024 by Weikang Feng

ISBN: 978-94-6384-554-0

To my family

CONTENTS

SUMMARY	IX
SAMENVATTING	XI
1 INTRODUCTION.....	1
1.1 Background.....	2
1.2 Research scope	3
1.3 Research objectives	5
1.4 Research questions	5
1.5 Research methodology	6
1.6 Structure of the thesis	6
2 LITERATURE REVIEW.....	9
2.1 Introduction	10
2.2 Fatigue strengthening of welded hollow section joints	13
2.3 Characterization of fatigue crack growth properties at the bonded interface.....	17
2.4 Fatigue crack growth in bonded joints	21
2.5 Summary.....	29
3 CHARACTERIZATION OF FATIGUE CRACK GROWTH PROPERTIES OF THE COMPOSITE-TO-STEEL INTERFACE	31
3.1 Introduction	32
3.2 Specimens and surface characterization	32
3.3 Experimental methods	38
3.4 Static test results	44
3.5 Fatigue test results	51
3.6 Conclusions	62
4 EXPERIMENTAL AND NUMERICAL STUDY ON THE FATIGUE DEBONDING BEHAVIOUR OF SIMPLE AXIAL SPLICE JOINTS.....	65
4.1 Introduction	66
4.2 Experimental study	67
4.3 Finite element modelling	79
4.4 Parametric study of fatigue crack growth.....	86
4.5 Conclusions	92
5 EXPERIMENTAL STUDY ON THE FATIGUE DEBONDING BEHAVIOUR OF CHS X-45 JOINTS.....	95
5.1 Introduction	96

CONTENTS

5.2 Specimens 96

5.3 Test set-up and instrumentation..... 99

5.4 Test results 100

5.5 Preliminary S-N curves 116

5.6 Upscaling capacity of the X45 joints..... 118

5.7 Conclusions 124

6 NUMERICAL MODELLING ON THE FATIGUE DEBONDING BEHAVIOUR OF CHS X-45 JOINTS 127

6.1 Introduction 127

6.2 Set-up of the model..... 128

6.3 Model validation by static tests 131

6.4 Modelling of stiffness degradation and crack propagation under cyclic loading 135

6.5 Probabilistic analysis 160

6.6 Conclusions 169

7 ASSESSMENT ON THE FAILURE CRITERION OF CHS X-45 JOINTS UNDER CYCLIC LOADING..... 171

7.1 Introduction 172

7.2 Model validation..... 172

7.3 Failure criterion determination 176

7.4 S-N curve 180

7.5 Conclusions 187

8 CONCLUSIONS AND RECOMMANDATIONS 189

8.1 Conclusions 190

8.2 Recommendations 192

REFERANCE..... 193

ACKNOWLEDGEMENTS 207

CURRICULUM VITAE 211

LIST OF PUBLICATIONS 212

SUMMARY

Steel jacket support structures for offshore wind turbine towers made of circular hollow sections (CHS) are becoming a competitive solution compared to monopiles in deeper waters. The current limitation to improving the durability and cost-effectiveness of the CHS structures is the low fatigue endurance of their welded joints. Fatigue-driven design of such structures usually leads to thicker profiles of steel members as well as costly welding of joints. Due to excellent corrosion and fatigue endurance, high strength-to-weight ratio, easy and locally made fabrication, fibre-reinforced polymer (FRP) composite materials have been widely used to strengthen welded CHS joints. Although this strengthening technique can enhance the resistance and fatigue performance of the welded CHS joints, welding still serves as the main way for load transferring in the joints. Therefore, welds remain the source of stress concentration and brittle fatigue failure. Recently, an innovative joining technique, wrapped composite joint, has been proposed at TU Delft. In this joint, the CHS members are connected through the composite wrap. Loads are transferred at the bonded composite-to-steel interface, and welding is completely avoided. While monotonic tensile tests have shown the superior stiffness and resistance of the wrapped composite joint over its welded counterparts, the fatigue performance of the joint still needs to be investigated.

As the first investigation of the fatigue behaviour of the wrapped composite joints, the present study focuses on the most unfavourable failure mode, debonding at the composite-to-steel interface. A typical joint geometry in the jacket support structures, the K-K joint, is chosen as the research object, which is simplified to be the uniplanar X-joint. The general objective is to accomplish knowledge sufficient to predict the debonding behaviour of CHS-wrapped composite X-joints under tensile cyclic loads.

To achieve that goal, the present work starts from the interface level, where the fatigue crack growth (FCG) properties at the composite-to-steel interface are characterised through fracture mechanics experiments, i.e. 4-point bending end notched flexure (4ENF) tests. The steel surface of the specimens is prepared with different roughness levels, and its impact on FCG properties is investigated. The obtained FCG properties provide the basis for predicting crack growth at the joint level. In the wrapped composite joints, friction exists at the composite-to-steel interface due to the confinement by the composite wrap, which may retard the crack growth. This phenomenon is quantified in cyclic tests on joints with simple geometry, i.e. the axial splice joint (A-joint), where the debonding crack growth is monitored through the 3D digital image correlation (DIC) system. At the joint level, tensile cyclic tests are conducted on the wrapped composite X-joints with different surface roughness and at different scales. Post-fatigue static tests are conducted to check the influence of cyclic loads on the residual resistance of the joints. Using the finite element model, the methodology to predict the crack growth and stiffness degradation of the wrapped composite joints is established, which can consider the interaction between debonding on the chord and brace members. The prediction methodology

is validated against the test results and used in a probabilistic analysis to explain and reproduce the scattering test results. Finally, the failure criterion of the joints under cyclic loads is proposed to establish the design $S-N$ curves.

The present study found that the surface roughness of the steel tube plays an important role in the FCG properties of the composite-to-steel interface. A minor increase of the surface roughness can significantly improve the joint's fatigue performance, with the parameter C of the Paris curve decreasing over magnitudes. At the joint level, the wrapped composite X-joints exhibited steady stiffness degradation during the tests due to debonding propagation at the composite-to-steel interface. Joints with reduced surface roughness show deteriorated fatigue performance but still have longer fatigue life over the welded ones. By including friction at the interface, the finite element model gives reduced strain energy release rates (SERR) at the crack front as the crack grows. Thus, the main source of the crack growth retardation is explained and can be quantified. The numerical results match well with test results of X-joints considering different surface roughness, different load levels and scales, and the relationship between debonding on the chord and braces is obtained. By studying the variability of surface roughness and FCG properties, the probabilistic analysis can reproduce scattering of the test results. Finally, , the design $S-N$ curves are obtained based on the experimental and numerical results, taking 5% resistance reduction as the failure criterion.

The present study provides a methodology for characterising and predicting fatigue debonding behaviour, not only for wrapped composite joints but also for other large-scale bonded joints with complex geometry, enhancing the application of bonded joints in engineering structures.

SAMENVATTING

Stalen jacket-ondersteunende constructies voor offshore windturbines, gemaakt van cirkelvormige holle secties (CHS), worden steeds vaker beschouwd als een competitieve oplossing in vergelijking met monopiles in diepere wateren. De huidige beperking voor het verbeteren van de duurzaamheid en kosteneffectiviteit van de CHS constructies is de lage vermoeiingsbestendigheid van de gelaste verbindingen. Het vermoeiing gedomineerde ontwerp van dergelijke constructies leidt meestal tot dikkere profielen en kostbare lassen van verbindingen. Vanwege uitstekende corrosie en vermoeiingsbestendigheid, een hoge sterkte-gewichtsverhouding, eenvoudige en lokaal vervaardigde fabricage, worden vezel versterkte kunststoffen (VVK) veel gebruikt om gelaste CHS-verbindingen te versterken. Hoewel deze versterkingstechniek de weerstand en vermoeiingsprestaties van de gelaste CHS-verbindingen kan verbeteren, blijft de las de belangrijkste manier om belasting over te dragen in de verbindingen. Daarom blijven lassen de bron van stressconcentratie en brosse vermoeiing valen.

Recentelijk is er een innovatieve verbindingmethode voorgesteld aan de TU Delft, genaamd "wrapped composite joint". In deze verbinding zijn de CHS-profielen met elkaar verbonden door de composiet omwikkeling. Belastingen worden overgedragen via de composiet-staal gebonden oppervlakken, en lassen worden volledig vermeden. Hoewel monotone trekproeven de superieure stijfheid en weerstand van de gewikkelde composietverbinding hebben aangetoond ten opzichte van de gelaste tegenhangers, moet de vermoeiingsprestatie van de verbinding nog worden onderzocht.

Als de eerste studie naar het vermoeiingsgedrag van de gewikkelde composietverbindingen, richt dit onderzoek zich op de meest ongunstige falingswijze, namelijk het loslaten van het composiet-staal oppervlak. Een typische verbinding geometrie in de jacket ondersteuning constructie, de K-K verbinding, is gekozen als het onderzoeksobject, dat is vereenvoudigd tot een enkel vlaks X-verbinding. Het algemene doel is om voldoende kennis te vergaren om het loslatingsgedrag van CHS-gewikkelde composiet X-verbindingen onder trek cyclische belastingen te voorspellen.

Om dat doel te bereiken, begint het huidige werk op het interfaceniveau, waar de vermoeiing scheur groei eigenschappen aan de composiet-staal interface worden gekarakteriseerd door middel van breukmechanica-experimenten, zoals 4-punts buig proef (4ENF) testen. Het staaloppervlak van de proefstukken wordt voorbereid met verschillende ruweheidsniveaus, en het effect ervan op de vermoeiing scheur groei eigenschappen wordt onderzocht. De verkregen eigenschappen vormen de basis voor het voorspellen van scheurgroei op knoop niveau.

In de gewikkelde composietverbindingen bestaat wrijving op de composiet-staal interface door het opsluitingseffect van de composietwikkeling, wat de scheurgroei kan vertragen. Dit fenomeen wordt gekwantificeerd in cyclische tests op verbindingen met eenvoudige geometrie,

zoals de axiale spleetverbinding (A-verbinding), waar de scheurgroei van het loslaten wordt gemonitord via het 3D digitaal beeldcorrelatiesysteem (DIC).

Op het verbindingniveau worden trekcyclusproeven uitgevoerd op de gewikkelde composiet X-verbindingen met verschillende ruwheidsniveaus en op verschillende schalen. Na vermoeidheid worden statische tests uitgevoerd om de invloed van cyclische belastingen op de reststerkte van de verbindingen te controleren. Met behulp van het eindige elementenmodel wordt de methodologie voor het voorspellen van de scheurgroei en stijfheidsdegradatie van de ingepakte composietverbindingen vastgesteld, waarbij rekening wordt gehouden met de interactie tussen het loslaten op de chord en de bracen. De voorspellingsmethodologie wordt gevalideerd aan de hand van de testresultaten en gebruikt in een probabilistische analyse om de spreiding in de testresultaten te verklaren en te reproduceren. Ten slotte wordt het falingscriterium van de verbindingen onder cyclische belasting voorgesteld om de ontwerp S-N curven vast te stellen.

Het huidige onderzoek heeft aangetoond dat de oppervlakteruwheid van de stalen buis een belangrijke rol speelt bij de vermoeiing scheur groei eigenschappen van de composiet-staal oppervlak. Een kleine toename van de oppervlakteruwheid kan de vermoeiingsprestaties van de verbinding aanzienlijk verbeteren, waarbij de parameter C van de Paris-curve aanzienlijk afneemt. Op het verbinding niveau vertoonden de gewikkelde composiet X-verbindingen een gestage stijfheidsdegradatie tijdens de experimenten als gevolg van loslatingspropagatie aan de composiet-staal interface. Verbindingen met verminderde oppervlakteruwheid tonen verslechterde vermoeiingsprestaties maar hebben nog steeds een langere vermoeiingslevensduur dan de gelaste verbindingen. Door wrijving aan de oppervlakte op te nemen, geeft het eindige elementenmodel verminderde rek energie (SERR) aan het scheur front als de scheur groeit. Hierdoor wordt de belangrijkste bron van de vertraging van de scheurgroei verklaard en kan deze worden gekwantificeerd. De numerieke resultaten komen goed overeen met de testresultaten van X-verbindingen, rekening houdend met verschillende oppervlakteruwheid, belasting niveaus en schalen, en de relatie tussen loslaten op de chord en brace wordt verkregen. Door de variabiliteit van oppervlakteruwheid en FCG-eigenschappen te bestuderen, kan de probabilistische analyse de spreiding in de testresultaten verklaren. Ten slotte worden de ontwerp S-N curven verkregen op basis van de experimentele en numerieke resultaten, waarbij een weerstandsvermindering van 5% als het faalcriteria wordt genomen.

Het huidige onderzoek biedt een methodologie voor het karakteriseren en voorspellen van vermoeiing ontbindingsgedrag, niet alleen voor gewikkelde composietverbindingen, maar ook voor andere grootschalige gelijmde verbindingen met complexe geometrie, wat de toepassing van gelijmde verbindingen in bouwkundige structuren verbetert.

Chapter I

INTRODUCTION

1.1 Background

Climate change, resulting from emissions of greenhouse gases, has deeply affected the entire world, with extreme weather conditions becoming more and more frequent. Carbon neutrality by mid-21st century has become a consensus as a target of the world. The European Union (EU) is committed to a 55% greenhouse gas emissions reduction target by 2030 (compared to 1990 levels). To reach the energy and climate objective, the EU has set a target of increasing the share of renewable energy to 45% (1236 GW) by 2030 [1]. One of the renewable energies which has attracted more and more attention is wind energy. It was estimated that the EU would need 453 GW of wind energy capacity by 2030 [2]. Unlike onshore wind farms, offshore wind farms are rapidly developing, driven by the higher and more consistent wind speeds at sea. The Netherlands' wind capacity growth over the next 5 years is expected to come from offshore sectors, with 4.3 GW of new capacity to be installed [2].

For offshore wind farms, the wind turbine is supported by the support structure, which transfers the loads from the turbine to the ground. A typical variety of supporting structures is shown in Fig. 1-1. The substructure is a part of the structure from the bottom of the wind tower to the seabed. The most commonly used substructure is the monopile due to the simplicity of fabrication, ease of installation and lower cost. It has been widely used for water depths up to 30 meters [3]. However, as offshore wind farms develop into deeper waters, the monopile substructure loses its preference due to its low bending moment resistance and substantial mass increase with water depth. One of the suitable substructures for water depth over 40 meters is the jacket structure, which consists of four mildly tilted "legs" interconnected by slender diagonal members (braces). Due to member placement away from the neutral line, the jacket structure comprises a higher stiffness over mass ratio than monopiles. This ratio influences the eigenfrequency of the structure and can be tweaked by varying global structural layouts, accommodating increasing mass and dimensions of wind turbines.

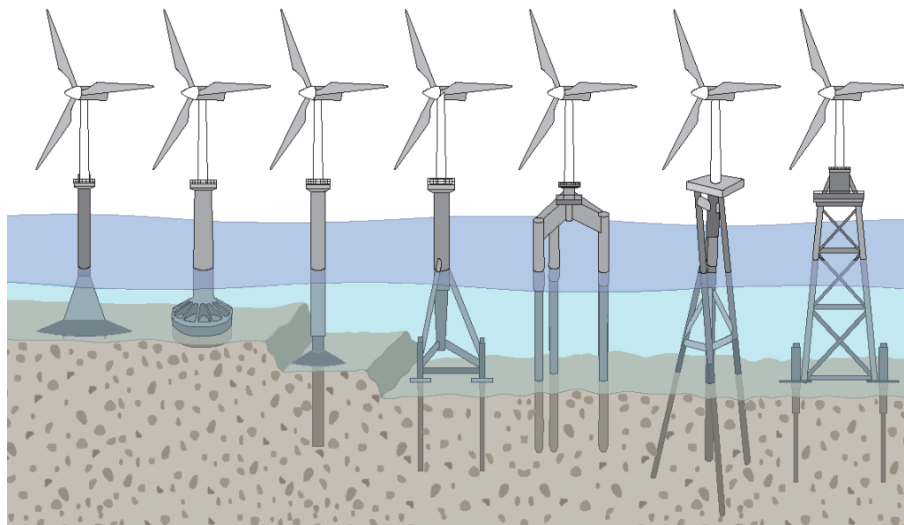


Fig. 1-1 Wind turbine support structures. From left to right: gravity-based, bucket, monopiles, tripod, triple, twisted jacket and jacket structures [4]

However, the support structures are usually subjected to aerodynamic and hydrodynamic loads in the harsh marine environment, which imposes high demands on fatigue endurance of welded tubular joints in the jackets. Meanwhile, the reduced fracture toughness and stress concentration resulting from the complex geometry and local bending of thin-walled truss members in the joint region further reduce the fatigue resistance. The fatigue-driven design of such structures usually leads to a thicker profile of steel members and costly welding procedures, reducing the cost-effectiveness of jacket structures.

In recent years, an innovative joining technique, the wrapped composite joint [5], has been developed in TU Delft to tackle this issue. In this joint, the steel hollow sections are connected by bonded composite wrap. A typical application of the wrapped composite on the commonly used K-K joint in the jacket support structure is shown in Fig. 1-2. This joint transfers the loads through a bonding area between steel and composite materials instead of welding in a narrow zone. The stress concentration can be significantly relieved, improving fatigue resistance. It has been shown from the previous study [6] that the elastic stiffness, static resistance, and fatigue behaviour are equivalent to or larger than those of their welded alternative for the properly designed composite wrap. However, the fatigue performance of the wrapped composite joints still needs to be clarified, and the corresponding prediction methods should be established.

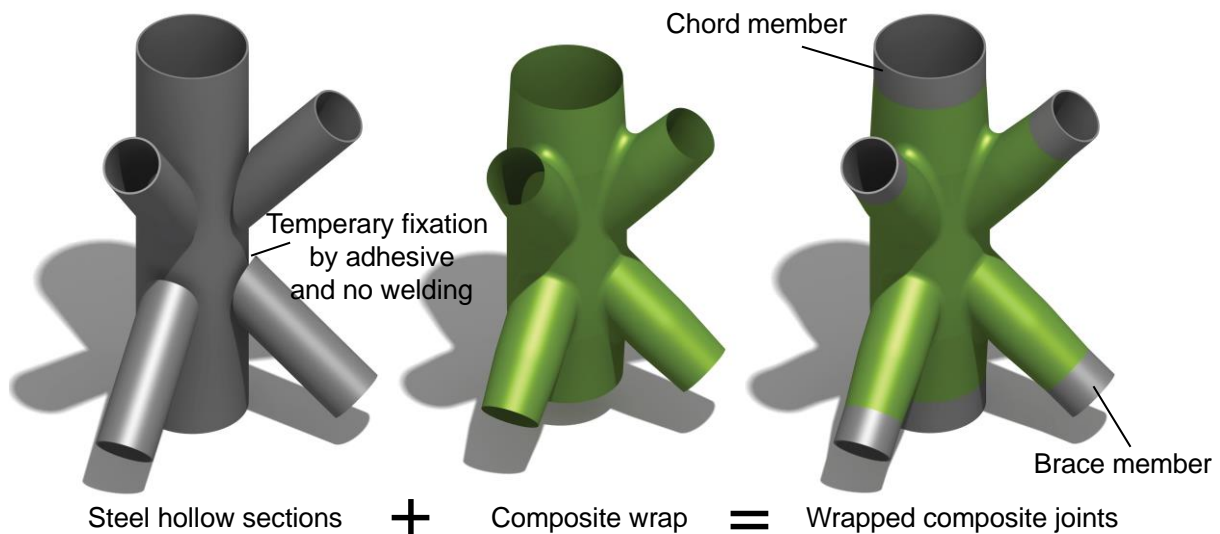


Fig. 1-2 Concept of wrapped composite joints

1.2 Research scope

In large-scale bonded joints, the debonding failure at the interface is more detrimental than other failure modes, e.g. material failure, since it is brittle and hard to detect. From the conceptual design viewpoint, debonding failure should be avoided in wrapped composite joints because the material failure should be governing. In addition, the circumferential butt welds are inevitable in the full-scale offshore structures to connect prefabricated wrapped composite joints of circular hollow section (CHS) tubes of 1–2 m diameter. The aim is to design and produce wrapped composite joints at the full scale with longer fatigue life than the

circumferential butt welds. Therefore in the first phase of the research, the focus is on investigating the unfavourable debonding failure mode. At the same time, the composite wrap is designed to be thick enough to prevent ultimate failure with excessive damage in the composite material.

It is challenging to predict fatigue debonding failure in the typical K-K joint shown in Fig. 1-2 due to its complex geometry, stress concentration, and size effect. Therefore, the K-K joint geometry is simplified to the K joint geometry as shown in Fig.1-3 (a) to limit the loading conditions to be uniplanar, thus making the fatigue debonding behaviour easier to analyse. The K-joint is further simplified to be the X joint, as shown in Fig.1-3 (b), which has comparable stress concentration factors with the K joint, considering the limitations of test set-up and loading efficiency in the lab experiments. Furthermore, it is known that the K-K joint in the jacket support structure is prone to tensile fatigue failure. To summaries, the scope of this study is to investigate the debonding fatigue resistance of the CHS wrapped composite X-joint under tensile loads.

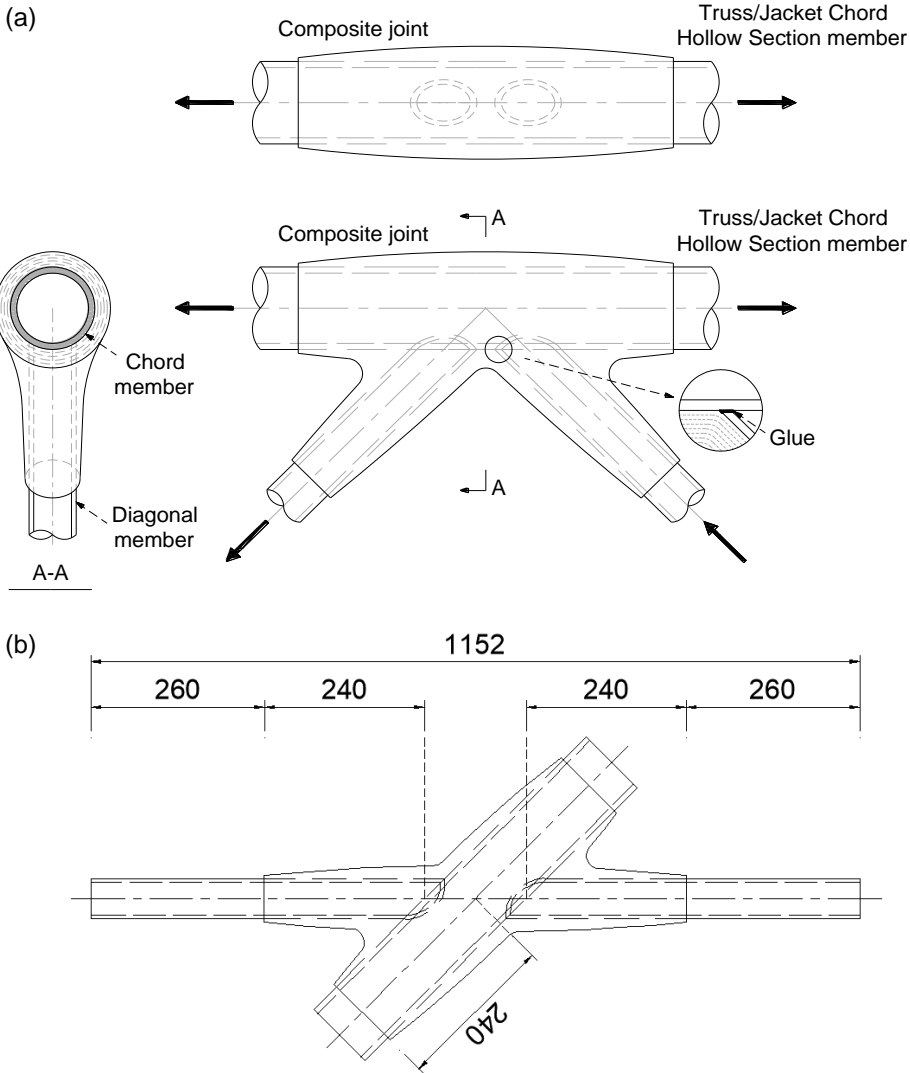


Fig. 1-3 illustration of K and X joints (a) K joint; (b) X joints

1.3 Research objectives

The general objective of this dissertation is to explain and predict the fatigue debonding behaviour of CHS wrapped composite X-joint subjected to tensile load. This is seen as the first step towards predicting the fatigue debonding behaviour of more complex joints which exist in real structures. To achieve this general objective, the following research objectives are considered:

- Explain and quantify the debonding crack growth at the complex composite-to-steel interface.
- Identify the fatigue crack growth (FCG) properties, mainly the mode II FCG properties, at the composite-to-steel interface from the coupon level, providing input information for predicting the joint behaviour numerically.
- Establish the numerical method to predict the debonding FCG, thus the stiffness degradation, of the wrapped composite X-joint under tensile cyclic loads.
- Identify the failure criterion of the wrapped composite X-joint under tensile cyclic loads, thus constructing the design $S-N$ curves of the joint.

1.4 Research questions

Based on the research objectives above, the research questions are defined as follows:

- Which governing parameters are relevant to quantifying the debonding crack growth at the complex composite-to-steel interface? What causes and how do we quantify the stiffness degradation of the wrapped composite X-joints under tensile cyclic loads? How to tackle a scale effect of the wrapped joints with respect to fatigue resistance?
- Which is the most dominating failure mode: mode-I, mode-II or mixed-mode interface failure? Is there any non-linear behaviour, e.g. friction, fibre bridging, etc., present at the failed interface?
- How do we characterise the fatigue crack growth properties at the composite-to-steel interface? What is the influence of the surface roughness of steel plate on the properties of the interface? What is the effects of non-linear behaviour such as friction at the interface, and how to quantify it?
- How do we predict the debonding crack growth and stiffness degradation of the wrapped composite joints based on the characterised interface properties? To which extent the non-linear effects (such as friction) affect the debonding behaviour in a joint and the prediction of the crack growth using the linear elastic fracture mechanics method, and how to consider it? How do we consider the interaction between debonding on the chord and brace members of X-joint? How do we explain and prove the scattering test results based on results of the numerical model?
- How does cyclic load influence the residual resistance of the wrapped composite joints? How do we determine the failure criterion of the joints under cyclic loads?

1.5 Research methodology

At the interface level, the fatigue crack growth properties at the composite-to-steel interface are characterised through fracture mechanics experiments, i.e. 4-point bending end notched flexure (4ENF) tests, with the steel plate prepared with different roughness levels. The strain energy release rates (SERR) are calculated by the extended global method (EGM) theoretically and the virtual crack closure technique (VCCT) in the finite element (FE) model where the influence of friction is considered.

Tensile cyclic tests on axially loaded splice joints are conducted to explain the crack growth in a bonded joint with a simple geometry, i.e. single curvature interface, and to establish the numerical prediction method. The numerical FE model is utilised to calculate the SERRs at the crack tip, and the fatigue crack growth at the interface is predicted based on the characterised interface properties using the fracture mechanics method.

At the joint level, tensile cyclic tests are conducted on the X-joint with different steel surface roughness and at different scales to investigate the fatigue debonding behaviour. Based on the SERR values extracted from the FE model, an iterative numerical script is developed to predict crack growth at the interface, which can consider the interaction between debonding on the chord and brace members. The method is firstly cross-validated with the joint experiments at different roughness levels and scales and then used in a probabilistic analysis to predict the scattering of the experimental results.

Post-fatigue static experiments on the X-joint are conducted to investigate the influence of cyclic loads on the residual resistance of the joint. A parametric study utilising validated FE models with different sizes of pre-crack embedded at the joint interface is carried out to find the relationship between the crack length and resistance reduction so that the failure criteria under cyclic loads can be established. The (design) S-N curves are constructed for the joint based on the failure criterion.

3D Digital Image Correlation (DIC) is used in the interface and joint-level experiments to measure the damage development and identify debonding.

1.6 Structure of the thesis

This dissertation is divided into eight chapters. The content of each chapter is as follows:

Chapter 1 is the introduction of the background, research scope, research objectives, research questions and research methodology of the dissertation.

Chapter 2 presents the literature review. The fatigue failure mechanisms of the welded tubular joints are introduced firstly. Then current strengthening techniques using composite materials on the static and fatigue performance of the tubular joints are reviewed. The methods and standards for characterizing the fatigue crack growth properties at the bonded interface are

summarised. Current research progress on the bonded joints, including fatigue experiments, numerical debonding prediction methods and debonding monitoring techniques is reviewed. Finally, research work on the wrapped composite joint until current stage is introduced.

Chapter 3 characterises the fatigue crack growth properties, namely the Paris curves, of the composite-to-steel interface with different surface roughness of the steel plate. The influence of steel surface roughness on the fracture toughness and fatigue crack growth properties of the bonded joint is investigated.

Chapter 4 presents experiments and numerical prediction on debonding behaviour of axial splice joints under tensile cyclic loads. The debonding propagation at the composite-to-steel interface is monitored by 3D DIC. The fatigue debonding retardation, correspondingly the stiffness degradation stabilization, is predicted by the FE model through the virtual crack closure technique (VCCT) with friction defined at the interface. Parametric studies on the influence of friction coefficients, failure modes, and Paris curve parameters are conducted based on the validated FE model.

Chapter 5 conducts tensile cyclic tests on small-scale and medium-scale X-45 wrapped composite joints. The performance of small-scale joints are compared with its welded counterparts. Wrapped composite joints made of different steel surface roughness are tested and compared. The medium-scale X-joints are tested to verify the upscaling capacity.

Chapter 6 establishes the numerical methodology for predicting debonding crack growth and stiffness degradation of X-joints under tensile cyclic load. The FE model is firstly validated against the static test results. Then an iterative numerical script is introduced to predict the crack growth thus stiffness degradation of the joint based on fracture mechanics. The numerical method is cross-validated against the test results at different joint scales with different surface roughness. Finally probabilistic analysis considering the randomness of surface roughness and fatigue crack growth properties is conducted.

Chapter 7 investigates the influence of cyclic loads on the residual resistance of the wrapped composite joints. FE models with pre-cracks embedded at the interface is validated against the post-fatigue static tests. The validated model is run with different crack lengths and the relationship between the crack length and residual resistance is established for small-scale and medium scale joints. Failure criteria of the joint under tensile cyclic loads are established based on the relationship and the $S-N$ curves of the joint are constructed for design purpose.

Chapter 8 summarises the conclusions of the dissertation and gives recommendations for future study.

The structure of the thesis is shown in Fig. 1-4.

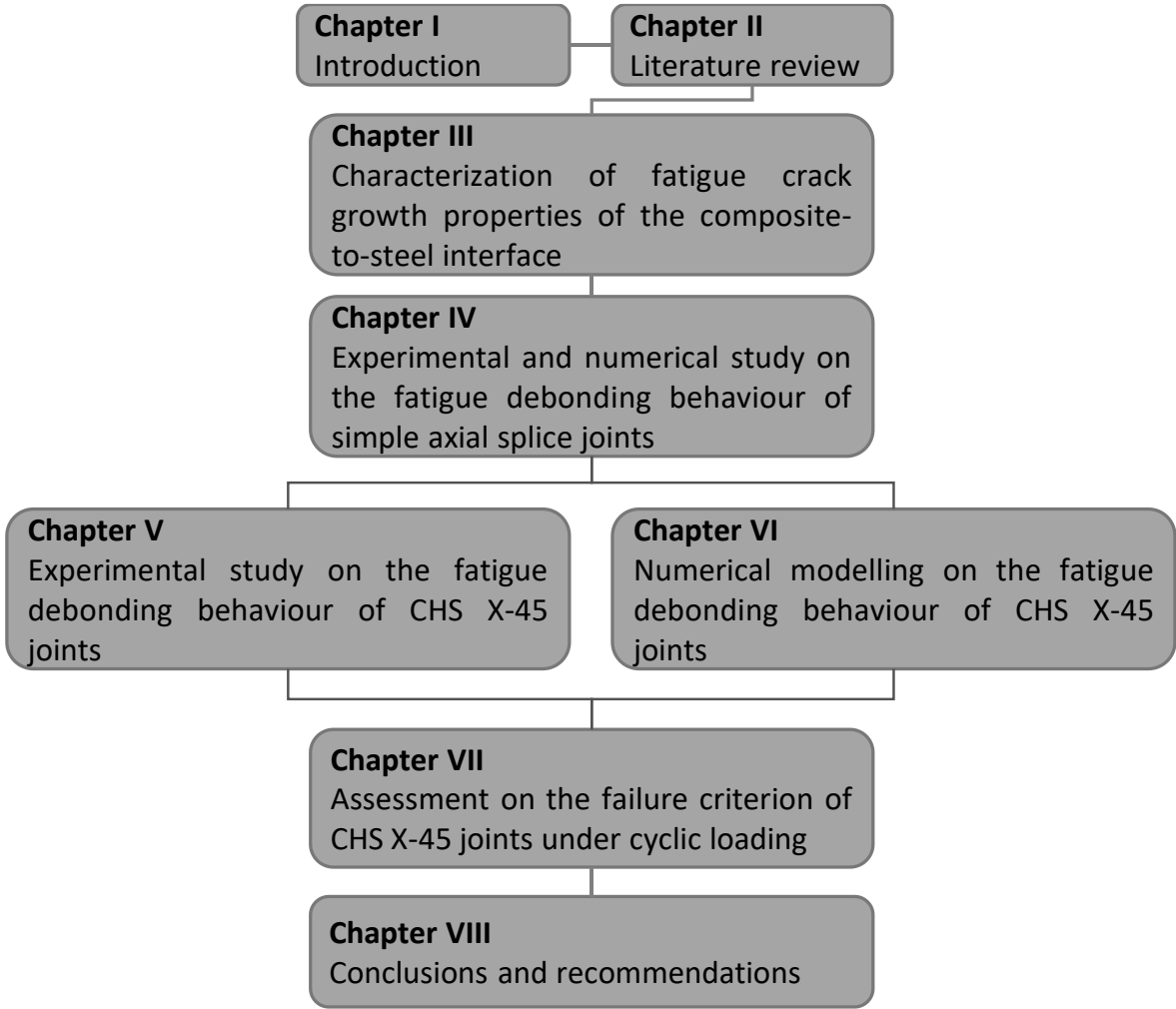


Fig. 1-4 Schematic outline of the thesis

Chapter II

LITERATURE REVIEW

2.1 Introduction

2.1.1 Jacket support structures

Compared to monopiles, jacket support structures for offshore wind turbine towers are applicable for greater water depths of 30 to 80 meters [7]. The 3-dimensional lattice structure usually consists of four mildly titled legs (chords) interconnected by slender diagonal braces as shown in Fig. 2-1 (a). Based on the layout of brace members, the jacket structure can have Z-braces, K-braces and X braces, respectively. Alternatively, the structure can be designed to have only three legs as shown in Fig. 2-1 (b), which have been proved to be more lightweight and cost efficient [8] compared to the four-leg ones. Another solution proposed recently is the ‘Hexabase’ shown in Fig. 2-1 (c) [9]. The advantages are its standard pipe sections, design-related weight savings and a modular method of construction. Regardless of various layouts, the jacket support structure comprises a higher stiffness over mass ratio than monopiles due to member placement away from the neutral line. This ratio influences the eigenfrequency of the structure and can be tuned by varying the global structural layout.

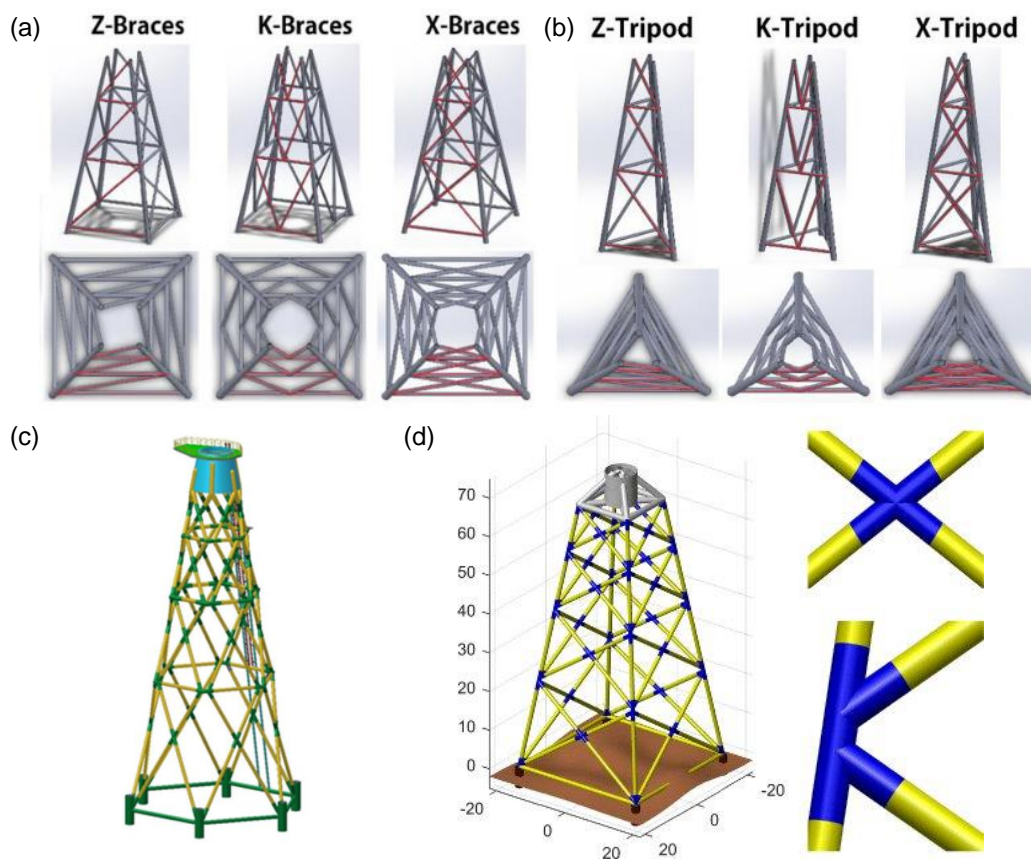


Fig. 2-1 Typical jacket support structures (a) four-leg jacket structures [10]; (b) three-leg jacket structures [10]; (c) Hexabase jacket structures [9]; (d) typical X and K joint in jacket structures [11]

The members of the jacket support structures are typically made of circular hollow sections (CHS). The diameter of the legs is usually more than one meter, with the wall thickness of about

50 mm. In the contemporary practice, the steel CHS members are interconnected through welding. Various types of welded CHS joints are formed due to different intersection angles at various locations as illustrated in Fig. 2-1 (d). Typical welded CHS joints include X type joints connecting different brace members, K joints between chord and brace members on one side of the frame and K-K joints as illustrated in Fig.1-2 at the corner of the frame. Under dynamic loads of winds, waves, currents and rotor operations, the welded CHS joints in jacket support structures are prone to fatigue failure, imposing challenges in the design of such joints.

2.1.2 Fatigue performance and design of welded hollow section joints

Fatigue damage as a major problem for welded structures, particularly in the case of offshore structures exposed to demanding marine environment, has caused huge economic losses. The fatigue phenomenon is characterised by a progressive degradation of strength under time variant stresses that result in the appearance of visible cracks and subsequent crack growth, which eventually may include fracture of a member or even the collapse of a structure [12]. Generally the fatigue cracks start at locations with high stress peaks [13]. For CHS joints, two resources for the high stress peaks are shown in Fig. 2-2: (a) the highly local stresses near the intersection lines between members, namely the welds and (b) the geometrical peak stresses due to the geometry, e.g. at holes or in hollow section joints due to the non-uniform stiffness distribution at the perimeter of the connection.

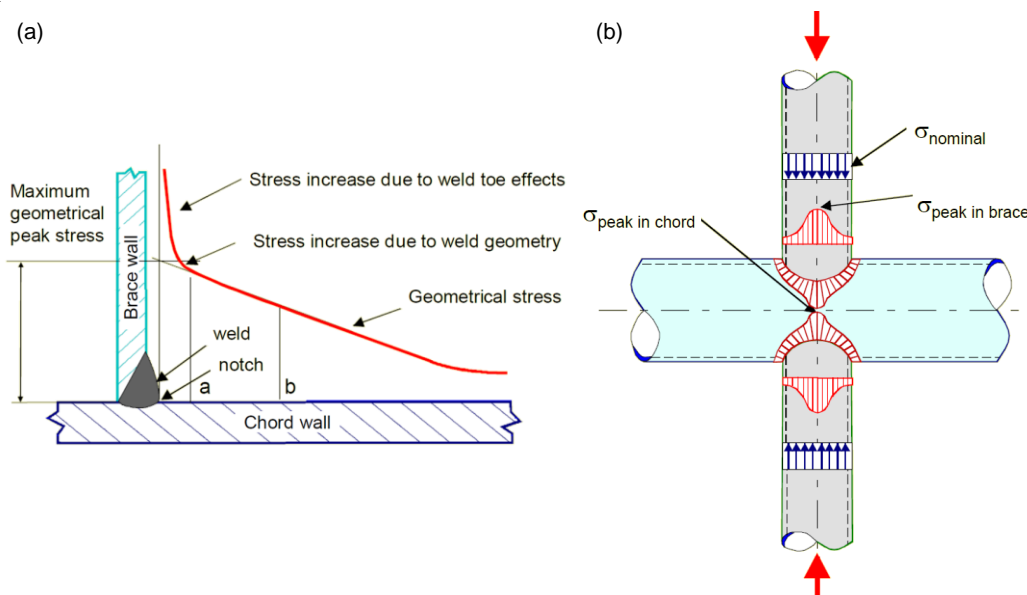


Fig. 2-2 Stress conditions around the welded hollow section joints (a) peak stress due to weld discontinuity; (b) geometrical stress distribution [13]

Moreover, the thermal processes involved in the welding procedure can induce tensile residual stresses in the vicinity of the welds, as illustrated in Fig. 2-3 (a), exacerbating the issue of stress concentration [14]. Meanwhile, material defects, some of which are introduced from the welding procedure as illustrated in Fig. 2-3(b), may exist at these high-stress regions. The high stress peaks contribute to an early initiation of cracks from these pre-existing defects, followed

by the macro crack growth. It has been found out that for welded joints, the major portion of the fatigue life is spent in the crack initiation phase, followed by a relatively shorter crack propagation phase and sudden fracture of the joints [15,16].

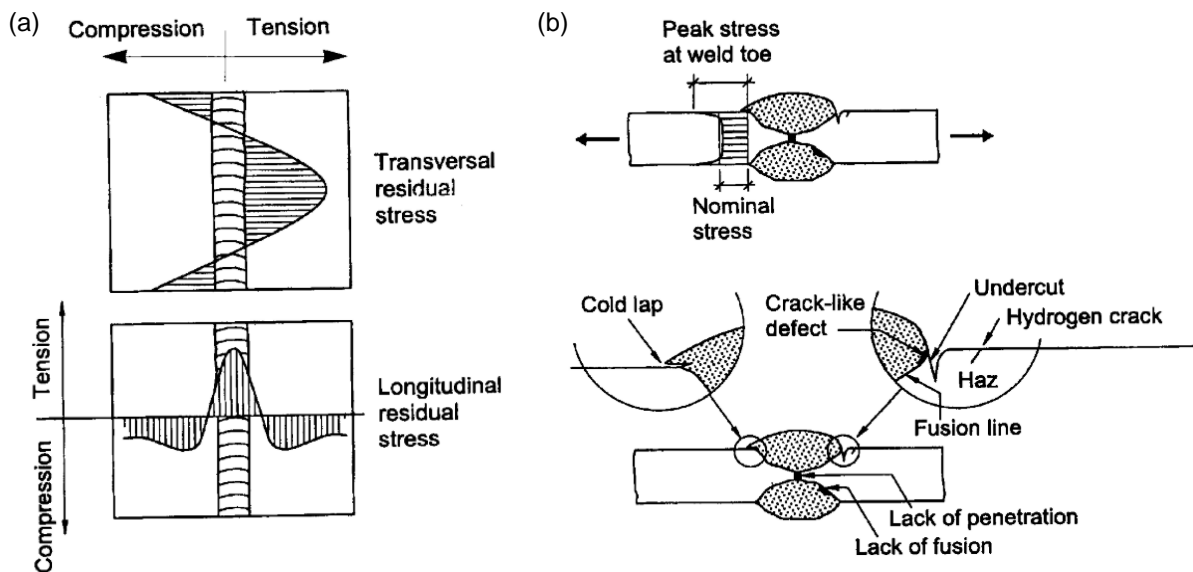


Fig. 2-3 Conditions that will reduce the fatigue strength of welded joints [14]

Currently, the most widely used methods for fatigue design and verification of welded hollow section joints are the $S-N$ curve method and fracture-mechanics-based method, which have been recommended by design guides such as Eurocode 3 [17], CIDECT [12], IIW [18] and DNV [19]. The $S-N$ curves are constructed based on an extensive experimental work, which correlate the stress ranges ($\Delta\sigma$) in the weld detail and the number of cycles to failure (N_f). Usually the hot-spot stresses (HSS) are used in this method, which is the maximum principle stress adjacent to the weld toe, resulting from the stress concentration effects due to overall geometry of the joint. The HSS is correlated with the nominal stress in the member by the stress concentration factors (SCFs), which can be calculated by the formula given in the design guides, obtained experimentally or numerically for a specific joint geometry. In such situation, one reference HSS $S-N$ curve can be applied for various joint geometries, while corrections would only be necessary for different member thicknesses or exposure conditions. As for the fatigue life N_f , a widely used failure criterion is defined as crack growth through the wall thickness. Typical reference mean and design $S-N$ curves for tubular joints in DNVGL-RP-C203 [19] are shown in Fig. 2-4. The design $S-N$ curve corresponds to 2 standard deviations of $\log(N)$ below the mean curve, providing a 2.3% probability of failure. It is roughly estimated that the number of cycles to failure in the design curve is 1/3 of that in the mean curve.

A more accurate method for the fatigue verification of the welded hollow section joints is based on fracture mechanics, by which the remaining fatigue life of the joint can be calculated. In this method, the crack growth rate is calculated by the Paris relationship:

$$da / dN = C(\Delta K)^m \quad (2-1)$$

where a is the crack length, K is the stress intensity factor (SIF), which is determined by the nominal stress and geometry of the member, C and m are the material parameters. Typical values for steel materials recommended by IIW [20] are $C=5.21 \times 10^{-13}$ and $m=3$. In order to obtain the fatigue life, an initial crack size a_0 needs to be assumed taking into account experienced imperfection or defect sizes for various weldments, geometries, access and reliability of the inspection method [19]. Subsequently, the fatigue life can be calculated by integrating Eq. (2-1) from the initial crack size to the critical size, until which the fracture toughness of the material (K_C) is reached.

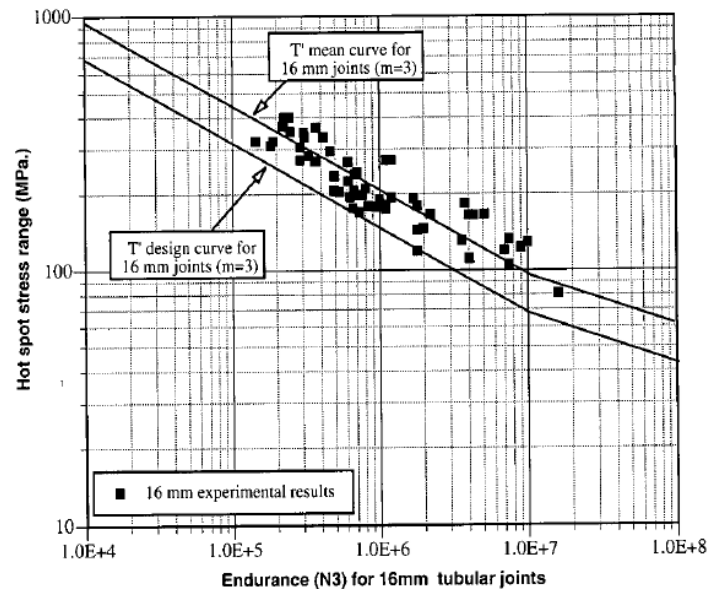


Fig. 2-4 *S-N* curves for tubular joints recommended by DNVGL-RP-C203 [21]

2.2 Fatigue strengthening of welded hollow section joints

2.2.1 Traditional weld improvement techniques

Fatigue-driven design usually leads to thick profiles of the steel members thus reducing the effectiveness of the structure made of hollow sections. Improvement techniques have been proposed in the design guides and literature to extend the fatigue lives. The first applicable method is to improve the welds by eliminating weld defects, reducing stress concentrations, or mitigating the tensile residual stresses in the joint [12]. Among different techniques, weld profiling by machining and grinding can result in a smooth weld toe transition thus reduced stress concentrations [19]. Weld toe grinding and re-melting, as well as TIG dressing [22] technique can help remove weld toe defects, slag inclusions and undercuts. In addition to improving the weld geometry, another approach involves mitigating tensile residual stresses by introducing compressive residual stresses. Commonly used methods are hammer peening, needle peening and shot peening [22]. Through these techniques, the fatigue life may be improved by a factor up to 4.0 according to [19].

2.2.2 Alternative strengthening method

Once fatigue damage has happened, another option is to reinforce the joint by welding attachments at critical locations. Taking circular hollow section (CHS) joint as an example shown in Fig. 2-5, the reinforcement can be carried out by welding (a) internal ring stiffeners; (b) side plates; or (c) boxed components made from RHS. A load redistribution to adjacent stiffeners may take place through these method, thus reducing the stress concentrations. Another alternative solution is to increase the wall thickness of the chord and brace at the joint region as shown in Fig. 2-5 (d), where the minimum length of the chord can and brace stub should meet a certain requirement [23]. Other rehabilitation methods include grout filling and mechanical clamping [24], which may also enhance the stiffness, load-bearing capacity and fatigue performance of welded hollow section joints.

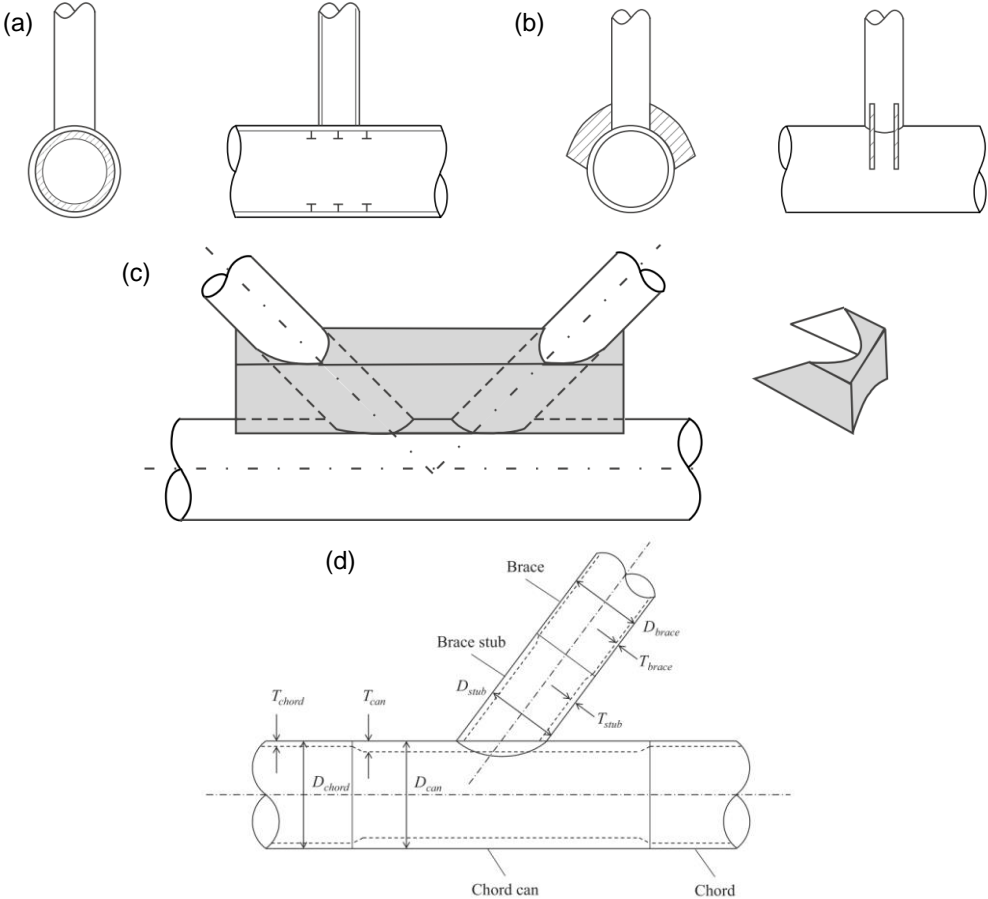


Fig. 2-5 Reinforcement of CHS joints through (a) internal ring stiffeners; (b) side plates; (c) corner components [12]; (d) chord can and brace stub [23]

Although being widely applied in practice, traditional improvement techniques still keep welding as the main loading transferring mechanism in the joint, which remains to be the source of stress concentration and brittle fatigue failure. Welding attachments to the joint not only increases the weight, but also may introduce new defects into the joint. Another option is to use

cast nodes [25] instead of welded joints. However, a large scale mold is usually needed and its application in offshore market is still limited.

2.2.3 Fatigue strengthening by composite materials

Fibre reinforced polymer (FRP) as an emerging construction material has been widely used to improve the mechanical performance of steel structures due to its light weight, high strength, good corrosion and fatigue resistance [26,27]. During the past decades, the tailarability of composite materials has made it appropriate to strengthen hollow section joints with complex geometry. Until recently, it has been successfully applied to strengthen axial splice joints [28,29], T-joints [30,31], Y-joints [32] and K-joints [33] in terms of their static performance. Through experimental and numerical study, it has been proved that this rehabilitation technique can significantly improve the stiffness and bearing capacity of the joints by mitigating unfavourable failure modes such as plastic deformation, local bending, punching shear or ovalization of the chord member.

In addition to improving the static performance of the joints, composite materials have been more and more frequently used to extend the fatigue life of the welded hollow section joints. The principle behind this retrofitting technique is to reduce the stress concentration factors (SCFs) at welded toes. Alireza Sadat Hosseini et al. [34] conducted a parametric study on the SCF reduction effect of CFRP strengthening in tubular T-joints subjected to in-plane and out-of-plane bending moment. It was observed that stiffer and thicker CFRPs can lead to further reduction of the SCF values, while the wrapping length has negligible effect. Meanwhile, the optimal fibre orientation is found. Hossein Nassiraei et al. [35–37] carried out a series of numerical study on the SCFs in tubular T/Y joints strengthened with FRP subjected to compressive load as shown in Fig. 2-6 (a) and X joint under in-plane bending load as shown in Fig. 2-6 (b). The results showed that SCFs can be reduced up to over 30% when the joint was retrofitted by FRP. The influence of FRP wrapping parameters (thickness, number of layers, orientation and modulus) and geometry parameters of the joint on the SCFs and SCF ratios over those of unretrofitted joints are investigated. Based on the results, parametric formulas were proposed to predict SCFs in these joints retrofitted with FRPs. The application of FRP strengthening technique on joints with more complex geometries are shown in Fig. 2-6 (c) and (d), where the SCF reduction efficiency is studied on the TK-joint [38] and DTK-joint [39], respectively. Once again, promising results are obtained and the reduction of SCFs at critical points can be up to 30% to 55%.

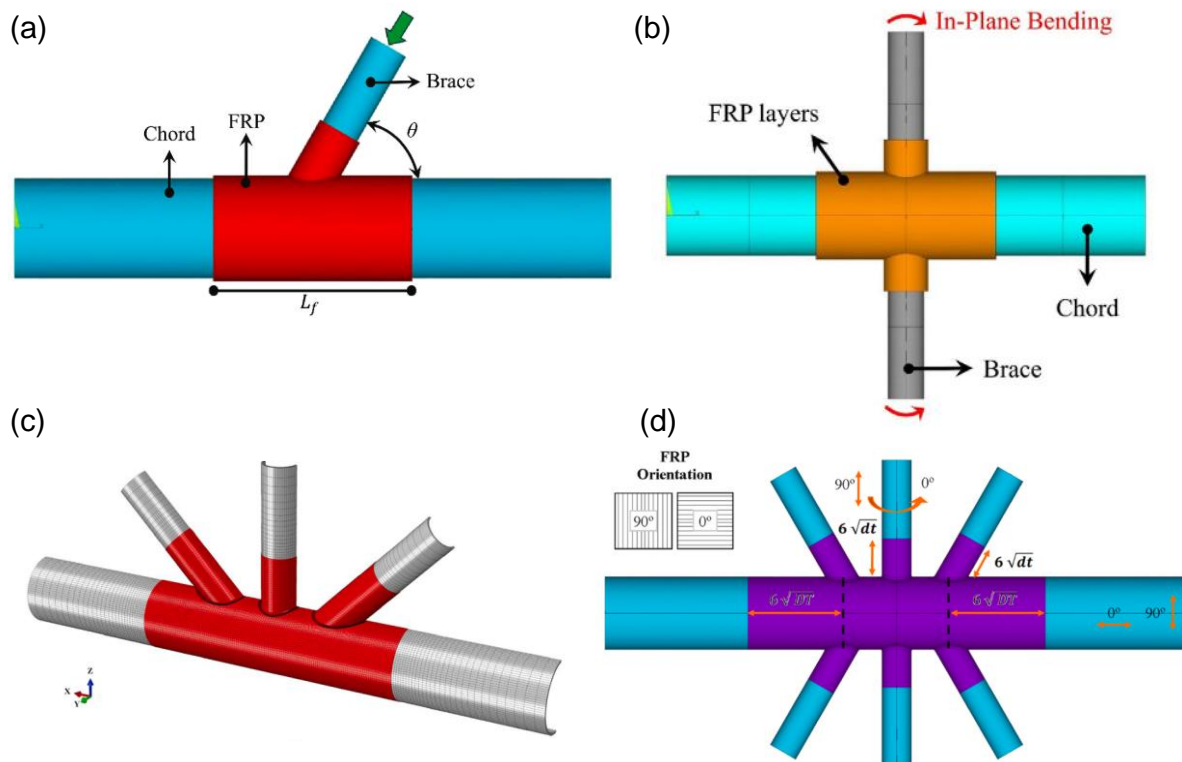


Fig. 2-6 FRP strengthening on (a) Y joint [35]; (b) X-joint [36]; (c) KT-joint [38] and (d) DKT joint [39]

In addition to numerical study, hot spot stress tests have also been conducted directly to investigate the efficiency of FRP strengthening technique. Tong et al [40] and Xu et al [41], conducted experimental and numerical studies on CFRP strengthened CHS gap K-joints under balanced axial loading as shown in Fig. 2-7. The SCF reduction efficiency was found to be influenced by CFRP strengthening parameters and non-dimensional geometric parameters. The maximum SCFs in the chord and brace can decrease by 20% and 15%, respectively. Fatigue tests were also performed on the gap K-joints [16]. It was proved that the CFRP strengthening technique can effectively improve the fatigue life of the joint, e.g. number of cycles before and after crack initiation was increased by 160% and 146%, respectively. Design $S-N$ curves were proposed based on the test results.

The FRP materials have also been applied to strengthen cracked welded joints. Justin D. Nadauld et al. [42] investigated the fatigue performance of cracked aluminium connections retrofitted by GFRP composites. It was shown that the repaired connections with 90% of the weld removed can still satisfy the constant amplitude fatigue limit threshold. Xiao et al. [43] repaired cracked cross-beam connections made of rectangular hollow sections by CFRP. Both the flexural stiffness and fatigue life of the connection were increased significantly.

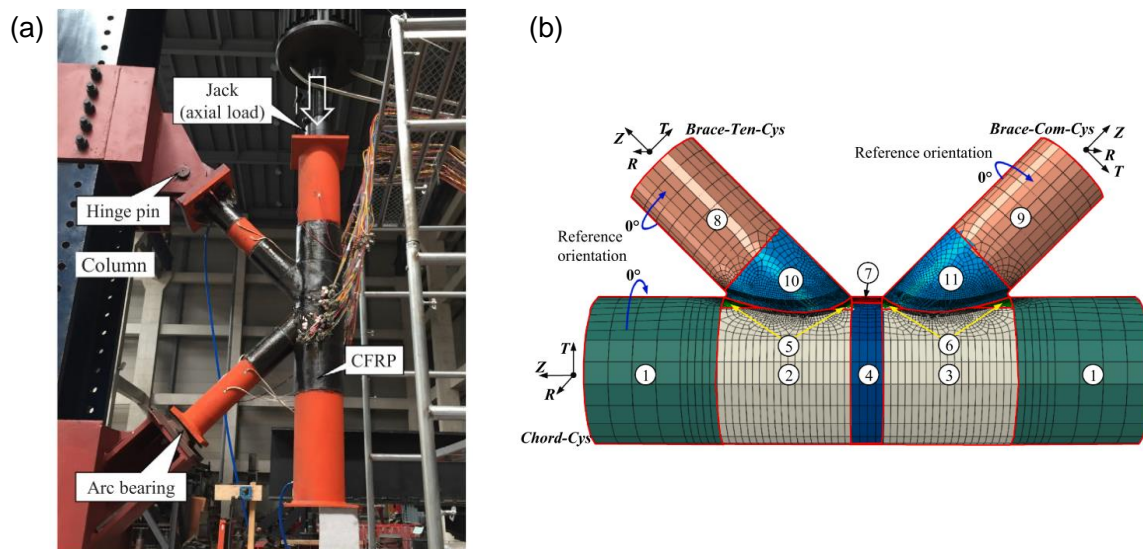


Fig. 2-7 FRP strengthening on gap K-joint (a) experimental study [16,40]; (b) numerical study [41]

It can be summarised from the literature that current application of composite materials in hollow section joints still functions as an additional strengthening technique. Welds still serve as the primary loading transferring mechanism thus brittle fatigue failure remains an inherent and inevitable risk. The fatigue life extension through FRP strengthening is limited. Furthermore, the applied FRP sheets are usually quite thin compared with the wall thickness of steel members. Perfect bond is assumed between composites and steel members and possible debonding at the interface is not considered. It can also be seen that most of existing research utilised CFRP as the retrofitting material. It has higher elastic modulus than other FRPs such as GFRP. However, one disadvantage of CFRP is that galvanic corrosion may happen when CFRP is attached to steel in offshore structures. Its lower flexibility during production may make it difficult to be applied in joints with complex geometry. The high cost is associated with carbon fibers but reduced labour may lead to optimized total cost compared to GFRP in specific applications.

2.3 Characterization of fatigue crack growth properties at the bonded interface

2.3.1 Basic fracture mechanics concepts

In the FRP bonded steel system, typical failure modes are summarised in Fig. 2-8 [26]. In the current study, composite wrap is designed to be sufficiently thick such that failure modes related to FRP failure (d) and (e) are avoided. The steel part remains elastic under relatively low cyclic load ranges thus failure mode (f) is not relevant. The focus will be mainly on the bonded interface. Since composite laminates were directly applied on the steel tubes in wrapped composite joints and no separate adhesive layer is present, the thickness of the adhesive in the current study is negligible (i.e. in the magnitude of 0.1 mm). Under such circumstance, failure

modes (b) does not exist. Finally, failure modes (a) and (c) are the focus of the current study and merged into a singular category referred to as debonding failure or interface failure.

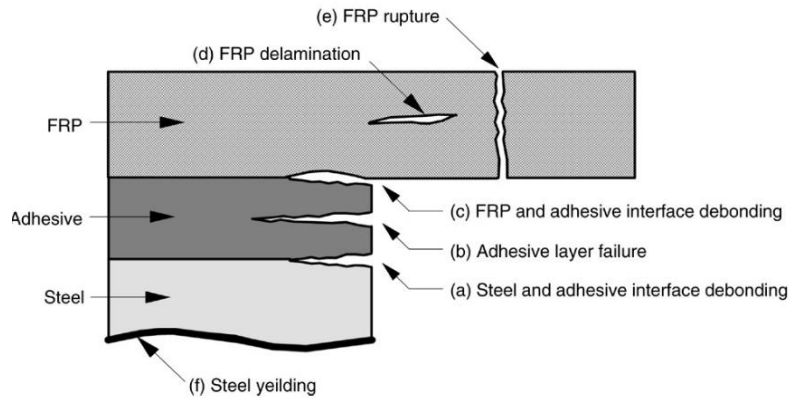


Fig. 2-8 Failure modes of bonded FRP-to-steel joint [26]

In the fracture mechanic domain, there are three basic fracture modes, mode I (opening), mode II (in-plane shear) and mode III (out-of-plane shear) [44]. In isotropic homogeneous materials, the crack driving force is the stress intensity factor (SIF), K [45]. Whereas in the bi-material case, singularities exist in the displacement and stress field near the crack tip. In this situation, strain energy release rate (SERR), G , is regularly chosen as the crack driving force [46]. The total SERR is the total energy loss in a system during unit crack extension, which can be calculated by either Irwin's crack closure integral [47] or the compliance method [48]. For different fracture modes, the total SERR usually needs to be decomposed into different components, namely the mode partitioning is needed. Commonly used mode partitioning methods in the bi-material joint are the "extended global method (EGM)" [49] and the numerical virtual crack closure technique (VCCT) [50].

Under cyclic loading, typical fatigue crack growth (FCG) curves are shown in Fig. 2-9, which correlates the crack growth rate, da/dN , to the crack driving force in a log-log plot [51]. There are three distinct regions in the FCG curve: the subcritical region around the fatigue threshold, the stable crack growth region and the unstable crack growth region near the fracture toughness. Paris et al. [52] observed that in the second region, the relationship between da/dN and the crack driving force follows a power law as expressed in Eq. (2-1). Instead of using ΔK , different crack driving forces have been proposed for crack growth in composite laminates. Commonly used crack driving forces are G_{max} or $\Delta G = G_{max} - G_{min}$. Some other versions of crack driving force were also proposed, such as $\Delta\sqrt{G} = (\sqrt{G_{max}} - \sqrt{G_{min}})^2$ [53], G_{max}/G_c , $\Delta G/G_c$ [54,55], or G_{max}/G_R [56] to take into account effects of R -ratio, mode mixity or fibre bridging et al. In addition to the simple power law in Eq. (2-1), a total fatigue life model was also widely used as expressed in Eq. (2-2) [57,58], such that all three regions of the FCG curve can be covered.

$$da / dN = C(G)^m \frac{\left[1 - \left(\frac{G_{th}}{G} \right)^{D_1} \right]}{\left[1 - \left(\frac{G}{G_c} \right)^{D_2} \right]} \quad (2-2)$$

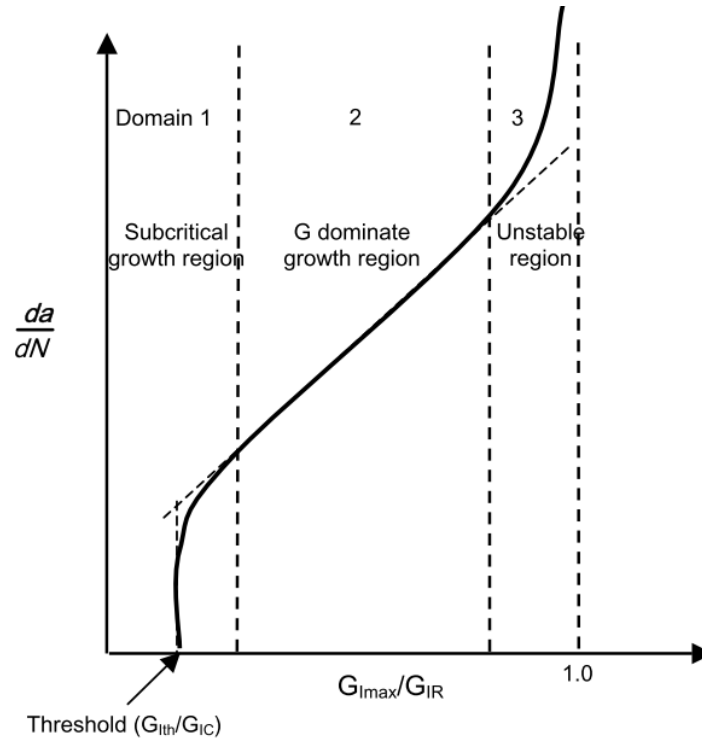


Fig. 2-9 Typical fatigue crack growth curve [51]

2.3.2 Characterization methods

Since the main failure mode in wrapped composite joints is the sliding shear, i.e. mode II failure, between the composite wrap and steel tubes, it is vital to characterize the mode II FCG properties at the composite-to-steel interface. Different test configurations have been developed for evaluating mode II fracture behaviour within composite layers or bonded interfaces. The most commonly used configuration is the end-notched flexure (ENF) test as shown in Fig. 2-10 (a) [59], which has been standardized for determination of interlaminar fracture toughness of unidirectional FRP matrix composites [60]. However, the ENF specimen is prone to unstable crack propagation if designed inappropriately and the transverse shear effect at the crack region may deviate the obtained mode II fracture toughness from the true value [61,62]. Recently, another configuration, namely the 4-point bending end-notched flexure (4ENF) test, have been developed [63,64] as shown in Fig. 2-10 (b). This allows constant bending moment between its two loading points and leads to stable crack propagation such that the whole fracture resistance curve (R-curve) can be obtained. Despite the stable characteristic of 4ENF tests, it is reported that the obtained fracture toughness can be 20-40% higher than that obtained by ENF tests due to the existence of friction at the interface of 4ENF specimens, depending on the friction coefficient defined at the interface[64].

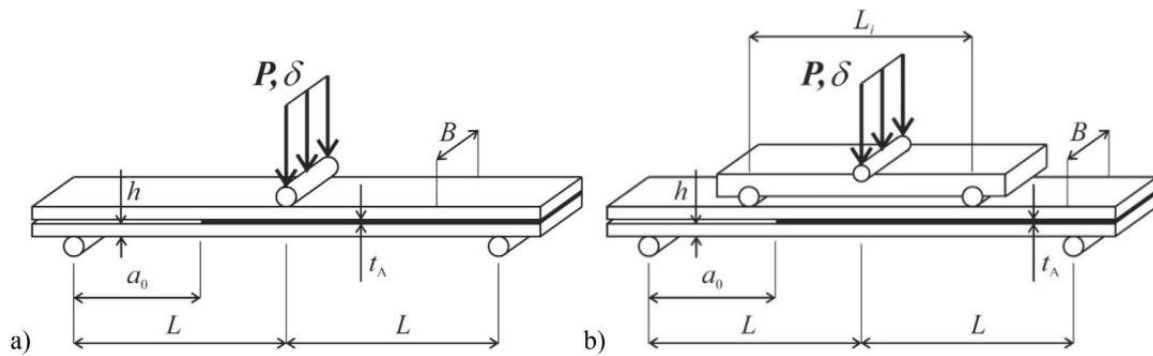


Fig. 2-10 Geometry of (a) ENF specimen; and (b) 4ENF specimen [59]

Widely applied to characterize FCG properties in composite laminates, the usage of ENF and 4ENF configuration has recently been extended for the fracture characterization of bi-material bonded joints. In bi-material interfaces, one critical issue is to achieve pure mode II fracture at the crack tip or to partition the mode I and mode II components if mode mixity exists [65]. Jiang et al. [66] employed the 4ENF test to evaluate the mode II fracture behaviour for adhesively bonded composite-steel joints. Specimens were designed to have the same bending stiffness for the upper and lower adherends to achieve pure mode II behaviour. The SERR values are calculated based on the extended global method (EGM) [49] and the results were found to be comparable with that obtained by the virtual crack closure technique (VCCT). Meanwhile, Ouyang et al. [67] proposed a bi-material ENF test configuration where the two arms have the same longitudinal strain distribution at the faying surfaces, instead of having the same bending stiffness, to remove the normal deformation components related to mode I fracture behaviour. It can be seen that no consensus has been made on this issue.

Although the mode II fracture behaviour has been extensively investigated under quasi-static loadings, there are limited research carried out to evaluate fatigue delamination or debonding resistance, especially for the bi-material case. Bieniaś et al. [68] characterised the FCG of CFRP and GFRP fiber metal laminates in mode II by force control ENF tests. Tests were conducted at different load levels and the similitude of the maximum SERR is utilised. Adamos et al. [69] successfully characterized the mode II fatigue behaviour of Titanium/CFRP adhesive joints based on displacement controlled ENF tests. While a limited SERR range is achieved by using the traditional relationship between crack length versus compliance during the compliance calibration method, the authors proposed a proper full cubic polynomial equation for this relationship which can avoid reducing the inspected SERR range. The results also show that the FCG is insensitive to the employed similitude parameter and residual thermal stress effect.

Overall, the existing research related to the mode II behaviour mainly focus on fracture and fatigue crack growth within composite layers. Research carried out to characterize fracture and fatigue crack growth at the bi-material interface is mainly limited to fiber-metal laminates. There is still no research for characterising fatigue crack growth at composite-to-steel interfaces.

2.3.3 Influence of surface roughness on the FCG properties

Surface roughness of the metal adherend resulting from different pre-treatments has a significant influence on the mechanical properties of the bonded joints. Although existing research mainly focuses on the static behaviour of the joints [70–73], some other researchers also investigated the influence of surface roughness on the fatigue performance of bonded joints. Azari et al. [74] investigated the effect of roughness on the steel bonded joints under cyclic loading by double cantilever beam (DCB) and asymmetric double cantilever beam (ADCB) tests. They found out that the fatigue threshold strain energy release rate, G_{th} , increased with the roughness, R_a , until a plateau is reached between 3.9 and 6.4 μm , then decreased for very rough surfaces. Shikimoto et al. [75] investigated the effect of laser patterning pre-treatment on the fatigue strength of adhesive bonded joints using thin steel plates. A significant improvement of the fatigue bond strength was achieved by producing an anchor effect and removing the weak boundary layer. A. Manoli et al. [76] conducted fatigue tests on single lap joints of GFRP plates joined by nanoparticles modified adhesive. Specimens with roughness of $R_a=3.3 \mu\text{m}$ exhibited an enhancement of 30% of the fatigue life than specimens with $R_a=3.3 \mu\text{m}$. Carrera [77] investigated the fatigue life, stiffness degradation and residual static strength of CFRP-to-steel joints with different surface conditions. It was shown that the fatigue life is not affected by the surface characteristic. Specimens with surface pits (high roughness) had a reduction of stiffness degradation under low to moderate fatigue loads compared to specimens with smoother surfaces.

It can be seen from above that existing related literature primarily focuses on the total fatigue life of simple joint designs, with limited attention given to study the fatigue crack growth behaviour. Additional research is required on both the static and fatigue fracture behaviour of bi-material bonded joints between metal and composite members.

2.4 Fatigue crack growth in bonded joints

2.4.1 Fatigue testing on bonded joints

While bonded joints have been widely used in various engineering applications, their fatigue performance has been investigated by fatigue testing on basic joint configurations as shown in Fig. 2-11 [78]. Although most efforts in the literature were put into plated bonded joints, limited attention was also given to the tubular bonded joints as shown in Fig. 2-12 [79]. Another aspect to be noted is that existing research mainly focused on the adhesively bonded joints, where a relatively thick adhesive present at the bonded interface. In the current study, the wet composite laminate is directly bonded on the steel surface, where the thickness of adhesive layer is negligible (i.e. in the magnitude of 0.1 mm). Fatigue performance, e.g. failure modes, of such joints may differ from those in adhesively bonded joints and need further investigation. Nonetheless, the testing and analysis method on adhesively bonded joints can still provide reference to those of direct bonded joints in the current study..

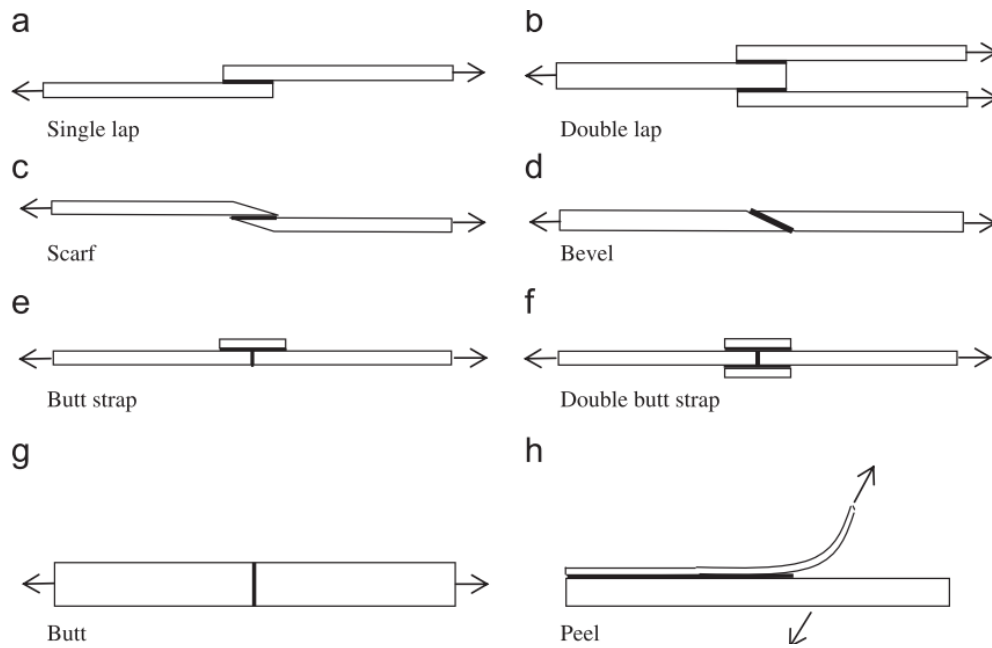


Fig. 2-11 Typical plated bonded joints [78]

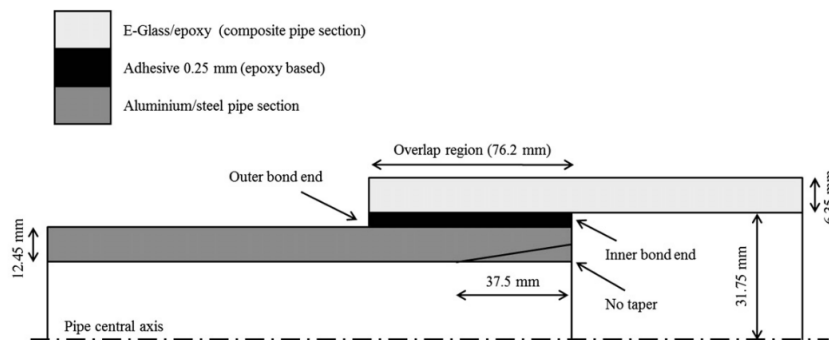


Fig. 2-12 Bonded tubular lap joints [79]

Fatigue testing on the bonded joints have been designed using different approaches. Commonly used approaches can be divided into three categories [77,80,81]: a) stress-life approach, where attention is only paid on the final failure of the joints under different stress levels; b) crack initiation / propagation approach; and c) phenomenological approaches, including strength and stiffness wear-out approach, where damage accumulation during the cyclic loading can be characterized.

In the stress-life approach, the bonded joints are subjected to constant cyclic loads of different levels. The number of cycles until failure is plotted against the stress / load amplitudes, ranges or maximum stresses / loads in a double logarithmic scale, such that a *S-N* curve can be obtained. At high cycles, the slope of the curve becomes nearly zero and a fatigue limit is seen, which could be 20% to 50% of the quasi-static failure stress [82]. Some others also argued that no obvious fatigue limit was found for adhesively bonded joints and the threshold is usually specified at a certain number of cycles, e.g. $1e6$ cycles [80]. Whereas in the low cycle regime, the slope of the *S-N* curve may also change due to plasticity occurring in the material. A strain-

life approach instead of stress-life approach is more valid in that case. Until recently, different aspects of the fatigue performance of bonded joints have been investigated using this approach such as the influence of overlap length [83,84], bond-line thickness [85,86], and loading conditions [87]. The investigated bonded joints not only includes adhesively bonded composite joints, metal-to-metal joints, but also includes bi-material joints such as CFRP-steel joints [88,89].

Although providing good prediction of the fatigue life of the bonded joints, the stress-life approach is only applicable for the specific geometry of the joint that is tested. Furthermore, this method contains no information related to the damage accumulation or crack development. Fatigue tests on bonded joints focusing on the crack propagation or damage accumulation were conducted. . Bocciarelli et al. [90] investigated the fatigue performance of double lap CFRP-steel joints. Stiffness degradation of the joints resulting from progressive debonding at the adhesive/metal interface was characterised. Doroudi et al. [91] conducted experimental study on CFRP-to-steel bonded interface under quasi-static cyclic loading. The stiffness decrease in the load-displacement curves indicated the damage while residual displacements indicated plasticity at the bonded interface when debonding propagated. In general, the fatigue life time is divided into two phases: crack initiation and crack propagation. Compared to crack propagation, investigation on crack initiation in the bonded joints is limited due to the difficulties in detecting and modelling the crack nucleation. A commonly used method to detect crack initiation in literature is the back-face strain method [92]. Similarly to the stress-life approach, the relationship between the crack initiation life, N_i , and a certain stress parameter, such as the stress singularity parameter in [93] can be established. Alternatively, different damage models have been proposed either empirically based on plastic / principle strain [94,95] or scientifically based on continuum damage mechanics theory [96,97] to make the initiation life prediction. Fatigue crack propagation has been widely studied in literature. Usually crack propagation is monitored through different ways during the tests, which will be further discussed in section 2.4.2. Fatigue life prediction can be done by integrating the FCG law, as described in section 2.3, from the assumed initial crack length, a_i , to the final crack length, a_f . The prediction method will be discussed in section 2.4.3.

In the phenomenological strength wear-out approach, specimens are loaded until a certain number of cycles then quasi-statically tested until failure. The relationship between the residual strength and number of cycles is established [82] as shown in Fig. 2-13 for different load levels. The fatigue life can be determined until reaching the failure criterion, where the residual strength decreases to the maximum applied load, L_{max} .

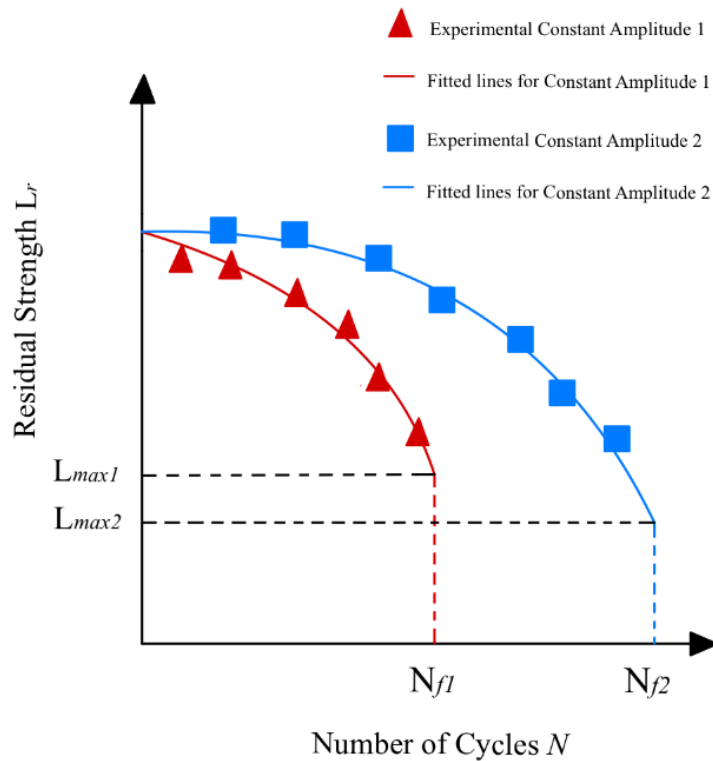


Fig. 2-13 Schematic of strength wear-out approach [77]

An alternative phenomenological approach is to relate the accumulated damage in the joint to the stiffness degradation. In this approach, the stiffness degradation can be correlated to the number of cycles by a power function [98]. The failure criterion can be defined as:

$$\frac{E(N_f)}{E(0)} = \frac{S_{\max}}{S_u} \quad (2-3)$$

Where $E(N_f)$ and $E(0)$ are the stiffness at the number of cycles to failure, N_f , and the original stiffness of the joint, respectively, S_u is the original ultimate strength of the joint.

In practice, there is always overlap among these different approaches. For instance, the relationship between crack initiation life and stress parameter is just another form of stress-life approach, where a different failure criterion is adopted. When the stiffness wear-out failure criterion is adopted, the stiffness-controlled S - N (S_c - N) curve can be obtained [89,99]. Anyway, existing research remains focusing on the fatigue performance of simple plated adhesively bonded joints, where a thick adhesive present at the bonded interface. The fatigue performance of the bonded joints with a more complex geometry such as the wrapped composite joints, where the composite material is directly bonded on the steel surfaces, may differ from those of adhesively bonded joints, especially in terms of failure modes (cohesive or adhesive failure). This needs further investigation.

2.4.2 Debonding crack growth monitoring

One critical issue for characterizing and predicting fatigue behaviour of bonded joints is to monitor the crack propagation at the bonded interface. When having difficulty in directly monitoring the crack growth from the side of the bonded interface as is done for ENF or DCB specimens, many researchers proposed to monitor crack growth at the bonded interface by tracing strain development in the composite material on top of the interface. For example, Kentaro [100] and Xinzhe Min [101] used strain gauges to measure strain distribution on surface of FRP to monitor debonding at FRP-concrete interface under fatigue loading. The results showed that the longitudinal strain kept a constant high value at the fully debonded zone, decreased gradually at the stress transfer zone and remained as low values at the bonded zone. The length of the plateau with high-stress level increased with number of cycles and was employed as debonding or crack length. However, strain gauges can only measure strain distribution along single lines, which cannot be used for full field measurements. Furthermore, the utilization of strain gauges may lead to unnecessary damage to composite materials. During recent years, the non-destructive technique (NDT) has been widely used for mechanical damage assessment in composite structures [102,103], especially for monitoring debonding at composite-to-steel/concrete interface. Current NDT techniques developed for civil engineering application include use of Acoustic emission (AE) [104,105], ultrasonic guided waves [106–108], infrared thermography [109,110], X-ray radiography [111], and digital image correlation (DIC) [112] et al.

Among these NDT techniques, the DIC technique has been widely used for monitoring debonding between composite to steel/concrete/masonry substrates due to its advantages of non-contact, full field and real-time measurements. DIC employs tracking and image registration techniques for accurate 2D and 3D measurements of deformations and strains on surfaces of specimens. For example, Bahman Ghiassi [113], Pei Zhang [114] and Mohamad Ali-Ahmad [115] investigated debonding between FRP and substrates under quasi-static monotonic loads by DIC. Strain contours were captured under different load levels, where increased strains indicated crack initiation or debonding at the interface. In their studies, a formula was proposed to approximate strain distribution along the bond length, such that the fully debonded zone, stress transfer zone (effective bond length) and bonded zone can be depicted quantitatively. The DIC method was also applied for investigating debonding behaviour under fatigue loading [116]. The strain plateau along the CFRP plate represented the debonding length which increased gradually with the increasing number of loading cycles. Other researchers [117] also employed gradient of surface strain to quantify debonded areas: a contour of high strain gradient indicates the debonding front and the region bounded by this contour with negligible strain gradient is the debonded area. In order to validate the crack monitoring method based on surface strain, some other researchers [118,119] also employed DIC to monitor damage in specimens with artificial delamination/debonding at the interface. The results showed that the location of the artificial delamination can be effectively detected

by DIC strain contours. The DIC results were also comparable with results from finite element (FE) models. But it should be noted that the thickness of the material above the delaminated interface may have influence on the monitoring results. However, existing research using DIC as the crack growth monitoring technique mainly focused on delaminated/debonded interface covered by thin laminates with constant thickness. Recently, the monitoring technique for debonding in joints with a complex geometry (i.e. under thick laminates with variable thickness), such as in wrapped composite joints, has been developed by the authors [120], which will be used in this dissertation for quantifying the debonding crack growth in the joints.

2.4.3 Numerical modelling on fatigue crack growth in bonded joints

The cumbersome fatigue testing and crack monitoring technique on the bonded joints makes it not always possible to predict the fatigue life of the joints by experimental work. Instead, numerical modelling techniques have been developed in the past decades to predict the fatigue delamination in composites or debonding in bonded joints. Roughly these methods can be classified into three categories [121]: 1) stress/strain methods; 2) fracture mechanics based methods and 3) damage mechanics based methods.

The stress/strain method is usually applicable to static delamination / debonding problems. Or it is commonly used to predict the final fatigue life instead of predicting the fatigue crack growth process. Limited work has been done to correlate the stress or strain in the material to the fatigue crack growth rate adopting similar form with Paris curve [122,123], which successfully predicted the test results. However, the complex and singularity arising at the bonded interface, especially at the bi-material interface, makes the application of stress / strain based methods still limited.

The most widely used numerical method for predicting crack propagation is based on the fracture mechanics, where the crack growth rates are linked to the strain energy release rates (SERR) at the crack tip as described in 2.3.1. The finite element method is usually utilised for calculating the SERR values and the most common one is the virtual crack closure technique (VCCT) [50]. This method assumes that the energy required to open a crack is the same as the energy required to close it. Fig. 2-14 schematically shows the principle of VCCT in a 3D 8-noded element case. Based on that, the mode I, mode II and mode III SERR can be calculated as:

$$G_I = -\frac{1}{2b\Delta a} F'_{zLi} (w'_{Li} - w'_{Li*}) \quad (2-4)$$

$$G_{II} = -\frac{1}{2b\Delta a} F'_{xLi} (u'_{Li} - u'_{Li*}) \quad (2-5)$$

$$G_{III} = -\frac{1}{2b\Delta a} F'_{yLi} (v'_{Li} - v'_{Li*}) \quad (2-6)$$

where Δa is the element length at the crack front, b is the element width, F'_{zLi} , F'_{xLi} and F'_{yLi} are the nodal forces at the crack tip, w , u and v are the nodal displacements behind the crack tip in the z , x and y direction, respectively.

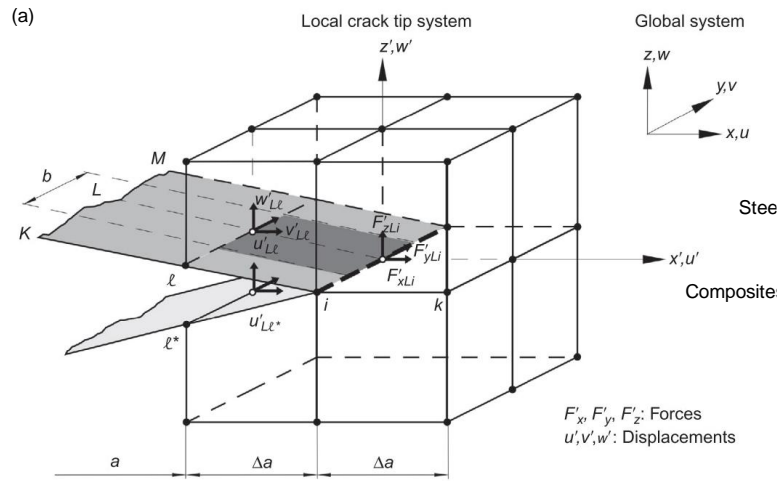


Fig. 2-14 Schematic of virtual crack closure technique (VCCT)

Knowing the SERR values, the crack growth can be calculated by integrating Eq. (2-1). In practice, the total number of cycles can be calculated numerically as shown below:

$$N_f = \sum_{i=1}^n \frac{\Delta a_i}{C \Delta G_i^m} \quad (2-7)$$

Quaresimin and Ricotta [97] used VCCT to calculate the SERR in a bonded joints. Combined with the Paris curves, they successfully predicted the fatigue life in the debond propagation phase which agreed well with the experimental results. Pirondi et al. [124] applied the direct cyclic (DC) analysis using VCCT for predicting the crack growth curves of DCB, ENF and SLJ joints where different mode mixity existed. The VCCT model gave rather good agreement with the test results with regard to crack length vs. number of cycles and G vs. crack length. Martulli et al. [125] developed a sequential static fatigue (SSF) algorithm to model the fatigue delamination in composite materials. The SSF method is based on static simulations thus needs reduced computational time than the DC analysis.

While the VCCT-based method requires the crack front to be positioned along the element boundaries and sometimes a predefined front shape, another fracture mechanics-based approach which can help solve the problem is the thick level set method [126,127]. This approach allows non-local computation of the SERR. A level set field is defined to describe the crack front location implicitly, which is updated according to the Paris relationship. The modelling results showed that the smooth and arbitrary crack shape can be modelled accurately compared to the experimentally results.

An alternative approach which is based on the damage mechanics is the cohesive zone model (CZM) [128], where the damage accumulation can be modelled. CZM is based on the traction-

separation law at the interface, where the important inputs include the initial stiffness, the maximum tractions and the critical energy release rate. Under fatigue loading, the traction-separation law is modified by degrading the stiffness, strength as well as the fracture energy as a function of load cycles [129]. This is usually realized by defining a damage parameter. Simulating fatigue crack growth in bonded joints based on cyclic CZM has been applied by lots of researchers. Fernandez et al. [130] successfully modelled the mode I fatigue debonding in a DCB specimen using the CZM. Rocha et al. [131] showed that the CZM can also be applied to simulate the fatigue debonding behaviour of adhesive joint in mixed mode loading conditions through a user defined material (UMAT) in Abaqus. Different from the damage elasticity behaviour of CZM assumed in most of the numerical study, Doroudi et al. [132] also proposed a damage plasticity model to simulate the residual displacement at the bonded interface when unloaded under cyclic loading. Besides constant fatigue loading, the fatigue damage of the adhesively bonded joints under variable amplitude loading is also successfully simulated by Khoramshad et al. [133]. For bonded joints of dissimilar materials, Choi and Kim [134] simulated the fatigue crack growth specimens with straight and penny-shaped cracks.

It can be seen that these modelling approaches mentioned above have been successfully applied for simulating fatigue damage in simple plated adhesively bonded joints. The application in simulating fatigue debonding behaviour in complex, e.g. 3 dimensional, bonded interface is still limited, especially for bonded joints with negligible thickness of the adhesive layer.

2.4.4 Probabilistic analysis on fatigue crack growth

Fatigue crack growth usually show a considerable statistical variability even in well-controlled laboratory conditions [135]. The variability may results from different factors such as small differences in material properties, geometries, loading conditions, et al. A commonly used method to reproduce and explain this phenomenon is through Monte-Carlo simulation, which has been widely applied for crack growth in metals. Bogdanov et al. [136] used the Monte-Carlo simulation method combined with the UniGrow FCG model to replicate the distribution of fatigue life in the aluminium alloy successfully. The variability of fatigue crack growth constant, C parameter, is considered. Sanches et al. [137] conducted the probabilistic analysis on fatigue crack growth in riveted joints using Monte Carlo simulation. Uncertainties of input parameters of clamping stress, friction coefficient, Paris law parameters and crack initiation criterion are considered. Probabilistic $S-N_f$ fields are obtained based on the modelling results, which agreed well with the test results. He et al. [138] applied the Kriging-based Monte Carlo simulation method to assess the probabilistic life of mixed-mode FCG. The probabilistic crack growth analysis is also applied for the bonded joints in [139], where the a rapid fatigue damage growth simulator is developed in combination with a Markov chain Monte Carlo (MCMC) method to estimate the probabilistic fatigue life of SLJ. It was observed that experimental fatigue life lies inside the prediction intervals.

2.5 Summary

It can be seen based on the literature review that although composite materials have been widely applied to strengthen the hollow section joints, welding still remains as the main load transferring mechanism in the joint, serving as the source of fatigue failure. An alternative joining technique, the wrapped composite joint, has been proposed where steel tubes are connected through a composite wrap. Its static performance has been studied in Ref. [140] which proves that the wrapped composite joint can have higher stiffness and sufficient loading carrying capacity compared with the welded counterparts. A preliminary study [6] on the fatigue behaviour of wrapped composite joints also demonstrated its better performance than welded ones. However, a deeper investigation on the fatigue behaviour of the newly proposed joints needs to be conducted, and the corresponding prediction method needs to be established.

Regarding the critical debonding failure mode, the FCG properties at the composite-to-steel interface need to be characterized. While fatigue ENF and 4ENF tests have been widely applied for characterising FCG properties in composite laminates, its application in bonded bi-material interface is still limited. The influence of surface roughness of the steel plate on the interface properties needs to be studied.

Comprehensive experimental and numerical studies regarding the fatigue performance of bonded joints can be found in literature. However, most of the studies were conducted on simple plated bonded joints, whereas the fatigue debonding behaviour in joints with a more complex geometry is limited. The present work will expand the study into that challenging field, taking the investigation on the fatigue debonding resistance of wrapped composite joints as the first step.

CHAPTER III

CHARACTERIZATION OF FATIGUE CRACK GROWTH PROPERTIES OF THE COMPOSITE- TO-STEEL INTERFACE

Parts of this chapter appear in the journal article: 'W. Feng et al., Influence of surface roughness on the mode II fracture toughness and fatigue resistance of bonded composite-to-steel joints. Constr Build Mater 2024;411:134358. '

3.1 Introduction

Since the investigation of debonding failure of wrapped composite joint is the primary focus in this thesis, it is crucial to characterize the fatigue crack growth (FCG) properties at the composite-to-steel interface level, such as to enable the prediction of the fatigue behaviour at the joint level. Furthermore, the bond quality of the joint highly relies on the surface preparation, e.g. surface roughness, of the steel members. Investigation on the influence of steel surface roughness on the FCG property of the bonded joint is another subject of this chapter. As will be revealed in the finite element analysis in the following chapters, the mode II crack, i.e. the shear mode crack, is the dominate fracture mode in the tensile loading case of the wrapped composite joint. Therefore, the mode II FCG property will be the primary focus. In this chapter, Static and fatigue 4-point end notched flexure (4ENF) tests are conducted for specimens with different surface roughness. The roughness of the steel plate and the fracture interface is characterised by a 3D profilometer. To account for the friction effect at the interface on the measured fracture toughness and fatigue resistance, the friction coefficients between the fractured interface are measured by a tribometer, serving as the inputs for interpreting strain energy release rates (SERR) through finite element models. The fracture toughness and the FCG curves of the composite-to-steel interface are obtained and correlated with the steel surface roughness, serving as the input for the following modelling on the joint level. Finally, a total life FCG model is applied to fit the test results in order to consider the decreased crack growth rates near the SERR threshold.

3.2 Specimens and surface characterization

3.2.1 *Specimens and materials*

In this study, a total of 18 bonded joint specimens are used for the static and fatigue 4ENF tests as shown in Table 3-1. For each loading type, surface of the mild S275 steel plates were grit blasted with low, medium and high blasting pressures, respectively, to achieve 3 different surface roughness. 3 identical specimens were tested for each configuration. The steel-composite specimens were manufactured by hand lay-up of the glass fiber plies on the steel treated surface. Before lamination, the surfaces of steel plates were chemically degreased to ensure good bonding quality and a non-adhesive insert of 32 μm thickness was placed to induce a pre-crack between steel and composite arms. Each composite ply is formed by woven glass fibre reinforcement fabric interleaved with chopped strand mat (CSM) and a vinyl ester matrix system with fibre volume fraction of approximately 30%. CSM layer is adjacent to the steel-composite interface. Finally, steel-composite specimens are cut from the plates using water jet. Geometry and dimensions of the specimens used in this study are shown in Fig. 3-1. The half-span (L), width (B), upper and lower arm thicknesses (h_1 and h_2), pre-crack length (a_0) and the load-to-support point distance (L_a) are indicated in the figure. For the bi-material configuration, the thicknesses of steel and composites are designed to meet the criterion described in Eq. (1),

such that the two arms have the same longitudinal strain at the faying surfaces to obtain a pure mode II loading condition [65].

$$E_1 h_1^2 = E_2 h_2^2 \quad (3-1)$$

where E_1 and E_2 are the elastic modulus in the longitudinal direction for the upper and lower arms, respectively. The actual thickness of the specimens vary among different roughness series due to variation of applied pressure during hand lamination and curing conditions. The measured average total thickness of the specimens are listed in Table 3-1.

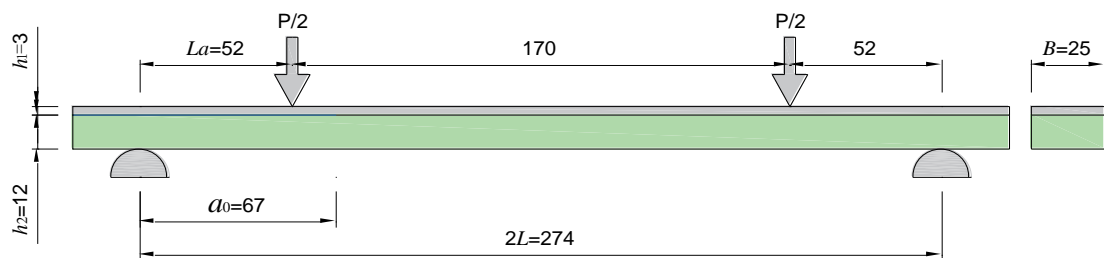


Fig. 3-1 Dimensions of specimen (in millimetres)

Table 3-1 Test specimens

Loading type	Blasting pressure	Specimens	Total thickness (mm)	Displacement rate / Frequency
Static	low	RL-S-1/2/3	17.64	1 mm/min
	medium	RM-S-1/2/3	17.47	
	high	RH-S-1/2/3	15.38	
Fatigue	low	RL-F-1/2/3	17.64	4 Hz
	medium	RM-F-1/2/3	17.47	
	high	RH-F-1/2/3	15.38	

The material properties of steel plates and composite laminate are obtained by standard tensile/compressive coupon tests according to ISO [141–144] and are summarised in Table 3-2. Mechanical properties of the polymer resin were provided by the manufacturer with $E=3300$ MPa, $f_y=77$ MPa and σ_u (elongation at fracture)=7%, respectively.

Table 3-2 Material properties

Material	Mechanical property	Average value and (CoV [%])
Composites	Longitudinal and transverse compressive modulus – $E_{x,c}=E_{y,c}^1$	12077.11 MPa (4.50)
	Longitudinal and transverse tensile modulus – $E_{x,t}=E_{y,t}$	11798.20 MPa (6.37)
	Poisson’s ratio – ν_{xy}	0.15 (6.50)
	In-plane shear modulus – G_{xy}	3120 MPa (6.81)
Steel	Young’s modulus – E^2	190000 MPa (5.42)
	Yield strength – f_y	278.30 MPa (0.22)
	Ultimate strength – f_u	637.83 MPa (0.40)

1: E_2 equals to the average of the compressive and tensile modulus in the present study
 2: equals to E_1 in the present study

3.2.2 Surface roughness

The surface treatment of the steel plates were measured by a 3D optical profilometer (Keyence VR6000) with 40× magnification. The surface roughness was obtained from two 20×20 mm areas selected on the steel plates of each roughness series. Optical images and 3D profile of the scanned areas for each roughness series are shown in Fig. 3-2. It can be seen that, compared to the relatively smoother surface of low roughness, sharper peaks and valleys are found in the medium and high roughness plates.

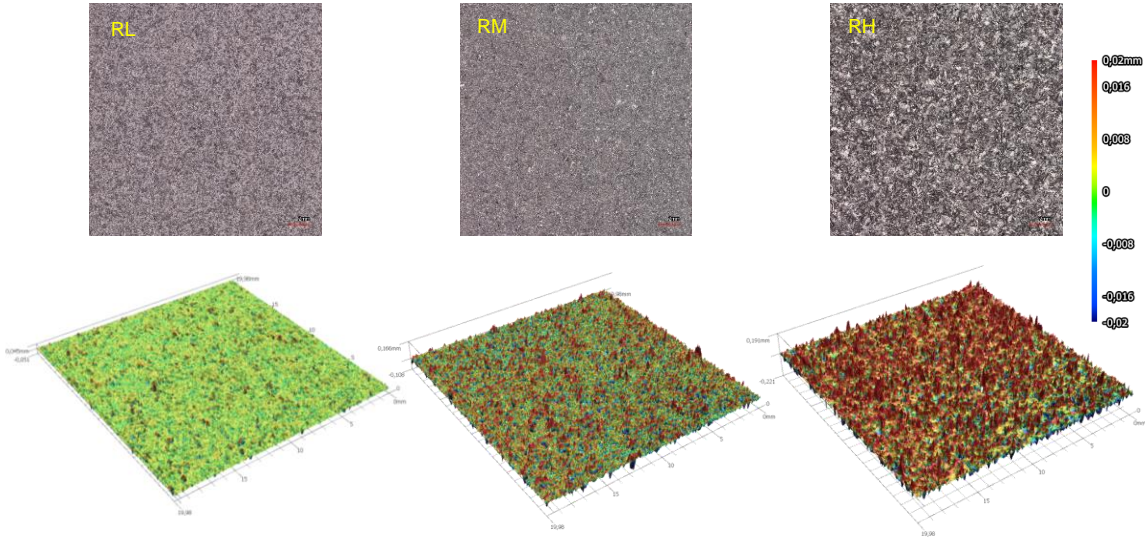


Fig. 3-2 Optical and 3D profile of steel surface with different roughness

Two surface roughness parameters, namely S_q and S_{dr} , are chosen here according to [145] with the definition given by Eq. (3-2) and (3-3). S_q represents the root mean square value of ordinate values within the definition area, A . It is equivalent to the standard deviation of heights. Since

different surface profiles can have similar S_q values, another parameter, the developed interfacial area ratio S_{dr} , is selected to assess the surface topology. S_{dr} is expressed as the percentage of the definition area's additional surface area contributed by the texture as compared to the planar definition area.

$$S_q = \sqrt{\frac{1}{A} \iint_A Z^2(x, y) dx dy} \tag{3-2}$$

$$S_{dr} = \frac{1}{A} \left[\iint_A \left(\sqrt{1 + \left(\frac{\partial z(x, y)}{\partial x} \right)^2 + \left(\frac{\partial z(x, y)}{\partial y} \right)^2} - 1 \right) dx dy \right] \tag{3-3}$$

The average measured results for each roughness series are summarised in Table 3-3. From low to high roughness, the S_q value increases from 4.56 to 21.99 μm , while the developed interfacial area ratio S_{dr} increases from 0.99% to 11.67%. S_{dr} is plotted against S_q in Fig. 3-3 and a quiet linear relationship can be found between these two parameters, indicating that a rougher surface leads to a larger developed interfacial area.

Table 3-3 Surface roughness measurement results

Parameters	S_q (μm)	S_{dr} (%)
RL	4.56±0.75	0.99±0.16
RM	14.14±1.24	5.87±0.06
RH	21.99±0.62	11.67±0.46

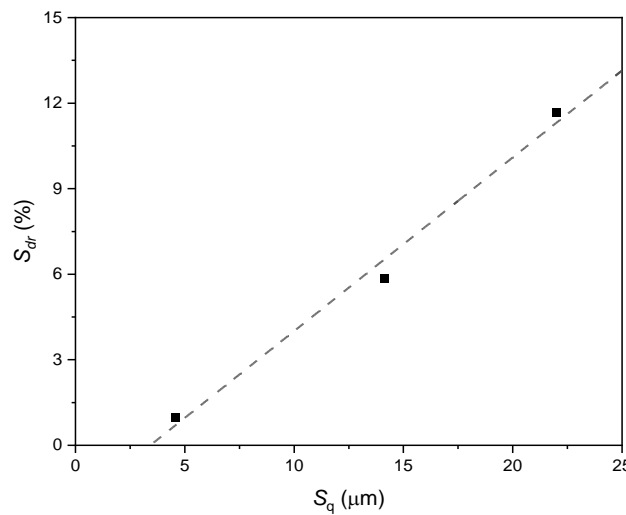


Fig. 3-3 Relationship between S_q and S_{dr}

3.2.3 Friction coefficient

In order to account for the friction effect between the cracked surfaces in fracture and fatigue crack growth tests, the friction coefficient was measured at the pre-crack region and the fractured composite-to-steel interface after the tests. Fig. 3-4 shows the samples cut from the

fractured specimens in static tests, whose failure modes will be discussed in detail in section 4.1. Three samples are cut from the pre-crack region, with the insert remaining on top of the composites. Nine samples are cut from the fractured interface, with three samples selected from each roughness series.

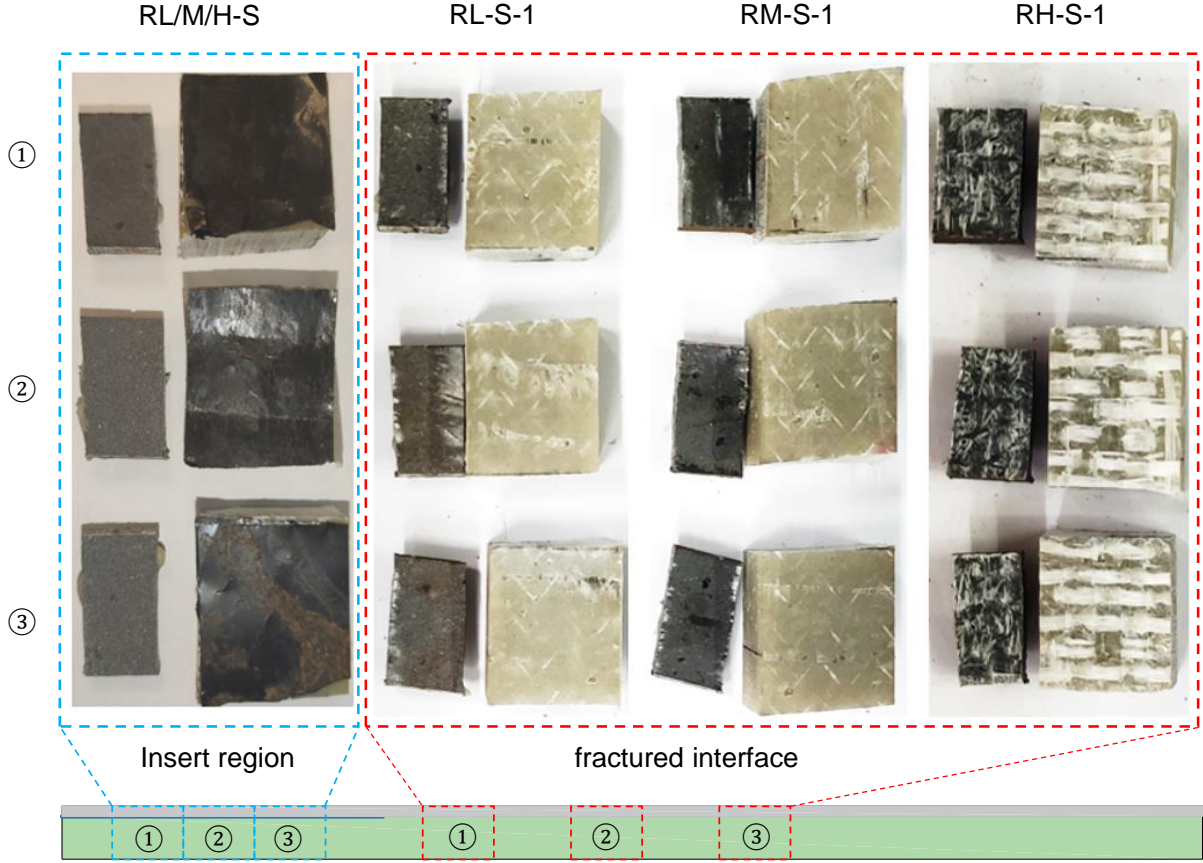


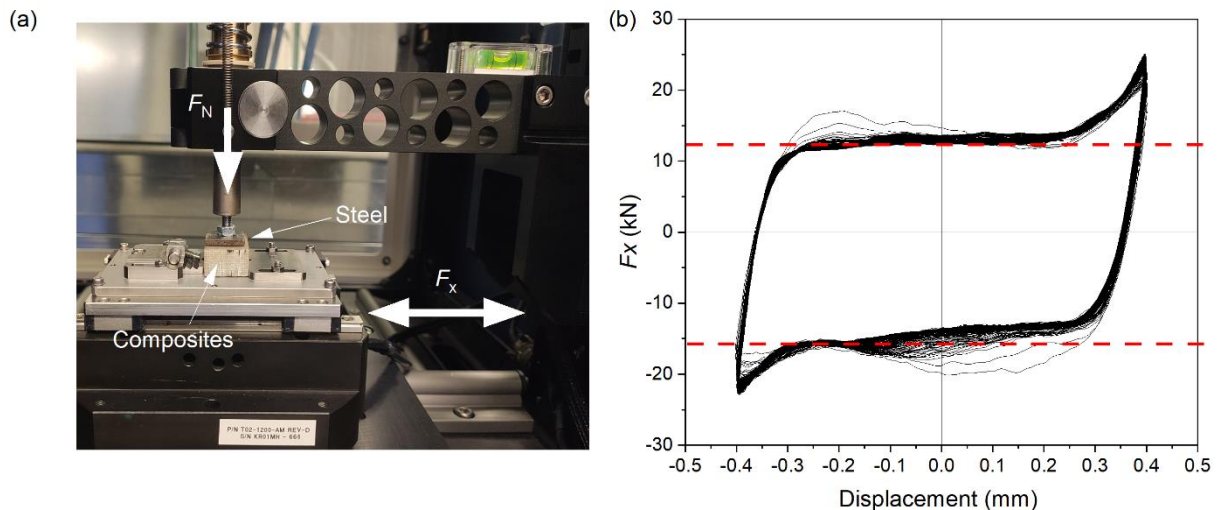
Fig. 3-4 Sample used for measuring friction coefficient (from static tested specimens)

The friction coefficient was measured by a multi-function tribometer (Rtec MFT-5000). As shown in Fig. 3-5 (a), the normal force, F_N , is applied on the steel plate through a customized cylinder. The composite laminate is fixed on the bottom and moved with the XY stage. A load cell embedded in the horizontal direction is used to monitor the friction force, F_x . During the fatigue 4ENF test, an obvious relative movement is observed between the fractured steel and composite arms. Therefore, a relatively large amplitude, i.e. 0.8 mm, is chosen here to mimic the reciprocating gross slip regime during the test. The composite laminate moves in the X direction, leading to the same relative movement direction against the steel arm during the 4ENF tests. Samples cut from fatigue tested specimen are measured with 4 Hz, which is the same as that used in the fatigue tests, while samples cut from the static tested specimen are measured with 0.2 Hz to mimic the quasi-static process.

A typical frictional hysteresis loop is shown as Fig. 3-5 (b). The friction force remains nearly constant around the middle position but increases obviously at the extreme position. This results from the decreasing velocity when the movement direction changes and the static friction, instead of kinetic friction, takes place. Since the influence of friction on the SERR at the crack

tip is related to energy dissipation mechanism during the kinetic friction process, the average friction force at the plateau (red dash line in the figure), \bar{F}_x , is employed to calculate the friction coefficient by the equation of $\mu = F_N / F_x$. The friction coefficient variation against number of cycles is shown in Fig. 3-5 (c), where each point in this figure represents average results of two directions. The plateau of the curve is taken as the result of each sample to exclude the possible ‘running-in’ effect [146] during the initial cycles.

Average friction coefficients between the cracked surfaces of the different roughness under fatigue (4 Hz) and quasi-static (0.2 Hz) loading protocols are shown in Fig. 3-5 (d). The friction coefficient increases slightly with the surface roughness for both cases. Specifically, friction coefficient at 4 Hz increases by 10.9% from 0.46 for low roughness series to 0.51 for high roughness, while friction coefficient at 0.2 Hz increases by 9.6% from 0.52 to 0.57. Friction coefficient at 0.2 Hz varies between 12% and 19% higher than that at 4 Hz for different roughness. It should be noted that the results of all the samples reflect friction coefficients at the fractured surfaces, instead of the pure interface between steel and composite materials. The failure modes will be further discussed in the following sections. In addition, the friction coefficients at the pre-crack region are 0.23 under 4 Hz and 0.3 under 0.2 Hz. This values are relatively lower than that in the fractured interfaces due to the existence of an insert between the surfaces. The measured friction coefficients will be used in the FE models for each roughness series under both static and fatigue cases in the later sections.



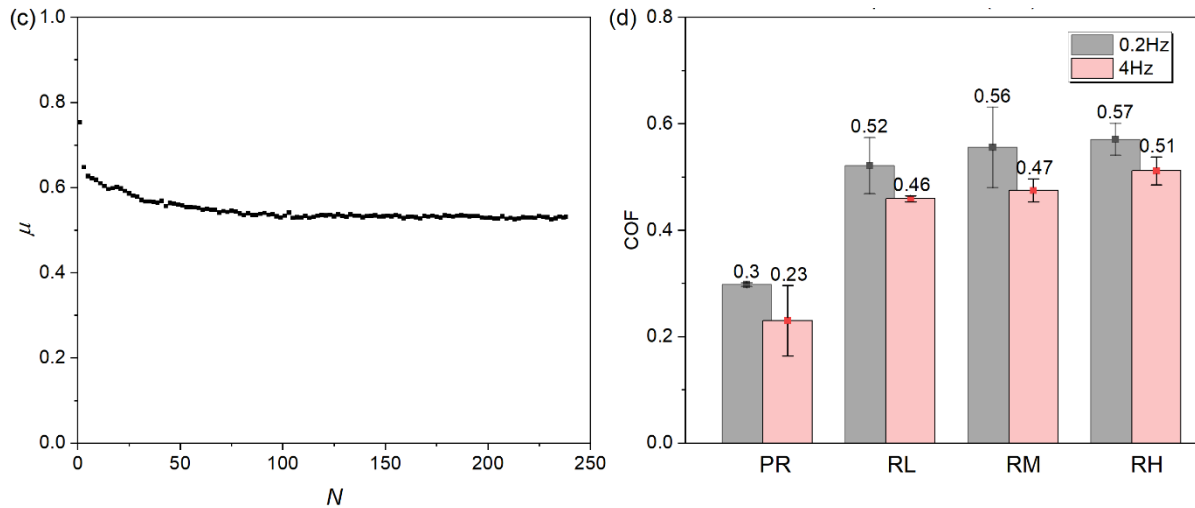


Fig. 3-5 Friction coefficient measurement (a) test set-up; (b) frictional hysteresis loops; (c) friction coefficient versus cycles; (c) friction coefficient versus surface conditions

3.3 Experimental methods

3.3.1 Test set-up, instrumentation and loading protocol

Tests were conducted in a universal testing machine (UTM) with a load cell of 15kN. The 4-point bending test set-up is shown in Fig. 3-6, where the steel arm is on top to avoid crack migration to the composite layers [147]. The specimens are loaded by two loading cylinders attached to a loading beam, which is connected to the actuator by a shaft such that equal forces are applied on the two loading points. The static tests are conducted by displacement control with the loading rate of 1mm/min. According to the separate study (not detailed in this thesis) [148], the fatigue tests on 4ENF specimens can be more stable and achieve wider SERR range under displacement control compared to force control. Furthermore, a fixed loading force will lead to a constant SERR value (just one point) on the Paris curve. Therefore, the fatigue tests are conducted by displacement control with the frequency of 4Hz. For the fatigue tests, the load ratio $R=0.1$, namely $F_{\min}/F_{\max}=0.1$, is adopted. For each roughness series, the fatigue tests are started with the force level (F_{\max}) corresponding to 60% of the critical SERR obtained by the static tests. This starting load level is chosen to be high enough to cover as wide SERR range as possible since the SERR values will decrease during the tests, but to be low enough to avoid too fast crack propagation (e.g. 0.1mm/cycle) for the convenience of crack length monitoring.

A white paint coating followed by a black speckle pattern is applied on one side of the specimens to allow measurements by digital image correlation (DIC). The speckle size is chosen between 0.2-0.5 mm based on the requirement of DIC analysis. A digital camera (51 Mpx) assisted by a LED light is positioned perpendicular to the specimen for crack length monitoring during the tests. With the camera connected to the controlling system, photos are taken at the minimum and maximum displacements every 500 cycles or every 1% stiffness degradation. Shear strains are extracted at the interface afterwards during the DIC analysis and

are quantified by the strain thresholds to determine the crack length. The explanation of crack monitoring technique can be found in section 3.3.3.

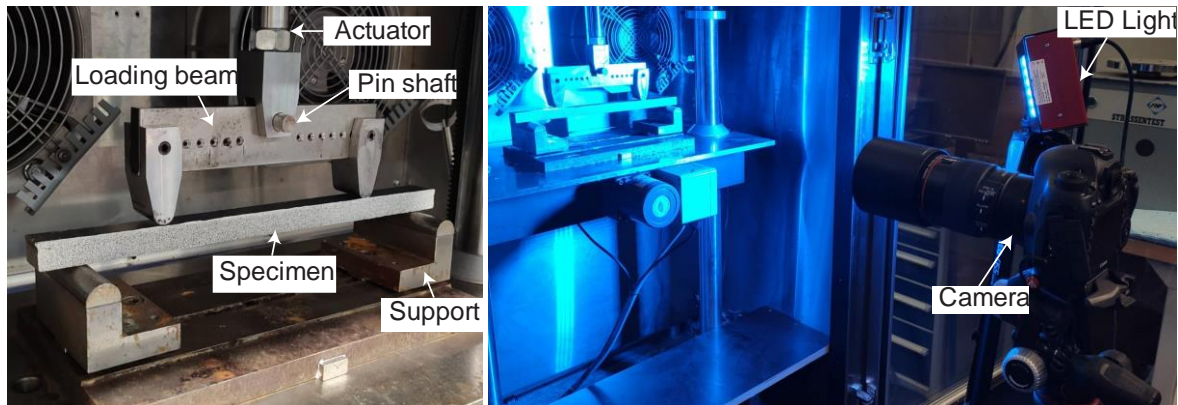


Fig. 3-6 Test set-up and instrumentation

3.3.2 Fracture data analysis

The crack growth driving force is calculated by the extended global method (EGM), proposed by Moslem, et al. [149] based on the global method by Williams [48]. The global method is developed based on the beam theory where the SERR is calculated by the bending moments and loads in a cracked specimen. EGM modified this global method in order to consider asymmetric cases where the crack propagates between two different orthotropic layers. The mode II SERR at the crack tip of 4ENF specimens can be calculated as:

$$G_{II,4ENF} = \frac{P^2 L_a^2}{8BE_1 I_1} \left(\frac{1}{1+\psi} - \xi \right) \quad (3-4)$$

where ψ and ξ are the bending stiffness ratios of arms for the specimens, which can be calculated by:

$$\psi = \frac{E_2 I_2}{E_1 I_1} \quad (3-5)$$

$$\xi = \frac{E_1 I_1}{(EI)_{eq}} \quad (3-6)$$

In Eq. (3-4), (3-5) and (3-6), E_1 and E_2 are the longitudinal modulus of the upper and lower arms. I_1 and I_2 are the moment of inertia of the upper lower arms, respectively. $(EI)_{eq}$ is the equivalent bending stiffness of the specimen.

Another commonly used method for calculating SERR at the crack tip is the virtual crack closure technique (VCCT), based on finite element (FE) model. The VCCT assumes the energy released for a small crack extension is equal to the work required to close the crack to its original length. Fig. 3-7 schematically shows the principle of VCCT in a 3D 8-noded element case. Based on that, the mode I, mode II and mode III SERR can be calculated as:

$$G_I = -\frac{1}{2b\Delta a} F'_{zLi} (w'_{Li} - w'_{Li*}) \quad (3-7)$$

$$G_{II} = -\frac{1}{2b\Delta a} F'_{xLi} (u'_{Li} - u'_{Li*}) \quad (3-8)$$

$$G_{III} = -\frac{1}{2b\Delta a} F'_{yLi} (v'_{Li} - v'_{Li*}) \quad (3-9)$$

where Δa is the element length at the crack front, b is the element width, F'_{zLi} , F'_{xLi} and F'_{yLi} are the nodal forces at the crack tip, w , u and v are the nodal displacements behind the crack tip in the z , x and y direction, respectively.

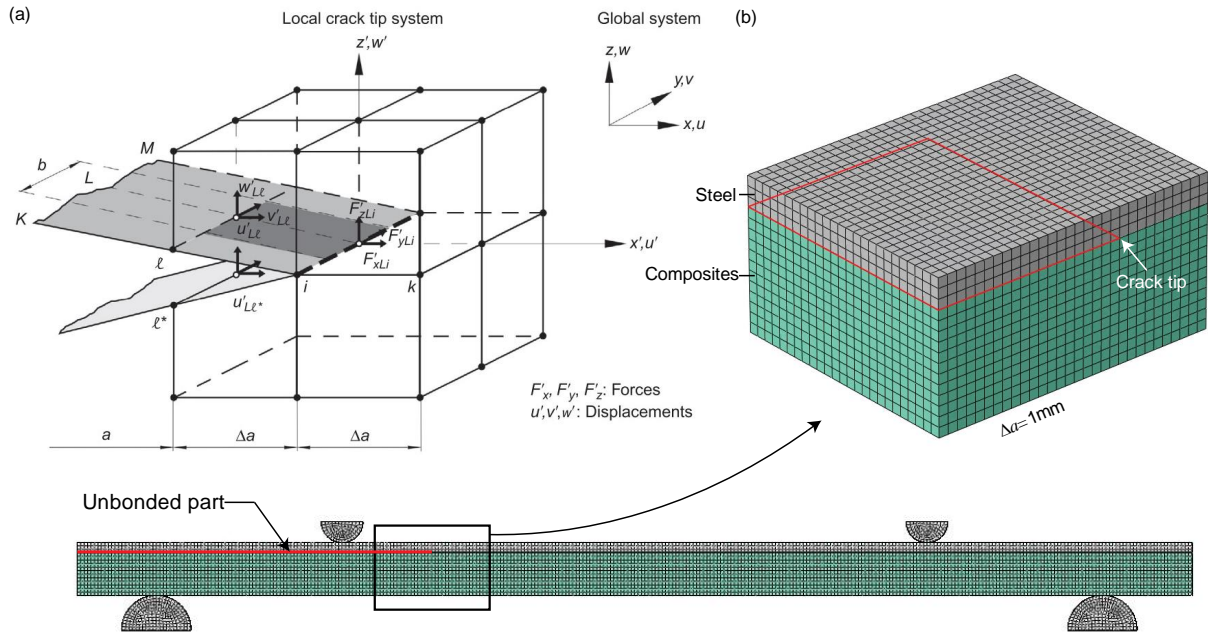


Fig. 3-7 schematic of virtual crack closure technique (VCCT)

By the VCCT, all components of the SERR can be obtained while the influence of friction on the SERR values at the crack tip is taken into account [148]. The geometry and boundary conditions of the FE model follow the design of the 4ENF specimens, as shown in Fig. 3-8. The specimen dimensions are taken as the average measured values indicated in Table 3-1. Elastic and plastic material properties, indicated in Table 3-2, are defined for the steel arm. The composite laminate is modelled as one piece of solid part in this model. As stresses in the composite during the tests are much lower than the strength of the material, only elastic material properties are used to model the composite laminate. Transversely anisotropic material properties are defined based on the tests results shown in Table 3-2 for the in-plane properties of the laminate: E_1 , E_2 , G_{12} and ν_{12} . In absence of experimental data, the out-of-plane elastic properties of the laminate E_3 , $G_{13}=G_{23}$, $\nu_{13}=\nu_{23}$ were estimated through the micromechanics (rule of mixture) for an equivalent unidirectional material. Linear, hexahedron 8-noded solid elements with reduced integration (C3D8R) are used for both steel and composite parts.

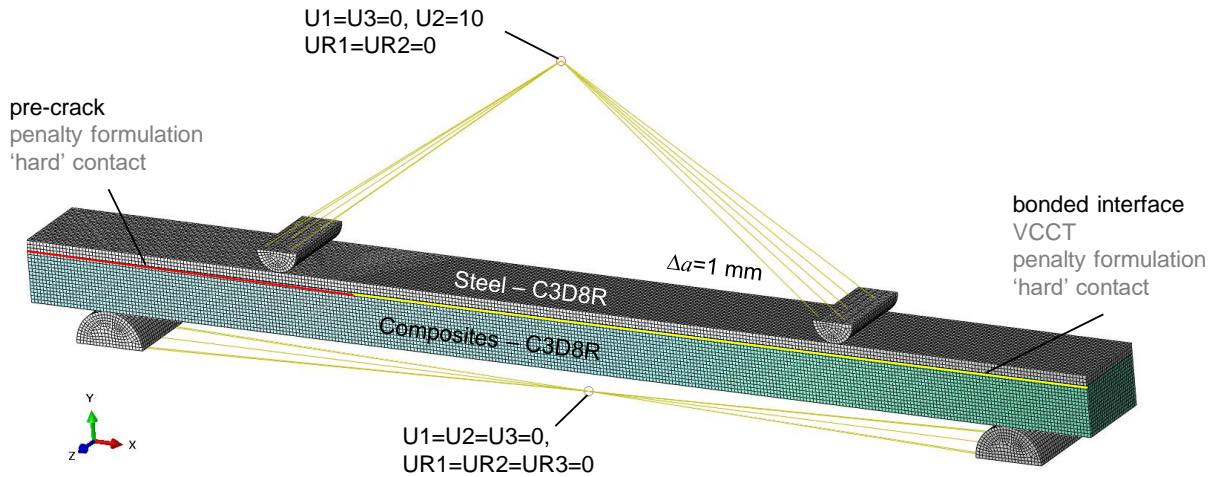


Fig. 3-8 Mesh topology and boundary conditions of FE model

The VCCT fracture criterion in combination with a friction behaviour are defined for the composite-to-steel interface. When modelling the fracture behaviour, the Benzeggagh–Kenane mixed-mode criterion is employed as Eq. (3-10):

$$G_{eqc} = G_{Ic} + (G_{IIc} - G_{Ic}) \left(\frac{G_{II} + G_{III}}{G_T} \right)^\eta \quad (3-10)$$

where G_{eqc} is the equivalent critical SERR, G_{Ic} and G_{IIc} are the critical mode I and mode II SERRs, $G_T = G_I + G_{II} + G_{III}$, and $\eta = 1.8$. Since mode I is not relevant in this study, the same critical value is defined for the mode I and mode II SERRs. While the FE model is used to obtain SERRs at a stationary crack tip, sufficiently high instead values of critical SERRs, e.g. 100N/mm, rather than the actual values, are provided in the analysis to prevent crack propagation. The penalty friction formulation is defined for the tangential behaviour. The friction coefficient of 0.3 and 0.23 are used for the pre-crack region and in the range of 0.46 to 0.57 for the fractured interface of different roughness series in the static and fatigue test models based on measurements presented in Fig. 3-5 (d). To account for the friction effect at the contact area between the loading/supporting cylinder and the specimen, a commonly used friction coefficient, 0.3, is also defined in these interactions.

A mesh sensitivity study is performed using a model with $a = 67$ mm. Different meshes with element length Δa of 0.5 mm, 1 mm, 1.5 mm and 2 mm and aspect ratio 1 are evaluated. The results of mode I/II/III SERR at the crack tip are extracted and normalized to 1 kN as shown in Fig. 3-9. Unrealistic values at the edges resulting from algorithm problems are excluded. It is shown in Fig. 3-9 (b) and (c) that mode II and III SERR converges for different mesh sizes. The mode I SERR is increasing as the mesh size decreases. This lack of convergence for mode I is also found in literature [150]. Mode I, II and III SERR values with mesh size of 1 mm are plotted together in Fig. 3-9 (d). It shows that contribution from mode I fracture component is negligible, thus the influence of non-convergence of mode I SERR is insignificant. Taking the convergence

of SERR values and computing efficiency into account, mesh size of 1 mm is chosen for the following analysis. The average mode II SERRs are considered for the analysis.

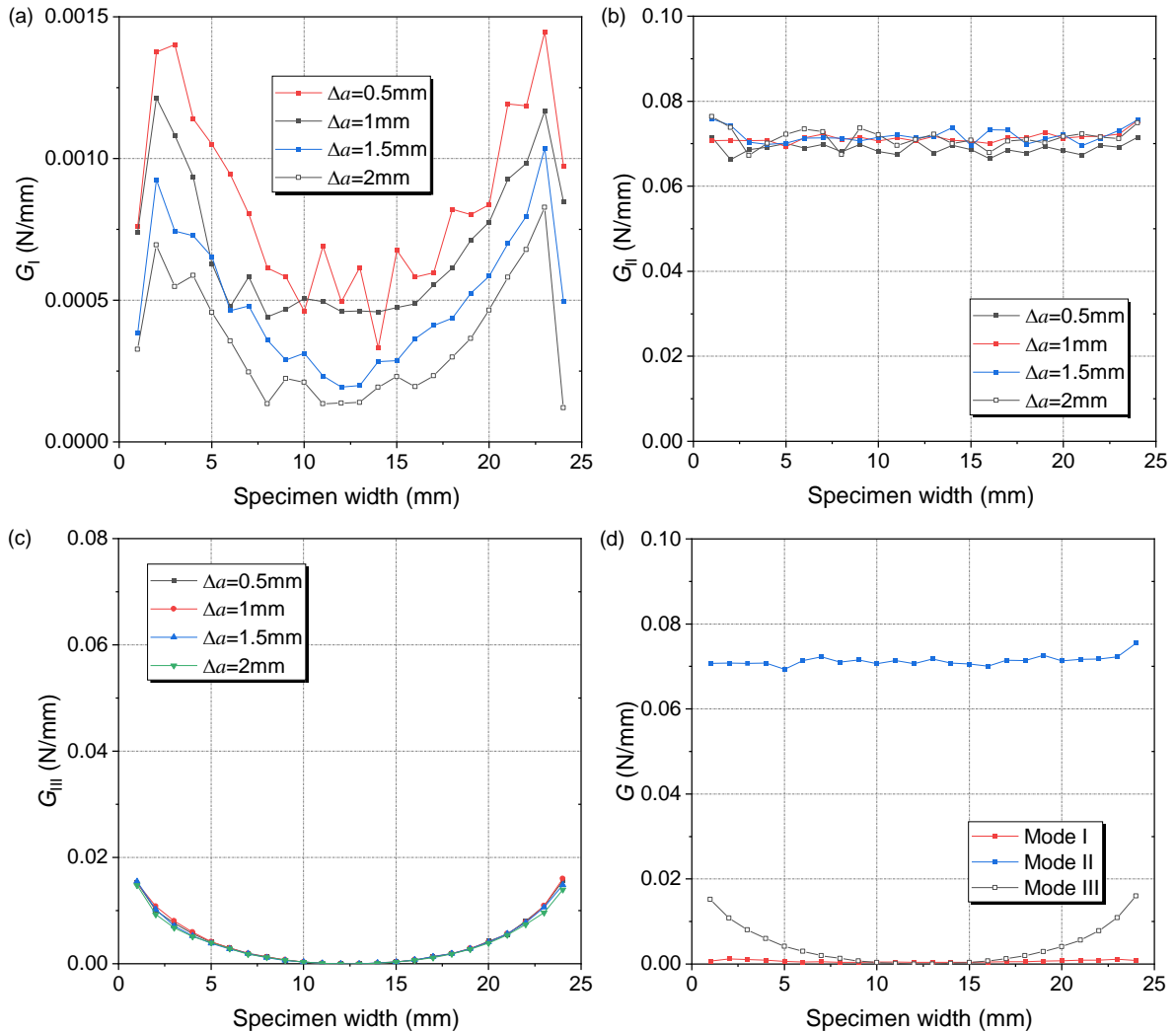


Fig. 3-9 SERR components and distribution along specimen width ($a=67\text{mm}$, $P=2\text{kN}$)

3.3.3 Crack growth monitoring technique

A widely used method for monitoring crack length, a , of an ENF specimen is the compliance calibration method (CCM), where the crack length is estimated by an experimentally measured or theoretically calculated compliance. The CCM is popular in mode II fracture tests for not requiring optical measurements. However, compliance-based methods require that all the materials remain in linear elastic behaviour such that the compliance increases solely from the crack growth. Therefore, it is not applicable in the presence of material nonlinearity, e.g. steel yielding in the steel-to-composite bonded joint.

An innovative method is proposed for measuring crack length based on DIC analysis of the strain along the interface. The shear strain distribution is extracted from a surface curve defined on top of the interface in DIC, as shown in Fig. 3-10 (a). The crack tip can be located by comparing the shear strain along the interface with a certain threshold, above which the

interface is considered to be debonded. As the shear strain at the crack tip is influenced by the local bending moments at the crack tip in the arms of the notched flexure specimen imposed by the external loading, a calibration test is done first. Purpose of the calibration test is to find the relationship between the shear strain threshold level and total bending moment, M (as indicated in Fig. 3-10) at the crack tip. The assumption is that the local bending moment in the steel and composite arms of the notched flexure specimen, namely M_1 and M_2 are correlated to the total bending moment at the crack tip $M=M_1+M_2$. During the calibration test, ENF and 4ENF specimens are loaded at levels below the critical force. The shear strains at the crack tip, namely the thresholds, under different bending moment levels are extracted as shown in Fig. 3-10 (b). A linear relationship between the threshold and moment at the crack tip is obtained, as shown in Fig. 3-10 (c). This fitted formula is then applied to the crack length measurements.

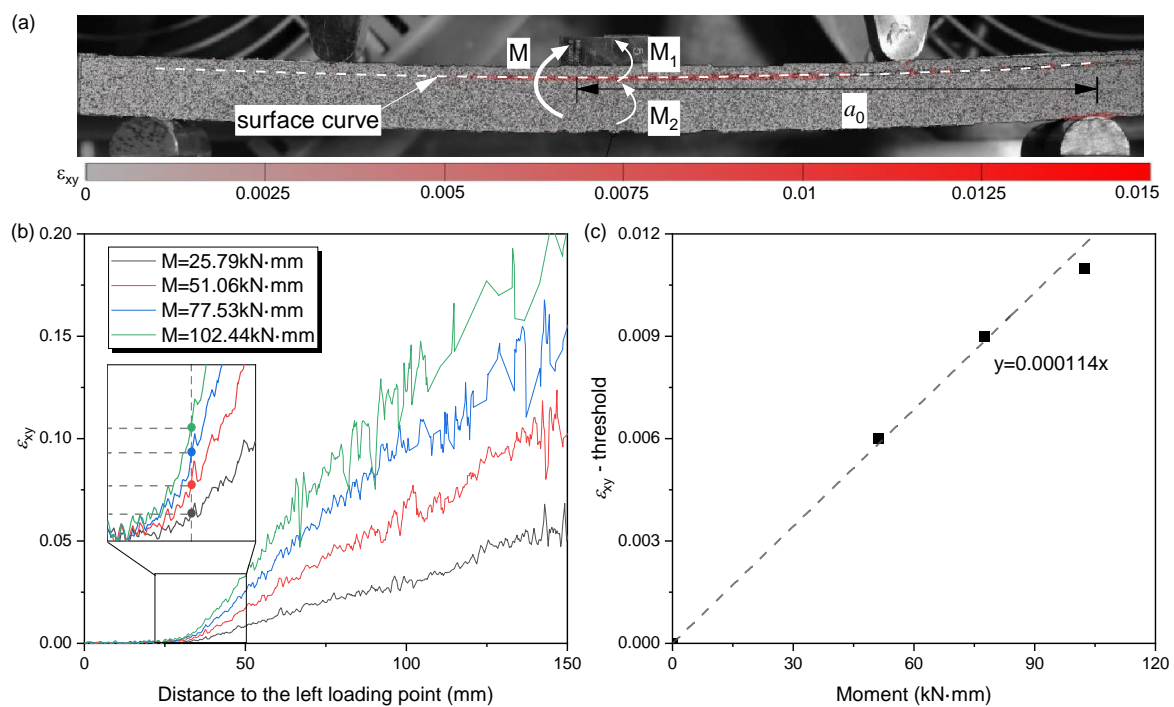


Fig. 3-10 Shear strain threshold for determining crack length (a) contour plot of shear strain from DIC; (b) shear strain distribution along the interface at different moment levels; (c) relationship between shear strain threshold and moment

The procedure for crack length determination analysis in a script is illustrated as a flowchart in Fig. 3-11. The shear strain along the interface is extracted at different cycles for each specimen, which serve as input for a script. For 4ENF tests, the moment at the crack tip is independent of the crack length, and the threshold used to calculate the crack length is updated solely according to the force variation for each cycle.

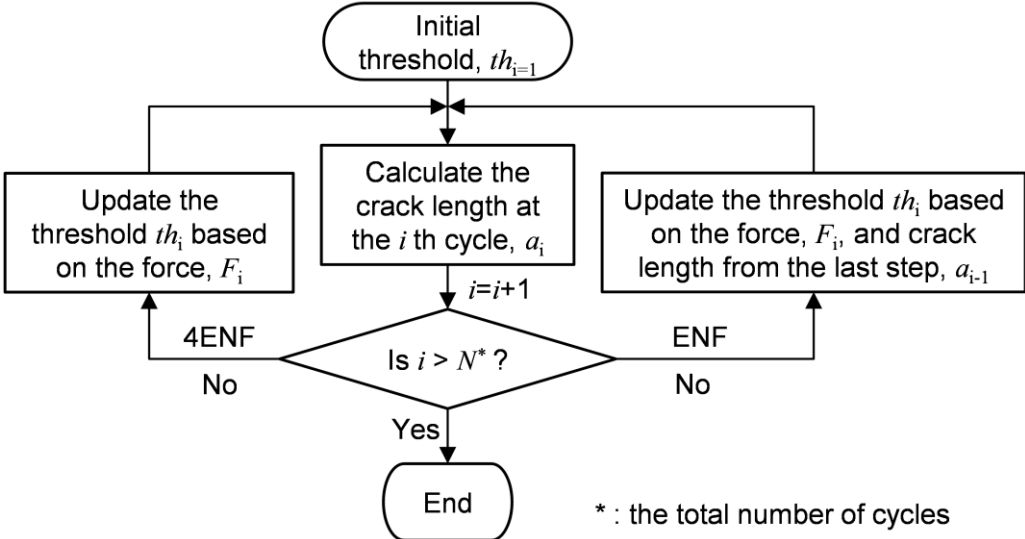


Fig. 3-11 Flowchart of script for crack length determination

3.4 Static test results

3.4.1 Failure modes

The full field shear strain is analysed using DIC. Deformations of a representative specimen (RH-S-1) is shown in Fig. 3-12 at three different stages during the static test. It is observed that the crack, represented by the region of high shear strain, develops along the composite-to-steel interface towards the right loading point.

After the static tests, specimens are opened along the fracture interface for observation of the failure modes and fracture surface morphology. Fig. 3-13 shows representative fracture surfaces of specimens from each roughness series, including both optical images and 3D height profiles. It can be seen that for low and medium roughness, only a limited amount of resin remains attached to the steel surfaces while no laminate tearing is found on the composite surfaces. This indicates a dominant adhesive failure at the interface. Voids are observed on the composite surface, indicated by the blue areas in the height profiles. Some residual resin is found at some of the corresponding locations on the steel surface, while others may have been formed during production. For these two roughness series, the strength of the composite-to-steel interface bonding is lower than that between composite layers.

For the high roughness series, however, a significant amount of resin and chopped strands remain on the steel fracture surface, except for the areas near the pre-crack, while woven fabric is exposed on the composite surface. This means that the crack initiated at the interface but immediately migrated into the adjacent CSM layer of the composite material. For this series, the steel surface roughness provided enough bond quality so that the strength of the composite-to-steel interface bonding is higher than that between the CSM and woven layers of the composite adherend.

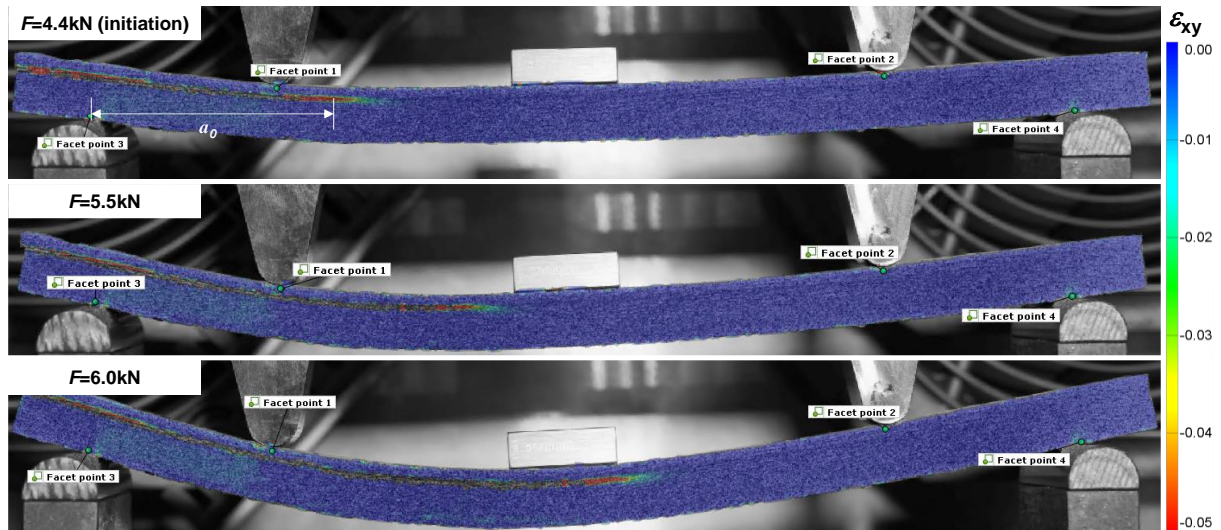


Fig. 3-12 Representative strain field and crack propagation at three different stages (specimen RH-S-1)

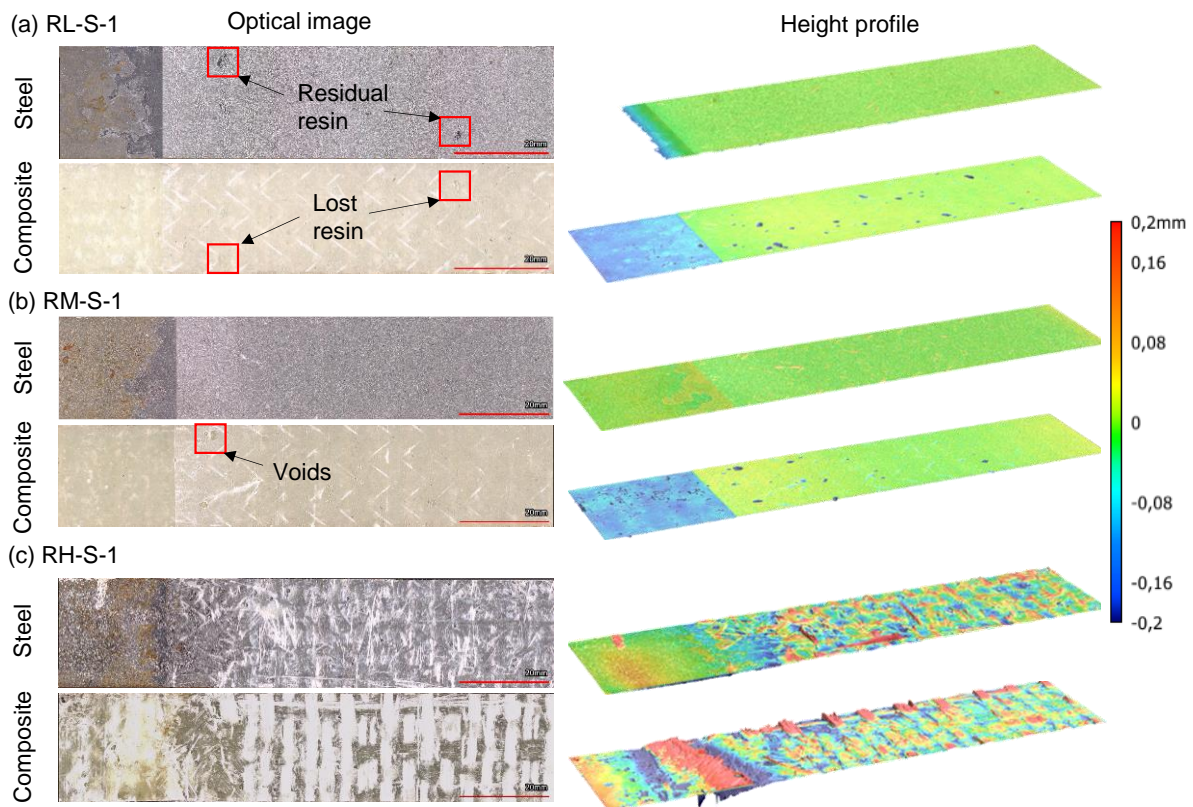


Fig. 3-13 Representative fracture surface of static tested specimens (The legend pertains to all the sub-images)

3.4.2 Force-displacement response

Force-displacement-crack length responses of all the specimens are shown in Fig. 3-14. The displacements were extracted from DIC using the average vertical displacements of the facet points 1 and 2 created on the specimen under the loading points, as shown in Fig. 3-12, minus the average vertical displacements of the faced points 3 and 4, created on the specimen next to

the support points. This excludes non-linearities of the loading fixture. The crack length is monitored by 2D DIC, analysed by the normalized shear strain method, introduced in [148]. As can be seen in Fig. 3-14 (a) and (b), for low and medium roughness series, the force-displacement curves remain linear until reaching the peak (critical) load level, after which a sudden drop of the force is observed. Correspondingly, cracks of the specimens propagated immediately once they initiated at the peak loads, indicating that the unstable crack growth is mainly due to adhesive failure. Specifically, for two of the low roughness specimens the cracks propagate instantly to 100-130 mm and gradually until 200 mm near the right loading point, while for the remaining one the crack fully propagates to the 200 mm immediately. For the medium roughness specimens the cracks propagate instantly to 140 – 180 mm and stabilized after that. The initial stiffness varies among different specimens due to small variations of specimen thickness and initial crack length. The critical loads are between 2 and 3kN for the low roughness series and from 4.7 to 5.7kN for the medium roughness series. High roughness series shows comparable critical loads to the medium roughness series due to its smaller specimens thickness as shown in Table 3-1. However, the force of high roughness specimens keeps increasing after crack initiation, at around 4.4kN, until reaching 6.5kN at end of the tests. In these specimens, cracks grow gradually after initiation.

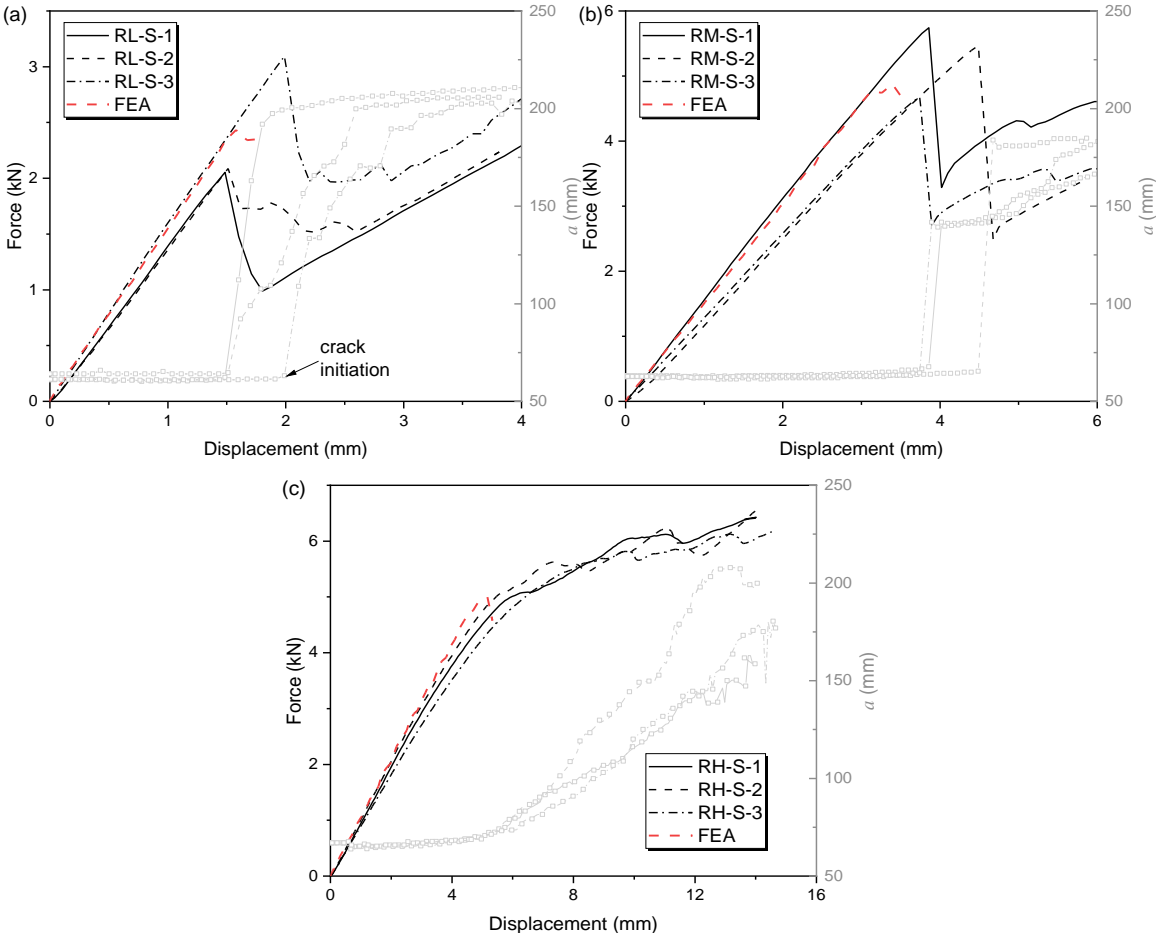


Fig. 3-14 Static force-displacement response and crack development of (a) RL series, (b) RM series and (c) RH series

Since no sudden force drop is observed in the force-displacement curves for the high roughness series, and the non-linearity of force-displacement curves may reflect not only crack development but also plasticity in the steel arm, the crack initiation for the high roughness series was determined based on the crack growth curves, instead of the force variation. To detect the crack initiation point, crack length-displacement curves are fitted with a piecewise function [151]:

$$a = f(d) = \begin{cases} a_0, & d \leq d_{ini} \\ k(d - d_{ini}) + a_0, & d > d_{ini} \end{cases} \quad (3-11)$$

where a_0 is the pre-crack length, d is the test displacement and k is the slope of the crack growth curve after crack initiation. The crack length remains constant, as a_0 , until the displacement at crack initiation, d_{ini} . After initiation, the crack length measurements are fitted using a linear function. The values of fitting parameters a_0 , k and d_{ini} are determined by the least squares method. The fitted results of d_{ini} values for the three specimens are 4.84, 5.38 and 6.05mm, respectively. The initiation values of SERR for these specimens are calculated based on the corresponding critical loads.

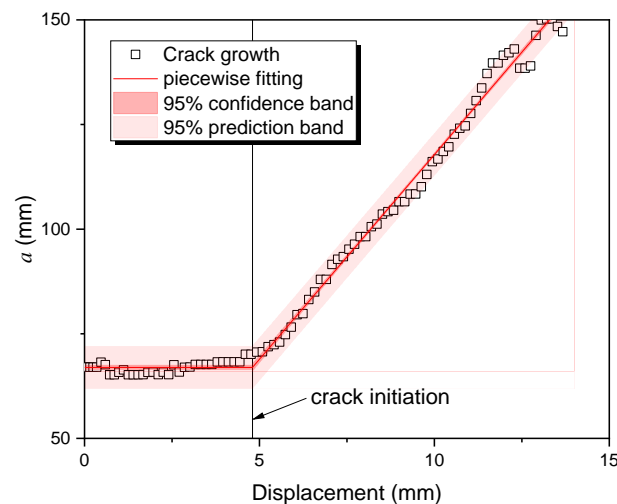


Fig. 3-15 Determination of crack initiation by piecewise fitting on crack growth curve

3.4.3 Fracture toughness

The initiation value of the mode II SERR, G_{ini} , was calculated by substituting the critical loads into Eq. (3-4) of the EGM. The SERRs are also extracted at the same load levels from FE models with the friction coefficient defined at the interface. The initiation SERR values obtained from the EGM and VCCT are summarised in Table 3-4. The average initiation SERR obtained from the VCCT for each roughness series serve as the critical SERR to model the fracture behaviour, as in Eq. (3-10). Force-displacement curves were extracted from the model and plotted together with the experimental results in Fig. 3-14. Due to the limitation of the VCCT in terms of simulating ductile crack behaviour, the numerical results are only exhibited

until the sudden force drop. The initial stiffness matches well with experimental results and the predicted critical loads are within 10% range of the test results, as shown in Table 3-4.

Since specimens from low and medium roughness series experienced unstable crack propagation, the resistance curves (R-curves) were only obtained for the high roughness series, as shown in Fig. 3-16. The SERR increases from 3.8N/mm corresponding to the initiation value, to a plateau, up to and above 6N/mm, as the crack propagates. Such high value of SERR corresponding to crack propagation is attributed to fibre bridging, identified in profile images in Fig. 3-13 (c).

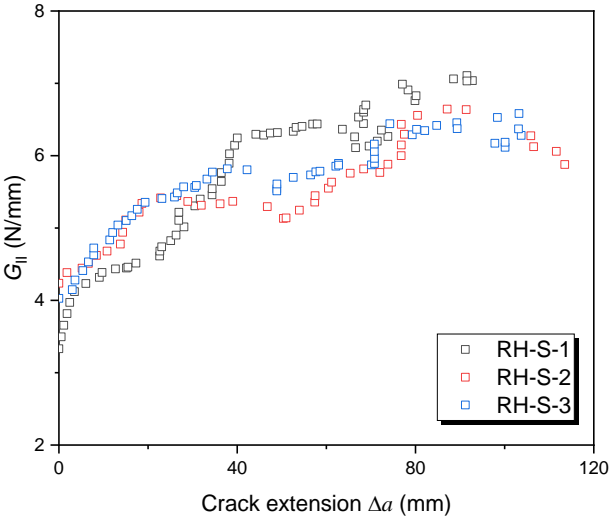


Fig. 3-16 SERR versus crack extension for RH specimens

Table 3-4 Fracture toughness

Specimens	$F_{crit,test}$ (kN)	$F_{crit,FEA}$ (kN)	Error (%)	$G_{ini} - EGM$ (N/mm)	$G_{ini} - VCCT$ (N/mm)
RL-S-1	2.05			0.49	0.39
RL-S-2	2.09	-	-	0.50	0.40
RL-S-3	3.10			1.11	0.85
Average	2.41	2.43	0.77	0.70	0.55
RM-S-1	5.74			3.82	2.27
RM-S-2	5.47	-	-	3.47	2.06
RM-S-3	4.68			2.54	1.86
Average	5.30	4.87	-8.07	3.27	2.07
RH-S-1	4.40			3.33	2.15
RH-S-2	4.96	-	-	4.24	2.61
RH-S-3	4.84			4.03	3.70
Average	4.73	5.00	-5.61	3.86	2.82

The initiation values of SERR are plotted against the surface roughness parameters S_q and S_{dr} , as shown in Fig. 3-17. It is found out that calculated based on EGM, the average G_{ini} increases dramatically by 367%, from 0.7 N/mm to 3.27 N/mm, as the roughness transitions from low to medium level, while increases by only 18%, from 3.27 N/mm to 3.86 N/mm, as the roughness shifts from medium to high level. The same variation trend is also found in results based on VCCT, where G_{ini} increases dramatically by 276%, from 0.55 N/mm to 2.07 N/mm, but only by 36%, from 2.07 N/mm to 2.82 N/mm for roughness transition from low to medium, and from medium to high levels, respectively. In addition, the G_{ini} calculated from the EGM is 0.15N/mm higher than the value calculated from VCCT for the low roughness, and over 0.7-1N/mm higher for medium and high roughness series. This difference is mainly from the energy dissipated by the friction effect at the cracked surface underneath the loading point, as well as the contact area between the loading/support cylinder and the specimen [148], which cannot be excluded in EGM. Higher roughness lead to relatively higher friction coefficients, as discussed in section 3.2.3. Furthermore, higher roughness corresponds to higher loading forces therefore larger frictional forces, thus resulting in a larger influence between the SERR values based on FEA and EGM.

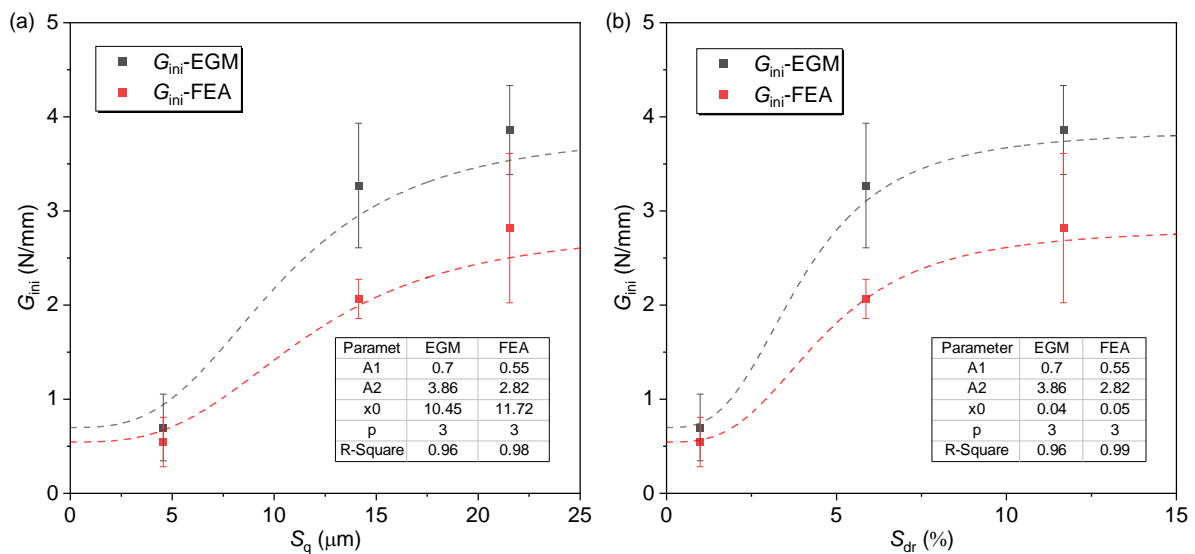


Fig. 3-17 Correlation between SERR and surface roughness using (a) S_q and (b) S_{dr} parameters

Literature [70,74,152] shows that the improvement of fracture toughness with the surface roughness is related to the increased effective bonding area. This is also the case in the current study from the relationship between G_{ini} and S_{dr} in Fig. 3-17 (b). However, the G_{ini} doesn't increase linearly with S_{dr} and tends to be a steady value at high roughness levels. This may be because that the effect of roughness diminishes when the fracture path moves away from the interface [74]. Other mechanisms may also be responsible for the variation trend of the fracture energy measured from the tests. The highly irregular surface, as shown in Fig. 3-2 (c), and height profile, shown in Fig. 3-18, of high roughness series enable the resin of the composites to deeply penetrate into the steel surface, thus enlarging the effective bonded area and

enhancing the mechanical interlocking between these two adherends. Furthermore, an increased surface roughness can make the abrupt transition in elastic modulus more gradual as the asperities transfer load to the resin, thereby decreasing the average stress concentration for a crack at the tips of the asperities [74]. The presence of fibre bridging, observed in Fig. 3-13 (c), most significantly contributes to the increased fracture toughness. Overall, a larger effective bonding surface, lower stress concentration at the crack tip due to gradual modulus transition, and fibre bridging are the major factors that contribute to the increase of fracture toughness. In addition, literature [70,74] indicates that the bond performance will deteriorate after reaching a certain roughness level. A typical explanation [74] is that the increase of roughness reduces the wettability of the substrate such that the adhesive cannot properly spread on the steel surface and contribute to the formation of air voids during production. The voids can be observed in Fig. 3-14 for the specimens with low and medium surface roughness. Meanwhile, it is reported in [74] that, above a certain roughness level, the stress concentration at the tip of asperities may reduce the strength of the adhesive joints. It is the combination of all the mechanisms mentioned above that contribute to the unique trend of G_{ini} versus roughness levels.

Considering the decreasing rate of the increase of SERR values as the roughness parameters increases, a logistic regression in ORIGIN software is applied for characterising the relationship between the two as defined in Eq. (3-12). SERR is chosen as dependent and roughness as independent variable.

$$y = \frac{A_1 - A_2}{1 + (x/x_0)^p} + A_2 \quad (3-12)$$

where A_1 , A_2 are the initial and final values of the depended variable, x_0 is the mid-point and p is the power of this function. The parameters in this equation is fitted by the least squares method and the results are listed in the table of Fig. 3-17.

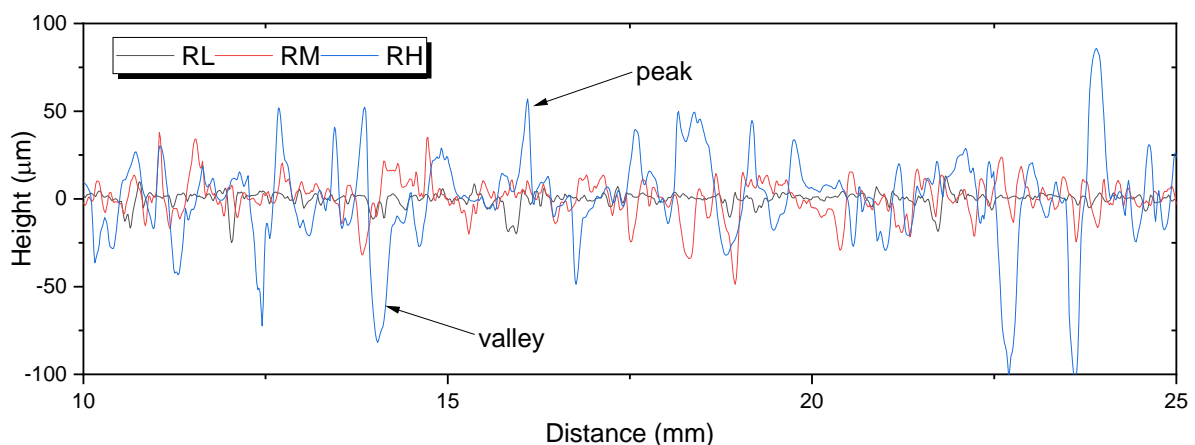


Fig. 3-18 Height profiles of steel surfaces with low (RL), medium (RM) and high (RH) roughness

3.5 Fatigue test results

3.5.1 Failure modes

A typical shear strain field of a representative specimen (RH-F-1) is shown in Fig. 3-19 at different number of cycles during the fatigue test at the state of maximum load. The crack is indicated by region of high shear strain at the interface, which grows from the pre-crack location towards the right loading point.

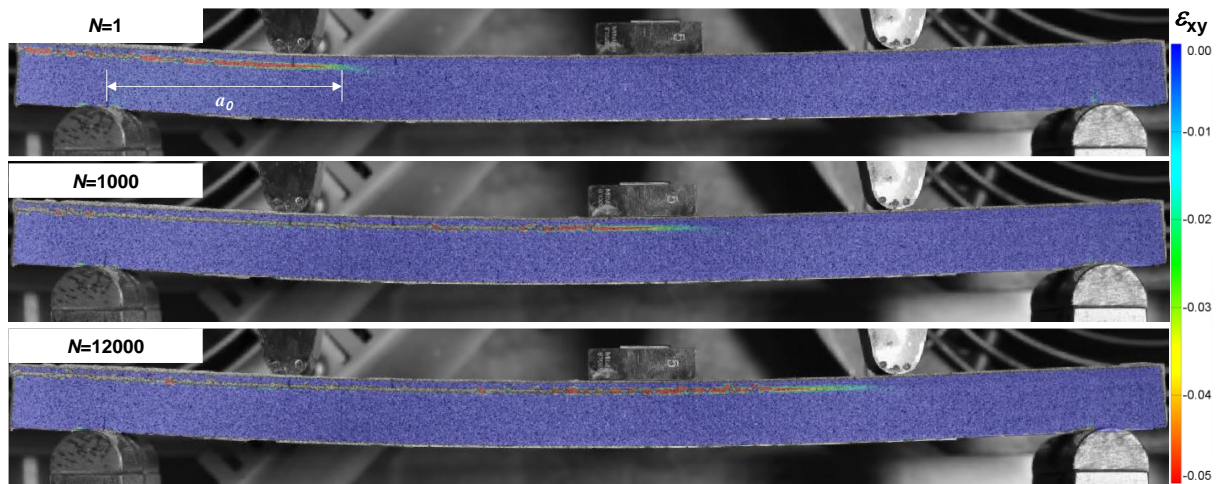


Fig. 3-19 Representative strain field and crack propagation at three different stages (specimen RH-F-1)

After the cyclic tests, specimens were opened along the fracture interface for inspection. Optical images and height profiles of a representative specimen from each roughness series are shown in Fig. 3-20. It is found that the predominate failure mode for the low and medium roughness series is adhesive failure at the composite-to-steel interface. The fracture surfaces are smooth with only small portions of resin remaining on the steel surface. The high roughness series experienced mixed adhesive failure and cohesive failure through thin layer of resin and limited through CSM. The fracture surfaces are more irregular, with a lot of resin and pieces of CSM remaining on the steel surface as shown in Fig. 3-20 (c) although much less than those under static tests. This means that the crack propagation occurs preferentially in the region of composite-to-steel interface under mode II cyclic loading. This difference between static and fatigue failure modes is also reported in literature [74,153], which stated that the fiber bridging effect is not pronounced for mode II interlaminar failure under cyclic loading.

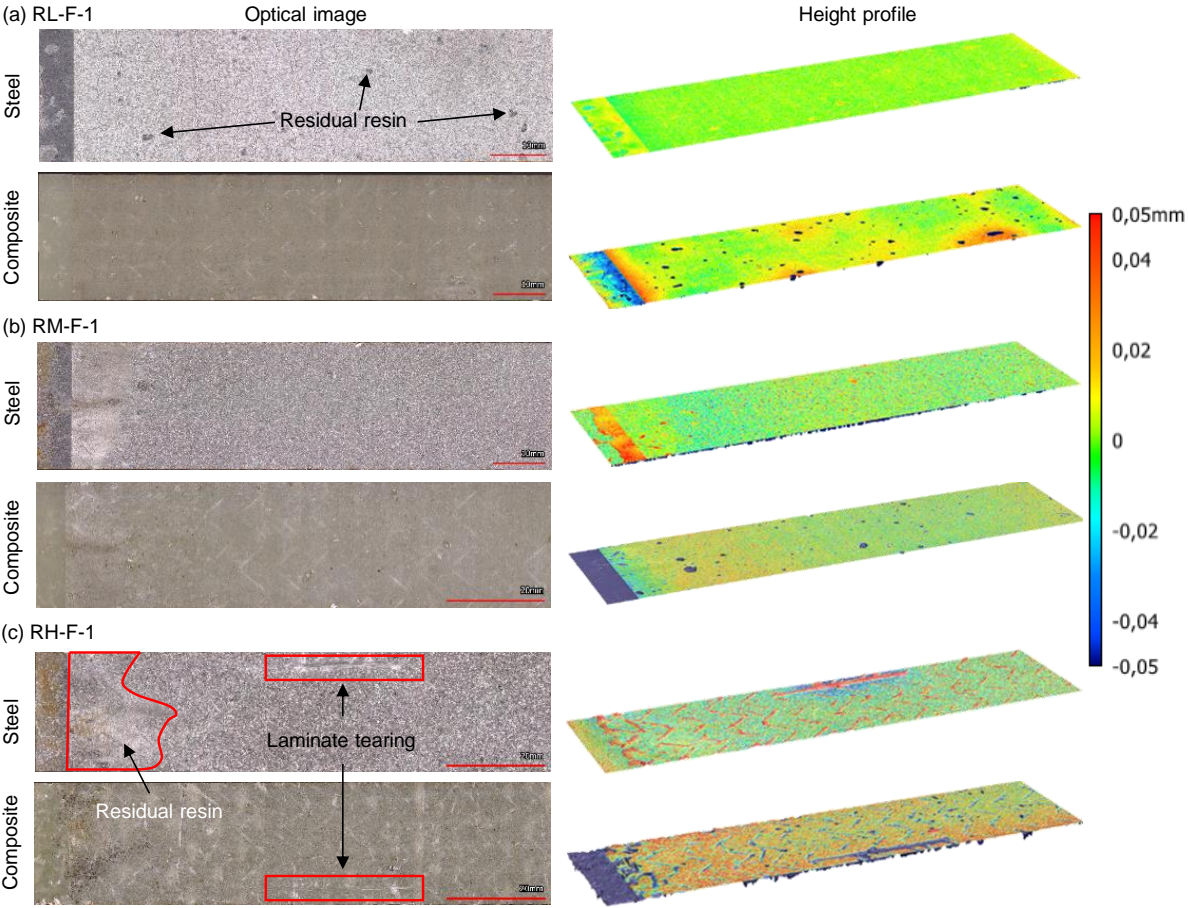


Fig. 3-20 Representative fracture surfaces of fatigue tested specimens (The legend pertains to all the sub-images)

3.5.2 Crack propagation and SERR development

The variations of mode II SERR of each specimen during the cyclic tests were calculated by the EGM and summarized in Fig. 3-21. The crack length measurements, determined by analysing the shear strains at the interface as in section 3.3.3, are also shown. Results of specimen RL-F-3 were not obtained due to a malfunction of the DIC system during the test. It can be seen that results of each configuration are reproducible. The SERR decreases rapidly from the initial cycles and stabilizes gradually as the test continues. Correspondingly, the crack grows fast initially and stabilizes gradually towards the end. Tests were stopped when no further crack growth could be detected by the DIC system, except for the low roughness specimens where the crack growth stabilised at 165 mm. The crack growth for other two roughness series both stabilised at around 220 mm, corresponding to the location of the right loading point.

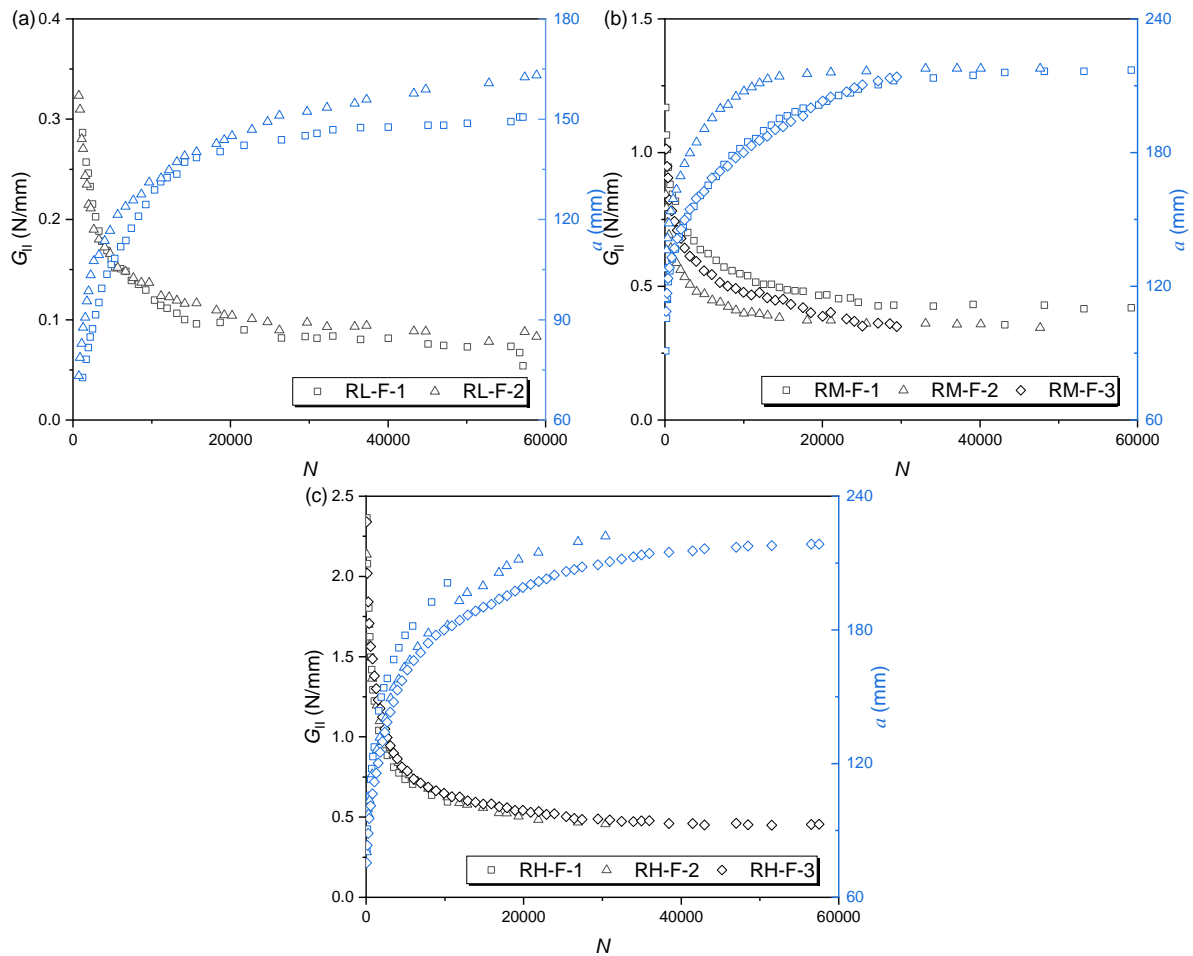


Fig. 3-21 Fatigue crack growth curves and SERR development (a) RL specimens; (b) RM specimens; (c) RH specimens

In order to consider influence of friction on SERR at the crack tip, FEA was performed as explained in section 3.3.2, next to EGM, to calculate the mode II SERR at different force levels and crack lengths. Three series of models are built for specimens with different roughness, each of which is defined with the friction coefficient obtained by the 4 Hz friction tests described in section 2.3 (see Fig. 3-5 (d)). A relationship between the test force (P), the crack length (a) and the G_{II} was established, as shown in Fig. 3-22. A non-linear surface fit was applied to the numerical results using Eq. (3-13).

$$G = k_1 P^2 + k_2 a + k_3 \quad (3-13)$$

The force term, P , is of second-order to be consistent with that in the EGM (see Eq. (3-4)). A linear correlation of the crack length, a , is included to take into account the geometrical non-linearity and friction effect [148] which cannot be considered by the EGM. Parameters k_1 , k_2 and k_3 are determined by the least squares method and are listed in Table 3-5 for different roughness series. Substituting forces and crack lengths from the tests into Eq. (3-13), the mode II SERR with friction effect considered, G_{II} , can be calculated. The calculated SERR based on the non-linear FEA will be used to establish the fatigue crack growth curves, where the

influence of friction can be taken into account. In addition to that the friction can be considered in the FE model, the modelling results presented in the separate study (not detailed here) [148] demonstrated that the composite and steel materials remain in elastic stage under the applied force in the current study, thus indicating the applicability of linear elastic fracture mechanics.

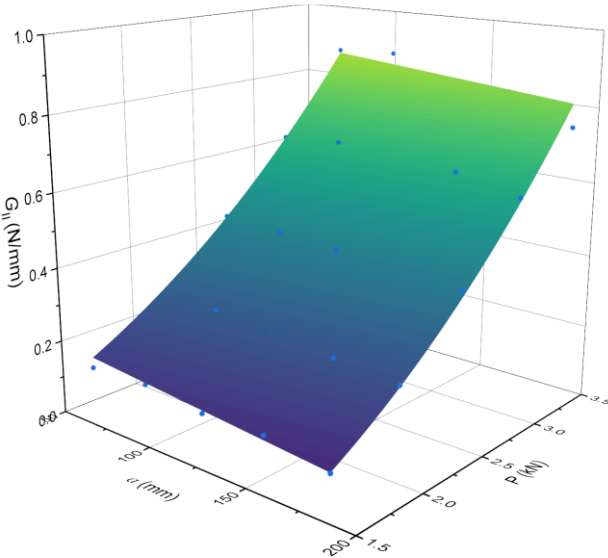


Fig. 3-22 SERR vs. force and crack length from FEA

Table 3-5 Fitted results for SERR vs. force and crack length

Eq. (10)	Coefficients			R^2		
	RL	RM	RH	RL	RM	RH
$G=k_1P^2+k_2a+k_3$	$k_1=0.084,$ $k_2=-2.14E-5,$ $k_3=0.0038$	$k_1=0.084,$ $k_2=-1.30E-4,$ $k_3=0.029$	$k_1=0.12,$ $k_2=2.23E-4,$ $k_3=0.019$	0.99	0.98	0.98

3.5.3 Fatigue crack growth (FCG) curves

To construct the fatigue crack growth curves, namely the Paris curves, the crack growth rate, da/dN , is calculated by the 7-point incremental polynomial method recommended in [154]. The value of ΔG_{II} associated with this da/dN is computed using the fitted crack length corresponding to the middle point (the 4th one) of the 7 successive data points. da/dN is plotted against the ΔG_{II} calculated by EGM and FEA in Fig. 3-23, and fitted by a power function as described in Eq. (3-14) such that the Paris curves can be obtained:

$$da / dN = C(\Delta G_{II})^m \tag{3-14}$$

where C and m are parameters determining the intercept and slope of the Paris curves, respectively. They were determined by the least squares method and listed in Table 3-6 for each specimen. It should be noted that data points corresponding to crack length above 200 mm are excluded in the Paris curves to eliminate the influence of compressive stresses resulting from the right loading point [148]. It can be seen from Fig. 3-23 that data points from each roughness series are within a reasonable scattering range. Curves based on calculation of SERR by use of

FEA (dashed lines) always shift towards the left compared to the EGM-based curves (solid lines). In case of the same slope parameter m the FEA-based results are reflected by the higher C values compared to EGM-based results as shown in Table 3-6. This difference is mainly related to the friction effect, as discussed in section 3.4.3 and Ref. [148]. Friction forces at the fractured interface, as well as between the loading/supporting point and the specimen, contribute to load transfer mechanism of the specimen, leading to reduced portion of forces that need to be transferred at the crack tip and therefore to reduced SERRs at the crack tip. This effect can be considered by a non-linear FE model but cannot be considered by the linear EGM method. By analysing the sets of FEA and EGM based results the pattern emerges at the bottom part of the Paris curves. Although the bottom part of the curve corresponds to an already developed crack, therefore larger fracture surface where friction could be exhibited, the contact stresses at the fractured and support/load region faying surfaces are lower at the stage of a developed crack due to reduced load applied in the displacement controlled experiment. In total there is less friction at the stage of developed crack which is shown by a slightly smaller difference between the curves from EGM and FEA at the bottom of the Paris curves in Fig. 3-23.

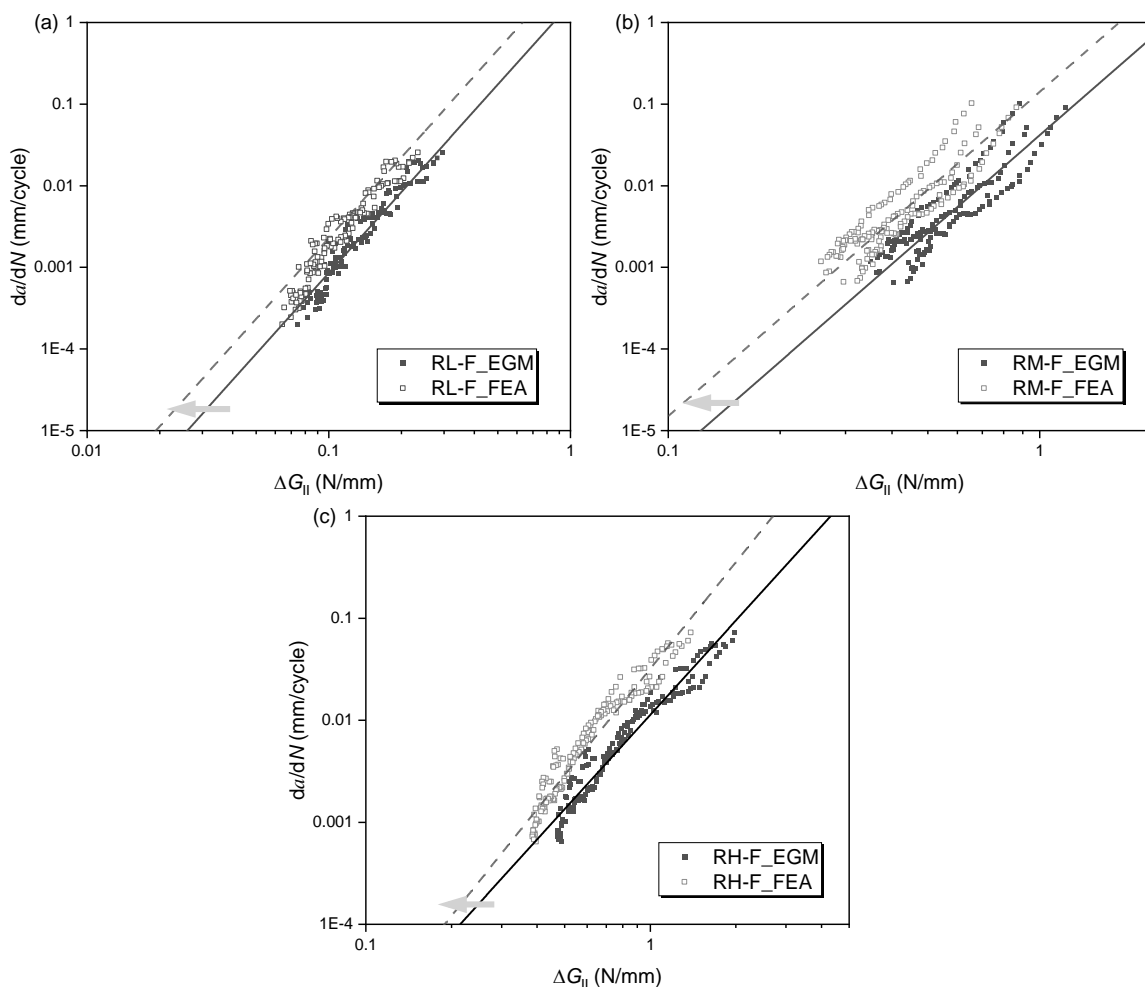


Fig. 3-23 Paris curves obtained by EGM and FEA (a) RL specimens; (b) RM specimens; (c) RH specimens

Data points from all roughness series were plotted together for evaluating the effect of steel surface roughness, as shown in Fig. 3-24 (a) (based on EGM) and (b) (based on FEA). The critical SERRs are also indicated in these two figures for each roughness series based on EGM and FEA. The least squares method is used to fit the C and m values for each roughness independently (solid lines), which are listed in Table 3-6. It can be seen that, for both numerical and analytical methods, Paris curves from different roughness series are generally parallel, namely showing similar slopes (m values is of same magnitude). The slope of Paris curve, m , is mildly dependent, up to 20 %, on the steel surface roughness. However, the position of the curves changes significantly among different roughness, with the C parameter decreasing up to two orders of magnitude as the roughness increases. This means that the crack growth rate of the high roughness series can be only 0.5-1% of the low roughness series at the SERR range of 1N/mm. On the other hand the fatigue resistance of RM series can be higher than that of the RH series at relatively low (e.g. below 0.1 N/mm) SERR ranges due to the higher curve slope (m value) of the RM series.

The m values are plotted against the roughness parameter S_q and S_{dr} in Fig. 3-25 (a) and (b), respectively. The variation of m is within an approximate range from 3.0 to 4.0 for EGM-based and FEA-based results, which is much smaller compared with the variation of magnitudes of the C parameter. Therefore, for further comparison of Paris curves from different roughness series, it is adopted that the m parameter is independent of the roughness levels. The average values of m for EGM and FEA based analysis are indicated in Table 3-6. The EGM-based m value overlaps well with the FEA-based result, despite the friction effect. The average values of m parameter, 3.45 and 3.58 for the EGM and FEA based results respectively, are therefore taken and the C parameters are determined again for each series and analysis method following the least squares method.

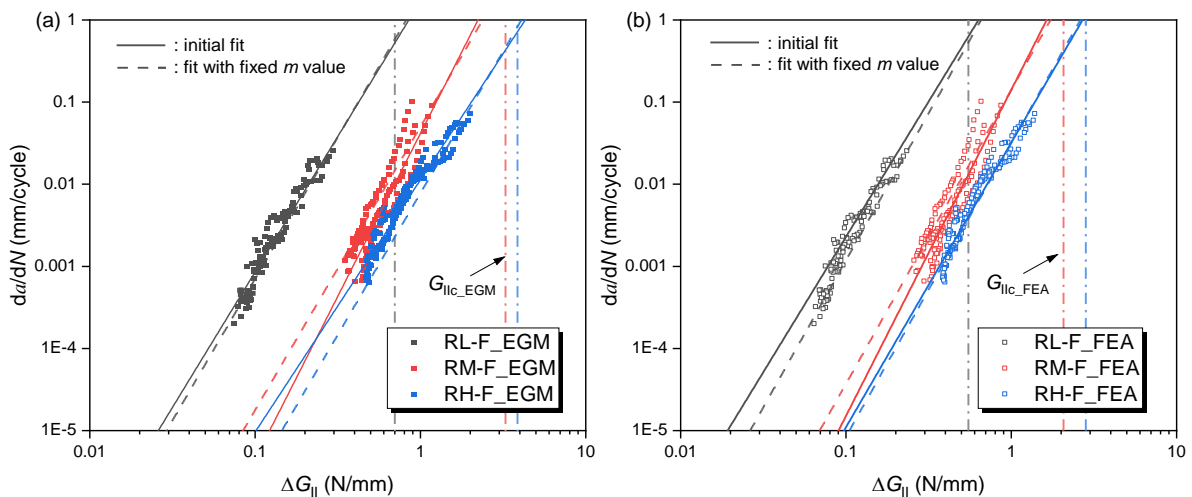
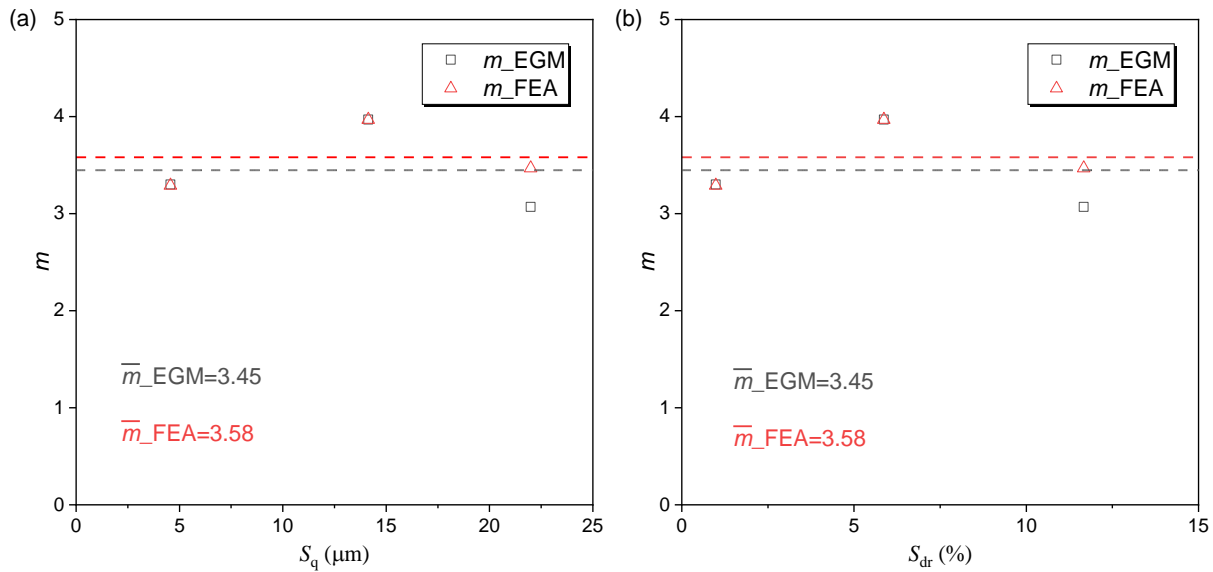


Fig. 3-24 Paris curves of different roughness (a) SERR obtained by EGM; (b) SERR obtained by FEA

Table 3-6 Paris curve parameters of different roughness series

Specimen series	EGM			FEA with friction		
	C	m	C'	C	m	C'
RL-F	1.70	3.30	1.99	4.51	3.29	6.85
RM-F	0.04	3.97	0.051	0.14	3.97	0.15
RH-F	0.01	3.07	0.0078	0.03	3.47	0.03
Average	-	3.45	-	-	3.58	-

**Fig. 3-25** Influence of steel roughness on the m value (a) roughness expressed by S_q ; (b) roughness expressed by S_{dr}

The new fitted Paris' curves are plotted as dash lines in Fig. 3-24. The fitting quality, represented by R^2 , of the initial and second round are listed in Table 3-7. The fitting quality of the second round decreases a bit due to the fixed slope m , but generally keeps at a satisfied level compared to the initial fit. The newly obtained C parameters, C' , are listed in Table 3-6 and are plotted against the roughness parameter S_q and S_{dr} in Fig. 3-26 (a) and (b), respectively. Compared with the initial C parameters, the new C' parameters change slightly due to the fixed m values. It can be seen from Fig. 3-26 that the C' parameter decreases as the roughness S_q and developed area ratio S_{dr} increases. Generally speaking, the C' parameter becomes one order of magnitude lower when the roughness increases from the low level to the medium level, and also from the medium level to the high level. Considering the variation trend of C parameter, a power function, Eq. (3-15), is used to depict the relationship between C and roughness parameters:

$$C = k(S)^b \quad (3-15)$$

where S is the roughness parameter, S_q or S_{dr} , k and b are the fitted parameters, determined by the least squares method. The fitted results of k and b are listed in Fig. 3-26. Comparing results obtained from EGM and FEA, the FEA based C parameters are higher than the EGM based

results. This is again due to the friction effect. Taking the friction at the interface and the support/load regions into account, the FEA-based Paris curves shift towards the left of the EGM-based curves as shown in Fig. 3-23, thus leading to apparently ‘lower’ fatigue resistance and higher C parameters.

Table 3-7 Fitting quality (R^2) of the initial and second round

Specimen series	initial	second
RL-F	0.70	0.67
RM-F	0.57	0.57
RH-F	0.71	0.68

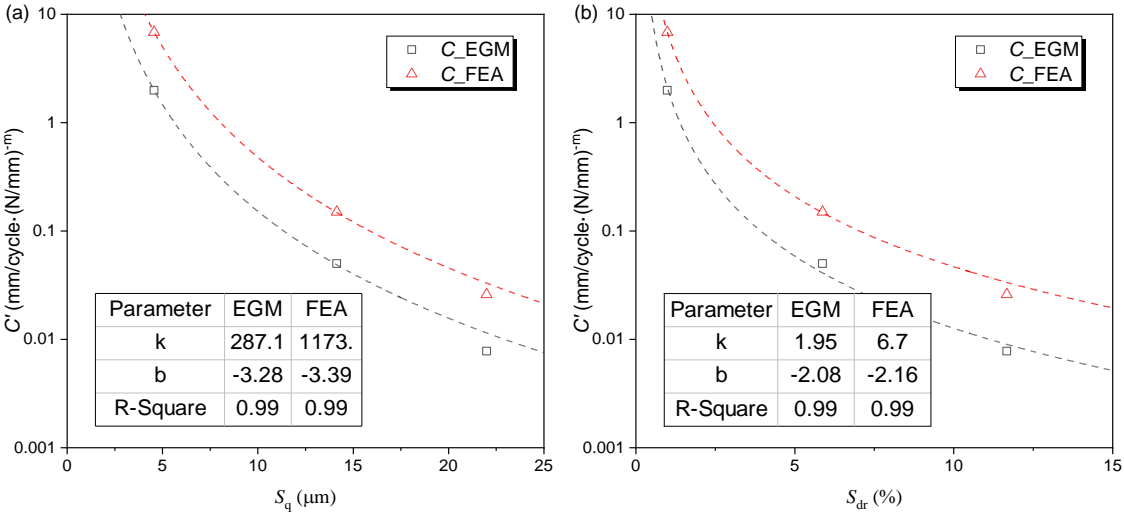


Fig. 3-26 Influence of steel surface roughness on the C' parameter expressed by (a) S_q and (b) S_{dr}

Compared to the fracture toughness, fatigue resistance of the composite-to-steel bonded joints seems to be more sensitive to the surface roughness of the steel adherend. Taking the FEA-based results as an example, the crack propagation rate at $\Delta G_{\text{II}}=1\text{N/mm}$ (represented by the C values) decreases by 98% from 6.85 mm/cycle to 0.15 mm/cycle when the roughness S_q increases by 2 times from the low to the medium roughness level. A 80% decrease of crack propagation rate is found when S_q increases by 50% from the medium to the high roughness level. A similar trend is also found when the roughness is expressed by S_{dr} . This means that the improvement of fatigue resistance comes essentially from a larger effective bonding area. The fatigue resistance is highly influenced by the roughness features on the steel surfaces possibly due to the fact that the adhesive failure is the predominate failure mode. This is different from Ref. [74], which stated that the fatigue performance is insensitive to the surface roughness when the crack path moved farther from the interface. However, it should be noted that in the current study the adhesive failure is forced by placing the steel adherend on the top in order to characterise the minimum possible fatigue resistance of the bi-material joints. In real

application, such as in wrapped composite joints [155], fibre bridging may be exhibited thus the bi-material bonded joints could have higher fatigue resistance. Furthermore, the enhancing effect on the fatigue resistance does not show a decreasing trend at high roughness level, as observed for fracture toughness, indicating that the bonded joint is not effected by the same deterioration mechanisms as for the static performance. In conclusion, the results show that in the adverse case of adhesive failure, the fatigue resistance of the bonded joint can be sufficiently ensured as long as an appropriate surface preparation is applied before joining.

3.5.4 Total life FCG curves

Although the power law in Eq. (3-14) can fit the test data well, it has the limitation of considering the threshold strain energy release rate and the static fracture toughness. This limitation may lead to overestimation and underestimation of crack growth rates near the threshold and fracture toughness, respectively. A total life FCG model was proposed by Martin and Murri [57] to cover all these three stages of fatigue crack growth curve: the subcritical region around the fatigue threshold (G_{th}), the power law controlled region and the critical region close to fracture toughness (G_c).

The total life FCG model is expressed in Eq. (3-16) and illustrated in Fig. 3-27. The constants C and m are determined by fitting the test data through a power law as described above. As G tends to the fracture G_c , the crack growth rate da/dN tends to be infinite. As G tends to the threshold G_{th} , the crack growth rate da/dN tends to be zero. The threshold SERR can be obtained by the crack growth onset tests [156] or by visual observation of the experimentally obtained FCG curves [58]. The exponents D_1 and D_2 determine the curvature of the FCG curve near the threshold and fracture toughness and can be obtained by fitting the test data. A larger D_1 (or D_2) value leads to the threshold and critical region approaching to the basic power function, whereas a smaller value leads to the threshold and critical region deviating away from the basic power function. In Fig. 3-27, $D_1 < D_1' < D_1''$, $D_2 < D_2' < D_2''$.

$$da / dN = C(G)^m \frac{\left[1 - \left(\frac{G_{th}}{G} \right)^{D_1} \right]}{\left[1 - \left(\frac{G}{G_c} \right)^{D_2} \right]} \quad (3-16)$$

Since neither crack growth onset test has been done nor the threshold behaviour can be observed from the test data in the current study, it is difficult to determine the threshold G_{th} and curvature exponent D_1 and D_2 by fitting the test data directly. According to the literature [57,157–160], the G_{th} can be 1% to over 20% of G_c , depending on the materials, stress ratio et al. Based on the test data in the current study, the ratios between the minimum SERR values of different roughness series, which are obviously above G_{th} , and the fracture toughness obtained in section 3.4.3 are 9%-13%. A sensitivity study is conducted on the threshold ratio G_{th}/G_c (in the range of 1%-9%), and curvature exponent D_1 (D_2) of different magnitudes to evaluate the fitting

quality by adopting different values. It is assumed in the current study that D_1 equals to D_2 , namely the FCG curve is assumed to be centrally symmetric about its midpoint.

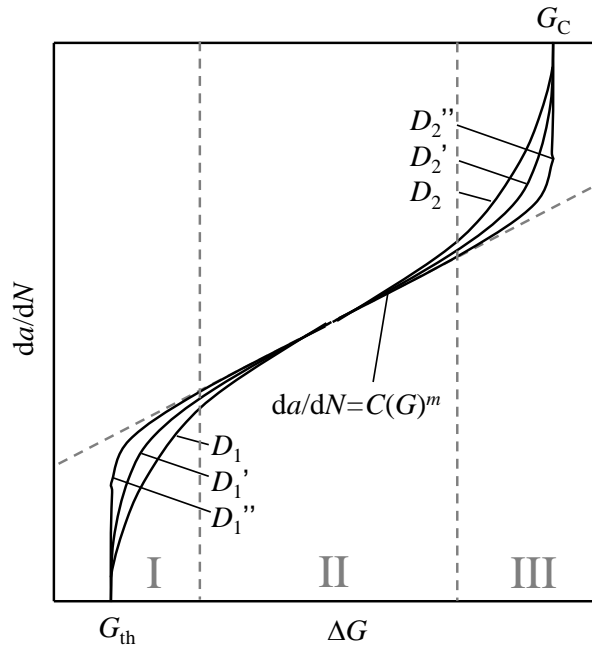


Fig. 3-27 Total life FCG curves

Fig. 3-28 shows two examples of application of the total life FCG model on the test data for the low roughness series. In Fig. 3-28 (a) the ratio G_{th}/G_c is kept as 3% and in Fig. 3-28 (b) the curvature exponent D is kept as 1. It can be seen from Fig. 3-28 (a) that as the exponent increases, i.e. as the fitting curve gets closer to the basic power function, higher R^2 values, indicative of improved fitting quality, will be obtained. $D=0.1$ leads to R^2 below zero indicating very bad fitting quality and is excluded for consideration. Meanwhile, it can be seen from Fig. 3-28 (b) that as the SERR ratio increases from 1% to 5%, the fitting quality also improves.

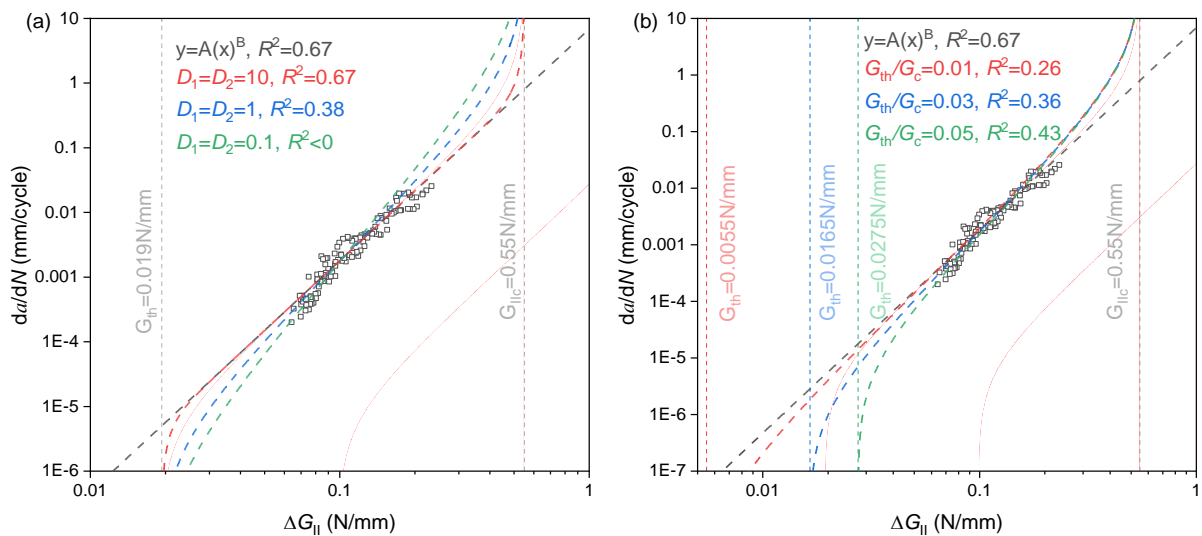


Fig. 3-28 Fitting results of low roughness series based on total life FCG curves (a) effect of curvature exponents D_1 (D_2); (b) effect of threshold G_{th}

The interactive influence of threshold ratio G_{th}/G_c and curvature exponent D on the fitting quality, R^2 , is shown in Fig. 3-29. The results show that the fitting quality improves as G_{th}/G_c and D increase but converges to a fixed value when D is above 3, which is approximately the same as the R^2 obtained by using the power function, 0.67. This is because that the total life FCG model overlaps with the power function in the range of test data when $D \geq 3$. Since $D \geq 3$ meets the criteria for fitting quality, a more extensive discussion on selecting the optimal threshold ratio G_{th}/G_c and curvature exponent D will be conducted in Chapter 6, specifically aligned with predicting crack propagation at the joint level.

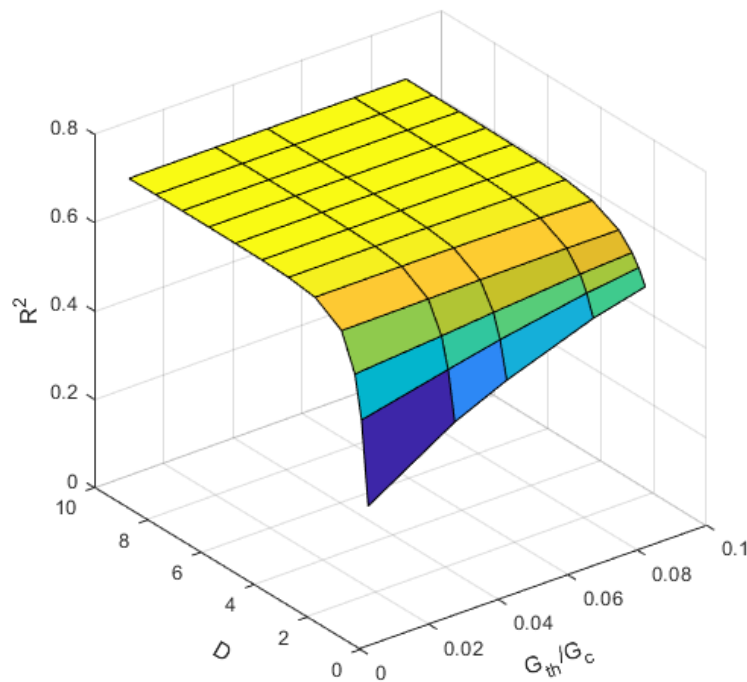


Fig. 3-29 R^2 variation against threshold ratio and curvature exponent

Example of fitting results by adopting that $D_1=D_2=3$ and $G_{th}/G_c=3\%$ on the FEA-based test data of 3 different roughness series are shown in Fig. 3-30. It can be seen that R^2 values of all roughness series can be close to those obtained from fitting with the power function as shown in Table 3-7. Meanwhile, the nonlinear region of the FCG curves near the threshold and fracture toughness can be considered.

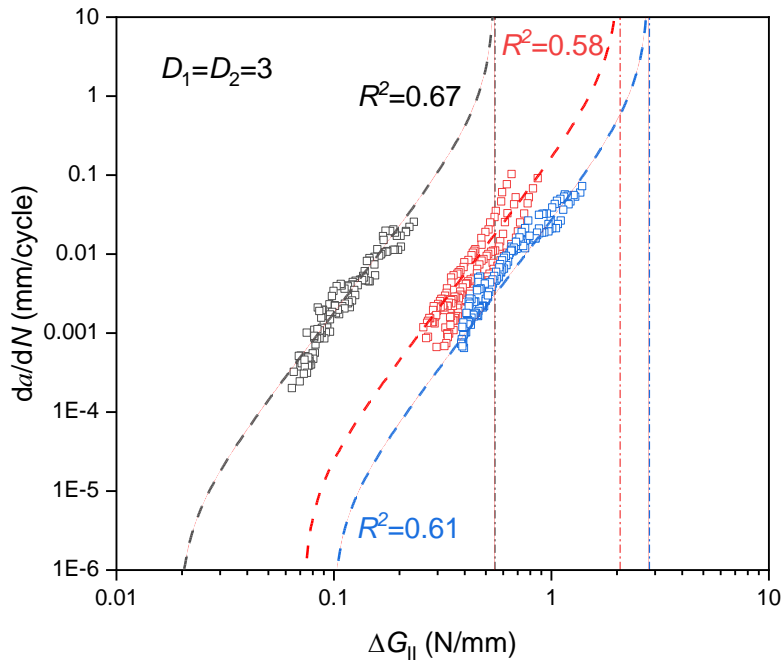


Fig. 3-30 Total life FCG curves of different roughness series ($D_1=D_2=3$)

3.6 Conclusions

In this study, the influence of the steel surface roughness on the mode II fracture and fatigue resistance of the composite-to-steel bonded interfaces is investigated. Quasi-static and fatigue 4ENF tests are performed. The bonded surfaces are characterised before and after the tests for surface roughness, friction coefficients and failure modes. By correlating the fracture toughness and Paris curve parameters to the surface roughness, the following conclusions can be drawn:

- Fiber bridging is only observed in specimens with high surface roughness under static loadings while adhesive failure is dominant when lower surface roughness are applied. In the case of fatigue loadings, no fibre bridging is observed regardless the steel surface roughness.
- Under static loading, the initiation fracture toughness of the bonded joint (G_{IIini}) increases with the surface roughness. The G_{IIini} is found to be 2.8 times higher from low to medium roughness series, and not more than 36% increase is observed from medium to high roughness series. The enhancing effect of the steel surface roughness shows a decreasing trend.
- Under cyclic loading, the slope of Paris curve, m , is not dependent on the steel surface roughness. However, the C parameter decreases one order of magnitude from low to medium and from medium to high roughness. This means that the fatigue resistance of the composite-to-steel bonded joint is largely affected by the surface preparation.
- The enhancing effect of increased roughness on the fracture toughness and fatigue resistance is related to the increased effective bonding area. The deterioration mechanisms at very high roughness levels, such as voids formation, may explain the

decreasing trend of the enhancing effect for fracture toughness. However, this trend was not observed on the fatigue resistance within the studied roughness levels.

- The FEA-based results exhibit lower G_{Iini} values and higher C values than the EGM-based results. This is proved to be due to the friction effect between the cracked surfaces during 4ENF tests, which was taken into account by the FE model. The higher is the roughness and cracked area, the more significant is the friction effect, thus the larger difference between FEA and EGM-based results.
- A total life FCG model is adopted to fit the test data to consider the nonlinear region of the FCG curves near the threshold and fracture toughness. It is found out through a sensitivity study that the fitting quality achieved with the total life FCG model can be comparable to that obtained with the power function, given that the curvature exponent D is greater than 3. A more extensive discussion on selecting the optimal threshold ratio G_{th}/G_c and curvature exponent D will be conducted in Chapter 6, specifically aligned with predicting crack propagation at the joint level.

Chapter IV

EXPERIMENTAL AND NUMERICAL STUDY ON THE FATIGUE DEBONDING BEHAVIOUR OF SIMPLE AXIAL SPLICE JOINTS

Parts of this chapter appear in the journal article: 'W. Feng et al., Interfacial fatigue debonding retardation in wrapped composite joints: experimental and numerical study. *Compos Struct* 2023;319:117146.'

4.1 Introduction

As discussed in the previous chapter, friction at the composite-to-steel interface may dissipate part of the cyclic energy, change the stress state around the crack tip and lead to higher fatigue crack growth resistance. The same goes for wrapped composite joints where debonding at the composite-to-steel interface is the predominate failure mode under cyclic load. During recent studies on uniaxial joints, as shown in Fig. 4-1 (a), it was found that the stiffness degradation rate of the joints shows a decreasing trend under cyclic loads. Correspondingly, the crack propagation monitored by DIC shows a retardation phenomenon, as schematically shown by solid lines in Fig. 4-1 (b). Whereas the FEA shows that the SERR values along the debonding path should remain constant within the region of uniform wrap thickness (see Fig. 4-1 (c), where a_c is length of the region of uniform wrap thickness). Subsequently, a crack growth with no retardation and stiffness degradation without any retardation should be achieved (see dashed lines in Fig. 4-1 (b)).

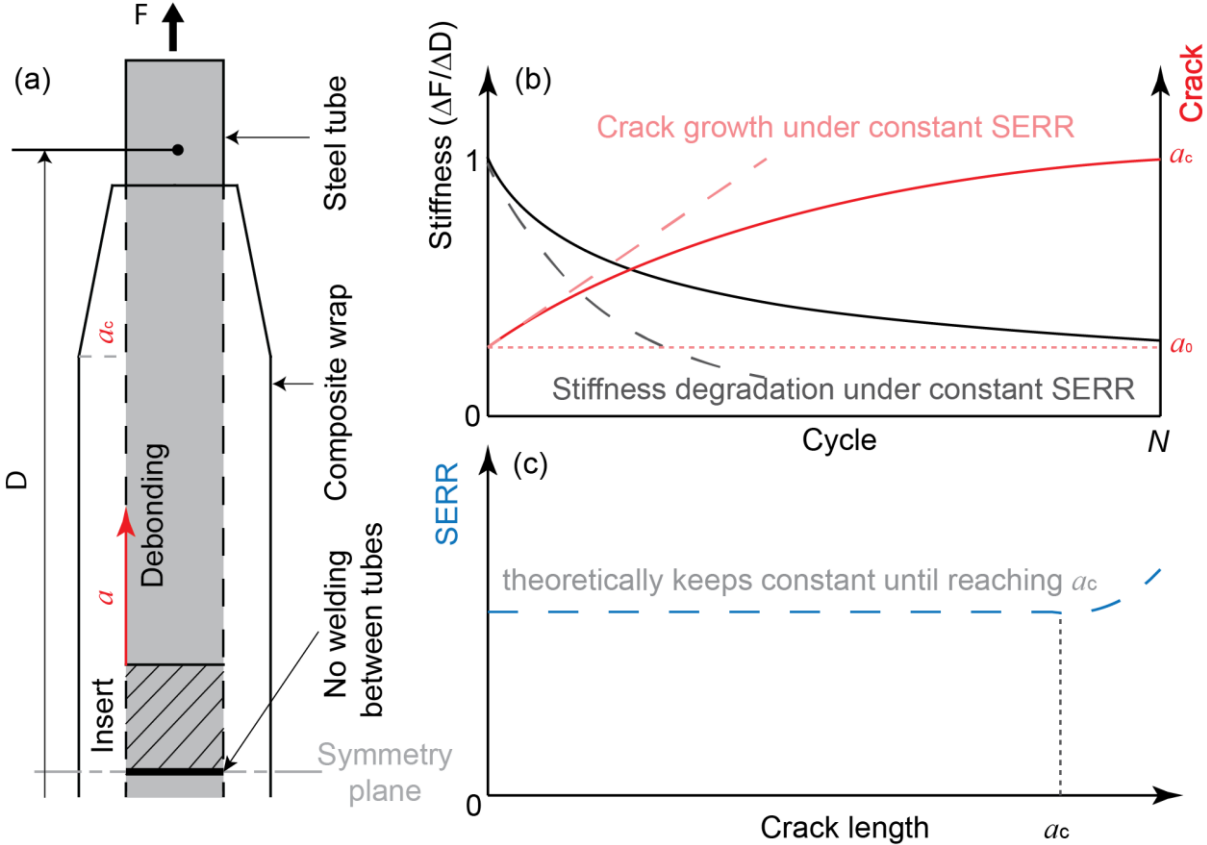


Fig. 4-1 Schematic of stiffness degradation stabilization and crack growth retardation at the bonded interface of wrapped composite joints

Considering the facts that 1) the wrapped laminates of wrapped composite joints around the steel tube may cause relatively high contact pressure at the composite-to-steel interface due to pre-strain and curing shrinkage of the laminates during and after production; 2) the contact area with friction forces between steel and composites is much larger than that in beam-type specimens such as ENF specimens, it is reasonable to make the assumption that the friction

effect at the interface dissipates part of the input energy, serving as the main reason for the crack growth retardation phenomenon observed during the tests.

In this chapter, the influence of friction effect at the composite-to-steel interface of wrapped composite joint on its debonding behaviour is investigated experimentally and numerically. Static tests on uniaxial wrapped composite joints are conducted to provide reference for the fatigue tests and serves as validation for FE model. Specimens are analysed in terms of stiffness, resistance, and ductility. In the follow-up fatigue tests, the stiffness degradation and crack propagation are monitored by 3D DIC and optical fiber systems. 3D finite element model is established and validated against test results in terms of load-displacement curves and strain distribution on the surface of composite wrap. Virtual Crack Closure Technique (VCCT) in FE, combined with friction behaviour, is defined at the interface, which is used to calculate SERR and to explain the crack growth retardation phenomenon. Crack propagation and stiffness degradation of the joints is predicted based on the SERR values from FE model and the preliminary established Paris relationship. Finally, parametric studies about the influence of friction coefficient, failure modes and Paris relationship parameters on the predicted results are conducted.

4.2 Experimental study

4.2.1 Specimens, test set-up and instrumentation

In this study, the A-joint, namely the uniaxial splice joint, is used due to its geometrical simplicity thus the opportunity for clear interpretation of mechanical behaviour of debonding in a simple tensile load condition. In such case, where the wrapping thickness is uniform, the SERR at the crack tip is supposed to be constant as the crack propagates, providing the stable crack propagation in static and constant crack propagation rate under constant amplitude fatigue loading. Six specimens are tested in this chapter as summarised in Table 3-1, where three of them are used for static tests and the other three for fatigue tests.

Table 4-1 Test specimens

Load type	Specimens	Loading rate/frequency	Loading range
Static	AS_1/2/3	1mm/min	-
Fatigue	AF_1/2/3	4Hz	15-150kN

Geometry and dimensions of specimens are shown in Fig. 4-2, where two steel tubes of $\Phi 60.3 \times 4$ with steel grade S355 are bonded together by composite wrap. Before applying the composites, surfaces of steel tubes were grit blasted and chemically degreased to ensure good bonding between composite laminates and steel tubes. Similar blasting pressure is applied as that used for the high roughness series of 4ENF specimen in Chapter 3, such that the roughness of $S_q > 15 \mu\text{m}$ can be achieved. The laminate of the composite wrap is formed with multi-

directional composition of E-glass reinforcement and a vinyl ester resin system. The composite wrapping thickness is 12mm. The wrapping length for static specimens is 300mm as shown in Fig. 4-2 (a), while a longer wrapping with the length of 480 mm as shown in Fig. 4-2 (b) is used for the fatigue ones in order to have longer stable crack propagation regions. A 25mm PTFE insert is applied at butt end of each tube forming two separate initial crack tips, such that the uncertainties related to crack initiation are reduced. A matt white paint is applied on the wrap, followed by a black speckle pattern to facilitate displacement and strain elastic measurements using 3D DIC system as shown in Fig. 4-2 (c).

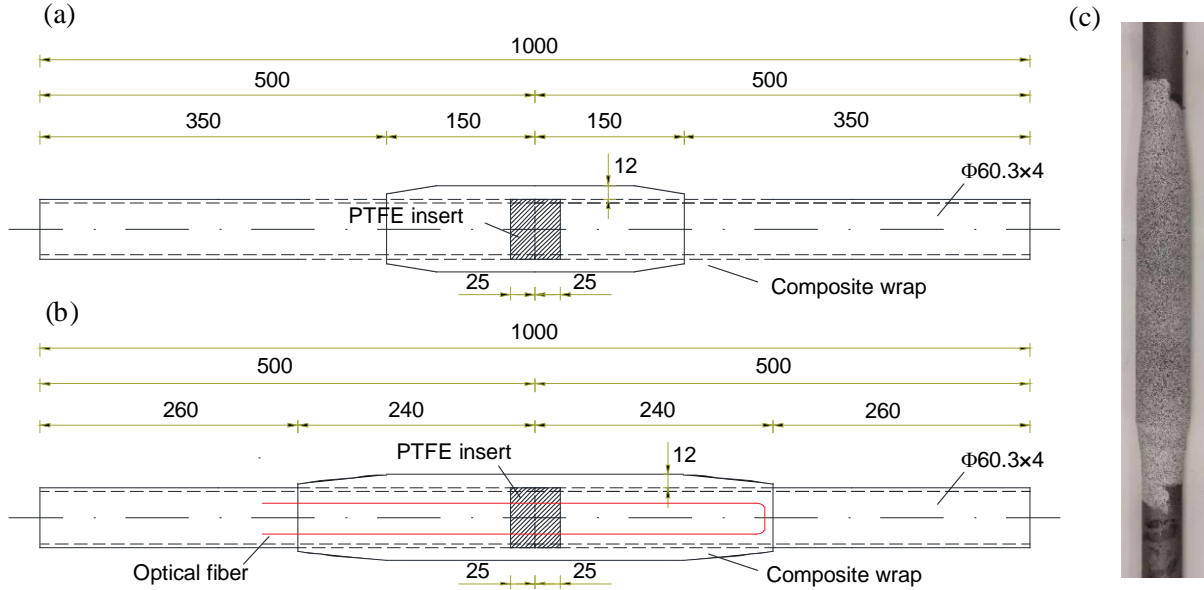


Fig. 4-2 Geometry and dimensions of specimens (a) static specimen; (b) fatigue specimen; (c) fatigue specimen with DIC pattern (in millimetres)

Material properties of composite laminates are obtained by standard tensile/compressive coupon tests according to ISO standards [142–144] and are summarized in Table 4-2.

Table 4-2 Material properties of the composite laminate

Mechanical property	Average value and (CoV [%])
Longitudinal and transverse compressive modulus, $E_{x,c} = E_{y,c}$	12077.11 MPa (4.50)
Longitudinal and transverse tensile modulus, $E_{x,t} = E_{y,t}$	11798.20 MPa (6.37)
In-plane shear modulus, G_{xy}	3120 MPa (6.81)

The tests are conducted by the PCX 001 Hydraulic Wedge Grip, as shown in Fig. 4-3, whose maximum loading capacity is 800kN for the static test and ± 600 kN for the cyclic test. During the tests, the ends of braces are clamped by tailor designed clamps fixed by the hydraulic jaws of the machine to introduce load to the specimens without involvement of any welding, potentially limiting the lifetime of the test by fatigue cracks at the ends. A displacement control with loading rate of 1mm/min is used for static tests. During the fatigue tests, all the specimens

are loaded with the force range of 15-150kN ($R=0.1$), while the maximum force is approximately half of the static resistance obtained in separate tests. The loading frequency is 4Hz. Fatigue tests are stopped when stiffness degradation of the joint stabilized by less than 0.5% reduction within 5000 cycles. After that static tests are conducted to check the residual resistance of the joints. All the tests are carried out at room temperature.

GOM Aramis 3D DIC system with 12MPx cameras is positioned to acquire the displacements and local strains as shown in Fig. 4-3. The debonding crack propagation can be monitored in real-time and processed afterwards by analysing the strain distribution on the surface of the composite wrap. During the static tests, pictures are taken at a constant frequency. During the fatigue tests, the frequency of DIC measurements is controlled by the testing machine. The cyclic loading is stopped every 5000 cycles or 1% of stiffness degradation, then photos are taken at the minimum and maximum forces, respectively.

LUNA ODiSI 6000 optical distributed sensor interrogator, in combination with an embedded primary coated optical fiber, is utilised to measure the longitudinal strains inside the composite. The location of the optical fibre is indicated in Fig. 4-2 (b) and within the first layer of the composite wrap. The LUNA interrogator uses a Rayleigh backscatter pattern which allows to measure strains with a spatial resolution up to 0.65mm. A low bend loss optical fibre, 125 μm with Ormocer coating, is used. During the test, measurements are taken at the same intervals as the DIC measurements, controlled by the testing machine.

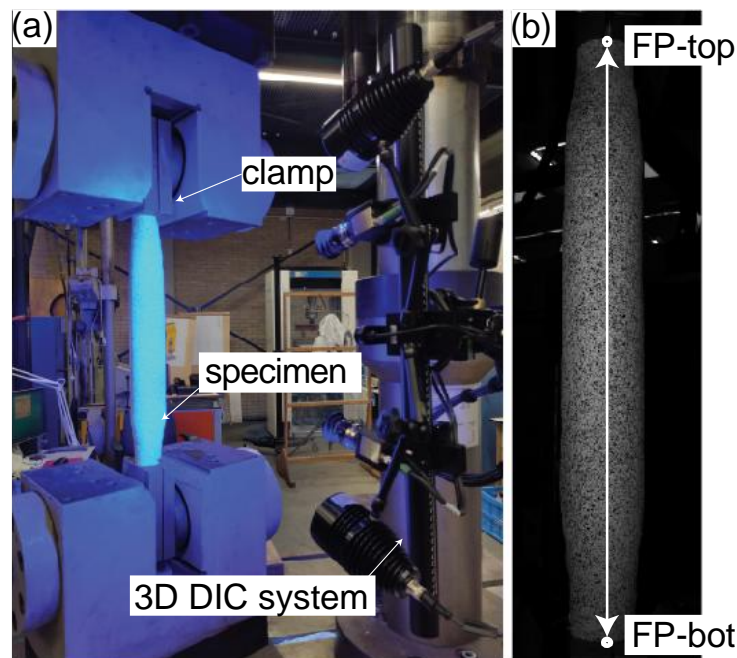


Fig. 4-3 Test set-up and 3D DIC system

4.2.2 Static test

Relative displacement between top and bottom facet points in DIC analysis, FP-top and FP-bot, as shown in Fig. 4-3 are extracted for further analysis. Note that the facet points are located

near the clamping ends outside of the composite wrap. Therefore, the results obtained from DIC reflect mechanical behaviour of not only wrapped joints but also part of steel tubes which is important for understanding the interaction of failure mode related to yielding of steel tube and debonding of the interface between the composite wrap and the steel tubes.

Load-displacement curves of all the 3 specimens summarised in Fig. 4-4. The response of the joint is analysed in detail in combination with a contour plot of strain distribution on the surface of the specimen obtained from DIC as shown in Fig. 4-5. In Fig. 4-6, strain distributions along longitudinal direction of the joint under different load levels are extracted for further analysis. The strain results are taken from one representative specimen AS_1, whose ultimate resistance, F_u , is 288kN. It can be seen from Fig. 4-4 that the load-displacement curves overlap with each other. The behaviour is linear before 180kN (around $0.6F_u$), representing the elastic response of the specimens.

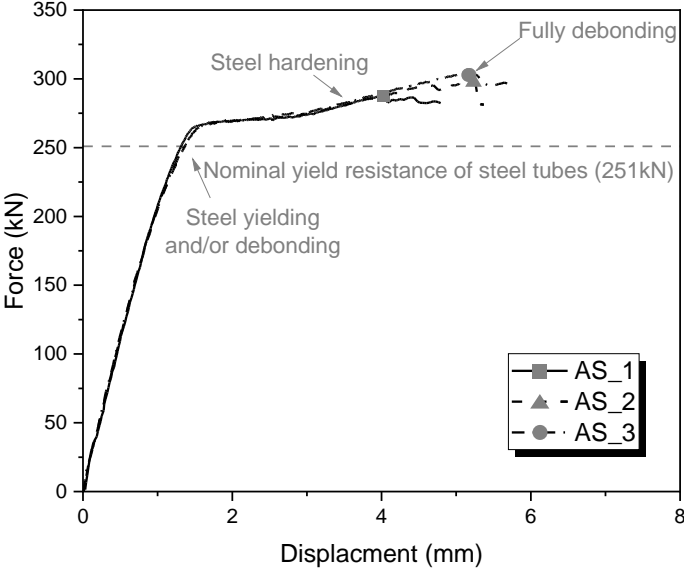


Fig. 4-4 Load-displacement curves of static tests

The strain distribution along the specimen peaks in the middle with the value from 0.1% to 0.4% as shown in Fig. 4-5 and Fig. 4-6 due to existence of the pre-crack. It is only the composite wrap that carries the load in this region in contrast to hybrid cross section of steel and composite in the rest of the specimen. As the load increases, the load-displacement responses becomes nonlinear and reaches a plateau at around 270kN. This may result from steel yielding outside of composite wrap as shown in Fig. 4-6, where strains at the steel part under $0.8F_u$ and F_u reached the elastic strain limit 0.2%. This can also be indicated by the nominal yield resistance of steel tubes, 251kN, as shown in Fig. 4-4. The increasing trend of the load-displacement curves between 270kN and 300kN is attributed to steel hardening. As shown in Fig. 4-5, the strain increased region expands towards both sides, indicating debonding crack propagation at the composite-to-steel interface [120]. This may also lead to the nonlinear behaviour of load-displacement curves. It should be noted that the steel tubes may contract due to yielding outside of the composite wrap, which may cause peel stress at the composite-to-steel interface at the

wrap end, leading to mode I debonding. The mechanisms will be further explained through FEA in section 4.3.2. After reaching the ultimate load, the force dropped abruptly due to full debonding of one of side of the joint. The steel yielding and debonding behaviour will be verified through finite element analysis in the following sections.

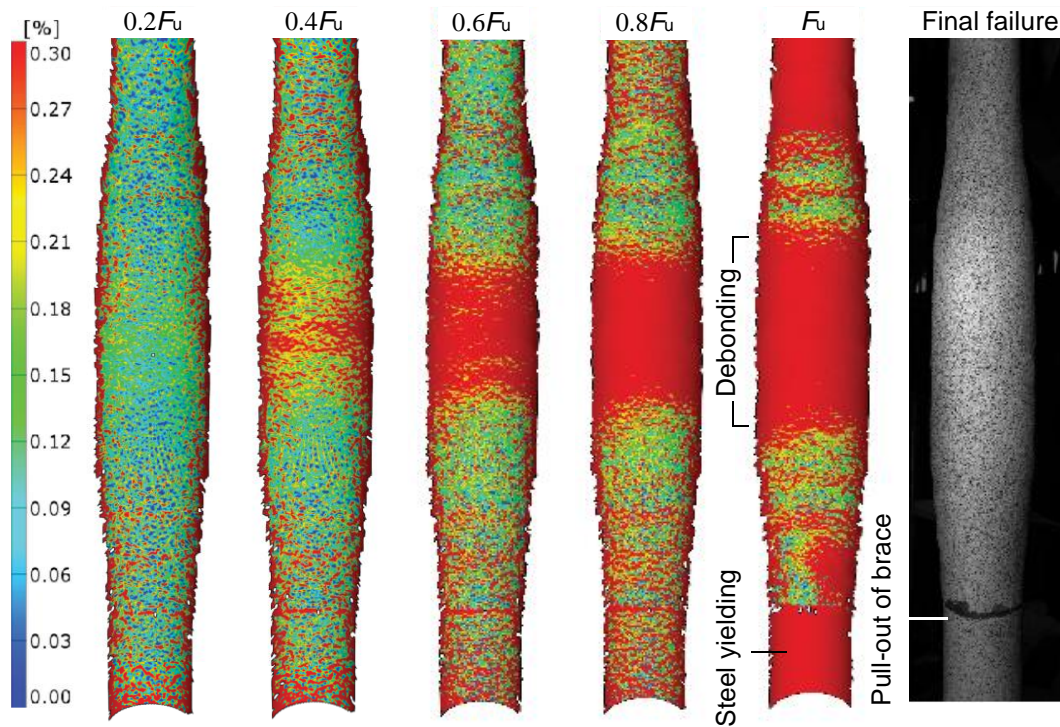


Fig. 4-5 Contour plot of strain distribution on surface of wrapped composite joint under monotonic load (AS_1)

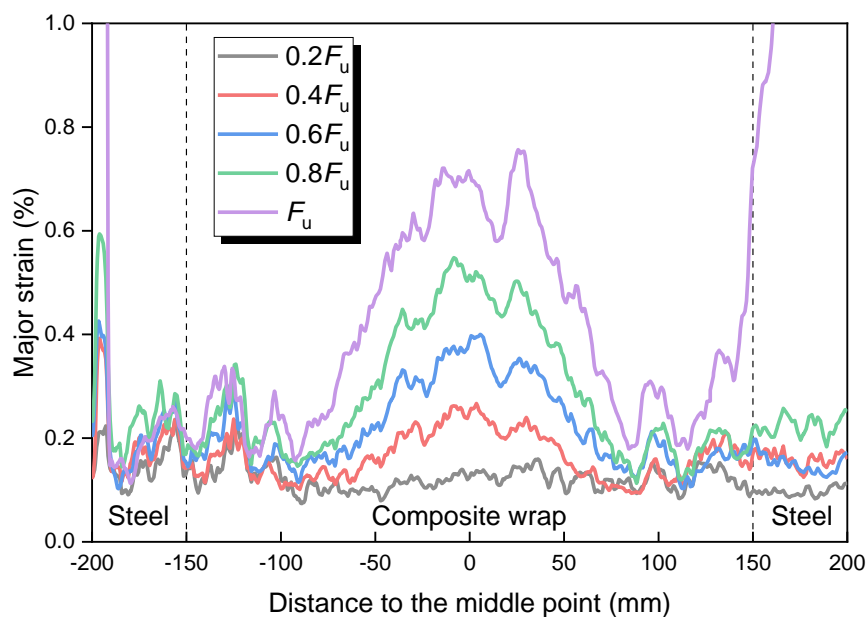


Fig. 4-6 Strain distribution along axis of the joint under different load levels (AS_1)

The initial stiffness K_{ini} , elastic load limit F_e , ultimate load F_u , as well as their corresponding displacements S_e and S_u , and the ductility index defined by S_u/S_e of all the specimens are summarized in Table 4-3 for detailed analysis. The elastic load limit is determined when the secant stiffness is degraded by 5% compared to the initial stiffness. The average initial stiffness is 222.25kN/mm. The elastic load limit is lower than the nominal yield strength of the tube as indicated in Fig. 4-4, with the average value of F_u being 190.98kN. This may result from the fact that debonding dominates the initiation of nonlinear response before steel yielding.

Table 4-3 Static test results

Specimens	K_{ini} (kN/mm)	F_e (kN)	F_u (kN)	S_e (mm)	S_u (mm)	S_u/S_e
AS_1	220.07	203.28	288.01	0.97	4.02	4.13
AS_2	217.69	184.52	298.05	0.89	5.26	5.92
AS_3	228.99	185.15	304.59	0.85	5.10	6.00
Average	222.25	190.98	296.88	0.90	4.79	5.35
(CoV [%])	(2.19)	(4.56)	(2.30)	(5.56)	(11.49)	(15.97)

4.2.3 Fatigue test

4.2.3.1 Stiffness degradation

Typical force-displacement responses of the specimen at different number of cycles are generalized in Fig. 4-7 (a) and one example from specimen AF_1 is shown in Fig. 4-7 (b). As the measurements by DIC are taken only at the maximum and minimum loads in the DIC system, no hysteretic loops can be presented but only straight lines are shown in the Fig. 4-7 (b). It can be seen from the figure that as the number of cycles increases, the stiffness K_i as indicated in Fig. 4-7 (a), defined by the load range divided by the displacement range of each cycle, decreased gradually. Dynamic secant stiffness is defined here to eliminate the influence of residual deformation on the calculated results. In such case the stiffness degradation only results from either debonding at the composite-to-steel interface or damage within the composite material [161]. The residual deformation accumulated during the test which is shown in Fig. 4-7 (a). The residual deformation may result from fatigue-creep behaviour of the composite materials [162] which will be discussed later.

Stiffness degradation of all the specimens is summarized in Fig. 4-8. It can be seen from the figure that stiffness of the specimens degrade continuously during the cyclic loading. Stiffness degradation rate sees a decreasing trend for all the specimens. A major stiffness degradation (about 45%) is found within the first loading stage of 100,000 cycles. Only 10% stiffness was lost in the remaining (secondary) stage until stop of the test at around 400,000 cycles. After the fatigue tests, joints were statically loaded until failure in tension. Load-displacement curves are shown in Fig. 4-8 (b). The possibility for damage tolerant fatigue design of the wrapped joints is demonstrated by these results. Even with the crack propagated almost 2/3 of the original

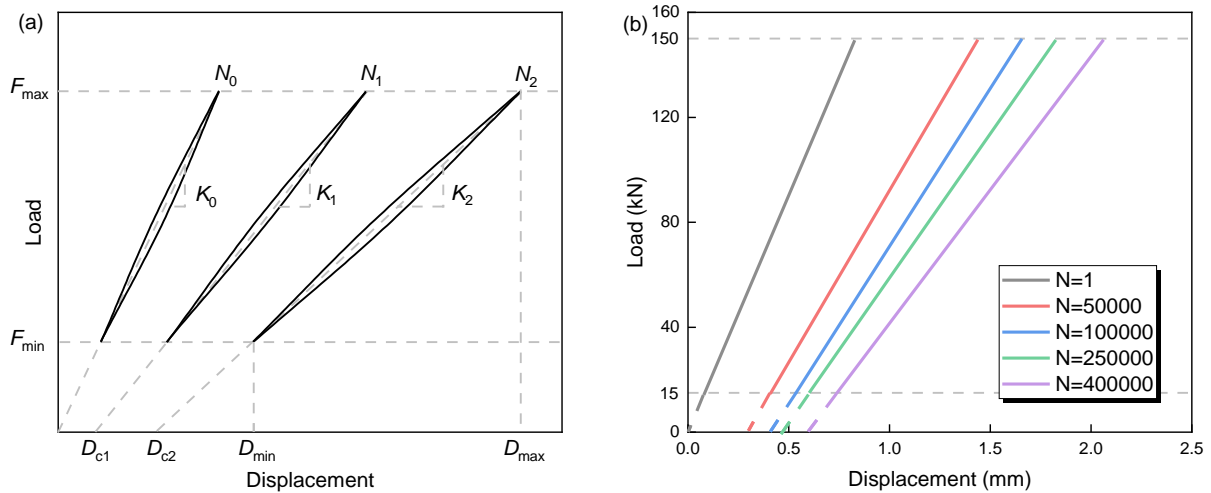


Fig. 4-7 Typical force-displacement curve (a) Definition of stiffness and residual deformation; (b) example from specimen AF_1

overlap length in all specimens (see section 4.2.3.2), the residual debonding resistance of approximately 300 kN is within the range of resistance of undamaged joints (Table 4-3) and surpasses the yield resistance of the steel tubes.

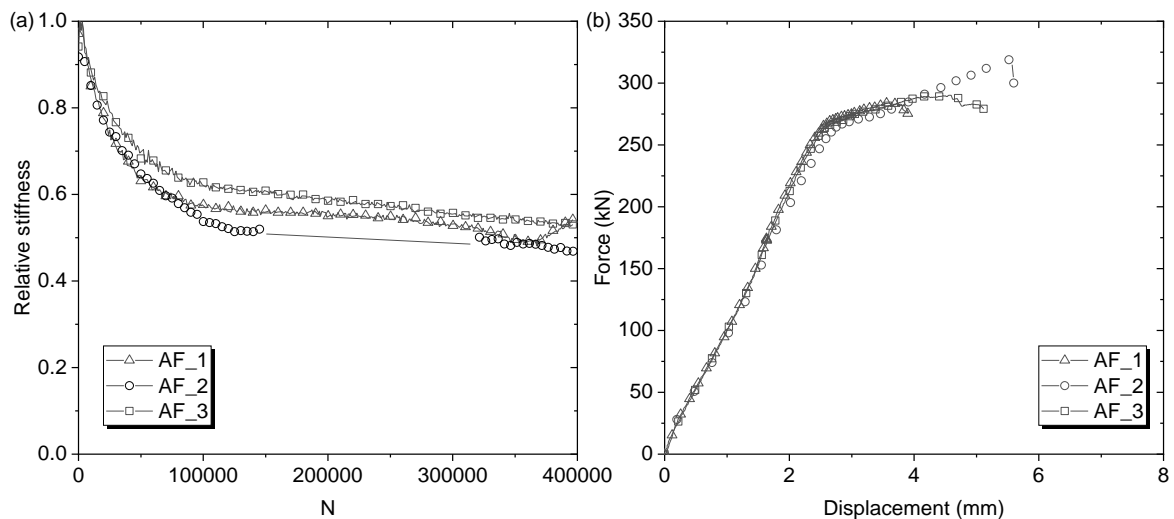


Fig. 4-8 Fatigue results of A-joints: (a) stiffness degradation due to cyclic loading 15-150 kN; (b) load-displacement behaviour in static test after fatigue

Stiffness degradation of the specimens may come from either debonding at the composite-to-steel interface or material damage within the composite wrap. Hypothesis is that the stiffness degradation in the presented test results is dominated by the debonding because the specimens were designed to behave in such manner to allow study of the deboning fatigue. The justification that the material damage in the tested specimens is not significantly contributing to the stiffness degradation is provided as follows. Firstly, average strain on the surface of the composite wrap within the initial crack part as shown in Fig. 4-9 (b), where load is mainly transferred by the composite material, is extracted through DIC system. The strain change within this region for each cycle, $\Delta\epsilon_{ini}$, is obtained. The stress amplitude, $\Delta\sigma_{ini}$, is calculated by

dividing the force range ΔF by the cross area of the composite wrap A_{cr} as shown in Fig. 4-9 (a). The stiffness of the composite material is then represented by $\Delta\sigma_{ini}/\Delta\epsilon_{ini}$ and the relative stiffness degradation is summarized in Fig. 4-9 (a). It can be found that the average stiffness degradation of the composite material is around 10% during the whole fatigue tests. An updated elastic modulus of the composite material based on this analysis is assigned in the finite element model, which will be shown in the following sections. The results show that 10% material damage leads to only 5.5% decrease of the initial stiffness of the joint, which is negligible compared to the overall stiffness degradation of 55% as shown in Fig. 4-8 (a). The results indicate that stiffness degradation of the wrapped composite joints mainly comes from debonding crack propagation at the composite-to-steel interface which will be discussed in the next section.

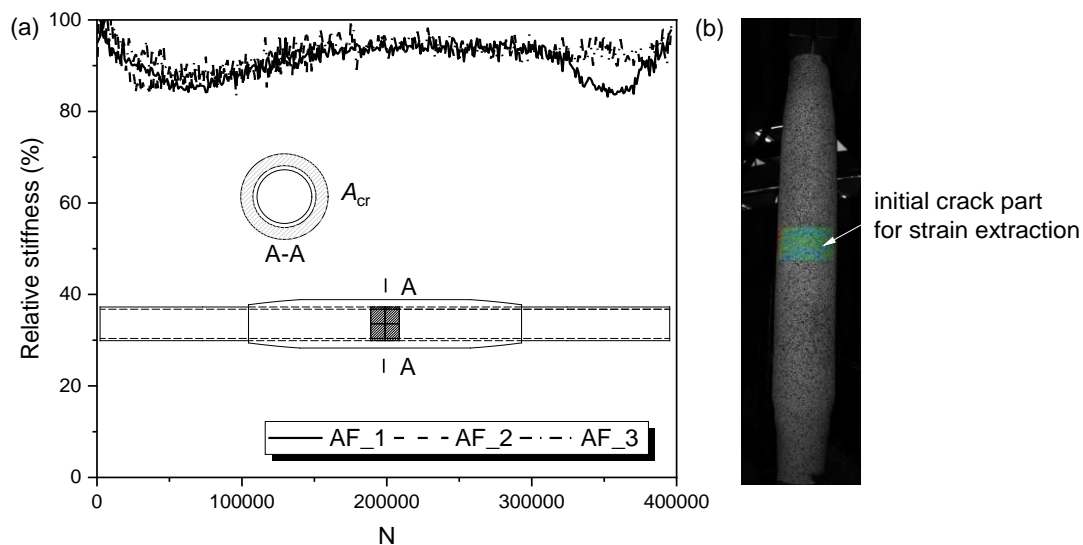


Fig. 4-9 Material damage check (a) stiffness degradation of composite material; (b) strain extraction at the initial crack part in DIC

Besides stiffness degradation, the specimens also show residual deformation during cyclic loading as shown in Fig. 4-7. Residual deformation of all the specimens are summarized in Fig. 4-10. The figure shows that specimens exhibit similar trend, namely the residual deformation developed rapidly during the first 130,000 cycles to around 0.5mm and increases gradually up to 0.8mm during the remaining 270,000 cycles. The maximum residual deformation corresponds to around 40% of the maximum applied displacement of 2mm, which is not negligible. The residual deformation accumulation procedure may result from cyclic creep behaviour of the composite materials [162,163]. Creep behaviour is the time-dependent deformation under a constant load, which in this case is the average level of the cyclic loads. Important to mention is that the cyclic load level applied to the tested specimens is much higher than the expected Damage Equivalent Load (DEL) in the case of real structures, such as offshore wind turbine jacket supporting structures. Thus, the relative accumulated deformation in the full-scale joints in real structures is expected to be much less than in the presented test,

even negligible. Material damage resulting from fatigue loads may increase the creep deformation. For specimen AF_1, a huge increase of residual deformation up to 1.2mm is seen after 350,000 cycles. This may be attributed to abrupt slip or debonding and built-up debris within the specimen.

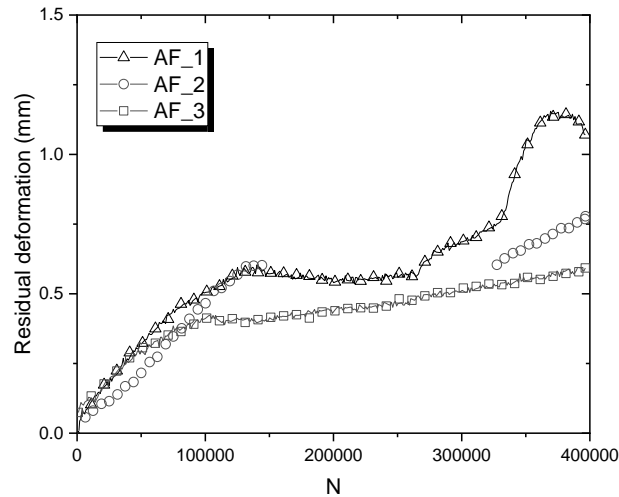


Fig. 4-10 Residual deformation of the joints

4.2.3.2 Debonding crack propagation

During and after fatigue tests, no significant surface cracks are observed in the specimens. Further inspection on strain development is conducted through DIC and optical fibre measurement systems. Fig. 4-11 (a) shows DIC contour plots of major strain range, namely the maximum strain minus the minimum strain, on the surface of composite wrap at different cycles. With an increasing number of cycles, the strain-increased zone (in red colour) propagates steadily from the region of the insert (pre-crack) towards the wrapping ends, qualitatively indicating debonding crack propagation at the composite-to-steel interface or within composite wrap layers. After fatigue test, namely around 55% stiffness degradation, steel tubes are pulled out of the composite wrap statically and cut into half pieces for further inspection. It can be seen from Fig. 4-11 (b) that the crack propagation transfers from composite-to-steel interface to the first plies of the composite wrap at a certain location.

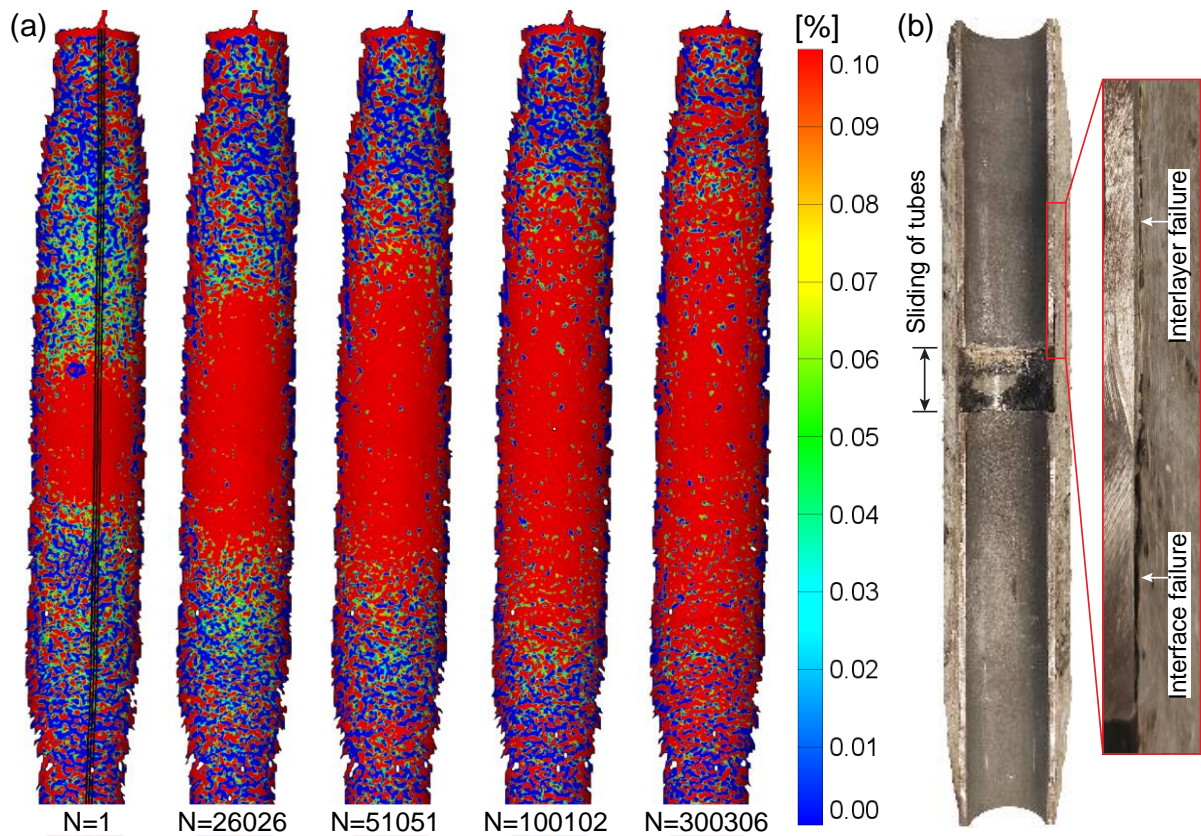


Fig. 4-11 Failure mode of specimens (a) debonding crack propagation at different numbers of cycles (AF_2); (b) steel tubes pulled out after static load

Strain distributions are extracted along the curves defined on the surface of composite wrap as shown in Fig. 4-11 (a) for further quantitative analysis. The strain ranges i.e. the difference of the strain distribution at the maximum load and the minimum load in each cycle is adopted here to eliminate the influence of residual deformation as mentioned above. The extracted strains at different number of cycles are plotted against the distance to the middle of the joint in Fig. 4-12 and compared with those obtained from optical fibers for specimen AF_2. It can be seen that the strains are peaked at the initial crack part in the middle, where the load is mainly transferred by the composite wrap, then decrease gradually towards both ends of the composite wrap. Different from literature [116] which shows that there is a strain plateau at the cracked part accompanied by sharp strain decrease at the bonded part, the plateau is not obvious in the current study. This may be attributed to the shear deformation gradient of such thick composite laminates, caused by restraining from the bonded part and residual interaction such as friction, fibre bridging et al. at the cracked interface. However, the strain decrease region extracted from optical fibers shows more rapid drop. This is because the strains from optical fibers are obtained inside the laminate close to the steel-composite interface instead of on surface of the composite wrap as in DIC. The influence of shear deformation of the wrap is smaller than in the case of DIC results. A sharper strain decrease provides more accurate information on the crack tip location. Results show that the crack length that would be determined by the optical fibres based on the strain fronts close to the interface and the crack length from the DIC system are in well

agreement. Unfortunately, due to damage of the optical fibers during the test, results from Luna system experienced data loss after 35,000 cycles. For the remaining part, the strain development is only analysed by the DIC results.

Fig. 4-13 (a) shows strain development at different cycles taking specimen AF_3 as an example. With an increasing number of cycles, the strain fronts expand in parallel towards both ends. A constant strain threshold is taken around this region to calculate the crack increments. The crack lengths are calculated separately for each brace and equal to the summation of crack increments from each cycle plus the initial crack length of 25mm. A sensitivity analysis of the strain threshold is carried out on one of these braces as shown in Fig. 4-13 (b), where strain threshold of 0.1%, 0.15% and 0.2% are adopted. The results show that within the strain fronts region, the influence of adopting different thresholds is insignificant, while a higher threshold may result in scattering calculated results due to scattering and overlapping of strain distribution curves in the middle. In the following analysis, strain threshold of 0.1% is adopted for all the specimens.

The measured debonding crack propagation for all the braces are summarized in Fig. 4-14. For all the specimens, crack grows rapidly at early stage and sees a decreasing growth rate during the following number of cycles. Specifically, crack lengths increase rapidly from 25mm to around 110mm during the first 100,000 cycles, while after that the additional 40mm crack length is achieved during the remaining 300,000 cycles leading to total crack length of 150mm. In other words, crack propagation of all the specimens experienced the retardation phenomenon, exhibiting a decreasing crack growth rate. Considering that fatigue crack propagation is driven by strain energy release rate (SERR) at the crack tip according to Paris relationship [164], the crack growth retardation may be attributed to decreasing of SERR values. The contact stress between composite and steel may lead to friction effect at the interface, dissipating part of the strain energy, which is thought to be the reason of decreasing SERR values at the crack tip. Note that the fibre bridging effect may also lead to retardation of crack growth at the interface, although this effect is not predominate under mode II fatigue loading [165]. The built-up debris and micro wedge effect behind the crack front can also contribute to friction effect, thus secondary load transfer and reduction of SERR at the crack tip. To explain this fatigue debonding retardation phenomenon due to the friction effect mentioned above, a finite element model is developed in the next sections.

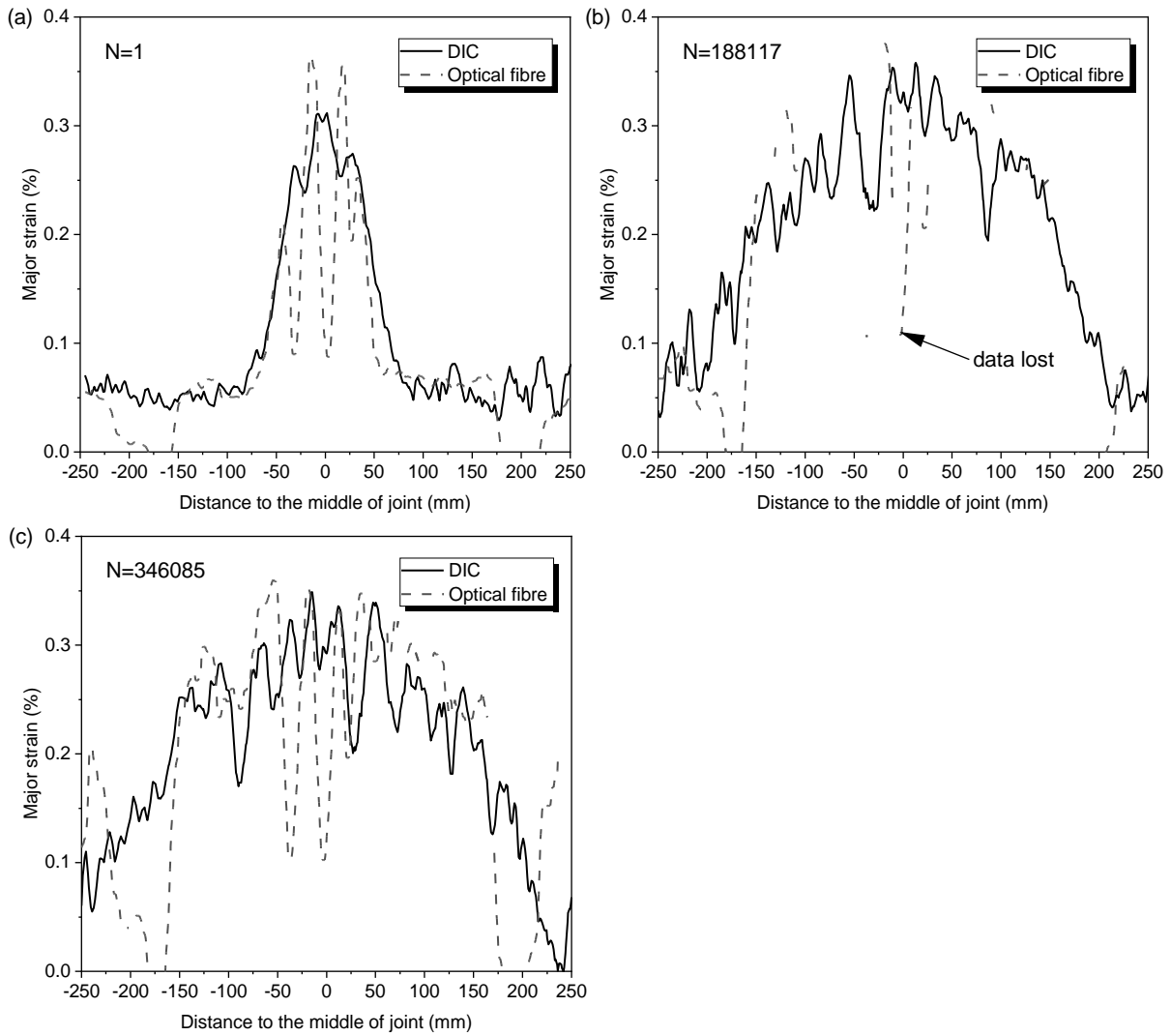


Fig. 4-12 Comparison on strain development from DIC and optical fiber systems (AF_2)

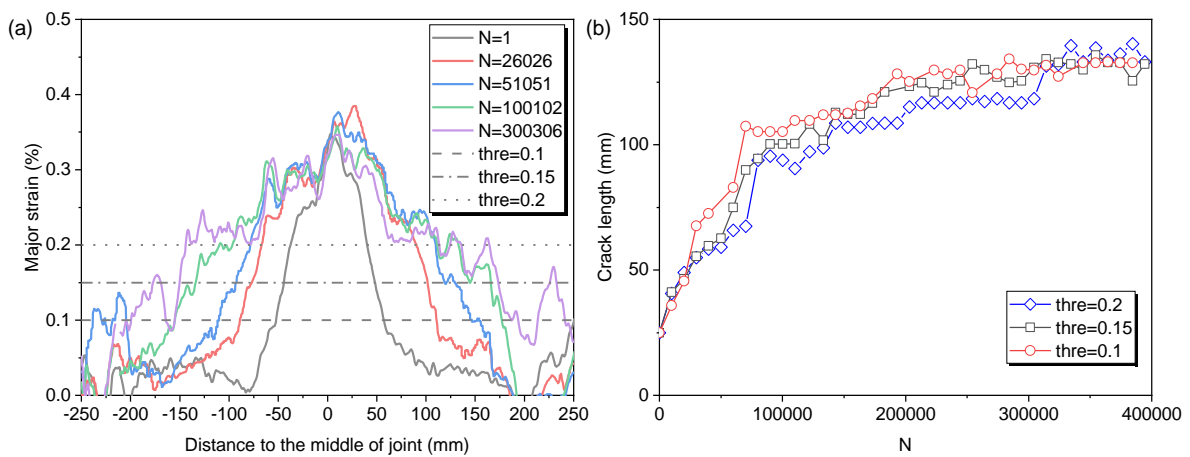


Fig. 4-13 Debonding crack propagation (a) Strain distribution along the specimen at different cycles; (b) debonding crack length determined by different strain thresholds (AF_3)

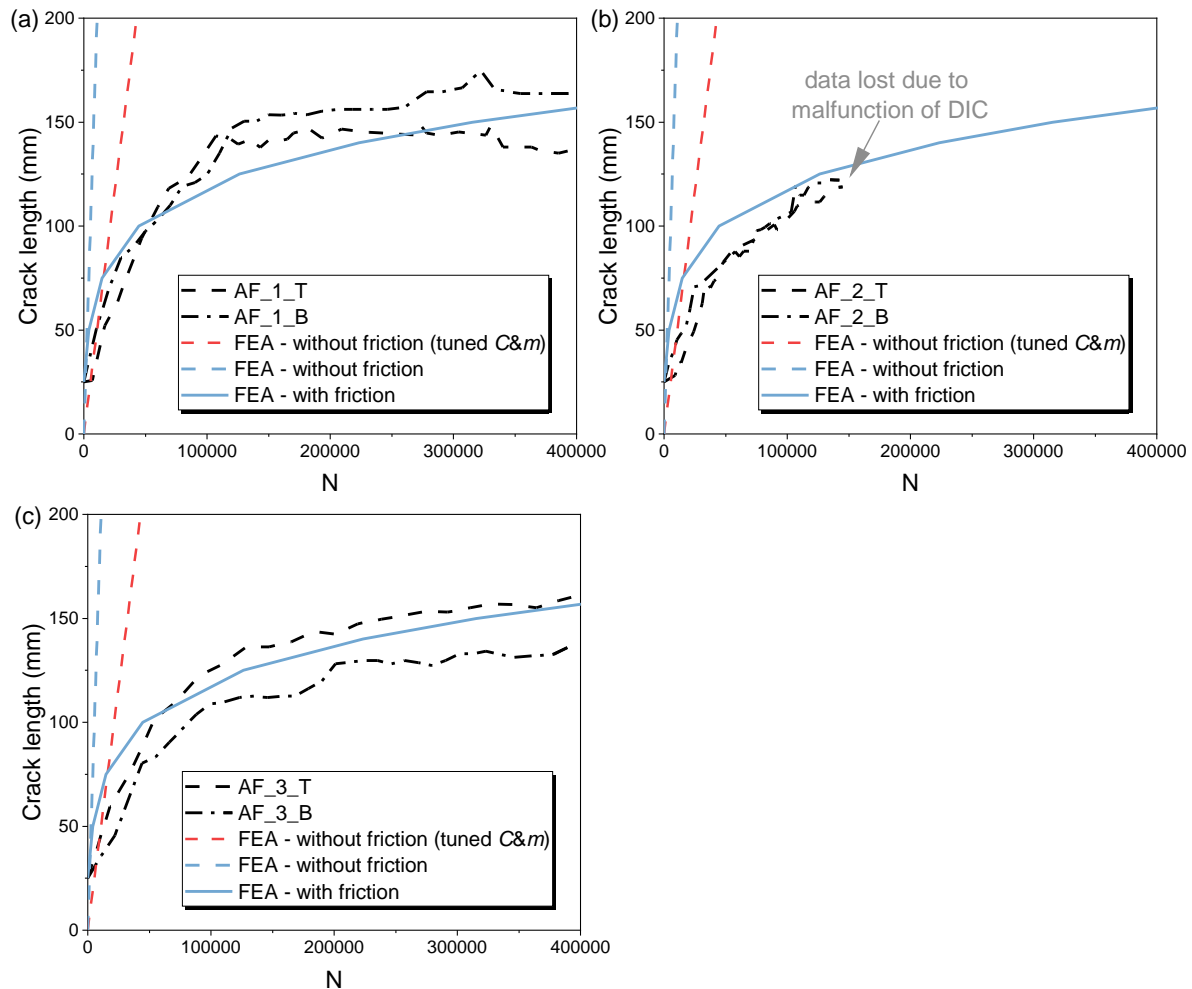


Fig. 4-14 Crack propagation under fatigue loads

4.3 Finite element modelling

4.3.1 Modelling strategy

A 3D finite element (FE) model is built in ABAQUS software [166] to interpret failure mechanisms of the tests, as well as the friction effect at the composite-to-steel interface. The geometry and dimensions of the FE model follow the design of the static and fatigue-tested specimens. The model is shown in Fig. 4-15. A half model is built to shorten the analysis time thanks to the symmetric character of the model. Cross section of the end of the steel tubes are coupled to a reference point, where boundary conditions are applied. All the degrees of freedom except for the U2 direction of the reference points are constraint to simulate the fixation condition resulting from clamps in the physical test. Displacement of 10mm is applied in the U2 direction for load application with a smooth step amplitude curve. A symmetry boundary condition of $U_3=U_{R1}=U_{R2}=0$ is applied on the symmetry plane. Linear, hexahedron eight-noded solid elements with reduced integration (C3D8R) are used for the steel parts, while linear tetrahedron elements (C3D4) are used for the composite wrap due to its complex geometry. A sensitivity study on the mesh size is conducted considering the dependency of strain energy release rates on the mesh size and computing efficiency. The result converges to 2mm.

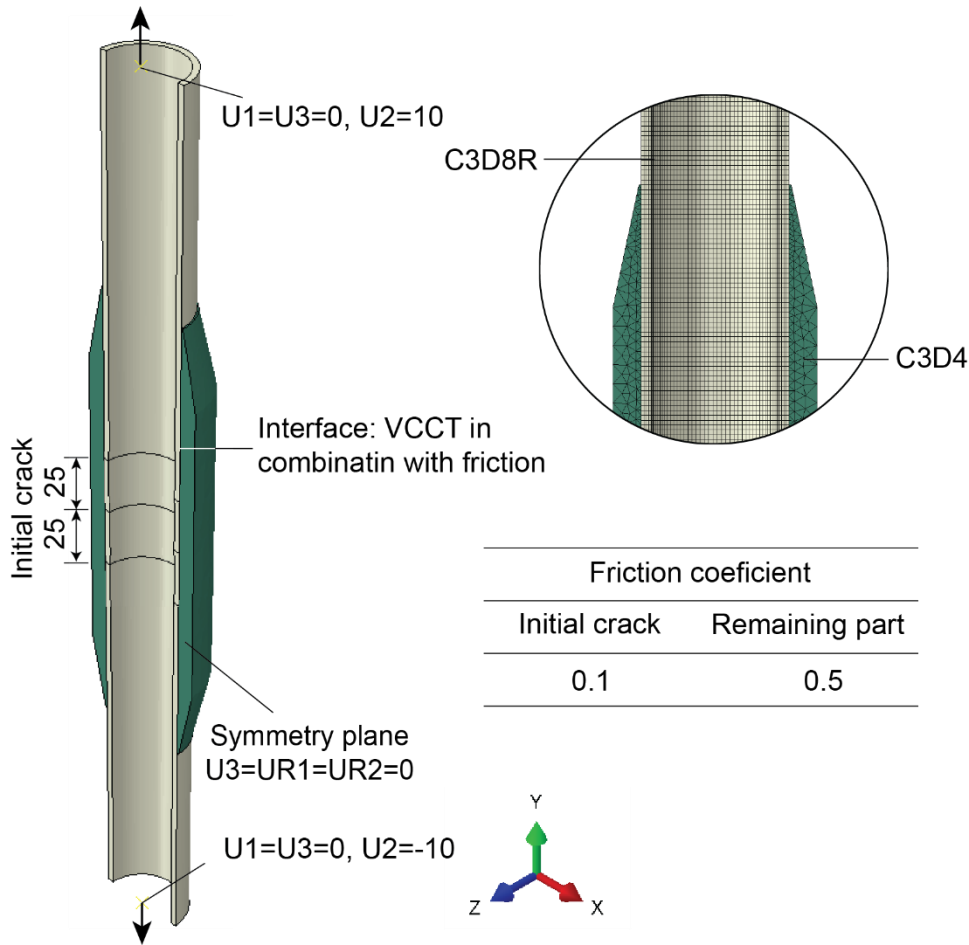


Fig. 4-15 3D finite element model of the joint

The virtual crack closure technique (VCCT) is utilized here to simulate the crack propagation at the bonded composite-to-steel interface and calculate the SERRs. The nodes in front of the crack tip from both steel and composite parts are coupled and will debond after the strain energy release rate (SERR) based fracture criterion, $G_T \geq G_{eqC}$, is met. For Benzeggagh–Kenane (BK) criterion used in this study, G_T represents the total SERR, i.e. $G_T = G_I + G_{II} + G_{III}$. G_{eqC} is the equivalent critical SERR, which is defined by:

$$G_{eqC} = G_{IC} + (G_{IIC} - G_{IC}) \left(\frac{G_{II} + G_{III}}{G_T} \right)^\eta \quad (4-1)$$

where G_{IC} and G_{IIC} are the critical mode I and mode II SERRs, and $\eta=1.8$. Different combinations are adopted for the critical SERRs according to different modelling strategies. The initiation and propagation values of SERRs are obtained through standard DCB and ENF tests in [140] and are listed in Table 4-4. In the current study, the initiation values and propagation values for mode I and mode II SERRs are adopted, respectively, in combination of friction defined at the interface. A third combination is obtained by calibrating the critical SERR values between the initiation and the propagation values until the force-displacement curve reaches a good match with the test results. For modelling fatigue behaviour of the joints, models

with stationary cracks of different lengths are created. The critical SERRs are set with relatively high values, i.e. 100N/mm, such that the criterion in Eq.(4-1) will not be met and the SERRs at the crack tips can be calculated. The friction coefficient is measured by the tribometer as introduced in chapter 3, which is found to be around 0.1 at the pre-crack with the insert at the interface and to be around 0.5 at the bonded interface. The modelling procedure is validated not only by comparing force-displacement curves with the static tests but also the strain distribution on the surface of the composite wrap from the cyclic load experiments obtained by DIC, which will be discussed in the next section.

Table 4-4 Critical values of SERR

SERR	Initiation values (N/mm)	Propagation values (N/mm)
G_I	0.30	1.40
G_{II}	0.56	3.50

Plasticity model in ABAQUS is used in this study to model non-linear behaviour of steel. Elastic constants ($E=210\text{GPa}$, and $\nu=0.3$) and nominal yield and ultimate stress (S355, $f_y=355\text{MPa}$, $f_u=510\text{MPa}$) in combination with isotropic hardening are used for the steel tubes. The composite wrap is modelled as one piece of solid part in this model. Stresses in the composite wrap in the ultimate load (static) and cyclic load (fatigue) tests are much lower than the strength of the material according to the preliminary analysis. Therefore, the composite wrap is modelled with elastic material properties. Transversely anisotropic material properties are defined based on the tests results shown in Table 4-2 for the in-plane properties of the laminate: E_1 , E_2 , G_{12} and ν_{12} . In absence of test data, the out-of-plane elastic properties of the laminate E_3 , $G_{13}=G_{23}$, $\nu_{13}=\nu_{23}$ are defined based on values obtained through micromechanics (rule of mixture) for an equivalent unidirectional material with the fibre volume fraction conforming of the tested laminate ($V_f = 30\%$). The elastic properties used are shown in Table 4-5.

Table 4-5 Anisotropic elastic properties of the composite material in the model

Elastic constants
$E_1=E_2=12000\text{MPa}$, $E_3=5000\text{MPa}$, $G_{12}=3120\text{MPa}$, $G_{13}=G_{23}=2500\text{MPa}$, $\nu_{12}=0.22$, $\nu_{13}=\nu_{23}=0.3$

4.3.2 Results of modelling the static experiments

The simulated force-displacement curves for ULS analysis are plotted versus test results in Fig. 4-16 (a). All the FE modelling results are overlapped with each other at the linear elastic stage and match well with the test results. Except for the model with initiation SERRs, other models also match well with each other at the non-linear stage until 275kN. This is because the nonlinearity of the force-displacement response until this stage mainly reflects yielding and hardening behaviour of the steel tubes outside the composite wrap, accompanied by relatively

short, up to 6 mm, debonding at the interface. Whereas the ultimate loads, which correspond to fully debonding at the interface, vary among different FE models. The model with the initiation value of SERR underestimates the ultimate load while the model with the propagation value of SERR overestimates the ultimate load and deformation drastically. In the next step, the mode I and mode II critical SERR values are calibrated between the initiation and propagation values proportionally until the good match with the test results is found. The best fitted model is found to have the critical SERR values of 1N/mm for mode I and 1.3N/mm for mode II, respectively. The model not only matches well with the force-displacement curves but also resembles the test results in terms of strain distribution from DIC as indicated in Fig. 4-17 (see the next section). After the critical SERRs are calibrated, another model is run without friction defined at the interface. As expected, the model without friction underestimates the ultimate load. The necessity of defining friction at the interface can also be justified by the comparison of strain distribution on the surface of composite wrap, as well as by explaining SERR reduction at the crack tip, which will be discussed in next sections.

Debonding stages obtained from the best fitted FE model is shown in Fig. 4-16 (b). The debonding crack initiates at the inner side of the bonded interface at the force level of 250kN (point A). After crack propagates by 6 mm at the inner side, a secondary crack initiates at the outer side, namely the wrapping ends, at the force level of 275kN (point B). The secondary crack initiates due to steel yielding outside of the wrap, which leads to contraction of the steel tubes and peel stress at the composite-to-steel interface as shown in Fig. 4-16 (b). After the peak load of 290kN (point C), cracks at the inner side and the outer side further develop until merging each other, resulting in full debonding at the interface (point D).

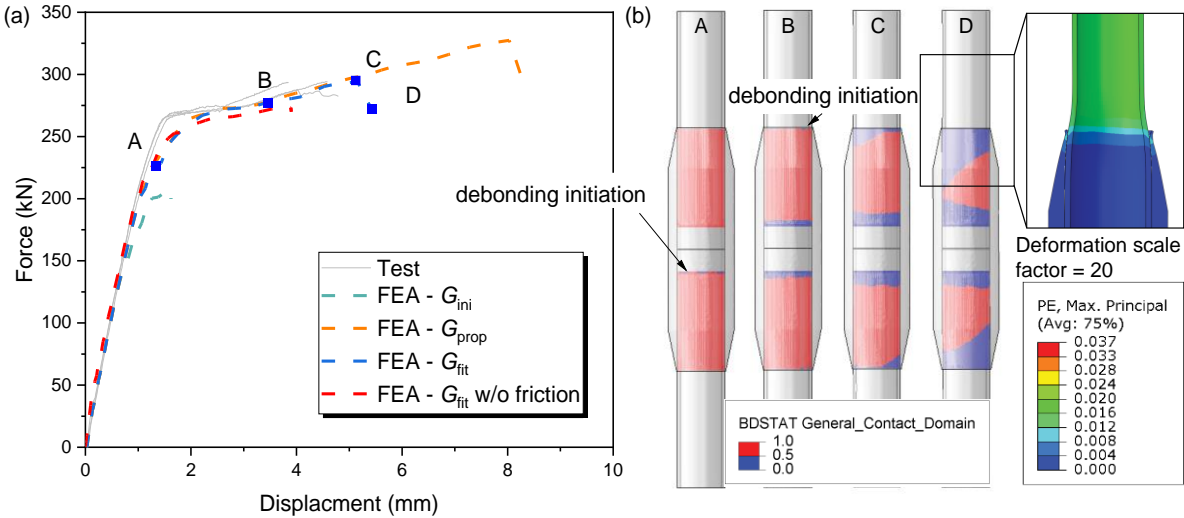


Fig. 4-16 Modelling results (a) force-displacement curves; (b) crack debonding process

4.3.3 Results of modelling the fatigue experiments

4.3.3.1 Strain distribution on the composite wrap

Models of fatigue tested specimens with stationary cracks of different lengths are loaded in a quasi-static manner until the maximum force level during fatigue tests, i.e., 150kN. The strain distribution ranges on the surface of the composite wrap are validated against the corresponding test results as shown in Fig. 4-17 (a). Friction at the interface is or isn't considered to highlight the rationality of its existence. As shown in this figure, strain distributions from the models with friction resemble well with the test results of corresponding crack lengths. The strain distribution follows a typical bilinear shape for each side of the joint, where the strain gradient at the cracked part shows a smaller slope than that at the bonded part. Whereas for models without friction, strain distribution at the cracked part exhibits a plateau. The reason behind the difference is explained with reference to Fig. 4-17 (b). In an idealistic case without the friction at the cracked interface, the strains in the composite are constant because it is only the tubular cross section of the composite wrap that transfers the axial load. On contrary, in the case with the friction defined, the deformation of the composite wrap at the cracked part is partially restrained by the friction at the interface. Therefore, a portion of the axial load is transferred to the steel cross section in the cracked region, leading to the non-constant strain distribution in the composite wrap. Restraint from the bonded interface is more significant, resulting in a larger slope of strain gradient (strain front) on the surface of the composite wrap. The strain front at the bonded part at different number of cycles again is parallel to each other from the FE results, providing the rationality of using a constant strain threshold within this region (0.1%-0.2%) to determine the crack length as discussed in the section of 4.2.3.2.

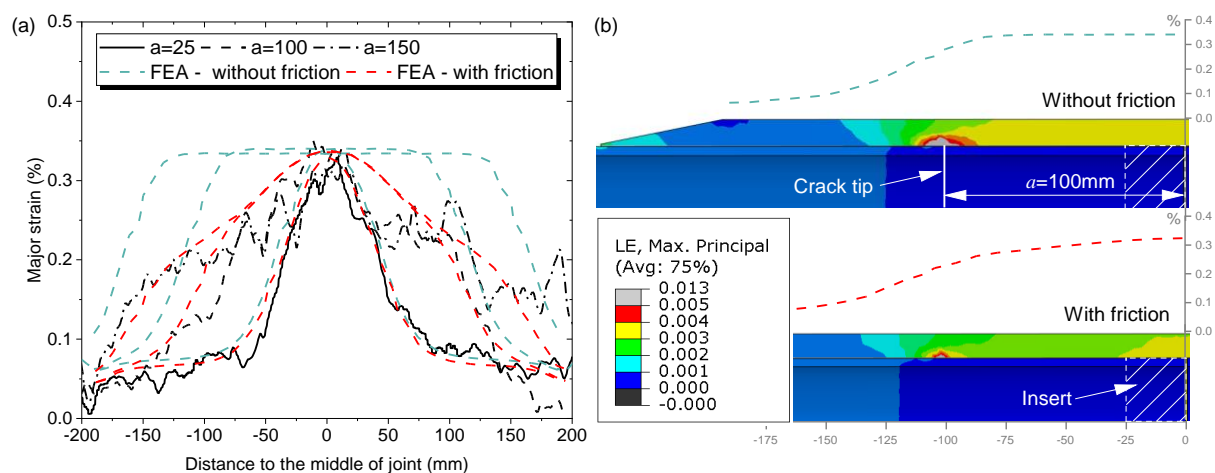


Fig. 4-17 Major strain distribution in the composite wrap (a) strains at surface from experiments and FE models (along the length, $x=0$ mm at connection of two tubes); (b) strain distribution from the FE models in the longitudinal cut through the composite wrap and the steel tube

4.3.3.2 Crack propagation and stiffness degradation

When multiple energy dissipation mechanisms exist at the interface, the crack propagation follows the Paris relationship interpreted in terms of SERR values at the crack tip G_{tip} [167,168]. SERR values at the crack tips of different locations are extracted for further analysis of the influence of friction effect on the crack propagation. SERR values of different modes are extracted at the crack tip for the FE model with the initial crack of 25mm corresponding to the PFTE insert as shown in Fig. 4-18 (a). The figure illustrates that mode II SERR is dominating, which is to be expected for such in-plane shear behaviour at the composite-to-steel interface. This is because the cylindrical shape of the interface prevents the radial deformation of the composite wrap and therefore eliminates the peel stresses. The average mode II SERR values at different crack lengths are obtained for FE models with and without friction applied as shown in Fig. 4-18 (b). It can be seen that when the friction is applied, the mode II SERR decreases from 0.85N/mm to 0.24N/mm as the crack length increases from 25mm to 150mm. Without the friction being applied in the cracked region, the mode II SERR is fairly constant. This is because the composite wrap is solely transferring the applied constant force, see Fig. 4-17 (b), and the thickness of the composite is constant, therefore the stresses around the crack tip are the same for all the crack lengths from 25 mm to 150 mm. However, in presence of friction the force in the cross section of the composite wrap near the crack tip reduces because larger and larger portion of the force is being transferred to the steel tube by the friction as the crack grows. The reduced force in the cross section of the composite wrap results in reduction of stresses and strains in the composite at the crack tip and therefore decreased SERR. The SERR curves with and without friction are fitted in Fig. 4-18 (b) with second order polynomial functions for further analysis.

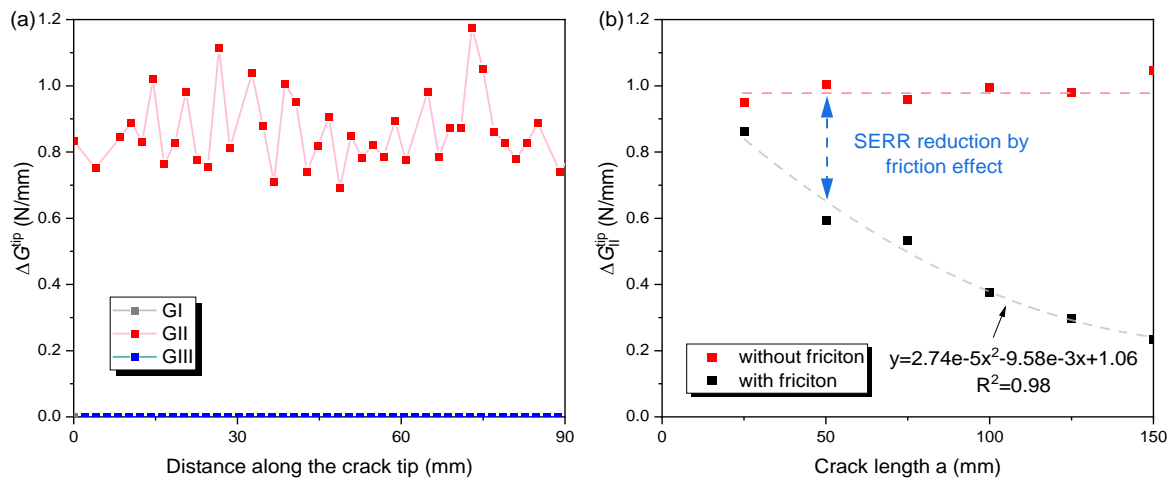


Fig. 4-18 SERR values (a) distribution along crack tip; (b) development with crack growth

With the SERR development calculated, the crack growth at the composite-to-steel interface can be predicted based on the Paris relationship, as shown in Eq. (4-2).

$$da / dN = C(\Delta G_{tip})^m \quad (4-2)$$

where the C and m parameters are obtained through the cyclic 4ENF tests from chapter 3. Test results of high roughness series of 4ENF specimens are used considering the similar surface preparations for the steel tubes here. Paris curves where the SERRs are calculated by FEA are adopted to ensure that the friction effect is taken into account and is comparable to the SERR obtained in the joint models. Based on the obtained Paris relationship parameters in Table 3-6 and regression of crack tip SERR versus crack lengths as shown in Fig. 4-18 (b), the number of cycles corresponding to a certain crack length can be calculated based on Eq. (4-3). Predicted crack growth are plotted together with the test results as shown in Fig. 4-14 and comparisons are made to the different joint specimens that were tested. The figures show that without consideration of friction effect, the predicted crack growth only matches with the test results in the initial stage even when the best tuned C and m parameters ($C=0.005$, $m=4$) are adopted (dash red lines). But the crack growth is significantly overestimated with relatively high constant crack growth rate at later stages. Whereas predicted results with friction effect taken into account exhibit a typical retardation phenomenon, which agree much better with the test results when adopting the best calibrated combination of Paris relationship parameters of $C=0.02$ and $m=3.75$ within experimentally obtained ranges. For comparison reasons, the predicted results without friction with the same C and m values are also shown in the figure (dash blue lines), which obviously overestimate the crack growth.

$$N = \int_{a_0}^{a_N} \frac{1}{C[\Delta G_{tip}(a)]^m} da \quad (4-3)$$

Stiffness degradation predicted by FE models with different crack lengths are plotted against the number of cycles and compared with test results as shown in Fig. 4-19. It is shown that similar to the test results, the predicted stiffness degradation curve with friction considered drops rapidly, i.e. 35% is lost, within the first 150,000 cycles. After that a stabilization trend is seen and additional 10% of the initial stiffness is lost during the remaining 250,000 cycles. On the contrary, the model without friction overestimates the stiffness degradation a lot, where 60% stiffness degradation is lost within just 10,000 cycles (dash blue lines). Again, even when the best tuned C and m parameters ($C=0.005$, $m=4$) is adopted for the model without friction, the predicted results can only match well with the initial stiffness degradation but overestimate it at later stages.

The model with friction and Paris relationship parameters of $C=0.02$ and $m=3.75$ underestimates the stiffness degradation obtained in tests in the later stages. Possible reasons could be that the prediction doesn't take into account the material damage.

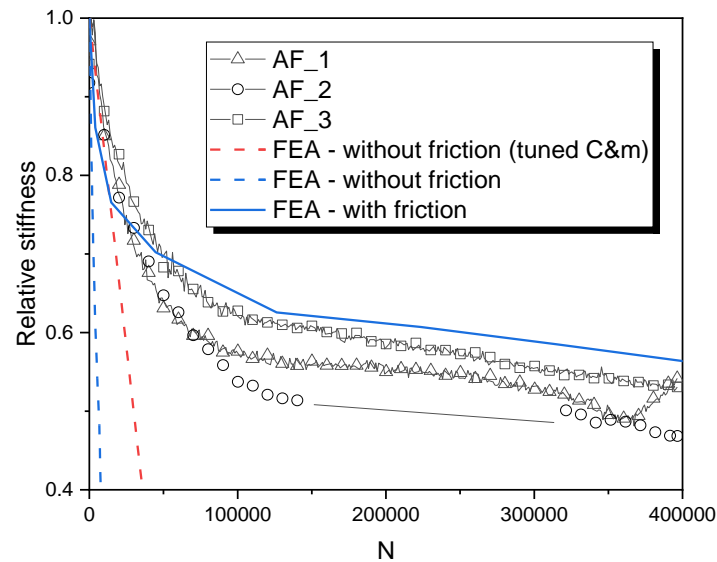


Fig. 4-19 Prediction on stiffness degradation

4.4 Parametric study of fatigue crack growth

The sensitivity of fatigue behaviour to the governing parameters of the FEA validation, namely friction coefficient, crack location (depth), and Paris relationship parameters C and m is investigated in this section. The damage tolerance up to 50% stiffness degradation has been demonstrated in the fatigue experiments, see section 4.2.3.1, which correspond to crack length of 150mm, i.e. 2/3 of the original overlap length. For the comparisons in this parametric study a more rigorous failure criterion, i.e. 30% stiffness degradation, is used to determine the number of cycles to failure.

4.4.1 Influence of friction coefficient

As the retardation phenomenon is caused by the friction effect at the interface, the utilized friction coefficient μ has a great influence on the predicted results. The physical reasoning behind varying value of the friction coefficient are variations of the surface roughness, amount of fiber bridging and built-up debris etc. In the current study, the friction coefficient at the cracked part is varied from 0.3 to 0.7 to investigate its influence on the SERR development and crack propagation and retardation. Note that the friction coefficient at the initial cracked part remains unchanged as 0.1 considering that the friction coefficient of this part is only influenced by the PTFE insert.

SERR development vs. crack growth from models with different friction coefficients are plotted in Fig. 4-20 (a). It can be seen that starting from the same level, i.e. 0.85N/mm, SERR values with higher friction coefficient decreases more as the crack grows. For instance, SERR value of model with friction coefficient of 0.7 has dropped by 88% to 0.10N/mm as the crack increases from 25mm to 150mm, while the same value from model with friction coefficient of 0.3 only drops by 56% to 0.39N/mm. 2.3 times higher friction coefficient leads to 53% higher SERR decrease. Based on Eq. (4-3), the fatigue crack growth curves can be obtained as Fig. 4-

20 (b). The results show that model with higher friction coefficient exhibits more obvious crack growth retardation phenomenon. According to Paris relationship, 2 times increase of SERR may lead to $(2)^{3.75}=13.5$ times higher crack growth rate, which is the slope of crack growth curves in Fig. 4-20 (b). Stiffness of different models are normalized against the initial value and plotted versus the obtained number of cycles from Eq. (4-3). As shown in Fig. 4-20 (c), higher friction results in more significant stiffness stabilization in the later loading stages. Taking 30% as failure criterion, the relationship between fatigue life and friction coefficient is shown in Fig. 4-20 (d). the model with friction coefficient of 0.7 may have 39 times longer fatigue life than that with friction coefficient of 0.3 (540,000 vs. 14,000 cycles). This means that if the surface is rough enough, the crack growth at the debonded interface may be totally arrested. The other failure modes such as material failure may take place.

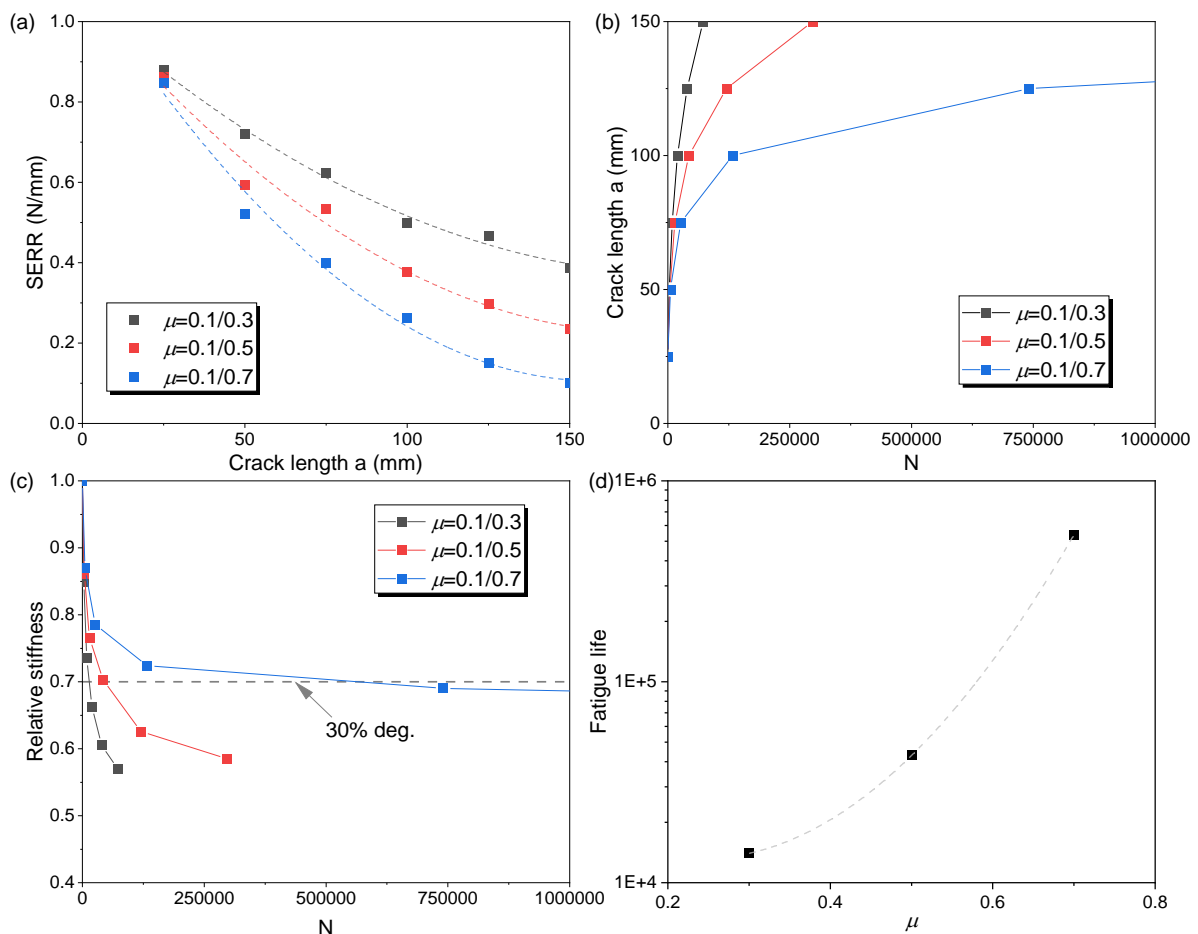


Fig. 4-20 Influence of friction coefficient (a) SERR development; (b) crack growth; (c) stiffness degradation; (d) fatigue life vs. friction coefficient

4.4.2 Influence of failure modes (crack location)

As shown in Fig. 4-11 (b), there are still remaining laminates on the steel surface after the tubes are pulled out, which means that the crack may exist within the composite layers (delamination) instead of composite-to-steel interface (debonding), or transfer from debonding in the beginning to delamination during later stages as illustrated in Fig. 4-21. In this section, the

influence of failure modes on SERR development, crack growth, as well as stiffness degradation is investigated. To simulate the delamination case, the composite wrap is modelled as two separate parts. A 1.05mm layer of laminate is tied with the steel surfaces, while the interface with VCCT and friction is defined between the thin laminate and the remaining composite part. The friction coefficient is kept as the reference values, namely 0.5.

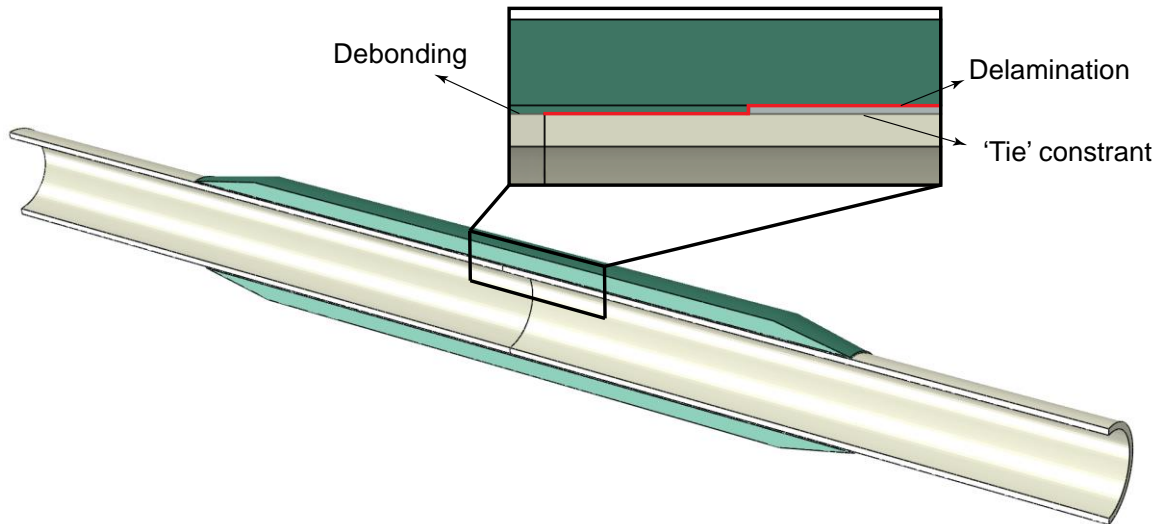


Fig. 4-21 Failure mode transformation from debonding to delamination

The results are summarized in Fig. 4-22. Due to existence of the insert, the crack must initiate at the composite-to-steel interface. That's why the SERR values at the initial crack length coincide with each other for the debonding and delamination cases as shown in Fig. 4-22 (a). As the crack propagates into the composite layers, the interlaminar SERR values are 10-20% lower than those at the interface at crack lengths of 50-100mm but become similar to those values at longer crack lengths of 125-150mm. As the SERR values are determined by the stress state around the crack tip, the shear stresses at interlaminar (for delamination case) and interface (for debonding case) are extracted at $a=75\text{mm}$ and $a=150\text{mm}$ for further interpretation as shown in Fig. 4-23. It is found that at 75mm, shear stresses around the crack tip are higher at the interface than those between composite layers, which may come from the stress singularity at the bi-material interface. As the crack grows, stresses around the crack tip decreases as more force is transferred by friction at the cracked part. The difference between debonding and delamination cases also vanishes possibly due to diminishing of stress singularity at the interface resulting from larger friction effect. For the sake of comparison the same preliminary Paris relationship is considered at the delaminated interface inside the first layer. The crack growth is predicted as in Fig. 4-22 (b). With higher SERR values, debonding crack shows a higher growth rate around 100mm but becomes closer to the delamination crack at later stages. The stiffness degradation of these two cases is shown in Fig. 4-22 (c) and is close to each other until 30% stiffness degradation. The debonding case exhibits a less stiffness degradation at later

stages as the joint shows a higher stiffness with the same crack length compared to the delamination case. Taking the 30% stiffness degradation as the failure criterion, model with delamination failure has a similar fatigue life as the model with debonding failure (both around 43,100 cycles).

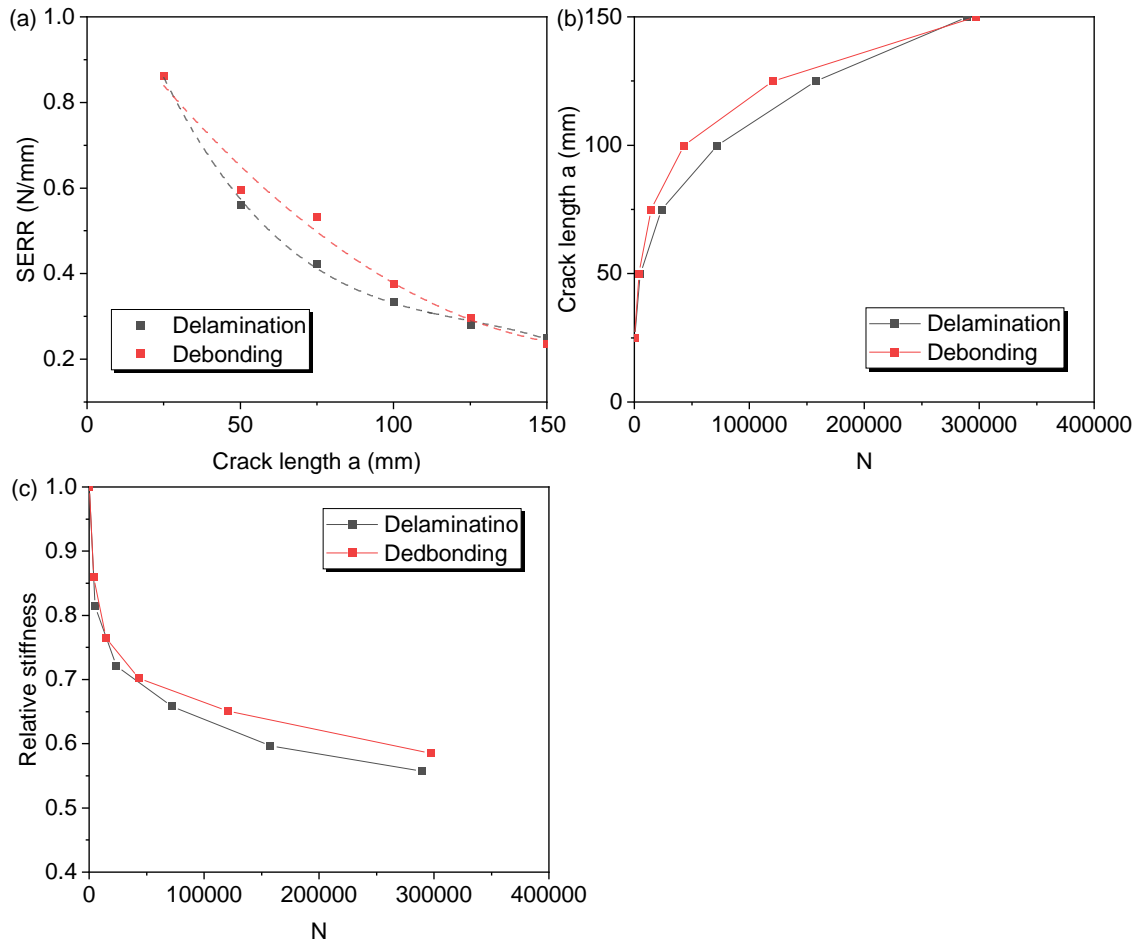


Fig. 4-22 Influence of failure modes (a) SERR development; (b) crack growth; (c) stiffness degradation

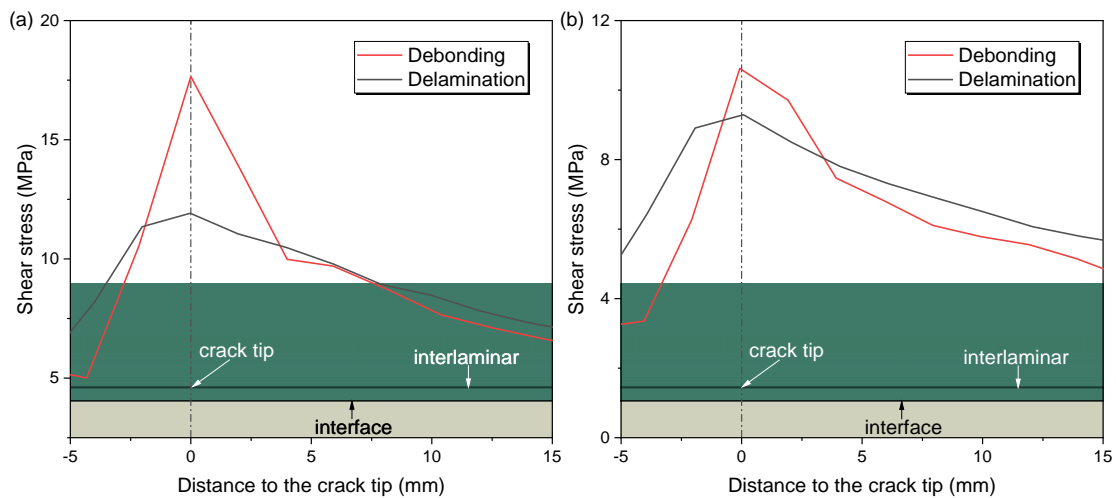
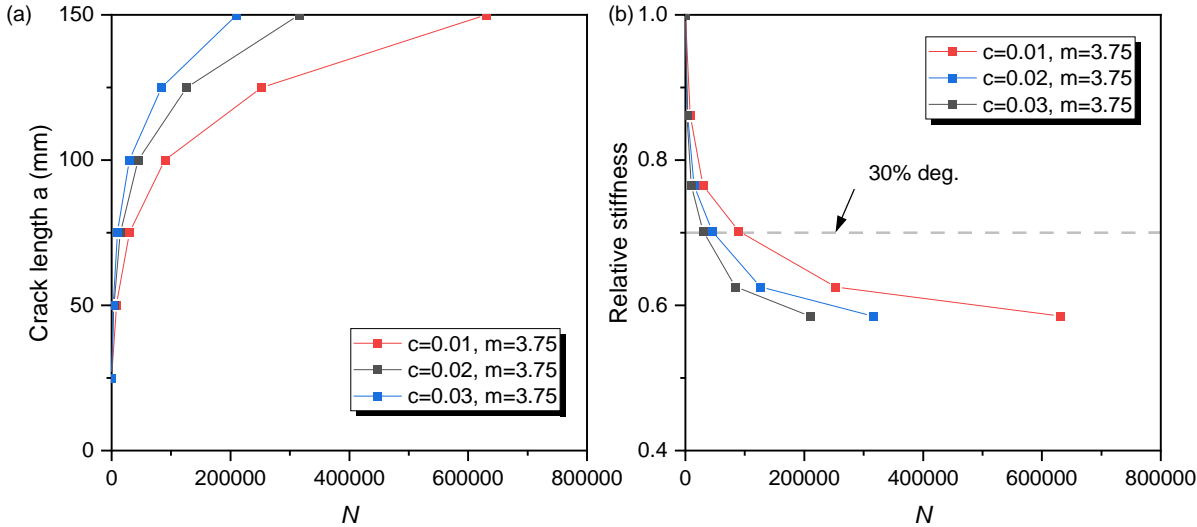


Fig. 4-23 Shear stress at the interface for debonding vs. interlaminar for delamination (a) for crack length of 75mm; (b) for crack length of 150mm

4.4.3 Influence of Paris relationship parameters

Paris relationship parameters, C and m which are obtained through fatigue 4ENF tests, are stochastic parameters influenced by surface preparation, fibre volume fraction, level of cure, etc. The influence of Paris relationship parameters on the predicted results are discussed here. Among these two parameters, parameter C determines the position (higher or lower) of Paris relationship curve. A higher C value means more rapid crack propagation. Herein C is varied between 0.01 and 0.03, while the friction coefficient is kept as 0.5. It can be seen from Fig. 4-24 (a) that with higher C values, crack length increases more rapidly. It takes around 630,600 cycles for model with $C = 0.01$ to reach crack length of 150mm, while it takes only 210,200 cycles to reach the same crack length when C is equal to 0.03. Despite the non-linear effects introduced by the friction, relationship between the crack growth and C value at constant amplitude load seems to remain linear as defined per Paris relationship in Eq. (4-3). The stiffness degradation curves are shown in Fig. 4-24 (b). Obviously, a higher C value corresponds to a higher stiffness degradation rate. Taking 30% stiffness degradation as the failure criterion, the relationship between fatigue life and C value is obtained in Fig. 4-24 (b). An roughly inverse linear trend is shown in this figure, namely, model with $C=0.01$ shows 3 times longer fatigue life than model with $C=0.03$ (89,450 vs. 29,800 cycles).



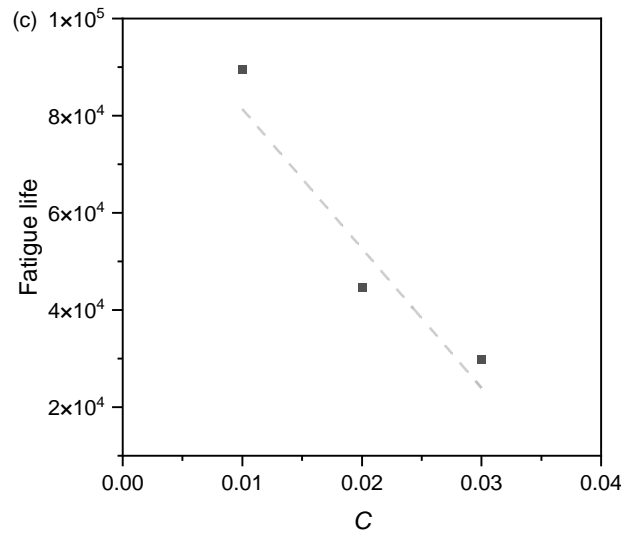
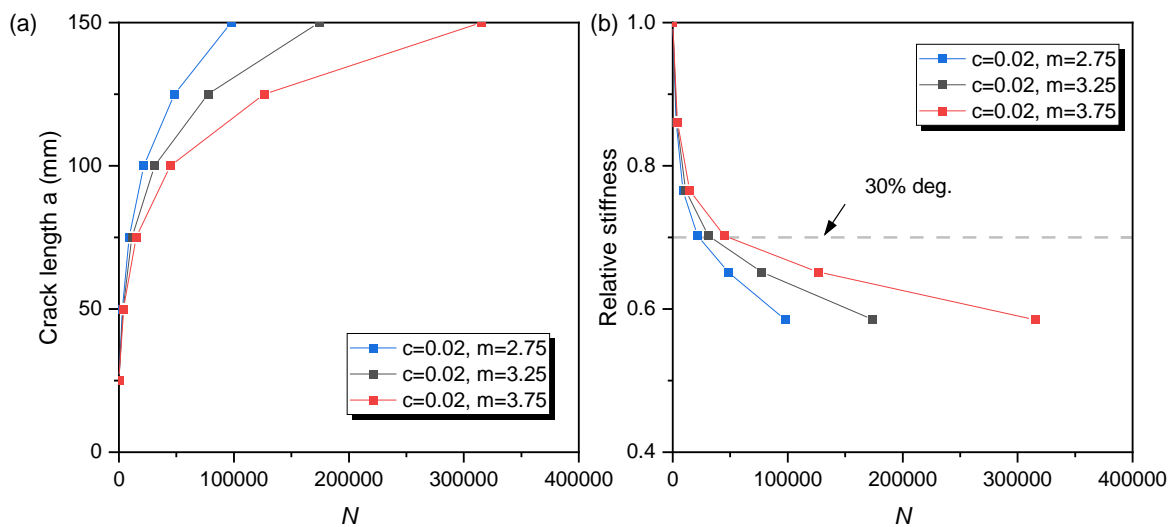


Fig. 4-24 Influence of C parameter on (a) crack growth; (b) stiffness degradation

The other parameter m determines the slope of the Paris relationship. As the SERR values are always below 1 in this study, as shown in Fig. 4-18, a higher m value with constant C parameter may lead to a lower crack growth rate. Herein the m value varies between 2.5 and 4, while the parameter C is kept constant as 0.02. As shown in Fig. 4-25 (a), It takes around 97,600 cycles for model with $m = 2.75$ to reach crack length of 150mm, while it takes 315,300 cycles to reach the same crack length when m is equal to 3.75. The same trend goes for stiffness degradation. Taking 30% stiffness degradation as the failure criterion, the relationship between fatigue life and m value is obtained in Fig. 4-25 (c). A linear trend is shown in this figure, namely, 18% increase of m from 2.75 to 3.25 leads to 43% increase of fatigue life (around 21,655 to 30,960), while 16% increase of m from 3.25 to 3.75 leads to 45% longer fatigue life (around 30,960 to 44,725).



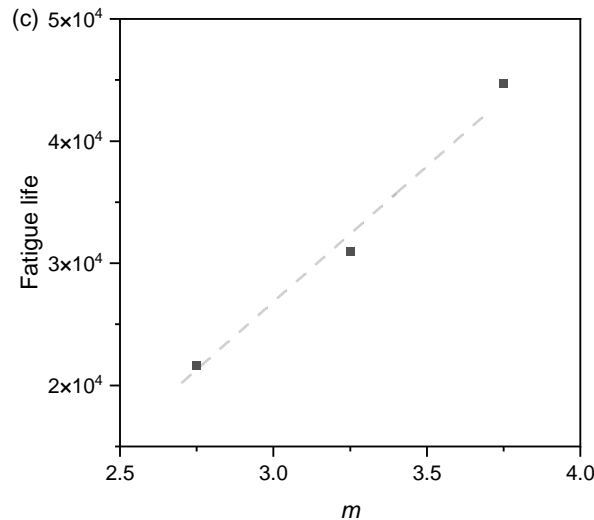


Fig. 4-25 Influence of m parameter on (a) crack growth; (b) stiffness degradation

4.4.4 Limitations of the parametric study

Through the parametric study, influence of several parameters on the predicted crack growth and stiffness degradation of wrapped composite joints have been investigated. Good agreement with crack propagation in fatigue experiments is found. However, there are limitations. For instance, only debonding/delamination is considered as the failure mode here. When the friction coefficient is large enough, the crack growth at the debonded interface may be totally arrested due to very low SERR values. Other failure modes such as material damage or fracture may take place during fatigue loadings. Secondly, the delamination failure and debonding failure mechanisms are investigated separately in this study. They may interact and there might be transition between these two failure modes at a certain crack length. Furthermore, the Paris relationship used in this study was obtained from fatigue 4ENF test which showed debonding failure at the composite-to-steel interface. Paris relationship for crack growth within composite layers may differ. Finally, the predicted results are sensitive to the Paris relationship parameters, especially parameter m as discussed in section 4.4. More fatigue 4ENF test should be carried out to support this kind of analysis.

4.5 Conclusions

In this chapter, crack retardation phenomenon in fatigue experiments on wrapped composite joints is found and explained based on experiments and FE modelling. The influence of friction effect on the debonding crack propagation at the composite-to-steel interface of wrapped composite joints is thoroughly investigated. Static and fatigue experiments are conducted on the uniaxial small-scale joints, where 3D DIC and optical fiber systems are used for monitoring crack propagation and stiffness degradation. The results are interpreted by 3D finite element model using VCCT to obtain the SERR at the crack tips. After being validated, the FE model is used to predict crack propagation at the interface and in the sensitivity analysis to evaluate

an impact of the friction. According to the studies conducted above, the following conclusions can be drawn:

- The static response of the axial wrapped composite joints loaded in tension shows a linear elastic and nonlinear behaviour. The non-linear behaviour is initiated by steel yielding as well as debonding at the composite-to-steel interface.
- The joints experienced 45% stiffness degradation during the first 100,000 load cycles under fatigue loads, after which a stabilization phenomenon is found. Only 10% stiffness is lost during the following 300,000 cycles with a diminishing trend. Cutting the specimens, after the ultimate load was achieved during the afterwards ULS test, reveals the debonding failure plane shifted from the interface to the first ply next to the interface. DIC measurements reveal that the stiffness degradation is mainly due to debonding crack propagation up to 150 mm, at or near the interface, rather than a consequence of the material damage.
- Friction effects, appear in the cracked region, are causing the crack retardation, which is concluded by the combination of 3D DIC results and FE modelling as it is shown in static and fatigue experiments. Friction coefficient at the cracked interface is measured by the tribometer and introduced in the FE model to simulate the friction effect.
- SERR values at the crack tip calculated in VCCT analysis are found to decrease from 0.85N/mm to 0.2N/mm when the debonding crack grows from 25mm to 150mm due to partial load transfer in the cracked (debonded) zone caused by the friction effect. Based on the SERR values and preliminary Paris relationship parameters, the retarded crack propagation and stabilized stiffness degradation of the joint can be predicted accurately.
- By increasing the friction effects in an FE sensitivity study through modification of the friction coefficient, a larger SERR decrease is obtained at the crack tip as the crack grows. For the sake of illustration, 30% stiffness degradation of the joint is taken as the failure criterion, 2.3 fold increase of the apparent friction coefficient (from 0.3 to 0.7) leads to 39 times longer fatigue life, where the crack growth at the debonded interface may be totally arrested and the other failure modes such as material failure may take place.

Chapter V

EXPERIMENTAL STUDY ON THE FATIGUE DEBONDING BEHAVIOUR OF CHS X-45 JOINTS

Parts of this chapter appear in the journal article: ‘W. Feng et al., Fatigue behaviour of non-welded wrapped composite joints for steel hollow sections in axial load experiments. Eng Struct 2021;249:113369.’

5.1 Introduction

In this chapter, the tensile fatigue behaviour of wrapped composite joints is fully characterised through the X-45 joint. The superior fatigue performance of the wrapped composite joint is proved by the comparison with its welded counterparts. The X-joint geometry is chosen to represent K-joint, which is commonly used in jacket support structures, in terms of stress concentration factors. During the tests, stiffness degradation of the joints is recorded under different constant amplitude load ranges. 3D DIC system is employed to monitor strain development on the surface of the composite wrap, based on which the debonding crack propagation at the composite-to-steel interface is characterised. The failure modes is further confirmed by inspecting the interface of cut specimens by a microscope. As investigated in Chapter 3, the surface roughness of steel plate plays an important role on the mode II fatigue crack growth properties at the composite-to-steel interface. In this chapter, the influence of surface roughness of steel is further investigated on the joint level, where the debonding failure is presented. The influence of re-testing on the fatigue performance is studied after the specimens are tested with a quiet low load level and exhibit almost no stiffness degradation. After a certain level of stiffness degradation, the specimens are tested statically to check the influence of cyclic loading the residual resistance of the joint. Finally, preliminary S-N curves of wrapped composite joints are established and compared with that of welded joints from the test results as well as different design codes. Tests described above are performed on the small scale specimens with the scale of 1:12 compared to the full scale joints used in a real jacket support structure. In order to evaluate the upscaling capacity of the joint, tests are also conducted on medium scale joints with the scale of 1:4 compared to full scale application. Their stiffness degradation and strain development is characterised as well.

5.2 Specimens

The small scale wrapped composite joints and welded joints used in this study is summarised in Table 5-1. Geometries and dimensions are shown in Fig. 5-1. These specimens are produced by joining two brace members made of circular hollow section (CHS) profile of $\text{Ø}60.3 \times 4$ to the chord member made of the CHS profile of $\text{Ø}108 \times 5$ with the intersection angle of 45° by welding (for welded joints) and glass fibre composite wrapping (for wrapped composite joints), respectively. For welded joints, the chord and braces were joined together by single sided, full penetration butt weld with the thickness of 4mm, after which grinding of the weld toes was performed to improve its fatigue performance. For wrapped composite joints, surfaces of steel tubes of wrapped composite joints were grit blasted before wrapping and chemically degreased to ensure enough bonding strength between composite laminates and steel tubes. Before applying the laminates, a corner fillet between the chord and braces is made with the combination of chapped strand mat (CSM) and glass filament, aiming to create a smooth surface transition and load transferring at the corner. There is no separate adhesive layer between the composite wrap and the steel tubes. The wet composite wrap is directly laminated on the steel

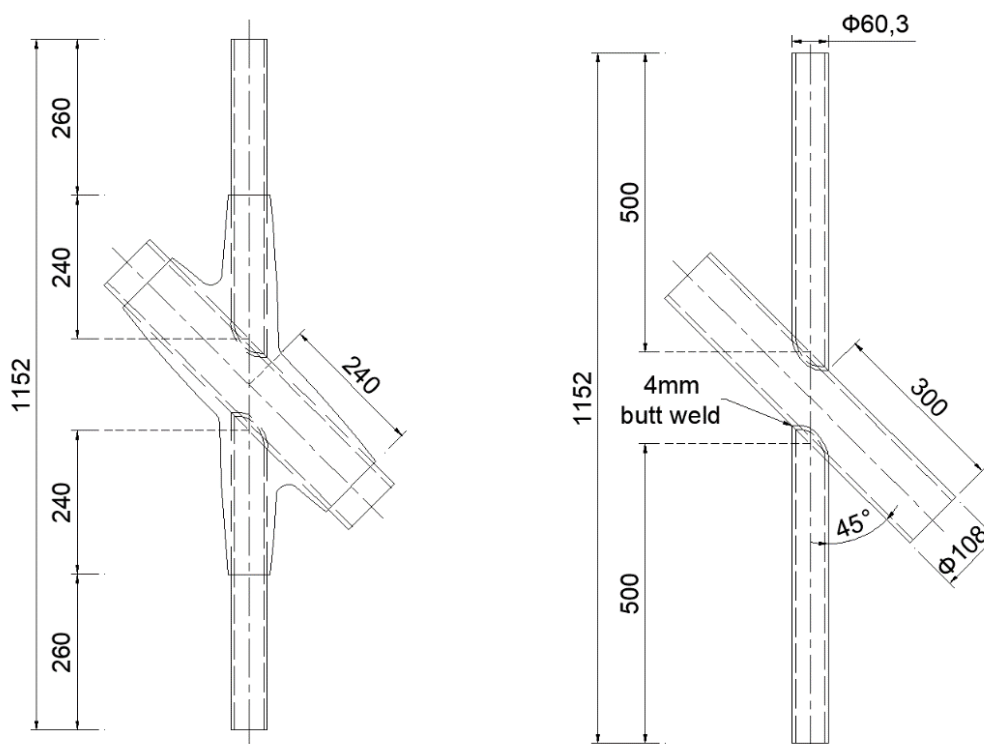
members. Therefore, the failure modes associated to the adhesive material are eliminated considering that the thickness of adhesive is negligible.

Table 5-1 Load ranges and specimens

Load ranges ΔF (kN)	Nominal stress ranges $\Delta\sigma_{nb}^1$ (MPa)	Specimens		Notes
		Welded joints	Wrapped composite joints	
6-66	85	wX45-Ss-T_F1	cX45-Ss-T_F1.1/2/3	Low roughness
10-110	141	wX45-Ss- T_F2.1/2/3	cX45-Ss-T_F2.1a/2a	High roughness
			cX45-Ss-T_F5.1/2/3	Low roughness
15-165	212	—	cX45-Ss-T_F2.1b/2b	Re-tested specimens
			cX45-Ss-T_F3.1/2/3	High roughness
			cX45-Ss-T_F4.1/2	Low roughness

Naming rule: w - welded; c - wrapped composite; Ss – small scale; T – tensile test; F – fatigue test; SF – static test after fatigue loading

1. Nominal stress range in the brace, i.e. $\sigma_{nb}=F/A$, where A = cross section area of the brace.



(a) Wrapped composite joint

(b) Welded joint

Fig. 5-1 Geometry and dimensions of small scale specimens (in millimetres)

The laminate of the composite wrap is formed with multi-directional composition of E-glass reinforcement and vinyl ester based thermoset resin system with fibre volume fraction ranging 30-32%. The wrapping thickness is maximum next to the root of the CHS braces with the nominal value of 14 mm and reduces to 0 mm at the composite wrap ends, see Fig. 5-1. The

thickness in the narrow zone of the corner between brace and chord walls is even larger, up to 25mm, due to the overlapping of the brace and chord composite layers. Such dedicated non-uniform thickness distribution of the composite wrap is used to optimize the load transfer mechanism by: 1. reducing stress concentrations in the composite wrap; 2. reducing concentrations of shear stresses at the bonded interface between the composite wrap and steel at the root of CHS braces and 3. eliminating peel stresses at the end of the composite wrap on the CHS braces.

The choice of using glass fibre instead of other types of reinforcement is due to the fact that: 1. the flexibility of glass fibre reinforcement fabrics makes it easy to be applied in joints with complex geometry. 2. There is no galvanic corrosion between steel and GFRP in marine environment. The application of other reinforcement materials can be explored in the future to meet other requirements but is out of scope of this study.

The production of specimens includes hand-lamination and wrapping in specified subsequent lamination stages in controlled factory conditions at room temperature, with controlled route of surface preparation, roughness registration and quality control. The hand lamination procedure is done in several stages to ensure smooth thickness transition and ply drops, as well as good compaction and avoiding air gaps. Orientation of the fibres is chosen to result in predominantly quasi-isotropic GFRP laminate. No post-curing is applied to the joint specimens. Specimens before wrapping and after being wrapped are shown in Fig. 5-2. It should be noted that all specimens are produced according to the same requirements. Two different batches are considered with focus on the influence of possible production quality deficiencies, namely different surface roughness of steel tubes, on fatigue performance of the wrapped composite joints. The average value of S_q in the batches with higher and lower surface roughness are $S_q = 17 \mu\text{m}$ and $S_q = 6 \mu\text{m}$, respectively. More details about roughness measurements are given in section 4.6.

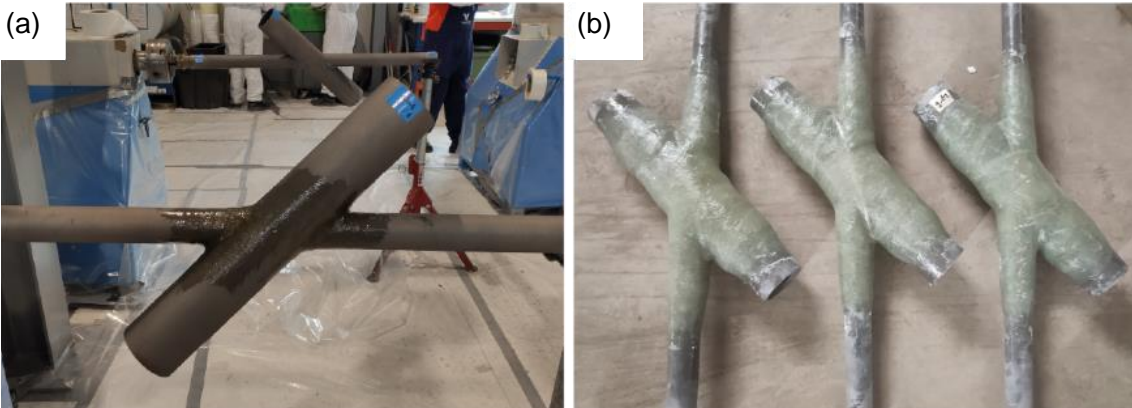


Fig. 5-2 Wrapped composite joints – small scale (a) before wrapping (b) after being wrapped

The material properties of composite laminates were obtained by standard tensile/compressive coupon tests according to ISO [142–144] and are summarised in Table 5-2.

Table 5-2 Mechanical properties of composite materials

Mechanical property	Average value and (CoV)
Longitudinal and transverse compressive strength – $f_{x,c}=f_{y,c}$	200.11 MPa (3.79%)
Longitudinal and transverse compressive modulus – $E_{x,c}=E_{y,c}$	12077.11 MPa (4.50%)
Longitudinal and transverse tensile strength – $f_{x,t}=f_{y,t}$	216.18 MPa (5.78%)
Longitudinal and transverse tensile modulus – $E_{x,t}=E_{y,t}$	11798.20 MPa (6.37%)
Poisson's ratio – ν_{xy}	0.15 (6.50%)
In-plane shear strength – τ_{xy}	72.19 MPa (2.59%)
In-plane shear modulus – G_{xy}	3120 MPa (6.81%)

5.3 Test set-up and instrumentation

The tensile fatigue tests were conducted by the PCX 001 Hydraulic Wedge Grip in Stevin Lab II of Delft University of Technology. Its maximum loading capacity is 800kN for static test and ± 600 kN for dynamic test. During the tests, the ends of braces were clamped by tailor deigned clamps fixed by the hydraulic jaws of the machine to introduce load to the specimens without involvement of any potentially limiting welded details, as shown in Fig. 5-3. The tests were carried out through force control at load frequency of 4 Hz. No significant heat-up effects ($<5^{\circ}$ C) were noticed in the composite material at this testing frequency. Three different load ranges at load ratio of $R=0.1$ were considered for wrapped composite and welded joints as shown in Table 5-1. It was shown from literature [157,169] that the R -ratio influences the fatigue crack growth properties at the bonded interface. Therefore, the R -ratio was kept unchanged throughout the study and a tensile-tensile cyclic load with relatively smaller R -ratio was considered as assumed to be most adverse for debonding failure mode. The two lower load ranges, 6-66 kN and 10-110 kN, correspond to 88 MPa and 141 MPa nominal stress ranges in braces, respectively. Such regime was selected to reach the failure in welded joints at least 100,000 cycles considering stress concentration factor and S-N curves from DNV-RP-C203 (2016) [19]. At those two ranges, the wrapped composite joint reached no failure or significant crack development up to approximately 2-3 million cycles. Therefore, one step higher load range of 15-165 kN, corresponding to nominal stress range in the steel brace member of 212 MPa, was used to develop wrapped composite joint degradation and study the failure behaviour. As shown in Table 5-1, 3 identical specimens of wrapped composite joints were tested for each load range. 4 welded joints were tested in total, with 2 identical specimens for each load range. The specimens cX45-Ss-T_F2.1/2 were tested under lower nominal stress range of 141 MPa in the first loading phase (named with '-a') and in the second phase under increased nominal stress range of 212 MPa (named with '-b') to accelerate the tests considering their negligible stiffness degradation in the first loading phase. The influence of re-testing was investigated meanwhile. All the specimens of wrapped composite joints are loaded up to 40% degradation of their initial stiffness measured between the loading points. Afterwards monotonic static tensile load was applied until full joint failure to investigate the influence of cyclic loads on the residual static behaviour by comparing to monotonic static load experiments with no prior cyclic loading.

Specimens which failed by steel CHS outside composite wrap during cyclic loading were not included in the follow-up static tests. The monotonic static load tests were displacement control with loading rate of 0.01mm/s.

The deformations and strains development of the specimens were measured by a 3D Digital Image Correlation (DIC) system: GOM Aramis 12MP, adjustable base, 12mm lenses with polarized blue led lights. The DIC was used to monitor absolute and relative displacements along the specimen, strain concentrations, and crack propagation such that failure modes of the specimens can be observed real-time during the test, but also processed afterwards in more details. The spackle pattern is applied on one side of the specimen for the DIC system while the other side is left unpainted for visual observation of cracks in composite wrap. Stroke displacement and applied force measured by sensors inside the hydraulic actuator were used to control the test cyclic load application. The 3D DIC measuring system was coupled with the load-control system to drive the image acquisition throughout cycles by a threshold increment of the joint stiffness degradation, as shown in Fig. 5-3.

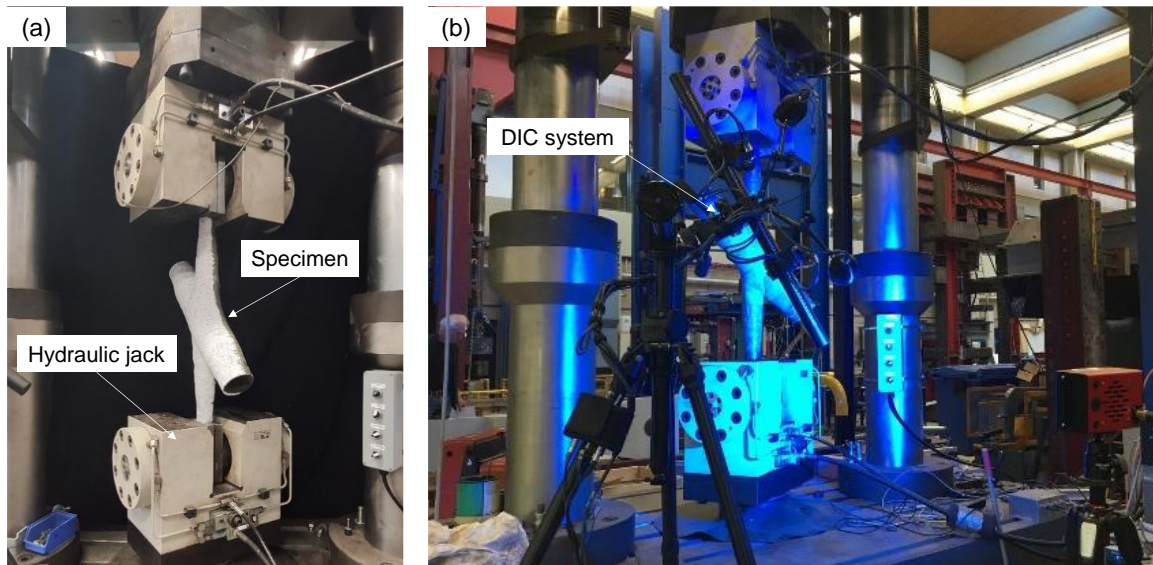


Fig. 5-3 Test set-up for small scale joints (a) test set-up (b) 3D DIC system

5.4 Test results

5.4.1 Stiffness degradation

Stiffness of the joint $k(N)$, at a certain number of cycle N , can be calculated by:

$$k(N) = \frac{F_{\max}(N) - F_{\min}(N)}{\Delta L_{\max}(N) - \Delta L_{\min}(N)} \quad (5-1)$$

where $F_{\max}(N)$ and $F_{\min}(N)$ are the maximum and minimum applied forces at the N th cycle, $\Delta L_{\max}(N)$ and $\Delta L_{\min}(N)$ are the elongations of the joint at the maximum and minimum forces respectively. Elongations of the joint were obtained by measuring the displacement changes at ends of the composite wrap by the DIC system. The same reference length was used to present the stiffness degradation of welded joints for comparison. Due to damage accumulation, stiffness of the joints degraded continuously during the loading process. Stiffness degradation

of the specimens, expressed by the relative stiffness $k(N)/k(1)$, under different nominal stress ranges is summarised in Fig. 5-4. It can be seen that welded joints degenerated at a relatively slow rate during the crack initiation phase corresponding to approximately 80% of the total life. The second stage shows progressive stiffness degradation rate and sudden failure after 350,000 and 70,000 cycles under low and medium load ranges, respectively. Under the same stress range, stiffness degradation of wrapped composite joints is much steadier. For specimens cX45-Ss-T_F1.1/2/3, which were tested at nominal stress range of 85 MPa, there was only up to 2% stiffness degradation after 2 million cycles. The assumption is that they would have almost infinite fatigue life in laboratory conditions and further testing at this load range would be unfeasible. The tests at 85MP stress range were stopped after 2 million cycles. Specimens cX45-Ss-T_F2.1/2 were initially loaded by applying the nominal stress range in the brace member of 141 MPa (results designated by '-a'). Again, a very limited (10%) degradation of stiffness was recorded after 3 million cycles as shown in Fig. 5-4 (b) and no signs of cracks or delamination on the surface of the composite wrap. The influence of re-testing will be discussed in 5.4.4. Under the nominal stress range of 212 MPa, the stiffness degradation of wrapped composite joints becomes more obvious as shown in Fig. 5-4 (c). Over 40% stiffness degradation was reached at about 60,000 to 100,000 cycles for the specimens cX45-Ss-T_F3.1/2/3 (some data of cX45-Ss-T_F3.3 is lost due to malfunction of DIC system in the beginning of the test).

Comparison to the A-joint discussed in Chapter 4 reveals that the X45 joints do not exhibit a significant stabilization of stiffness degradation. This difference could potentially be attributed to the combined influence of friction at the interface and the reduction in wrapping thickness as the crack propagates towards the wrapping end. The presence of friction at the interface can impede crack growth, thereby slowing down the degradation of stiffness. Meanwhile the reduction in wrapping thickness may result in an increased SERR at the crack tip, potentially accelerating the degradation of stiffness. This phenomenon will be further validated by the finite element model in the next chapters.

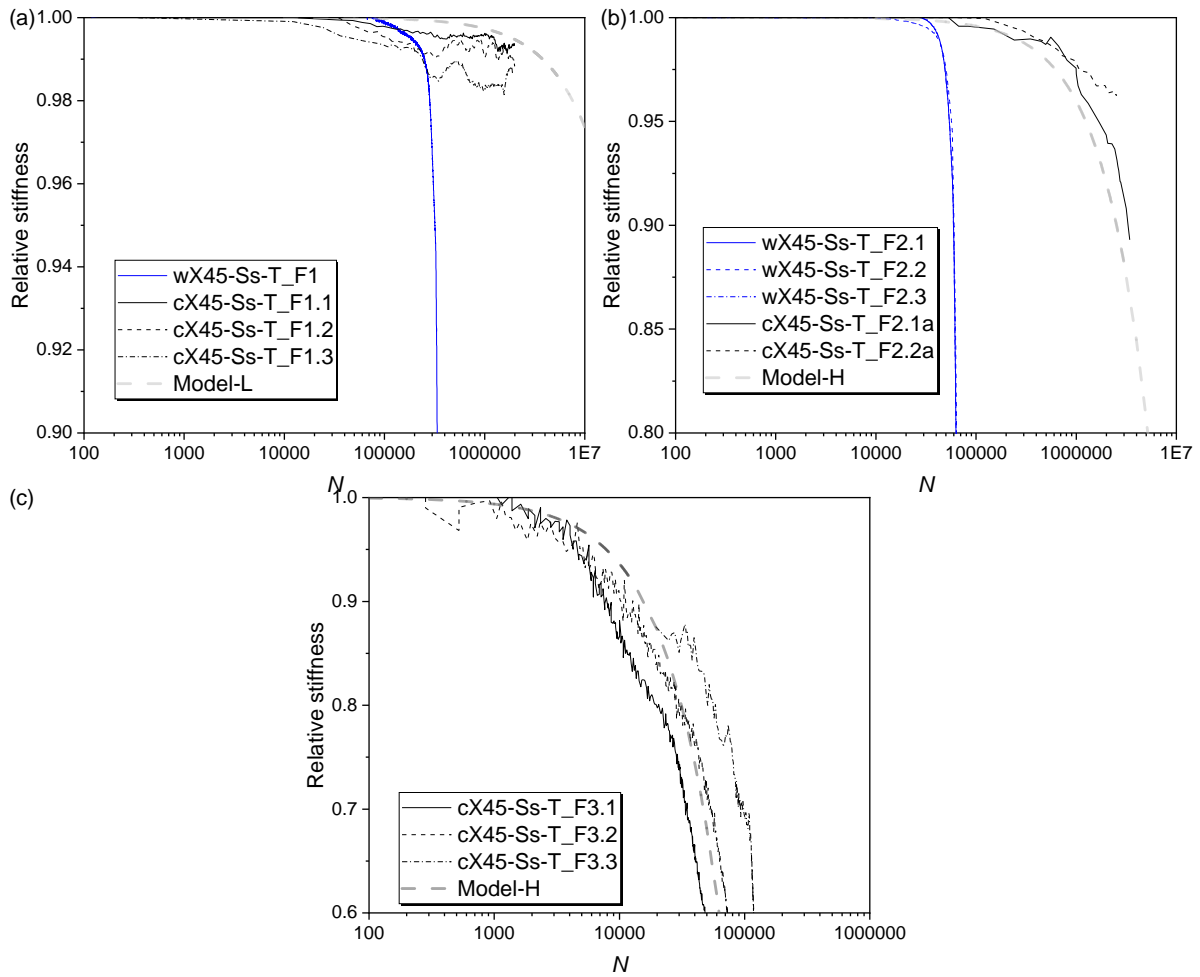


Fig. 5-4 Stiffness degradation of joints (a) 6-66kN (85 MPa); (b) 10-110kN (141 MPa); (c) 15-165kN (212 MPa);

By defining tangent lines of stiffness degradation curves at the steady stiffness degradation stage, stiffness degradation rates can be obtained for the wrapped composite joints and were summarized in Table 5-3. As it would be expected, the stiffness degradation rate increases with the stress range. Considering that stiffness degradation is linear at the propagation stage, a linear model [170] was employed to phenomenologically characterise stiffness degradation of the wrapped composite joints. The model can be expressed as:

$$\frac{k(N)}{k(1)} = 1 - m_1 (\Delta\sigma_{nb})^{m_2} N \quad (5-2)$$

where parameters m_1 and m_2 can be obtained by curve fitting of experimental results and are assumed to be independent of number of cycles and nominal stress range. Based on Eq. (5-2), the fatigue life of the joint at a certain degree of stiffness degradation under a certain stress range can be calculated by:

$$N_f = \frac{k(1) - k(N_f)}{k(1)m_1 (\Delta\sigma_{nb})^{m_2}} \quad (5-3)$$

such that the $S-N$ curve can be obtained for a certain stiffness degradation percentage. Relative stiffness degradation rates of specimens for the examined load ratio $R=0.1$ are plotted against

nominal stress ranges in braces $\Delta\sigma_{nb}$ in Fig. 5-5. Curve fitting was applied for specimens of lower roughness with 3 different nominal stress ranges and specimens of higher roughness with 2 different nominal stress ranges, respectively. Parameters m_1 and m_2 were determined as 1.16e-29 and 10.55 for specimens with lower roughness, 1.12e-38 and 14.08 for specimens with higher roughness, respectively. The influence of roughness will be further discussed in section 5.4.5. Based on the parameters obtained above, stiffness degradation curves for specimens with higher (Model - H) and lower roughness (Model - L) according to the linear model depicted by Eq. (5-2) are shown in Fig. 5-4 and Fig. 5-15, which shows good match with test results.

It should be noted that the model used here to replicate the stiffness degradation is a phenomenological model which only takes into account the dependency of stress range instead of stress ratio. In chapter 6, a physics-based model, e.g. a fracture-mechanics-based method, will be used to predict the stiffness degradation related to crack growth within the joint. In that way, multiple influencing factors such as stress ration can be taken into account.

Table 5-3 Summary of test results

Load ranges ΔF (kN)	Nominal stress ranges $\Delta\sigma_{nb}$ (MPa)	Specimen	Failure modes	Stiffness degradation rate (/cycle)	Average value (/cycle)	Note
6-66	85	cX45-Ss-T_F1.1	DB	-2.51e-9	-2.79e-9	LR
		cX45-Ss-T_F1.2	DB	-3.56e-9		
		cX45-Ss-T_F1.3	DB	-2.30e-9		
10-110	141	cX45-Ss-T_F2.1a	DB	-2.77e-8	-2.03e-8	HR
		cX45-Ss-T_F2.2a	DB	-1.28e-8		
		cX45-Ss-T_F5.1	DB	-1.47e-6	-2.48e-6	LR
		cX45-Ss-T_F5.2	DB	-1.77e-6		
		cX45-Ss-T_F5.3	DB	-4.21e-6		
		cX45-Ss-T_F2.1b	FT*	-6.23e-7		
cX45-Ss-T_F2.2b	DB	-1.75e-7				
15-165	212	cX45-Ss-T_F3.1	DB	-7.61e-6	-5.02e-6	HR
		cX45-Ss-T_F3.2	DB	-5.01e-6		
		cX45-Ss-T_F3.3	DB*	-2.44e-6		
		cX45-Ss-T_F4.1	DB	-3.79e-5	-4.1e-5	LR
		cX45-Ss-T_F4.2	DB	-4.41e-5		

Note: Stiffness degradation rate - $[k(n_i)-k(n)]/[(n-n_i)k(1)]$; DB – debonding failure; FT – Fracture of steel tube; LR – low roughness; HR – high roughness;

* Specimens fully failed during fatigue loading

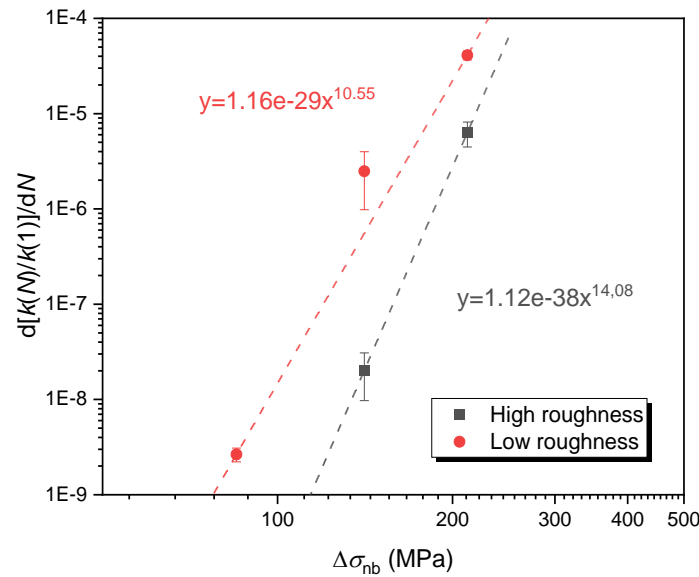
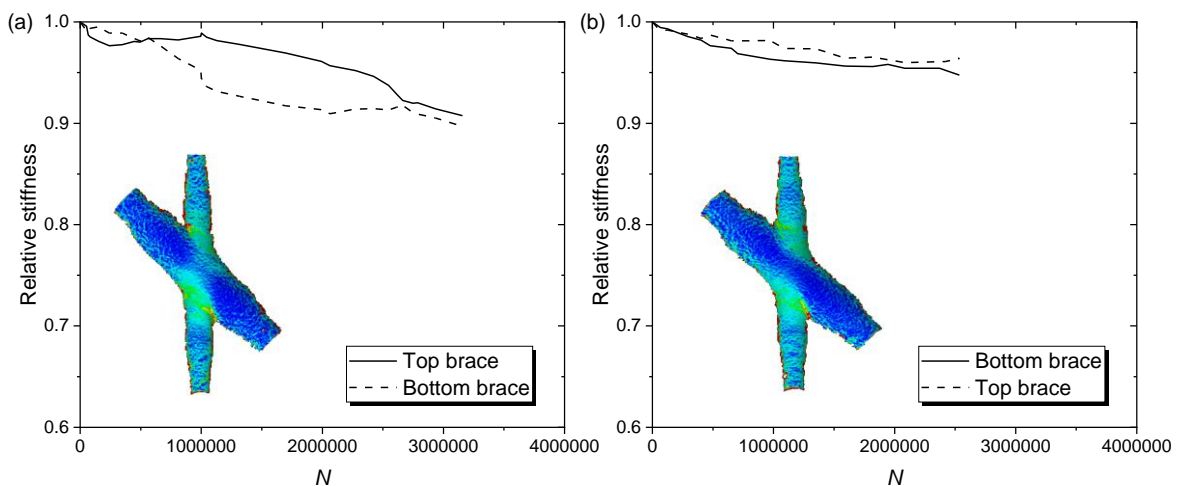


Fig. 5-5 Stiffness degradation rate versus nominal stress range in the brace

When substituting elongation of separate brace obtained from DIC into Eq. (5-1), stiffness degradation of the joint can be decoupled into two separate parts, with each part reflecting stiffness degradation of one brace, respectively, as shown in Fig. 5-6. It should be noted that the stiffness degradation used to control and to stop the cyclic loading is the global stiffness of the whole joint, namely the average value of stiffness degradation of the top and bottom braces. However, it is shown that stiffness of one brace always degrades more than the other one, especially for specimens under higher load ranges (cX45-Ss-T_F3.1/2). This can also be reflected by the DIC contour plots of major strains on the surface of specimens at the maximum loads below the stiffness degradation curves. For specimen cX45-Ss-T_F3.1 as shown in Fig. 5-6 (c), more severe damage is indicated by the increased strains on the bottom brace, corresponding to stiffness degradation of over 50%. While damage on the top brace is less obvious, corresponding to stiffness degradation of less than 40%. The same goes for specimen cX45-Ss-T_F3.2, where more damage and stiffness degradation is found for the top brace. As the failure mode found to be debonding at the composite to steel interface as will be discussed in the next section, the difference between top and bottom braces may come from different interface features or crack locations.



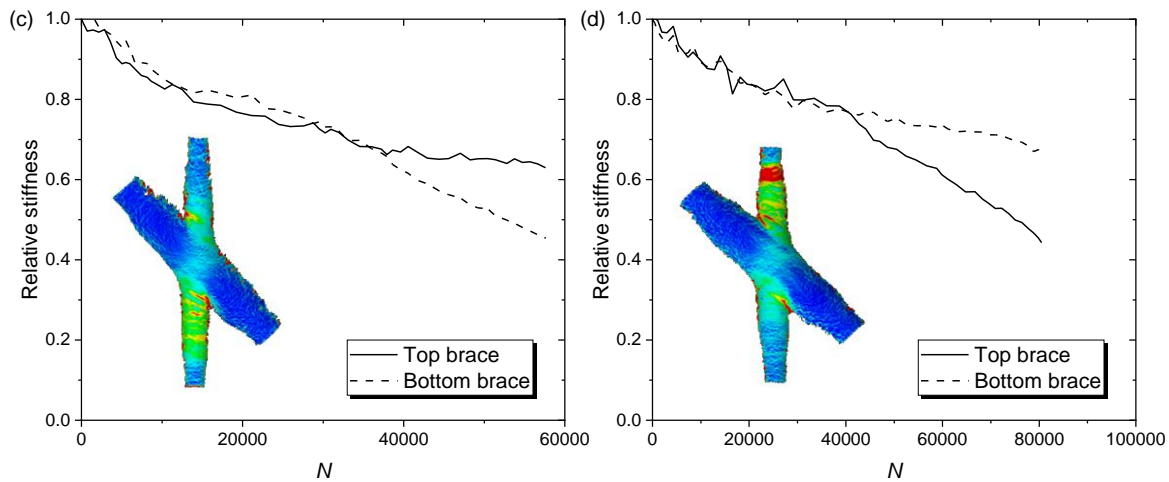


Fig. 5-6 Stiffness degradation of different braces (a) cX45-Ss-T_F2.1a; (b) cX45-Ss-T_F2.2a; (c) cX45-Ss-T_F3.1; (d) cX45-Ss-T_F3.2

5.4.2 Failure modes

Typical failure modes of welded and composite joints are shown in Fig. 5-7. All the welded joints failed at the welded detail. The cracks initiated in the chord on the crown toe location and progressed toward chord saddle as shown in Fig. 5-7 (a), although the largest SCF is calculated as to be at the chord saddle according to DNV-RP-C203 [19]. Once the global stiffness degradation of the welded joints of more than 50% was reached, and crack developed across more than 50% of the circumference, the cyclic loading was stopped.

In order to monitor the strain development on the surface of specimen for interpreting failure modes of the wrapped composite joints, the DIC pictures were taken at the minimum and maximum loads for the load cycles at which significant accumulated increment of the joint stiffness degradation (more than 0.4%) was registered. For each specimen, approximately 200 of such min/max load measurement pairs were recorded. A typical DIC contour plot of major principal strains on the surface of composite wrap at the maximum load is shown in Fig. 5-7 (b). The strain increases zone on the composites surfaces can indicate both the composite-to-steel debonding failure as well as the smeared material damage and delamination within the composite wrap. It is confirmed by post-test cutting of the specimens that the governing failure mode is debonding at the composite-to-steel interface. The debonding crack propagation will be further discussed in section 5.4.3. The DIC contour plot also indicates stress concentration in the sharp corner of the joint root between the brace and the chord wrapping as indicated in Fig. 5-7 (b). However, no significant surface cracks were observed in this region during cyclic loading.

Most of the wrapped composite joints didn't fully debond during the cyclic loading i.e. braces were not pulled out from composite wrapping. The cyclic loading was intentionally stopped at stiffness degradation up to 40% to perform monotonic test until failure and check the residual static resistance. The exception is specimen cX45-Ss-T_F3.3, which was left to fully debond during the cyclic tests and finally failed at 50% of stiffness degradation, as shown in Fig. 5-7

(c). One of the wrapped composite joint specimens, cX45-Ss-T_F2.1b, failed suddenly at approximately 3 million load cycles at stiffness degradation of 30% due to fracture of the steel member at its end outside the wrapped part as shown in Fig. 5-7 (d). This demonstrates that the wrapped composite joints can have fatigue endurance which is comparable to endurance of the non-welded details of steel circular hollow sections. Failure modes of all the specimens are summarized in Table 5-3.

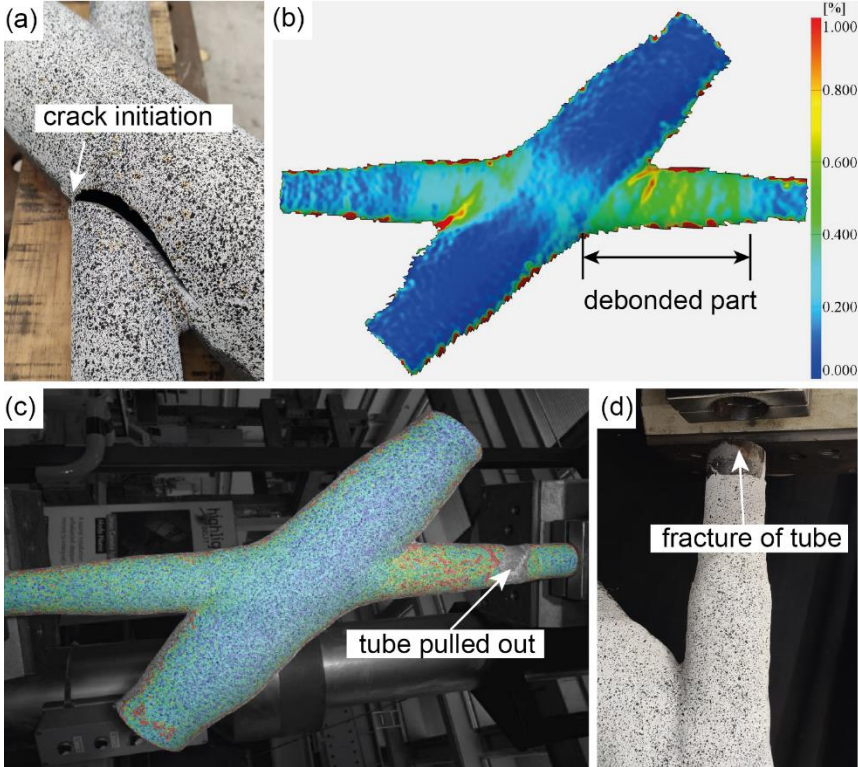


Fig. 5-7 Other failure modes (a) fracture of welded joints; (b) debonding of wrapped composite joint indicated by strain increase on the surface; (c) debonding during the fatigue test (cX45-Ss-T_F3.3); (d) fracture of steel tube of wrapped composite joint cX45-Ss-T_F2.1b

A detailed analysis of failure mechanisms was carried out for wrapped composite joints on a micro-scale. A typical specimen cX45-Ss-T_F3.3, which failed during fatigue loading by full debonding, was chosen to be inspected. This specimen was cut through its mid-plane after testing as shown in Fig. 5-8. The cut surfaces were grinded by sand paper and polished. It can be seen from the figure that the top brace has slid away from the chord and was fully debonded along the brace-to-composite interface. Debonding by peeling also occurred at a small portion of the chord-to-composite interface near the sharp corner. Except for debonding, there are delamination marks present between different composite layers and fracture of composites as well, which occurs near the end of the wrapped part so that can be excluded as the predominate failure mode. For the bottom brace, macro-scale failure mechanisms are not obvious.

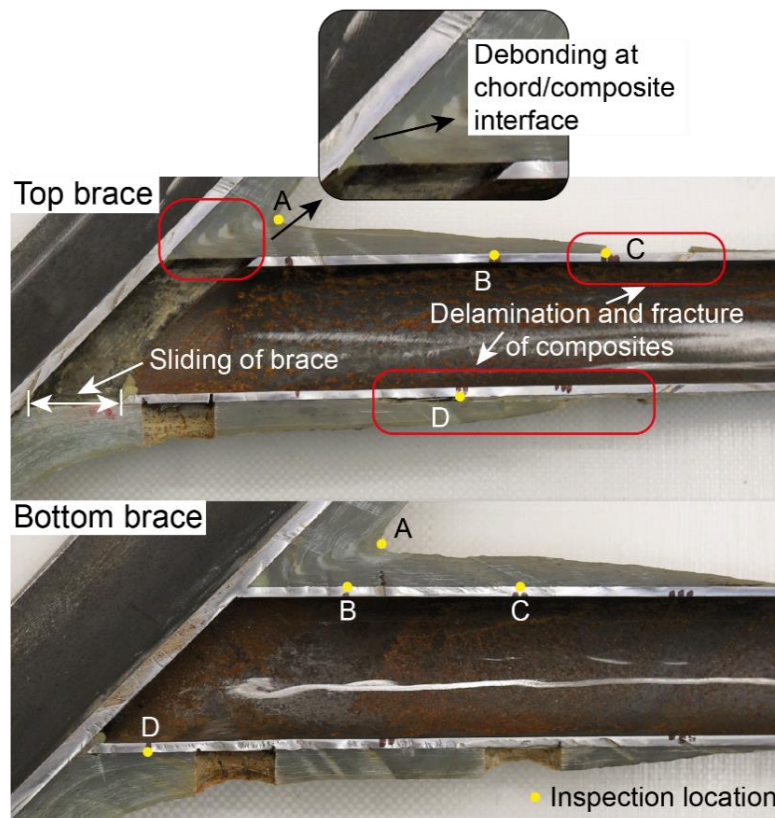
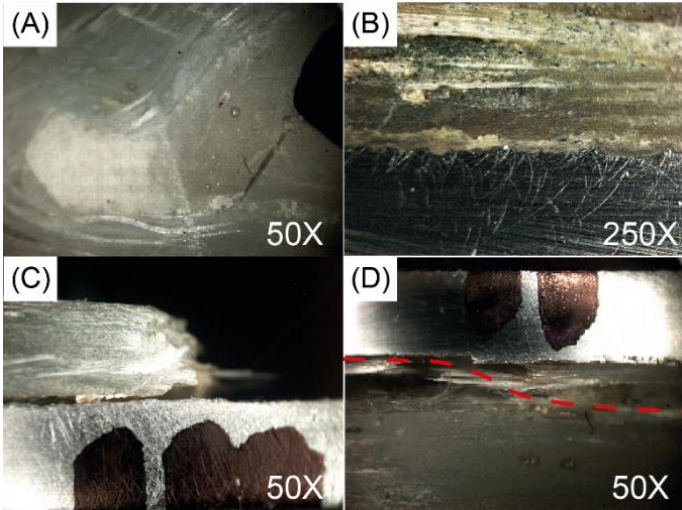
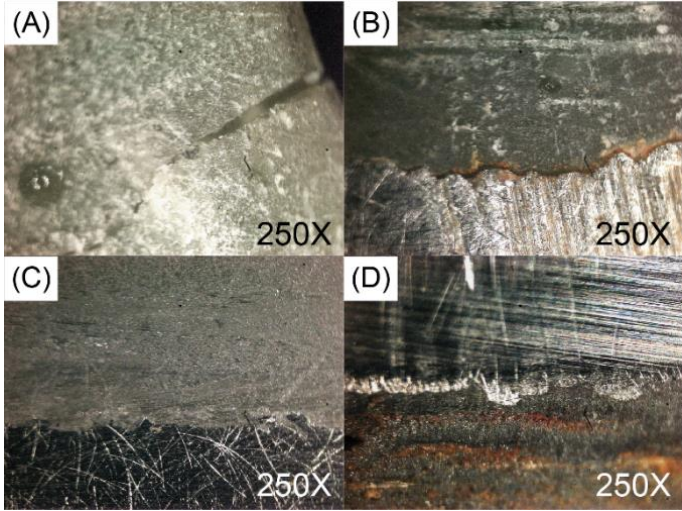


Fig. 5-8 Inspection of cut surface

Observation is continued on micro-scale with magnification of 50 and 250. For both braces, inspection locations include sharp corner of the composite wrapping and several points along the brace-to-composite interface as shown in Fig. 5-8. with the aim to check failure mechanism development. Four distinct locations A, B, C and D are analysed in Fig. 5-9 (a) and (b) for the top (full debonding) and the bottom brace (partial debonding), respectively. Detail A shows crack on the wrapping surface in the sharp corners for both top and bottom braces, which was also observed in DIC results (see stress concentration in Fig. 5-7 (b)). These cracks however only extend to a limited depth through a resin rich layer at the wrapping surface and do not seem to jeopardize the integrity of the composite plies in the corner. For the top brace, which definitely fully debonded, point B shows a typical debonding mechanism where there is a layer of crashed matrix debris between the composite laminate and steel surface. Debonding on the top brace developed until the point C where fracture of composite laminate occurred. Point D on the opposite side of the top brace shows location where debonding of the composite-to-steel interface switches to delamination inside the composite laminate and fracture of the first plies. This means that the failure mechanism may be different around the circumference of the brace. The bottom brace suffered much less debonding. For the bottom brace, an obvious gap between the composite laminate and the steel surface of the brace tube could only be identified at point B. Point C, further away from the joint root, shows no visible signs of debonding. Limited debonding and resin debris are observed up to and in the point D.



(a) Top brace



(b) Bottom brace

Fig. 5-9 Microscale inspection of composite-to-steel interface

5.4.3 Debonding crack propagation

Fig. 5-10 shows the typical DIC contour plots of major principal strains on surface of specimen cX45-Ss-T_F3.1 at the maximum loads at different numbers of cycles. The increase of major principal strains in certain regions on the surface of composite wrapping (light blue and green areas) can indicate the composite-to-steel debonding failure as observed in section 5.4.2, which initiate form the root of the brace and develop towards the wrapping ends. Development of strains on top and bottom braces are quite different, indicating larger crack propagation and stiffness degradation rates at the bottom side.

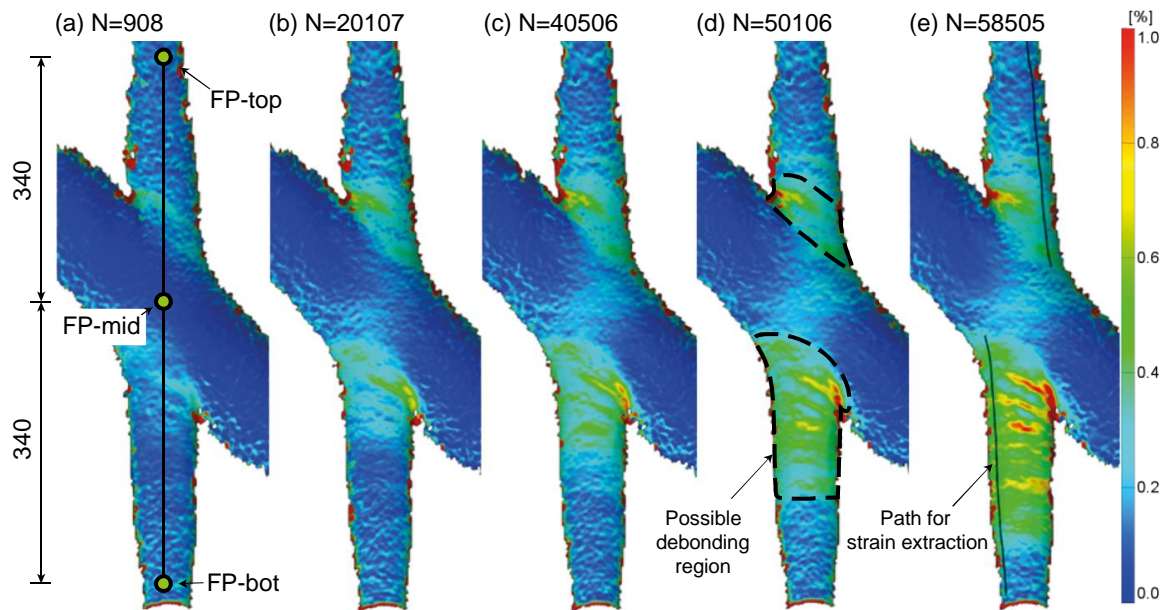


Fig. 5-10 DIC contour of progressive strain development on the surface of cX45-Ss-T_F3.1

Strain distribution along surface curve defined on the brace as shown in Fig. 5-10 is further extracted for determining the debonding length. One example of extracted strains along the bottom brace of cX45-Ss-T_F3.1 at different number of cycles is shown in Fig. 5-11. In order to remove scatter resulting from DIC measurements, all these curves are smoothed with adjacent-averaging method during post-processing of data using ORIGIN software. It shows that at initial stage, the surface strains mainly develop around root of the brace, followed by gradual decrease and again slight increase towards the end of composite wrap. With the increase of loading cycles, the peak strain increases and develops gradually towards end of the wrap, indicating debonding propagation at the composite-to-steel interface. It should be noted that the surface strain distribution will also be influenced by at least another two phenomena. One phenomenon is the nonlinear in-plane and through thickness shear behaviour of the thick composite laminate with complex (variable) geometry. Another phenomenon is the interaction with the chord debonding. The debonding on the chord interface is contributing deviation of the strain filed on surface of braces and vice versa. To overcome the influence of these multiple factors, an innovative combined DIC and FEA method is proposed in Ref. [171] to capture crack development along the brace and chord quantitatively.

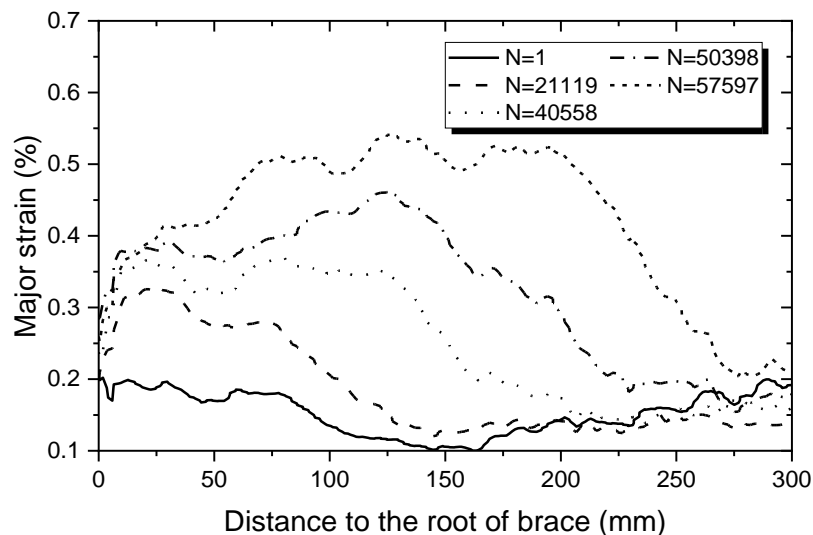


Fig. 5-11 Strain distribution along bottom brace of cX45-Ss-T_F3.1

The definition of crack lengths on the brace, l_b , and chord, l_c , is shown in Fig. 5-12. As will be shown by FE models in Chapter 6, the crack on the brace initiates from the obtuse corner and gradually becomes perpendicular to the axis of the brace as it propagates. Crack on the chord initiates from the intersection between the chord and brace, developing approximately as a semi-circle. l_b is defined at the longer edge of the brace, while l_c is defined as to be perpendicular to the axis of the chord, starting from the middle point of the intersection line between the chord and brace.

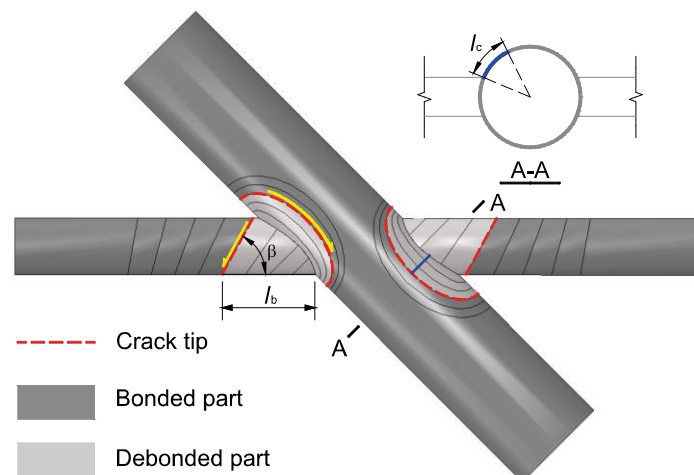


Fig. 5-12 Definition of crack length on the chord and brace

By considering the interaction between the chord and braces, as well as employing a variable strain threshold, the crack length development on the brace for specimen cX45-Ss-T_F2.1/2a and cX45-Ss-T_F3.1/2 is shown in Fig. 5-13. It can be seen from the figure that the crack propagates much faster under the higher load range. The largest crack length on the brace under 15-165kN reaches above 200mm at end of the test while under 10-110kN, the longest crack only reaches 60mm. It can also be seen from the figure that for the same specimen, crack propagation rates on different braces are different, e.g. bottom brace of cX45-Ss-T_F3.1 has

crack length of 200mm in the end, while crack length on the top brace only reaches 80mm. It should be noted that below 100mm, the crack lengths on the braces are obtained with the influence of debonding on the chord, while above 100mm, debonding on the braces is the predominate reason for strain increase on the surface so that the obtained crack lengths are more accurate.

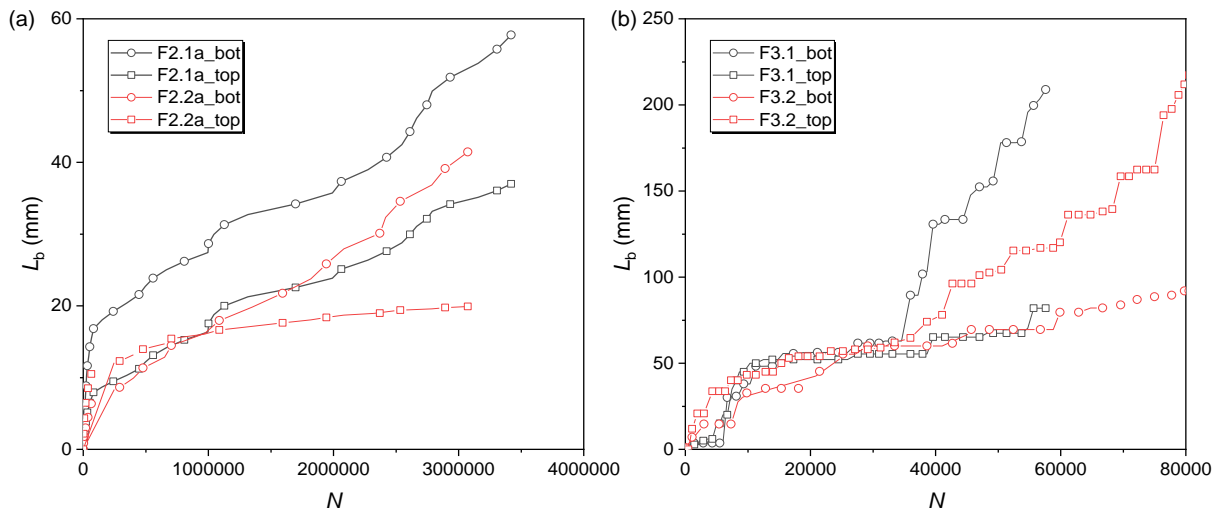


Fig. 5-13 Debonding crack length on the braces of different specimens (a) specimens under 10-110kN (b) specimens under 15-165kN

5.4.4 Influence of re-testing

Load range for specimens cX45-Ss-T_F2.1/2a was increased after no significant damage was observed after approximately 3 million cycles in order to demonstrate the impact of load history on fatigue performance of wrapped composite joints. The results of re-tested specimens are shown in Fig. 5-14. It took approximately additional 0.4 and 1.0 mil cycles for the re-tested specimens cX45-Ss-T_F2.1b/2b under the increased nominal stress range of 212 MPa until stiffness degradation of 20%, which performed better than virgin specimens cX45-Ss-T_F3.1/2/3 without previous load cycles. The same conclusion can be obtained from Table 5-3, where the average stiffness degradation rate of the re-tested specimens cX45-Ss-T_F2.1b/2b is $-3.99e-7/\text{cycle}$, which is an order of magnitude lower than that of the virgin specimens, $-5.02e-6/\text{cycle}$. The hypothesis can be that initial low load range result in plasticization and favourable reduction of stress singularities at the bonded interface inside the root of the joint.

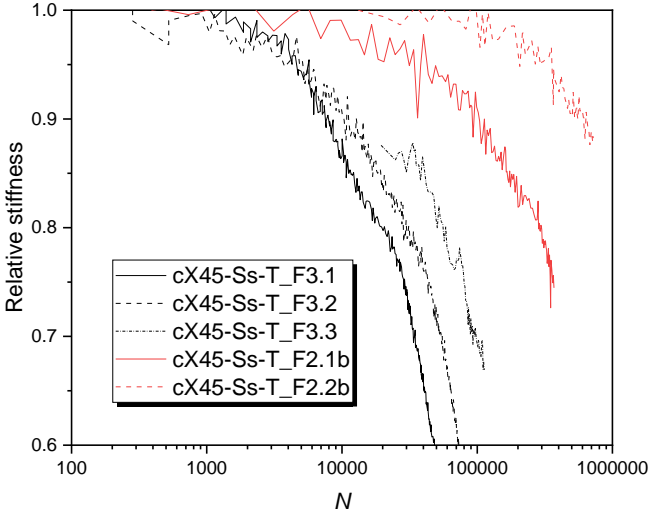


Fig. 5-14 Influence of re-testing on stiffness degradation of wrapped composite joints

5.4.5 Influence of surface roughness

Surface roughness of the steel adherent plays an important role for the mechanical behaviour of a bonded joint, as also proved in Chapter 3. To investigate the influence of roughness on the fatigue behaviour of the joint, surface roughness of the steel tubes is evaluated by the same parameter as used for ENF specimens, the root mean square height, S_q . The measuring results are summarised in Table 5-4. It is shown that average values of S_q for cX45-Ss-T_F3 series ranges from 16 to 19 μm , approximately 1.2 to 2 times of those for cX45-Ss-T_F4 series, which ranges from 7.5 to 11 μm .

Table 5-4 Summary of S_q of different specimens (μm)

Position		Specimens				
		cX45-Ss-T_F3.1	cX45-Ss-T_F3.2	cX45-Ss-T_F3.3	cX45-Ss-T_F4.1	cX45-Ss-T_F4.2
	A	19.88	16.09	19.12	5.22	5.98
	B	19.63	20.64	18.37	16.60	9.01
	Top average	19.76	18.37	18.74	10.91	7.50
	C	17.61	15.58	21.40	29.24	11.54
	D	16.85	17.10	21.15	13.06	9.77
	Bottom average	17.23	16.34	21.27	21.15	10.66
Minimum average		17.23	16.34	18.74	10.91	7.50

Stiffness degradation curves for different roughness series are compared in Fig. 5-15. It can be seen that specimens with lower surface roughness, cX45-Ss-T_F4.1/2, reached 40% stiffness degradation at less than 10000 cycles under the load range of 15-165kN, while the same amount of stiffness was reached after 60000 to 100000 cycles for specimens with higher roughness. Under load range of 10-110kN, the difference is even more obvious. Specimens with lower

roughness, cX45-Ss-T_F5.1/2/3 showed 40% stiffness degradation after 100000 to 400000 cycles while specimens with higher roughness showed only limited stiffness degradation of 5%-10% after 3 million cycles. Relationship between the stiffness degradation rate and the surface roughness is given in Fig. 5-16. The horizontal axis represents the minimum average S_q within the top or bottom brace of the specimen (underline averages in Table 5-4) which is dominant for the stiffness degradation process. It shows that the stiffness degradation rate of low roughness series can be 8 times higher than the high roughness series under the load range of 15-165 kN, and 120 times higher under the load range of 10-110kN. Very correlated dependency of stiffness degradation rate vs. surface roughness is found, which means that uniform and controlled surface roughness is crucial for consistent fatigue performance of the bonded interface and controlled scattering of the behaviour. More detailed research in the future could propose linear or asymptotic interpolation models to predict the stiffness degradation rate by a known (measured) surface roughness.

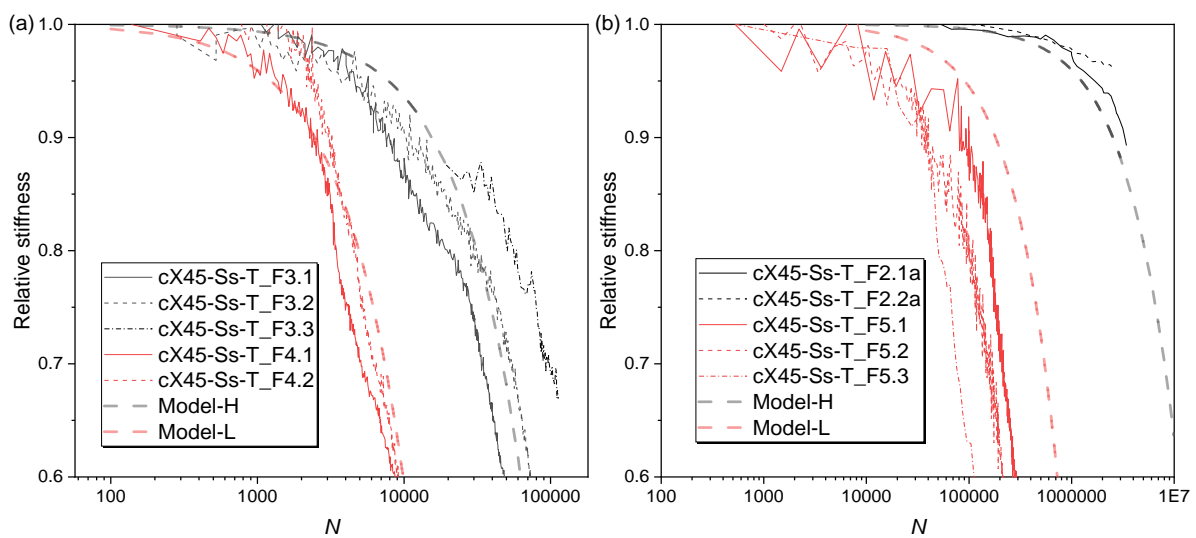


Fig. 5-15 Influence of roughness on stiffness degradation (a) 15-165kN; (b) 10-110kN

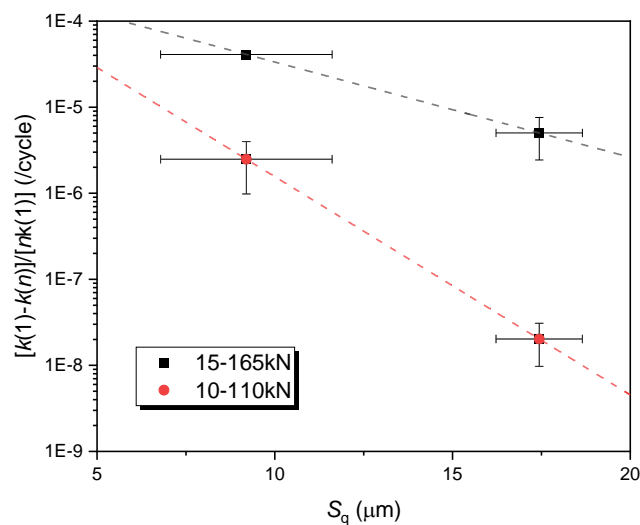


Fig. 5-16 Influence of roughness on stiffness degradation rate

The mechanism of the beneficial effect of increased surface roughness on fatigue performance can be further explained by Fig. 5-17, which shows representative profiles with different S_q . It can be seen that profiles with higher S_q exhibits deeper valleys, resulting in larger contact areas between adherends, such that the mechanical interlocking and surface energies are increased.

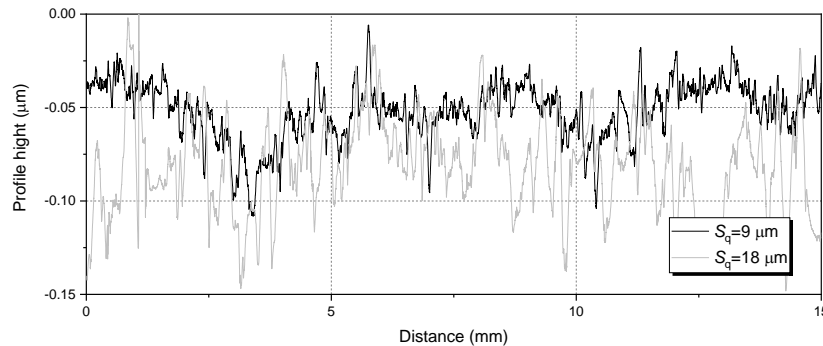


Fig. 5-17 Representative roughness profiles with high and low S_q

5.4.6 Influence of cyclic loads on the residual resistance

After stiffness degradation up to 40% in cyclic load test for the two higher load ranges (F2 and F3), monotonic static load was applied to determine the residual static resistance of the specimens. All the specimens failed due to full de-bonding of the composite-to-steel interface at one of the two braces in the follow-up monotonic load test as shown in Fig. 5-18.

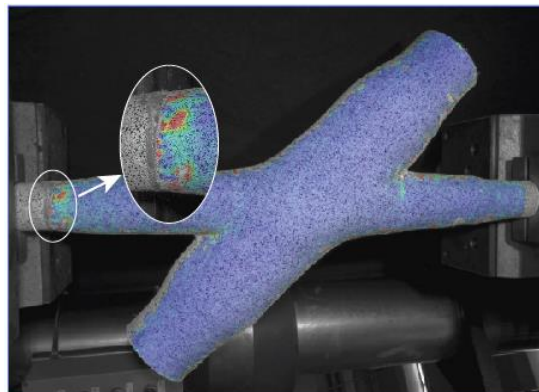


Fig. 5-18 Full debonding during static test after cyclic loading

Force-displacement behaviour of specimens with previous cyclic loading is compared with those of reference specimens cX45-Ss-T_S1.1/2 [172] which did not experience any cyclic loading in Fig. 5-19 (a). All of the specimens showed decreased initial stiffness in the follow-up monotonic load test which corresponds to stiffness reduction due to partial damage (debonding) during cyclic load. The specimen with lowest stiffness degradation (approximately 20%) after more than 3 million cycles of load, cX45-Ss-T_SF2.2b, shows no reduction of static resistance. The other two specimens with significant (>40%) stiffness degradation during the cyclic load test show up to 30% reduction of static resistance.

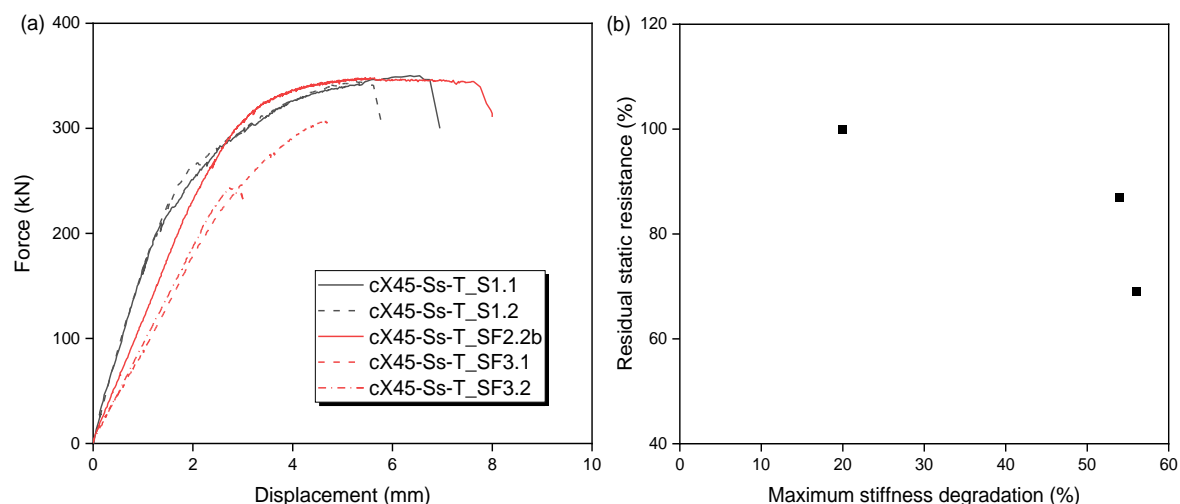


Fig. 5-19 Static behaviour of wrapped composite joints after cyclic load tests (a) load-displacement vs. original static tests from [172]; (b) residual static resistance vs. maximum stiffness degradation

Table 5-5 shows dependency of stiffness degradation in each specimen and the residual static resistance. It should be noted that the global stiffness degradation used to control and decide on stopping the cyclic loading is the average value of degradation of top and bottom brace-to-chord joints. However, one side is always suffering more damage, see Fig. 5-6, which means that one side degraded more while the other side degraded less than the target stiffness degradation limit of 40%. Therefore, the separate stiffness degradation of the top or bottom brace is calculated with help of DIC results and presented in Table 5-5. The value of maximum stiffness degradation of top or bottom is correlated to the relative residual static resistance in Fig. 5-19 (b). It can be seen that although the values of specimens with very high stiffness degradation ($> 50\%$) show an obvious decrease of static resistance, the results presented indicate that wrapped composite joints have the potential to sustain its original axial tension resistance even after experiencing substantial stiffness degradation of 20% due to cyclic (fatigue) load.

Table 5-5 Residual static resistance in function of stiffness degradation in cyclic load tests

Specimen	Initial stiffness (kN/mm)	Stiffness after cyclic test (kN/mm)	Global stiffness reduction (%)	Stiffness reduction – bottom (%)	Stiffness reduction – top (%)	Static resistance (kN)	Residual static resistance after cyclic test* (%)
cX45-Ss-T_S1.1	137	-	-	-	-	354	-
cX45-Ss-T_S1.2	136	-	-	-	-	349	-

cX45-Ss-T_SF2.2b	130	100	23	13	<u>20</u>	352	100
cX45-Ss-T_SF3.1	139	84	40	<u>54</u>	37	307	87
cX45-Ss-T_SF3.2	138	84	39	33	<u>56</u>	244	69

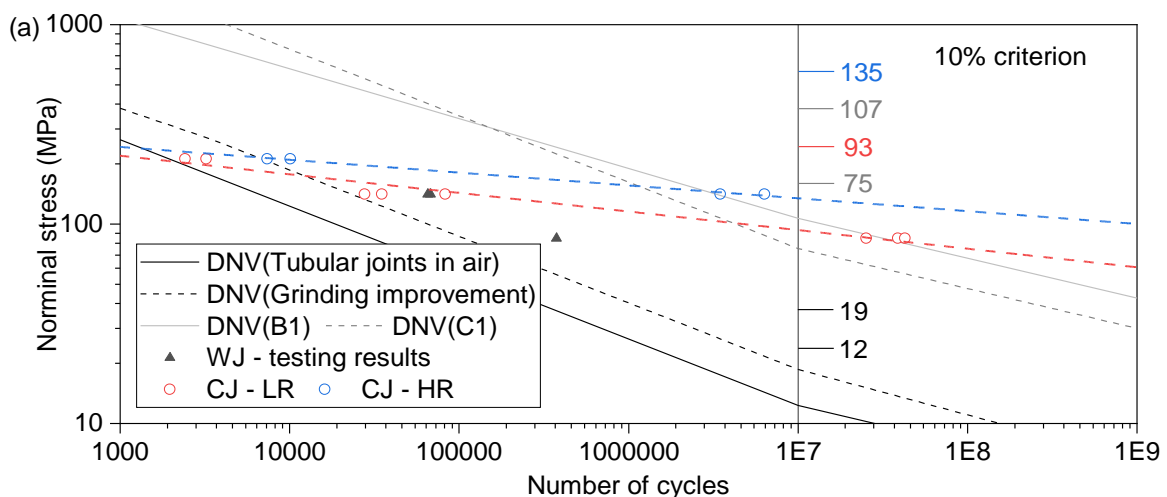
* Static resistance of specimens after cyclic loading compared to the average static resistance of reference specimens

5.5 Preliminary S-N curves

S-N curves for welded steel details in many design codes (DNV-RP-C203 (2016) [19], IIW Recommendations [20], Eurocode 3 [173], etc.) are defined for the number of cycles at the end of initiation life as it represents more than 90% of the total life of a welded joint, which is also confirmed in our own experiments shown in Fig. 5-4. Wrapped composite joint on the contrary, show gradual development of stiffness degradation and fatigue life can be defined only by setting explicit threshold on stiffness degradation. The experiments executed in this research show that wrapped composite joints can still sustain its original resistance with stiffness degradation of 20% and do not fail even with stiffness degradation of 40%. In order to define the preliminary S-N curves of the wrapped composite joints, different levels of allowable stiffness degradation (10% – 40%) are taken as criteria shown in Fig. 5-20. Virgin tested specimens from both the batches with the higher and lower roughness are included in generation of the S-N curves. For each stress level, at least two results are considered for wrapped composite joints. The least square method regressions are conducted based on the average value of each stress level to form the S-N curves defined by different failure criteria. Number of cycles obtained for 10% stiffness degradation at all stress levels is actual. To assess potential S-N curves allowing larger degree of damage, the number of cycles at lower stress level (141 MPa and 85 MPa) are extrapolated based on regression of degradation curves shown in Fig. 5-4 and the linear model presented in Eq. 5-2. The stress range indicated on the vertical axis is the nominal stress in the steel brace members, therefore comparable to nominal stresses in brace members of welded joints. S-N curves for welded tubular joints (class T in air) from DNV-RP-C203 (2016) are also shown on the graph for the comparison reasons. In order to be able to compare the wrapped and welded joints on the basis of nominal stress in the brace, the class T S-N curve from DNV is divided by Stress Concentration Factor $SFC = 7.7$ which was the maximum value at the chord saddle location for the considered dimensions and angle of the welded joints. Data points obtained from 4 reference experiments on welded joint specimens are also shown in the same figure. The S-N curve B1 from DNV representing the characteristic fatigue endurance of non-welded circular hollow sections (S355), as well as the S-N curve C1 representing characteristic fatigue endurance of CHS with circumferential butt weld made from both sides is also presented for comparison. The welded joint specimens were delivered with weld improvement by grinding, which provides improvement of fatigue life of joint by factor of 3.5 according to DNV-RP-C203 (2016) design recommendation. Satisfactory agreement

between experiment results on welded joints and $S-N$ curve for grinded joint from DNV is found. The slope of the curve and the experiment data points is comparable. The relative difference in number of cycles of approximately 1 decade from experiments and $S-N$ curve from DNV is due to the fact that the $S-N$ curve is based on characteristic values of multiple experiments.

It can be seen that wrapped composite joints, even with the lower roughness, show superior fatigue performance versus their welded counterparts when the lowest damage tolerance for stiffness degradation of only 10% is allowed. Such superior performance is especially present in range of high-cycle range ($N > 10^7$ and further) corresponding to the lower load range. Under higher load range, fatigue performance of composite joints with lower roughness show comparable or a little bit lower fatigue life than welded ones when stiffness degradation of 10% or 20% is considered as the failure criterion as shown in Fig. 5-20 (a) and (b). However, the fatigue life of wrapped composite joints is greatly improved in the low cycle range, as well in the high-cycle range as long as enough roughness is guaranteed. It should be noted that the high-cycle load range is dominant for fatigue design of offshore structures. Generally speaking, the fatigue life of the tested wrapped composite joints subjected to tension-tension cyclic loading is 10-100 times longer based on different failure criteria than their welded counterparts under the same stress range. The same conclusion can also be obtained by comparing slopes of $S-N$ curves. For $S-N$ curves of wrapped composite joints, the negative inverse slope m is approximately 13.5 and 10.7 in case of higher and lower roughness, respectively, which is much higher than that of welded tubular joints ($m=3$ or 4 according to Ref. [19]). In terms of comparison with B1 and C1 curves, it can be concluded that wrapped composite joints are able to have longer fatigue life than the circumferentially welded or even non-welded steel members in high-cycle load range (see the higher critical stress ranges of wrapped composite joints corresponding to 10^7 cycles).



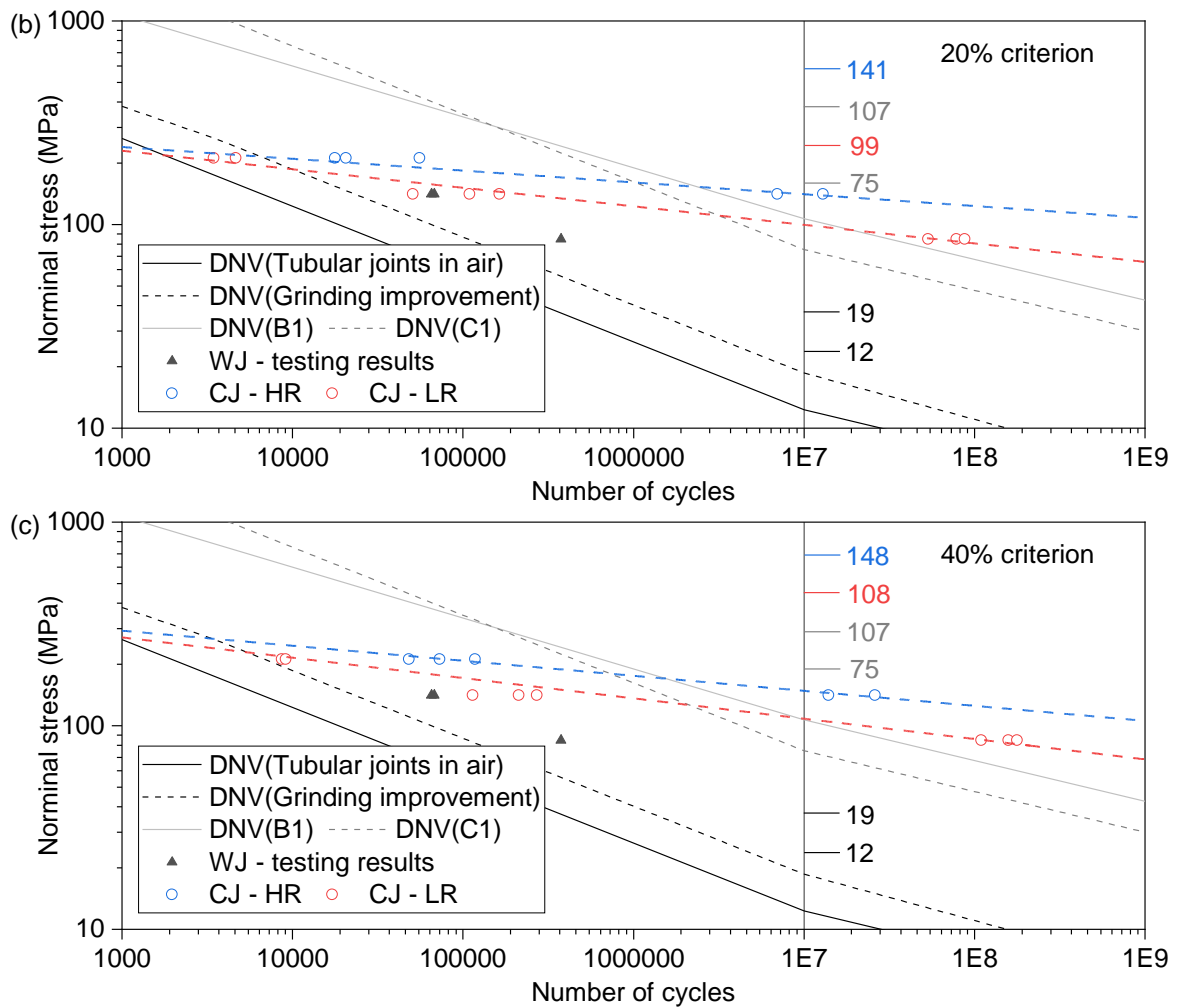


Fig. 5-20 Comparison between test results of different failure criteria with existing curves
 (a) 10% criterion; (b) 20% criterion; (c) 40% criterion

5.6 Upscaling capacity of the X45 joints

5.6.1 Specimens

In order to test the upscaling capacity of the wrapped composite joint from the fatigue behaviour perspective, the medium size joint (1/4 of the full scale joint) is tested in this section. Additional objective is to estimate scatter of the fatigue results for specimens whose scale is closer to full-scale production. Geometry and dimensions of the medium scale joint is shown in Fig. 5-21. Dimensions of the chord are $\text{Ø}273 \times 10$ mm with braces $\text{Ø}168 \times 12.5$ mm. The wrapping length on the brace is 4 times the brace diameter, which is the same ratio as used for the small scale joint. The maximum wrapping thickness at the root of the joint is around 50 mm. Ear plates are welded at ends of the steel tubes for the load application. The full penetration butt weld details is designed carefully to avoid possible premature failure. A hole is drilled at the end of the plate to ensure the welding quality. White paint followed by the spackle pattern is applied on one side of the joint to facilitate the DIC monitoring during the tests. Summary of specimens is shown in Table 5-6, where a total of 3 identical specimens are tested.

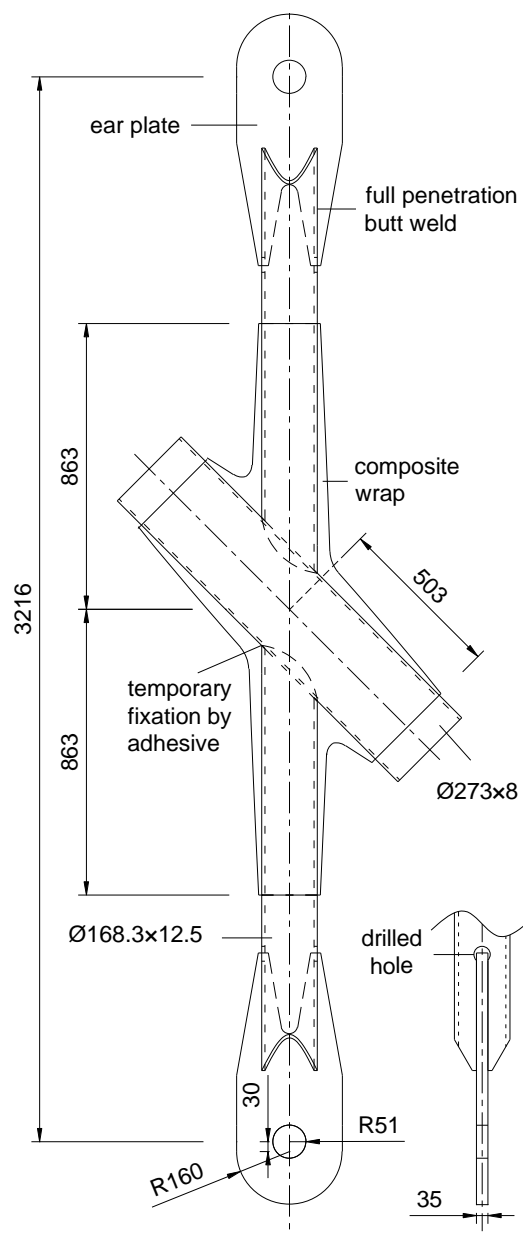


Fig. 5-21 Geometry and dimensions of specimen (in millimetres)

Table 5-6 Medium scale specimens

Load ranges ΔF (kN)	Nominal stress ranges $\Delta\sigma_{nb}^1$ (MPa)	Specimens
30-330	49	cX45-MS-T_F1.1/2/3

5.6.2 Test set-up and instrumentation

Test set-up is shown in Fig. 5-22. As shown in the figure, a self-equilibrium custom modular frame is built and equipped with the synchronized hydraulic jack on the top. The specimen is connected with the hydraulic jack through the ear plate. A pin shaft is used for the connection such that no bending moment is transferred at the loading ends. The tension-tension cyclic load is applied by the force control. The applied load range on the specimen is 30-330kN, approximately 30% of its static resistance, which has been predicted by FE model calibrated based on small scale experiments previously. The load range is chosen to be comparable with

the medium load range (10-110kN) in the small scale test. The loading frequency is 1 Hz considering stability of the loading system.

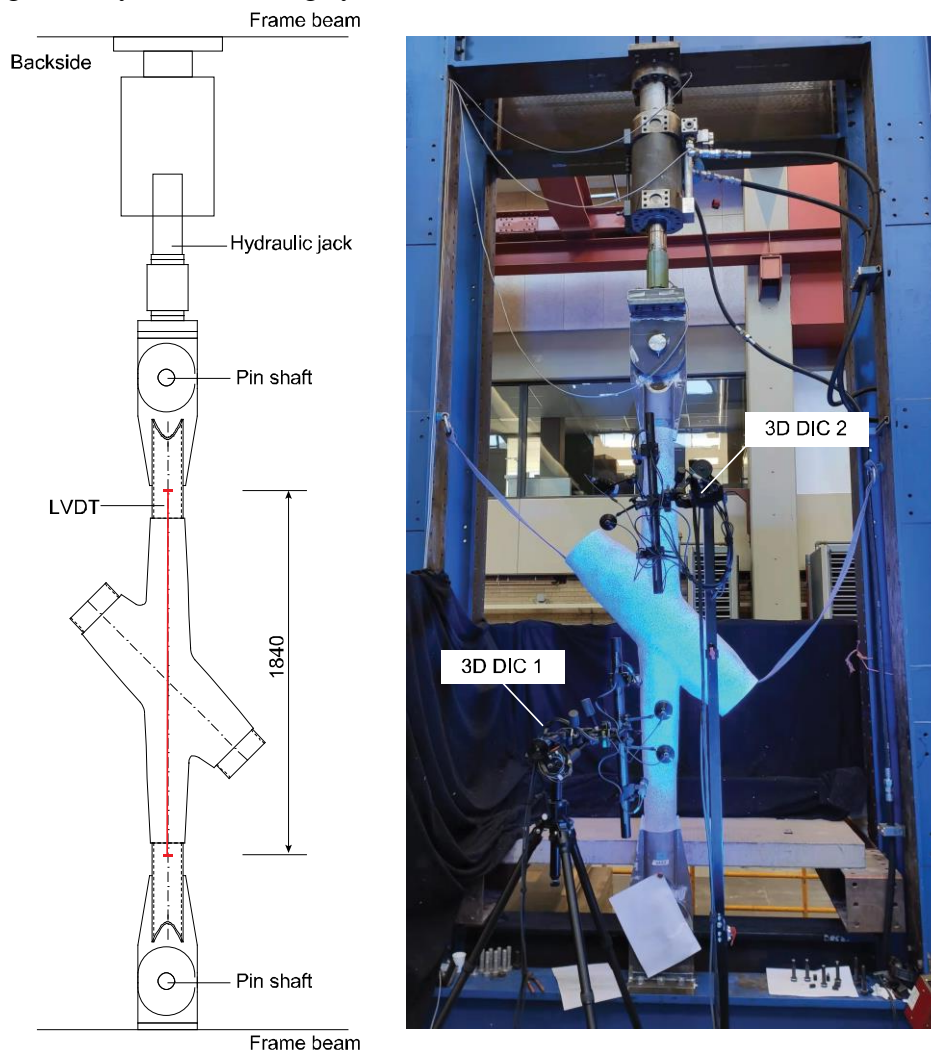


Fig. 5-22 Test set-up (in millimetres)

The identical 3D DIC system utilized for the small-scale test is employed to observe the deformation and displacement of the specimens throughout the test. To enhance the measuring accuracy of the DIC system and account for the measuring volume, two distinct DIC setups are established, each dedicated to one side of the chord-to-brace connection, as depicted in Fig. 5-22 (a). The two DIC systems are controlled synchronously, taking photos at the maximum and minimum loads every 10000 cycles. An LVDT system is installed on the backside of the specimen to accurately measure its deformation, enabling the calculation of the global stiffness of the joint. The measuring length is 1840 mm as shown in Fig. 5-22, encompassing not only the composite wrap but also a portion of the steel tube.

5.6.3 Stiffness degradation

Global stiffness degradation of the 3 specimens is summarised in Fig. 5-23. The stiffness is calculated based on Eq.5-1, where elongation of the specimen is obtain from the LVDT results. It can be seen that results of the 3 specimens is within a reasonable scattering range. 2 of the 3

specimens, cX45-Ms-T_F1.1/3, failed after 1,300,000 – 1,500,000 cycles due to fracture of weld details around the end of ear plate, showing a stiffness degradation of 13%. On the other hand, the third specimen, cX45-Ms-T_F1.2, did not exhibit any weld fracture during the testing. The test was stopped around 2,000,000 cycles as the stiffness degradation appeared to have stabilized. Since crack initiation at the weld details will not result in significant stiffness degradation and the fracture always happens abruptly as confirmed by Fig. 5-4, it can be safely said that the stiffness degradation observed in the specimens prior to weld fracture can be attributed to damage occurring within the composite joints.

The stabilization phenomenon of stiffness degradation is more noticeable in the current study compared to the small-scale joint. This can be attributed to the fact that the crack growth within the specimen is limited and the variation of wrapping thickness is insignificant until current crack length.

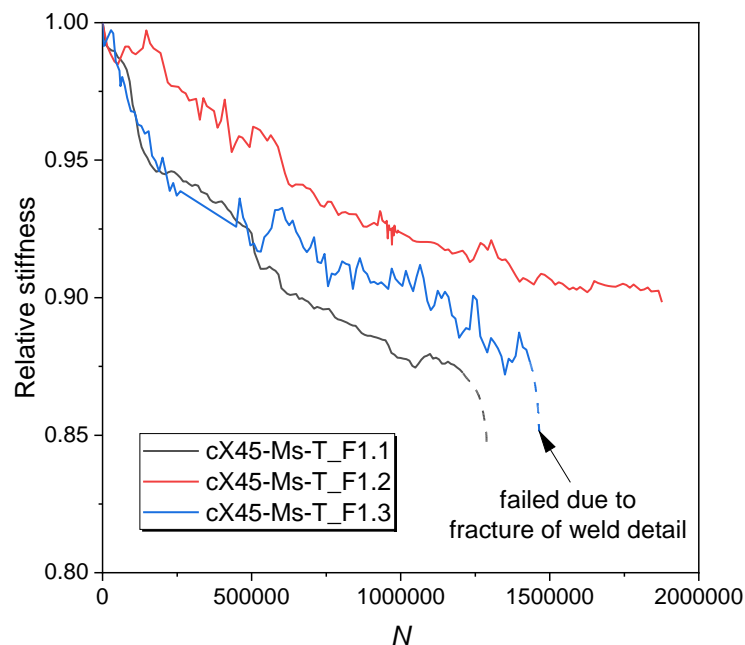


Fig. 5-23 Stiffness degradation of medium scale joints

5.6.4 Strain development

Typical contour plots of strain distribution on the surface of the composite wrap is shown in Fig. 5-24 at different loading stages. Images from the 2 DIC systems are put together for interpreting strain development on both the top and bottom braces. Similar to the small-scale joint, the strain development focuses primarily on the intersection between the chord and braces, suggesting potential damage, such as debonding, within the specimens. Surface curves are defined on the surface of top and bottom braces, from which the strains are extracted for each loading stages as shown in Fig. 5-25. It shows that there is no significant difference among different loading stages. This suggests that under current load range, the damage occurring within the interface is limited and insufficient to cause significant alterations in the surface strains. Therefore, it is impossible to derive the crack growth curves for these specimens.

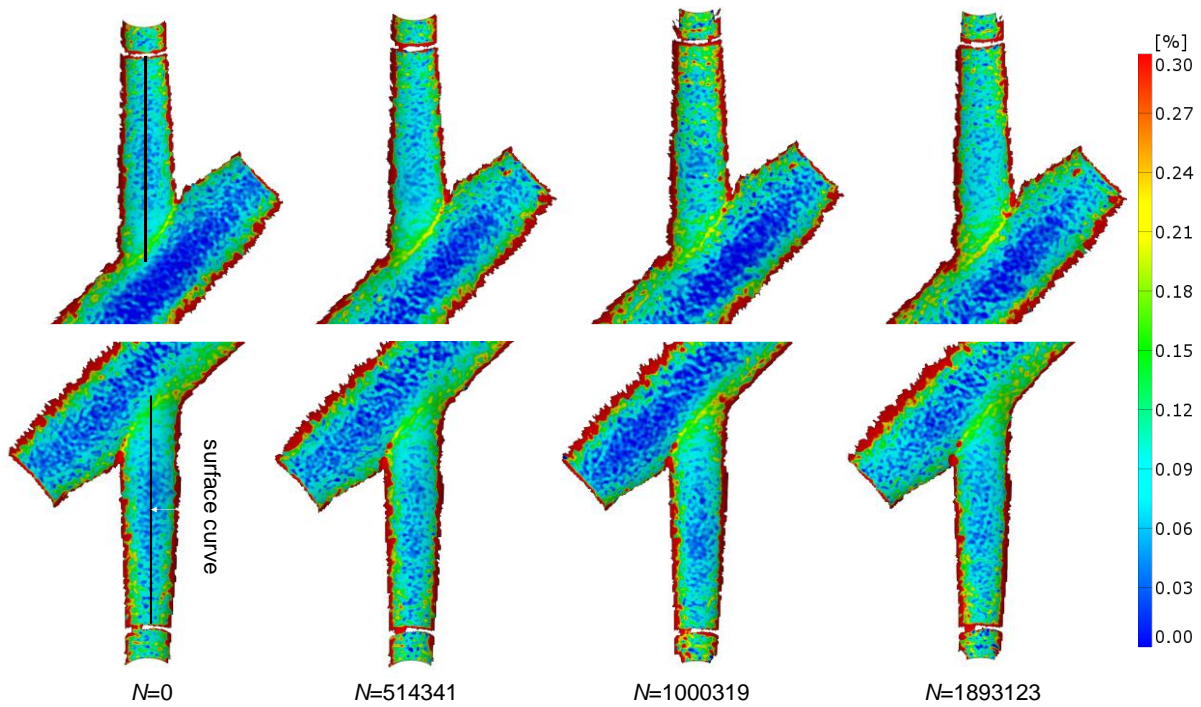


Fig. 5-24 Strain development on the surface of composite wrap (cX45-Ms-T_F1.2)

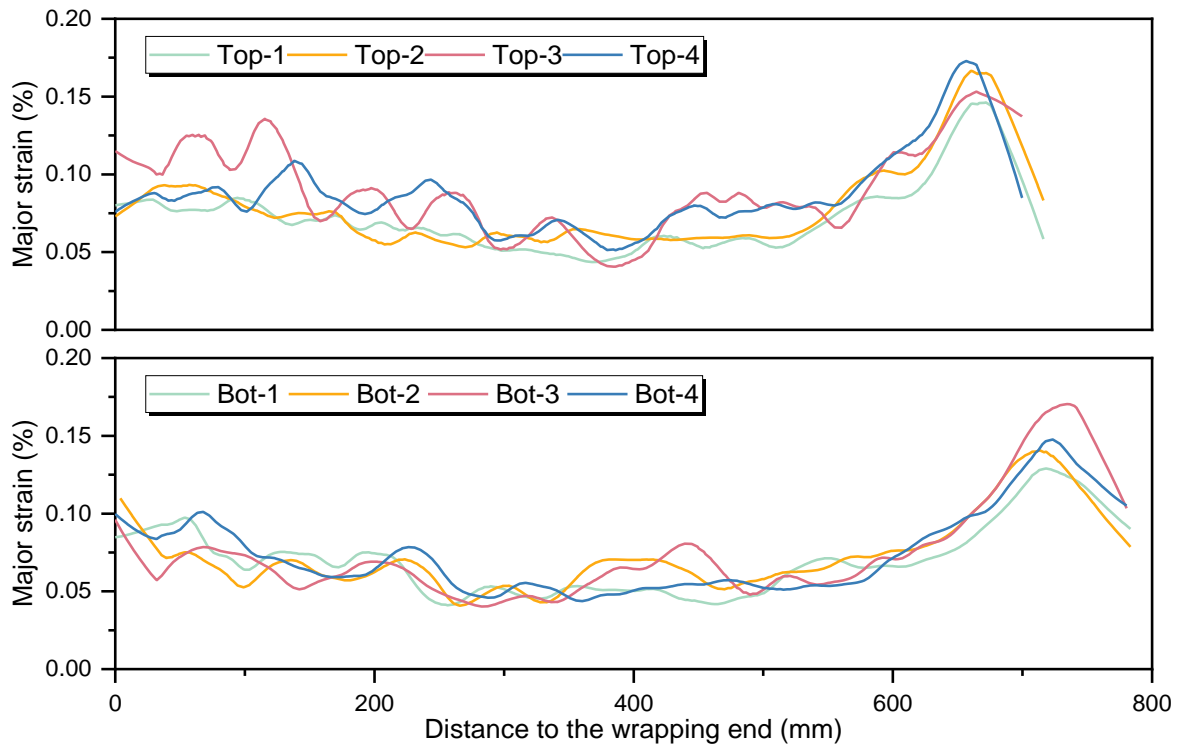


Fig. 5-25 Extracted strain distribution on the surface of composite wrap (cX45-Ms-T_F1.2)

5.6.5 Comparison with small-scale joints and existing curves

Considering that the medium scale joints are designed in a manner that is roughly proportional to the small-scale joints (except for the wrapping thickness) and are subjected to a force level equal to one-third of their static resistance, it is justifiable to compare the fatigue behaviour of the medium scale joints with those of the small-scale joints loaded within the range of 10-110kN.

Stiffness degradation curves of all the small-scale and medium scale joints are summarised in Fig. 5-26. It is evident that the medium scale joints experience a more rapid stiffness degradation compared to the small-scale joints. This is probably due to the fact that the relative wrapping thickness of medium scale joints is smaller than that of the small-scale joints. Thinner composite wrap may lead to increased SERRs at the crack tip, thus resulting in accelerated crack propagation.

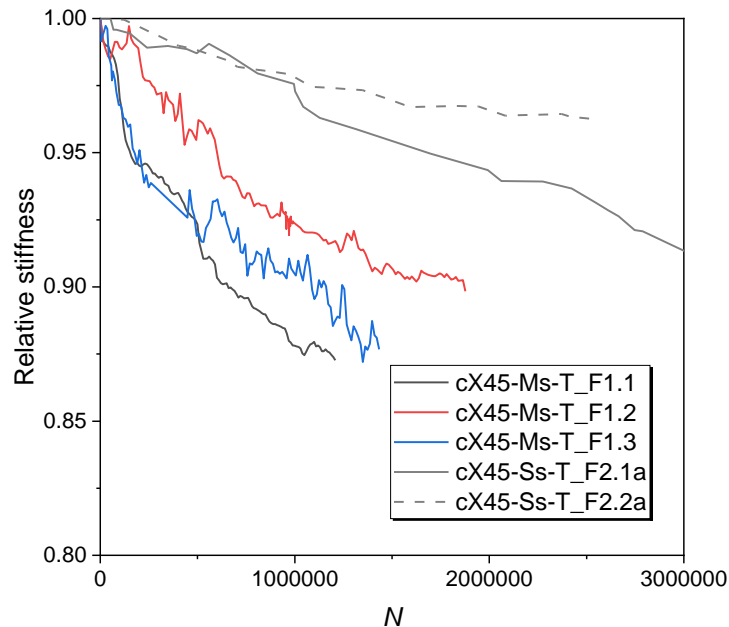


Fig. 5-26 Comparison with small-scale joints in terms of stiffness degradation

Test results of the medium scale wrapped composite joints are put together with existing design curves in Fig. 5-27 to assess their fatigue performance in comparison to the welded counterparts. The design curves are derived from welded joints with identical geometry, including the diameter and thickness of steel tubes, as the wrapped composite joints. The vertical axis represents the nominal stress range in the brace member, which is obtained by dividing the design curves by the Stress Concentration Factor (SCF) of 15.4, as calculated according to DNV-RP-C203 (2016). A stringent failure criterion of 10% stiffness degradation is adopted here to determine the fatigue life of wrapped composite joints, considering that the stiffness degradation remains relatively constrained. The results demonstrate that even when employing such a rigorous failure criterion, the fatigue life of wrapped composite joints can still be 100 times longer than the design value of welded joints when subjected to a stress range of 49 MPa. The fatigue performance of wrapped composite joints at this scale is deemed to be more than adequate.

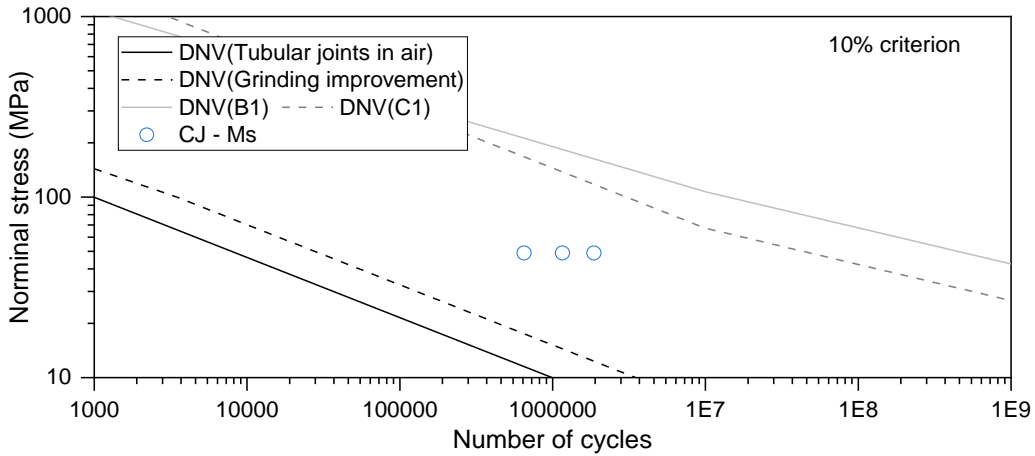


Fig. 5-27 Comparison of test results with existing curves

To evaluate the scattering level in the test results, the coefficient of variation (COV) for the fatigue life of the medium scale joints is compared with that of the small-scale joints at various failure criteria, as shown in Table 5-7. The table reveals that the coefficient of variation (COV) for the medium scale joints, 0.41, is higher than that of the small-scale joints at the same failure criterion. However, it falls within a reasonable range when compared to the results of small-scale joints at different failure criteria. It is important to note that employing a more tolerant failure criterion (20%, 40%) may result in increased variability in the test results. This can be attributed to the flattening of the stiffness degradation curves at lower stiffness levels.

Table 5-7 Comparison with small-scale joints in terms of scattering level

Failure criterion	Coefficient of variation (COV)		
	Small scale		Medium scale
	10-110kN	15-165kN	30-330kN
10%	0.20	0.16	0.41
20%	0.15	0.55	-
40%	0.16	0.36	-

5.7 Conclusions

In this chapter, behaviour of CHS wrapped composite X-joints is assessed under axial load in a cyclic regime with constant amplitude. Small-scale wrapped composite joints are compared with the reference welded joints, and preliminary S-N curves are presented. Stiffness degradation of the joints is analysed by examining strain distribution on the surface of composite wrap, while failure modes are inspected with help of 3D DIC system and micro camera. The influence of load range, re-testing and surface roughness of steel tubes on fatigue behaviour of wrapped composite joint is studied. Additionally, after fatigue tests, monotonic loads are applied to the joints to investigate the impact of cyclic loads on the residual static resistance. Finally, upscaling capacity of the wrapped composite joints is evaluated by conducting tests on medium scale joints. Based on the aforementioned studies, the following main conclusions can be drawn:

- The wrapped composite joints exhibit superior fatigue performance than their welded counterparts both in terms of number of cycles to failure and damage tolerance. The welded specimens experience abrupt failure shortly after crack initiation, typically at a stiffness degradation level of only up to 5%. In contrast, the stiffness of wrapped composite joints exhibit a gradual degradation, reaching up to 40% without failure. Only 2 out of 13 specimens exhibit failure in cyclic load tests with up to 3 million cycles. Specimens loaded under lowest load range, corresponding to 85 MPa nominal stress range in the brace tubes, show almost no stiffness degradation up to 3 million cycles which leads to estimate of practically infinite fatigue life.
- Preliminary S-N curves are obtained for the wrapped composite joints considering different levels of damage tolerance (10% - 40%) and surface roughness. Even with the most rigorous damage tolerance where allowable stiffness degradation is only 10%, wrapped composite joints with lower roughness still show superior fatigue performance than welded ones. Fatigue life of tested composite joints subjected to tension-tension cyclic loading is 10-100 times longer than that of their welded counterparts under the same stress range. The negative inverse slope m of the wrapped composite joint S-N curve is approximately 13.5 and 10.7 in case of higher and lower roughness, respectively, which is much higher than that of welded tubular joints ($m=3$ or 4).
- Stiffness degradation of wrapped composite joints is mainly due to debonding of the composite-to-steel interface. Except for debonding, one of the wrapped composite joints even fractured at the steel tube outside of the wrapped part, which demonstrates that the wrapped joints can have fatigue endurance which is comparable and exceeding that of the non-welded details of steel circular hollow sections.
- During the re-testing scheme, specimens tested by a low and then by a high load range exhibit approximately 10 times lower stiffness degradation rate than the virgin specimens that were only tested at high load range.
- Influence of surface roughness of steel tubes obtained by grit blasting is significant. 70% increase of average roughness S_q from 10 μm to 17 μm leads to 8 to 120 times decrease of stiffness degradation rate, i.e. 8-120 times extension of the fatigue life.
- The residual static resistance of the wrapped composite joints, even after undergoing more than 3 million load cycles resulting in a 20% stiffness degradation, remains unchanged. The joint is still capable of sustaining a load equivalent to the yield resistance of the steel brace. In cases where the wrapped composite joints experienced a 56% stiffness reduction due to cyclic loading, the static resistance is reduced by 30%.
- The upscaling test conducted on the medium-scale specimens reveals that the wrapped composite joint, when closely resembles the full-scale application, maintains a desirable stiffness degradation trend and exhibits superior fatigue performance compared to the welded joints. The level of scattering observed in the test results falls within a reasonable range when compared to the small-scale joints.

Chapter VI

NUMERICAL MODELLING ON THE FATIGUE DEBONDING BEHAVIOUR OF CHS X-45 JOINTS

Parts of this chapter appear in the journal article: ‘W. Feng et al., Numerical prediction on the fatigue debonding behaviour in a complex bi-material interface: a case study on wrapped composite joints. (*In preparation*)’

6.1 Introduction

In this chapter, finite element models are built to predict the fatigue crack propagation thus stiffness degradation behaviour of wrapped composite joints, as well as to gain deeper insights into the failure process. The FE model is validated against the static test results of the small scale X45 joints, in terms of load-displacement responses and strain distributions on the surface of composite wrap. Virtual crack closure technique (VCCT) and cohesive zone model (CZM) is employed to simulate the debonding process at the composite-to-steel interface. The VCCT is also utilised to calculate the SERR at the crack tips.

The fatigue debonding behaviour is simulated by proposing the stationary crack method, where debonding crack patterns during the fatigue loading are assumed to be the same as those under monotonic loading. After extracting SERR values at different crack tips, the crack propagation and stiffness degradation are predicted based on the FCG curves established in Chapter 3 through an automatic iterative algorithm. The modelling results are validated against the test results for small scale and mid-scale X45 joints with different roughness and load levels. Sensitivity analysis on the modelling parameters, such as the FCG model, SERR averaging method, threshold SERR values and so on is conducted for parameter calibration and justification.

Probabilistic analysis considering the uncertainty of the FCG curve parameters and surface roughness of the steel tubes is conducted. The probabilistic distribution of the simulation results are compared with those of the test results. Based on the probabilistic analysis, the cumulative distribution function of the fatigue lives under different failure criteria are established, which can be used to derive the probabilistic $S-N$ curves in Chapter 7.

6.2 Set-up of the model

6.2.1 Geometry and boundary conditions

Geometry of the small scale X45 joint FE model in ABAQUS software is shown in **Fig. 6-1**. Due to the symmetric geometry, only half of the joint is modelled to reduce the computation time.. The composite part is created in Inventor software parametrically and imported into ABAQUS. Its geometry and dimensions (thicknesses on flat parts and corners) follow the designed drawings of the specimen and are calibrated with the help of 3D scanning of the specimen. The composite parts are modelled with 3 layers as has been applied during the production process. Surfaces representing the end cross sections of the braces are coupled to reference points, RP1 and RP2, as shown in the figure. All degrees of freedom except for the U2 (y) direction are constrained for the reference points to replicate the fixation constraints at the tube ends due to clamping in physical test. The symmetric tensile load is applied by vertical displacement on both RP1 and RP2. Symmetric boundary conditions are applied in the middle (cut) plane.

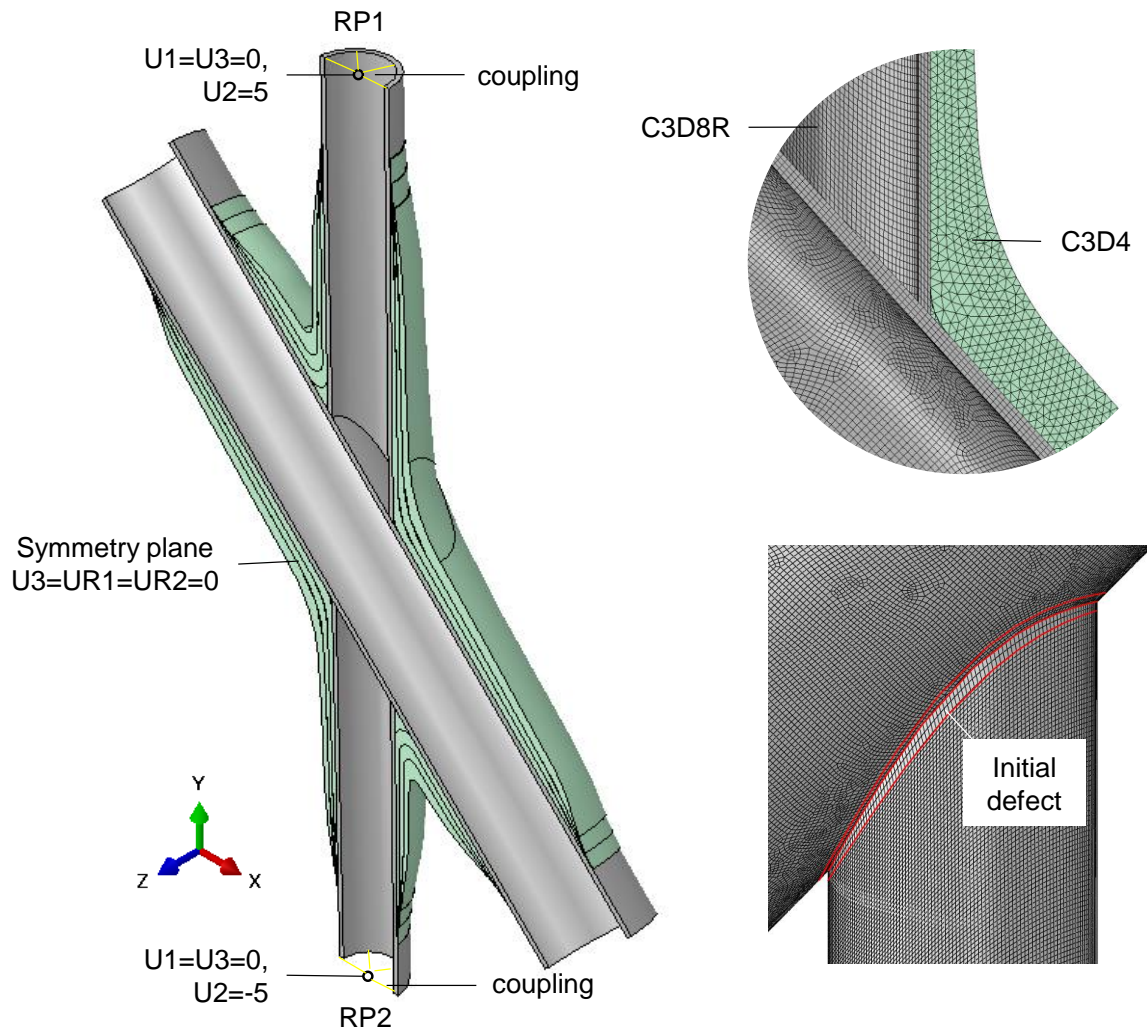


Fig. 6-1 Boundary conditions and mesh topology of the FE model

6.2.2 Analyses method

Geometric and material nonlinear analysis is performed as quasi-static using the dynamic explicit solver in ABAQUS. To mitigate inertia effects in quasi-static explicit dynamic analysis, the displacement is applied using a smooth step amplitude curve. The time period of the analysis was chosen similar to its real time period (e.g. 300s for fracture loading). But the quasi-static analysis is sped up by employing non-uniform, semi-automatic mass scaling in the explicit solver. The desired time increment for integration is set to be 0.005 s, which is small enough to match the input and output forces as suggested by [140].

6.2.3 Materials

Material of composite wrap is considered as transversely isotropic. The elastic constants are the same as used in ENF model shown in Table 3-2 in chapter 3, which are obtained through standard material tests on the GFRP laminate ($E_x=E_y$, G_{xy} and ν_{xy}) or based on micromechanics and rules of mixture for data not obtained directly by tests (E_z , $G_{xz}=G_{yz}$, $\nu_{xz}=\nu_{yz}$). Further

information on plasticity and material damage can be found in [140]. Plasticity model is used in this study to model non-linear behaviour of steel. Elastic constants ($E= 210$ GPa, and $\nu=0.3$) and nominal yield and ultimate stress (S355, $f_y = 355$ MPa, $f_u = 510$ MPa) in combination with isotropic hardening are used for the steel tubes.

6.2.4 Interactions

Tie constraint is applied between different wrapping layers considering the fact that limited interlaminar damage was found during the test. As for the composite-to-steel interface, VCCT is utilized here to simulate the crack propagation at the interface in the static model and calculate the SERR at the crack tips for fatigue analysis. A 2 mm virtual initial defect is introduced at the intersection of the chord and braces as depicted in **Fig. 6-1** to initiate the crack propagation. The nodes in front of the crack tip from both steel and composite parts are coupled and will debond after the fracture criterion, $G_T \geq G_{eqC}$, is met. For the Benzeggagh–Kenane (BK) law used in this study, G_T represents the total SERR, i.e $G_T = G_I + G_{II} + G_{III}$. G_{eqC} is the equivalent critical SERR, which is defined by:

$$G_{eqC} = G_{IC} + (G_{IIC} - G_{IC}) \left(\frac{G_{II} + G_{III}}{G_T} \right)^\eta \quad (6-1)$$

where G_{IC} and G_{IIC} are the critical mode I and mode II SERRs, and $\eta=1.8$. Considering the limitations of VCCT in simulating the fracture process zone, the critical SERR values (the initiation value) obtained by the standard DCB and ENF test cannot be directly used as the inputs as discussed in Chapter 4. A friction behaviour in combination with a calibrated critical SERR values are defined at the interface as listed in **Table 6-1**. The friction coefficient $\mu=0.5$ is measured by the tribometer as introduced in Chapter 3. The critical SERR values are tuned between the initiation value and propagation value which are obtained in [140] until achieving a satisfactory alignment with the force-displacement curves. The mode I critical SERR value is adjusted proportionally to the mode II value during the tuning process.

Table 6-1 Interaction property parameters

Mode I				
Parameter	G_{Ic} (N/mm)	G_{Iini}^* (N/mm)	G_{Iprop}^* (N/mm)	$(G_{Ic} - G_{Iini}) /$ $(G_{Ipro} - G_{Iini})^{**}$
Values	1.02	0.3	1.2	77%
Mode II				
Parameter	G_{IIc} (N/mm)	G_{IIini}^* (N/mm)	G_{IIprop}^* (N/mm)	$(G_{IIc} - G_{IIini}) /$ $(G_{IIpro} - G_{IIini})^{**}$
Values	1.34	0.45	1.6	77%

* Obtained from Ref. [140]

** The critical values are tuned between the initiation value and propagation value. This percentage (weight) expresses the contribution of initiation and propagation SERR to the fracture criterion.

In modelling of fatigue behaviour, the critical SERR values are intentionally set to a sufficiently high level (e.g. 100 N/mm) to prevent crack propagation, such that SERR values can be calculated at a specific stationary crack tip.

6.2.5 Finite element mesh

Linear, hexahedral solid elements, C3D8R, with reduced integration are used for the brace and chord steel members. Linear tetrahedron elements, C3D4, are used for the composite wrap due to its complex geometry, as well as its lower computational cost compared to the quadratic hex elements at the same computational accuracy. The composite parts are modelled as 3 non-uniformly thick laminates by 3D solid instead of multiple plies by shell elements since the delamination is insignificant during the fatigue tests, as shown in cut specimens in Ref. [161]. The solid homogeneous cross section, instead of composite layups, is employed due to its higher accuracy of defining material orientations and its capacity of simulating the through-thickness shear behaviour of the composite wrap with highly non-uniform thickness. Since the SERR values calculated by the VCCT is sensitive to the mesh size [50], a sensitivity study on the global mesh size is conducted as shown in **Fig. 6-2**, where mode II SERRs at the initial crack tip are extracted at the load level of 165 kN (the maximum force in fatigue loading). The figure illustrates that the mesh size within the investigated range, namely 0.5-2mm, has resulted in converged SERR values. Taking into account both accuracy and computational efficiency, a global mesh size of 1 mm is chosen for the subsequent analysis.

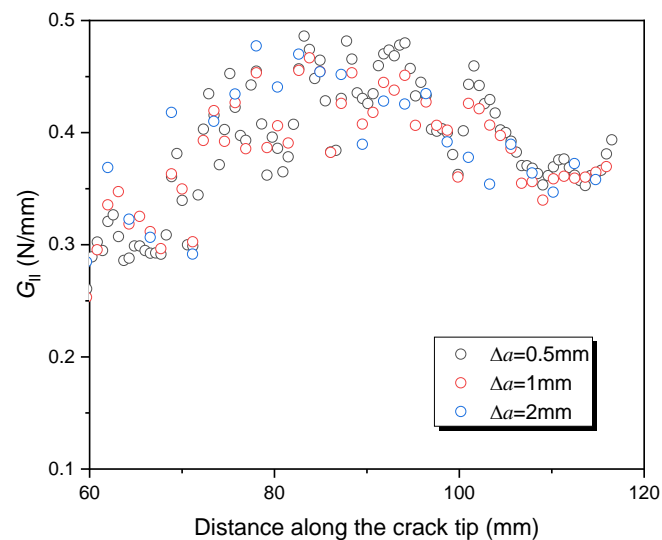


Fig. 6-2 Mesh sensitivity study results

6.3 Model validation by static tests

6.3.1 Force-displacement responses

Force-displacement curves from the VCCT-based FE model with and without friction defined at the interface are plotted and compared with experimental results presented in Ref. [140] in **Fig. 6-3**. The figure shows that the VCCT-based model with friction matches well with the test

results in terms of curve shapes, initial stiffness and ultimate resistance. Detailed comparison between the FEA and test results is also shown in **Table 6-2**, indicating that the mismatch for the initial stiffness and ultimate resistance is less than 5%. On the contrary, FE model without friction exhibits an abrupt failure after reaching the elastic limit, i.e. after the fracture criterion (6-1) is met. This contrast proves that friction can effectively simulate the residual interaction (friction, fibre bridging, et al.) behaviour at the interface after fracture.

A significant mismatch between the VCCT-based FEA result and test results is observed in the elastic limit as indicated in **Fig. 6-3**, where the FEA tends to overestimate the test results. However, the mismatch is not observed in the CZM-based model as in Ref. [140]. This is again due to the limitation of VCCT in simulating the fracture process zone. The elastic limit in the force-displacement curve corresponds to onset value of SERR in the CZM [140], which is lower than the tuned critical SERR values in the VCCT model. A sawtooth behaviour is also evident in the VCCT-based results, wherein drops of the force are associated with node releases every time the new crack front forms [50]. This nonlinear and sawtooth behaviour is above the target maximum force during the fatigue test thus will not influence the SERR calculation for the following analysis on fatigue behaviour.

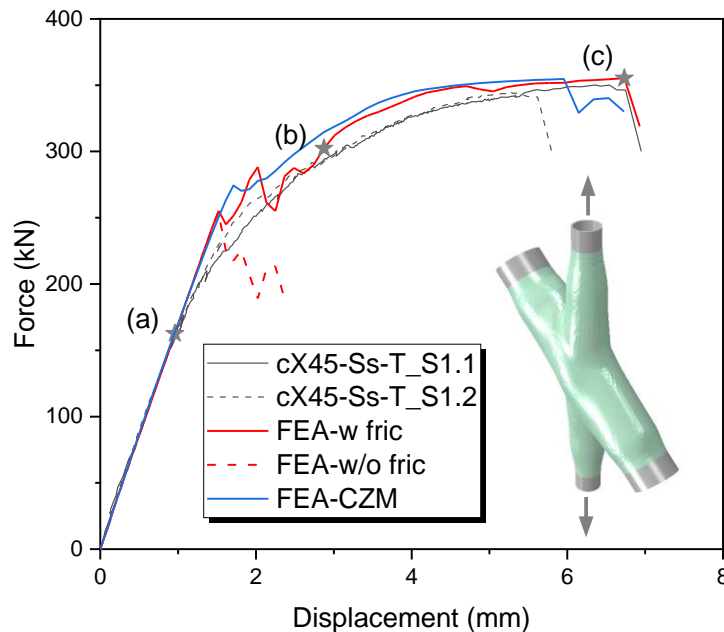


Fig. 6-3 Validation of FE model via force-displacement responses

Table 6-2 Comparison between FEA and experimental results

Mechanical property	FEA-w fric	Test [140]	Ratio of FEA/Test
Initial stiffness (kN/mm)	167	165	1.01
Ultimate resistance (kN)	355	346	1.03

6.3.2 Strain distribution along the composite surface

In **Ref.** [171], the crack propagation at the interface is monitored based on strain distributions on the surface of composite wrap through a combined DIC-FEA analysis. The FE model is

further validated by comparing strain distributions on the surface of the FE model with DIC results of specimen cX45-Ss-T_S3.1&2 at different loading stages as shown in Fig. 6-4. Fig. 6-4 shows the debonding patterns in the FE model under monotonic loading at (a) 165kN (the maximum load in cyclic loading), (b) 300kN and (c) the ultimate load respectively. On the brace, the crack initiates at the obtuse corner of the intersection between the chord and brace, and propagates towards the end of the composite wrap. While on the chord, the crack initiates around the intersection and propagates as a semi-circle towards the centerline of the chord.

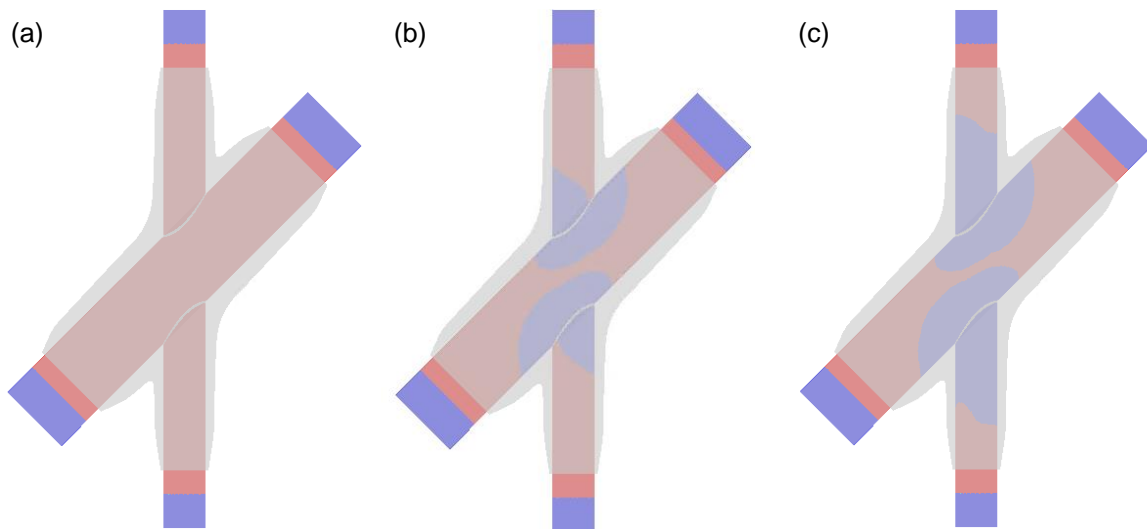


Fig. 6-4 Debonding pattern in FE model under monotonic loading

Contour plots of major strains on the surface of the FE model and specimen are compared at the force level of 165 kN and 300 kN in Fig. 6-5 and Fig. 6-6 respectively. The stress states of steel tubes are also shown aside. As shown in Fig. 6-5 (a) and Fig. 6-6 (b), the pattern of strain distribution from FEA resembles well with those from DIC analysis regardless of the loading stage (whether steel is in elastic stage as in Fig. 6-5 (a) or already yields as shown in Fig. 6-6 (b)). The strains concentrate at the brace-to-chord corners and decreases gradually towards the end of brace. A quantitative comparison between FEA and test (DIC) results are shown in Fig. 6-5 (b) and Fig. 6-5 (b), where major strains are extracted on the surface of braces starting from the middle of the joint. The figures illustrate that the FEA results matches well with the DIC measurements, although there are a lot of noises because of relatively low level of strains.

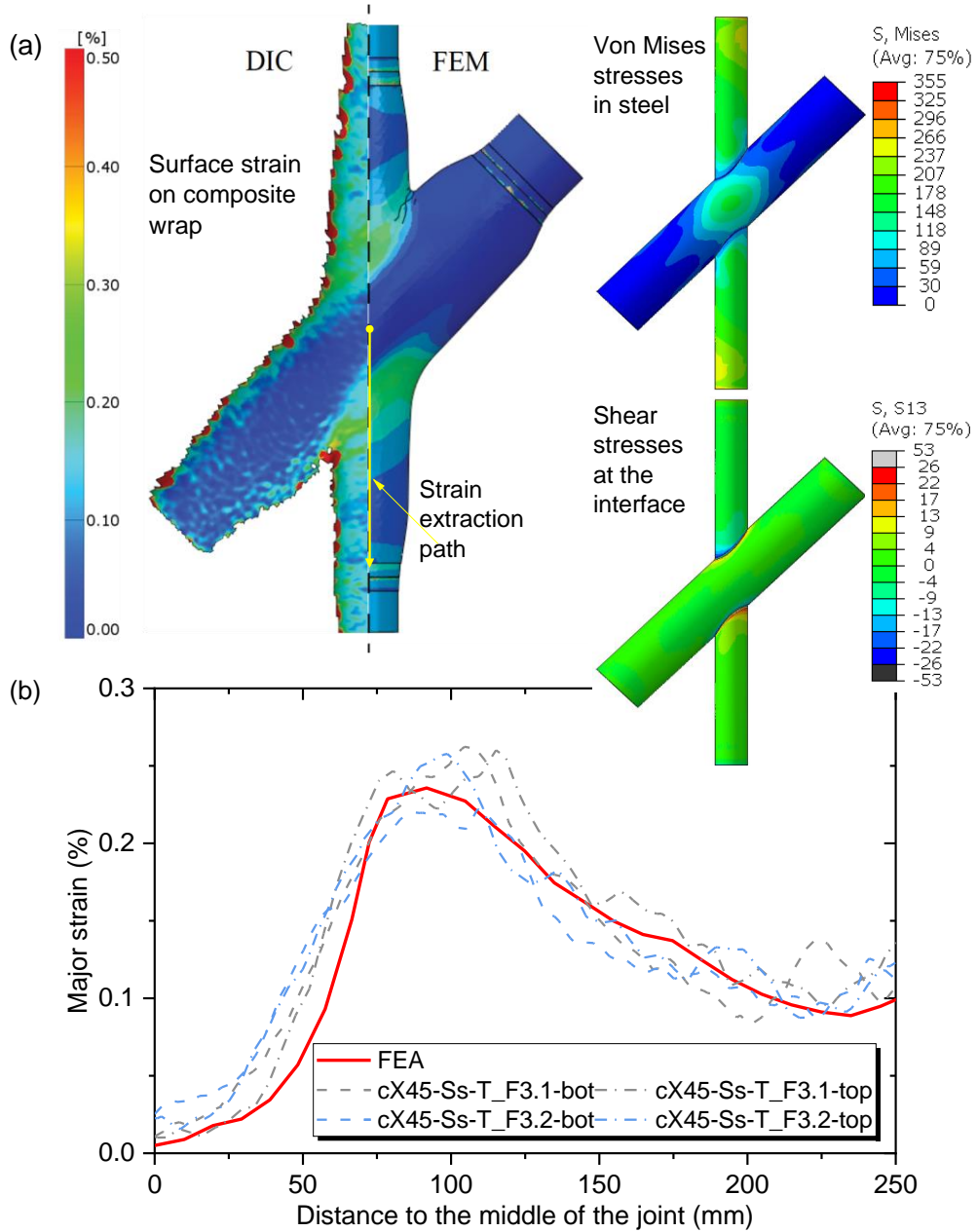


Fig. 6-5 Comparison on strain distribution on the surface of composite wrap between DIC and FEM (at 165kN)

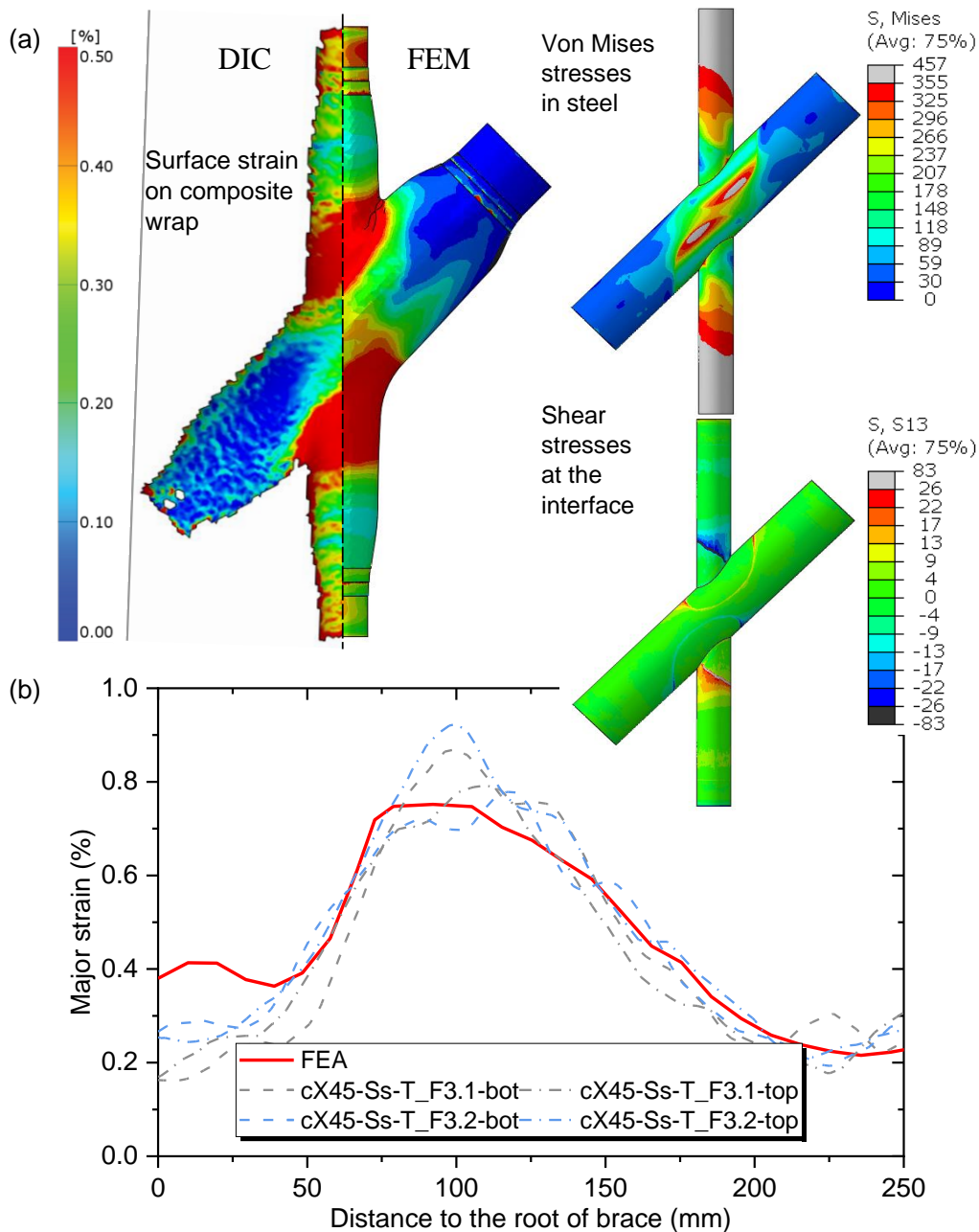


Fig. 6-6 Comparison on strain distribution on the surface of composite wrap between DIC and FEM (at 300kN)

6.4 Modelling of stiffness degradation and crack propagation under cyclic loading

6.4.1 Modelling strategy

Since the failure modes of wrapped composite joints under cyclic loading, namely the debonding failure at the composite-to-steel interface, have been confirmed by the experiments in Chapter 5, the main task of this part is to predict crack growth at the interface, thus stiffness degradation of the joints with the pre-determined failure mode. The following assumptions are made for the prediction:

- 1) Debonding at the composite-to-steel interface is the only failure mode under cyclic loading, with all the materials remaining elastic;
- 2) The debonding patterns under cyclic loading are consistent with those observed in quasi-static loading. But the relationship between the debonding crack length on the chord and braces may be different;
- 3) Debonding on the top and bottom sides of the joints are centrally symmetric about the origin;

Based on the assumptions above, the fatigue debonding behaviour of the wrapped composite joints is predicted using the procedure outlined in the flowchart in **Fig. 6-7**. This procedure includes finite element modelling, followed by a post-processing script [174] for the final prediction. Detailed explanations and intermediate results obtained from each step will be discussed in the subsequent section.

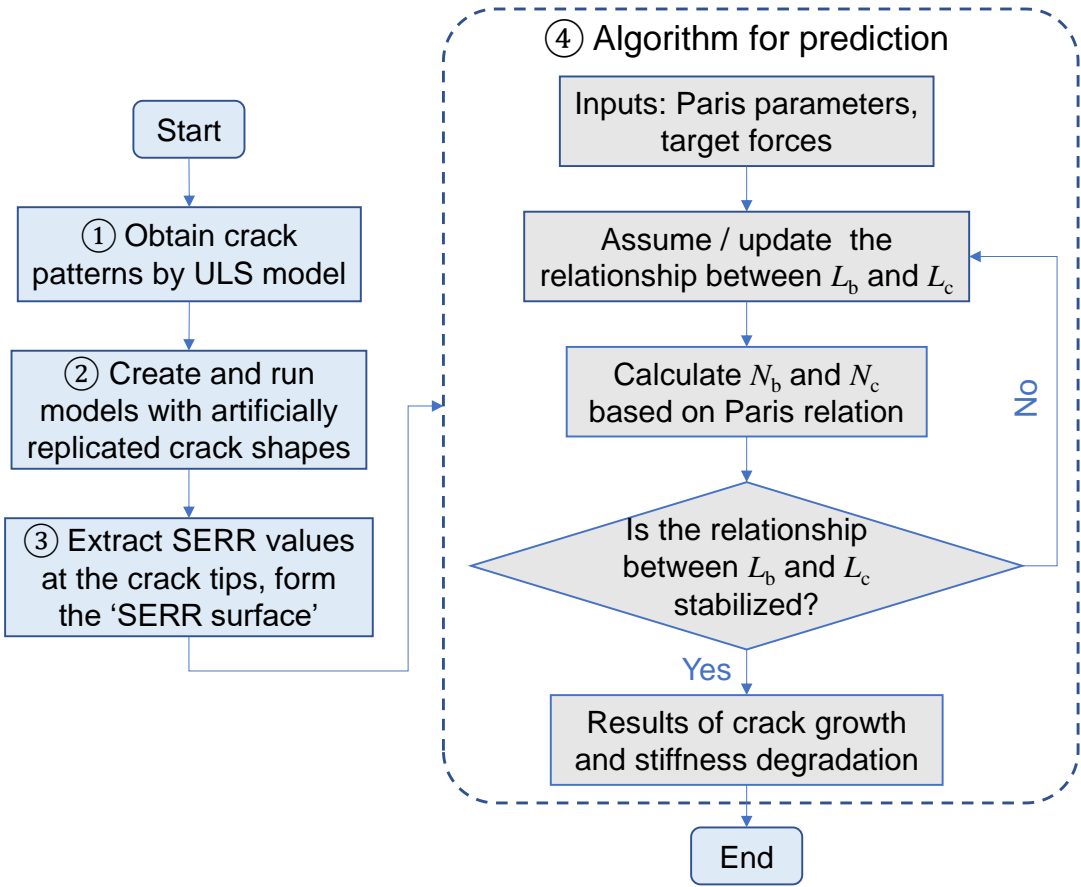


Fig. 6-7 Flowchart for prediction on the fatigue debonding behaviour of wrapped composite joints

Step1: obtain crack patterns from static model

As the debonding crack pattern under cyclic load is assumed to be consistent with that during the quasi-static load, the first step would be to obtain the crack patterns by running the static model. However, it should be noted that the materials are assumed to remain elastic in cyclic loading since the composite wrap is thick enough and the maximum force (e.g. 165 kN for small scale X45 joints) is below the elastic limit. In this case, damages only evolve at the interface,

which is different from the static model where damages evolve both at the interface and within materials. This discrepancy in the damage evolution between the static model and the fatigue model may result in variations in the debonding patterns observed in the two models. To eliminate the influence of such difference, the static model is rerun with all the material properties set to be elastic. The force displacement curves obtained from the elastic static model is plotted and compared with that obtained from the plastic static model in **Fig. 6-8**. It can be seen from the figure that without energy dissipated by the material damage, more energy is concentrated at the interface in the elastic model thus causing earlier debonding failure. Additionally, this phenomenon also results in a more pronounced sawtooth behaviour during the debonding process.

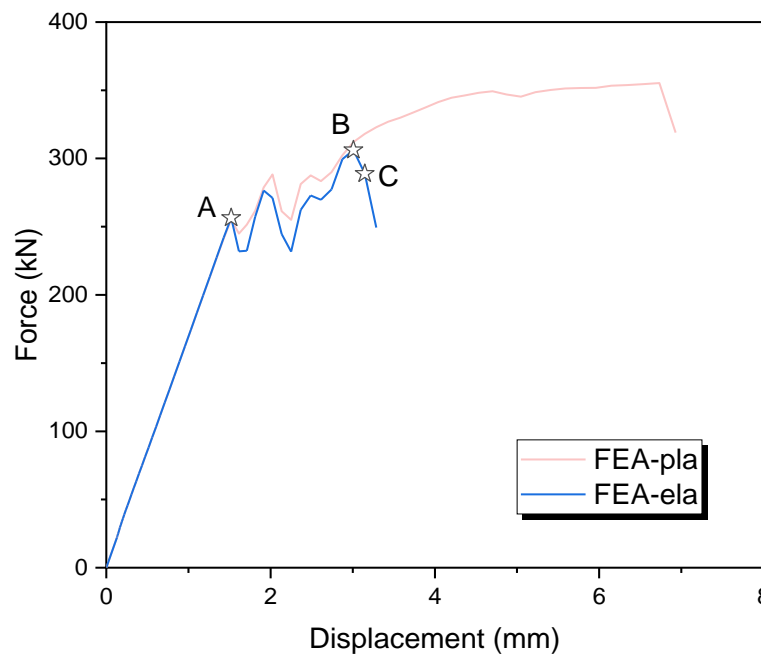


Fig. 6-8 Force displacement curves from plastic and elastic models

One typical debonding pattern of the elastic model under monotonic loading is shown in Fig. 6-9, where the crack length on the brace, L_b , and crack length on the chord, L_c , is defined. L_b is defined as the distance from the obtuse corner to the midpoint of the crack tip along the brace's axis, while L_c is defined as length of the arc perpendicular to the chord's axis, starting from the midpoint of the intersection between the brace and chord to the crack tip. Debonding patterns at different loading stages in the elastic model are depicted in Fig. 6-10. The bonded and debonded part is clearly distinguished due to the limitation of VCCT in simulating the fracture process zone. It is evident that the crack initiates at the obtuse corner of the brace initially. The crack front propagates in a triangular pattern towards the end of the brace, eventually aligning perpendicular to the axis of the brace, until sudden failure at the peak load. The crack on the chord initiates around the intersection between the chord and braces, propagating in a semi-circle pattern towards the centre of the chord.

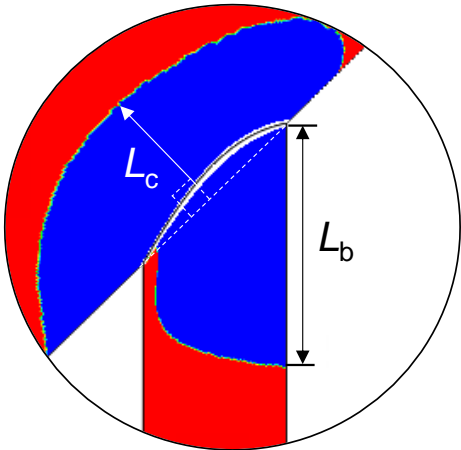


Fig. 6-9 Definition of crack length on the chord and brace

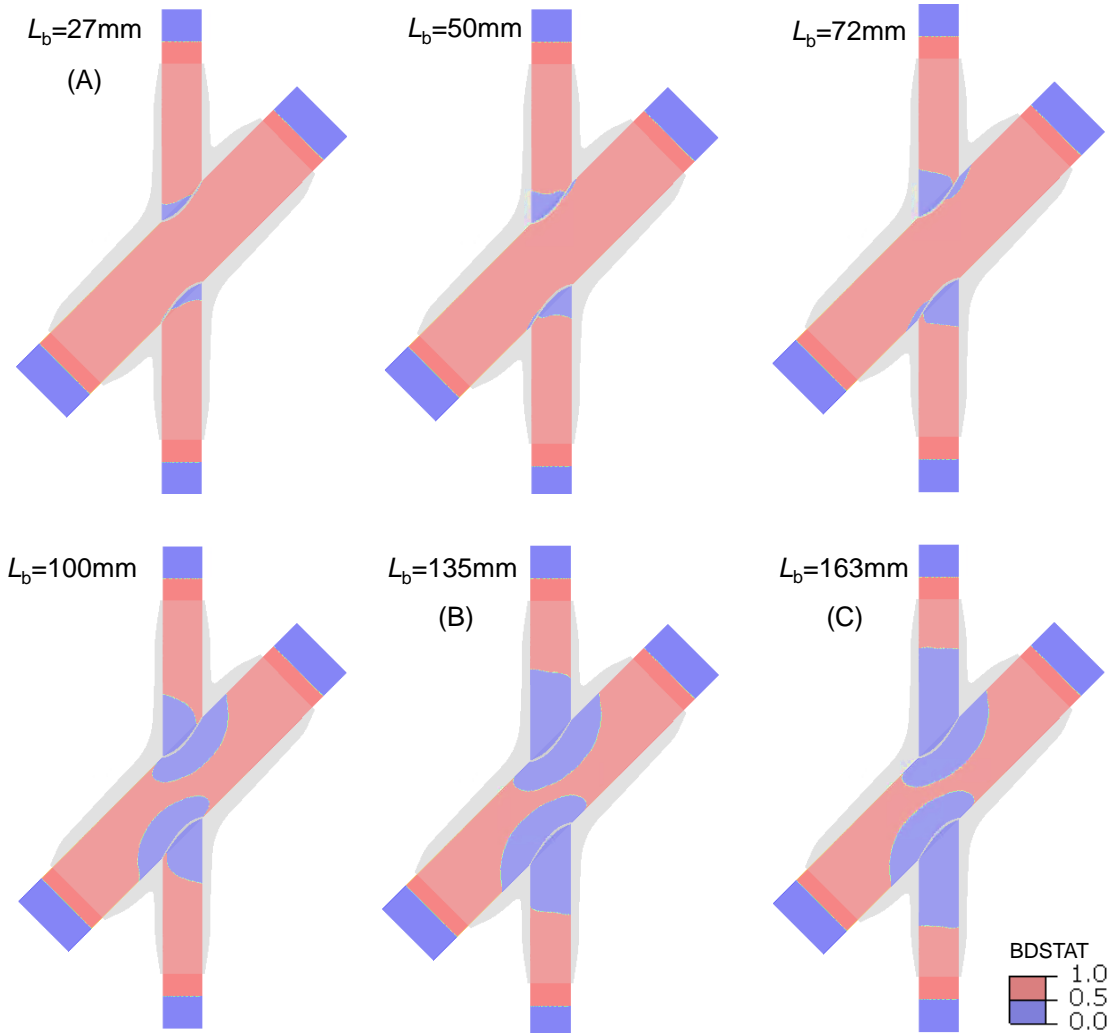


Fig. 6-10 Debonding crack pattern at different loading stages (elastic model)

Step 2: run models with artificially replicated crack patterns

In order to predict the crack growth at the interface, the crack growth driving forces, namely the SERR values at the crack fronts, need to be obtained. Artificially replicated crack patterns

are created on the chord and braces based on the static modelling results as shown in Fig. 6-11. It should be noted from Fig. 6-11 that the crack shape on the chord is assumed as a semi-circle around the intersection between the chord and brace for any crack length for simplification, even though it initiates around the sharp corner. Furthermore, the relationship between L_b and L_c under cyclic loading may be different from those under static loading, since the crack driving mechanisms are different, with one determined by the fracture toughness while the other controlled by the FCG model. On the other hand, the SERR distribution on the crack fronts of the chord may be influenced by the crack length on the braces, and vice versa. In order to form the basis for predicting crack growth interactively on the chord and brace, a model matrix with different combinations of crack lengths on the chord and braces are created as shown in **Fig. 6-12**. A total number of $6 \times 7 = 42$ models are run for the first round, but optimised to 21 models during the following analysis. The relationship between L_b and L_c will be assumed initially and determined based on the SERRs by a iterative procedure in an algorithm.

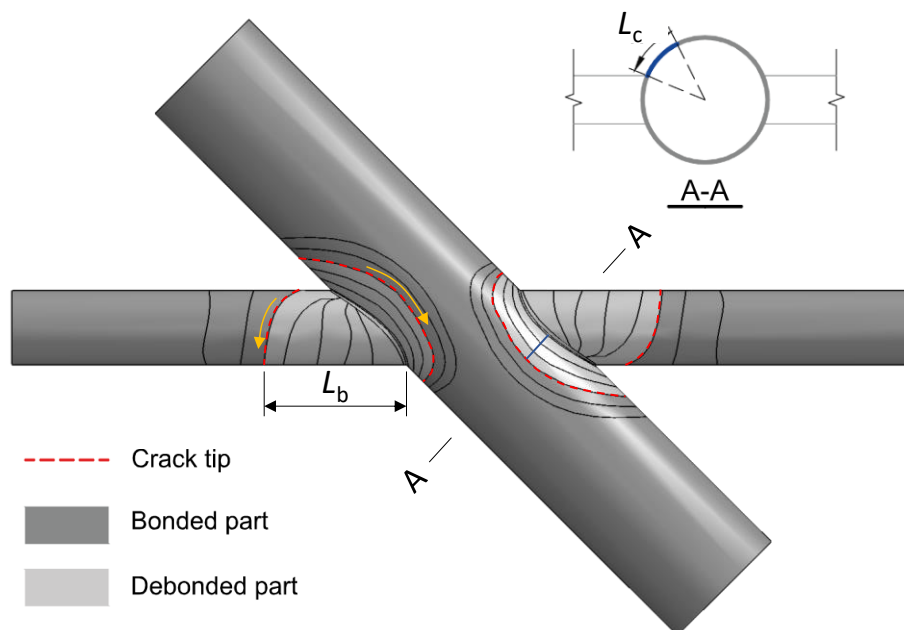


Fig. 6-11 Artificially replicated crack pattern in the FE model

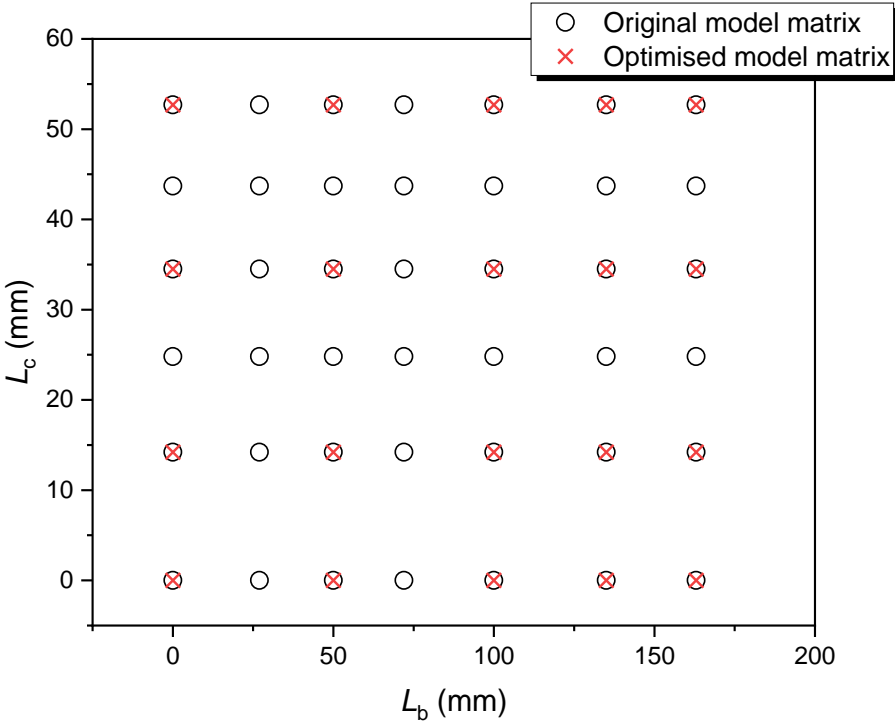


Fig. 6-12 Model matrix

Step 3: extract SERR values at the crack fronts and form the SERR surface

SERR values of different fracture modes are extracted at crack fronts for different models. Typical SERR distributions along the crack fronts of 4 extreme combinations of crack lengths on the chord and braces of small scale joint, L_{c_min} - L_{b_min} , L_{c_min} - L_{b_max} , L_{c_max} - L_{b_min} , L_{c_max} - L_{b_max} , are shown in Fig. 6-13. It can be found out that the shear fracture mode dominates the crack growth both on the chord and braces, namely the mode I SERR component is limited. Specifically, the mode II fracture behaviour dominates the crack growth on the brace, although a small portion of mode III SERR component is also found when the L_b is small. On the chord, however, equivalent amount of mode II and mode III SERR components arise at the crack tips regardless the crack length. It should be noted that the mode III SERR, which is due to out-of-plane shear behaviour at the interface, may arise due to simplified semi-circle crack shapes on the chord. It is also proved in literature that the crack growth rates can be more than 2 orders of magnitude lower due to existence of mode III SERR [175,176] compared to the mode II dominated case. For simplification and also for a conservative prediction, only the mode II SERR components are considered during the following analysis.

Normally crack growth at a specific location should be driven by the SERR values at the corresponding point [174]. However, the simplified crack shapes may cause unrealistic SERR values at the point where the crack length is defined. An effective SERR value is defined as follows, shown in Fig. 6-14. Such an integral approach is used to consider the fact that each point at the crack tip cannot grow independently and will be influenced by the adjacent portions. In this definition, the SERRs are averaged in a region where the value is above the crack growth threshold (the pink region in Fig. 6-14). The third method is simply averaging the SERR along

the entire crack tip. The following analysis adopts the effective SERR method. A sensitivity analysis on the SERR definition method will be conducted in section 6.3.3.

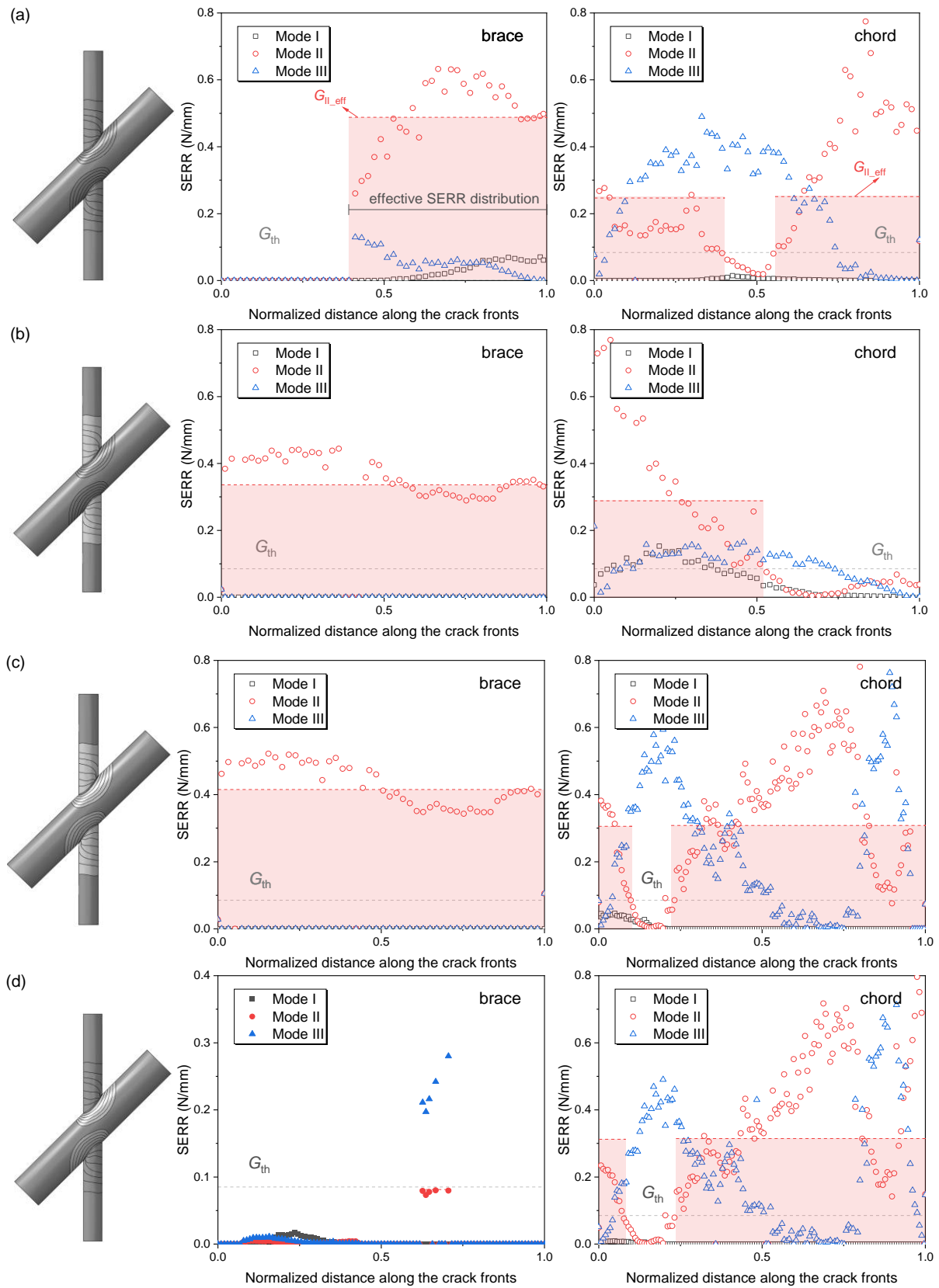


Fig. 6-13 SERR components and distribution along crack fronts on the chord and braces (a) $L_{c_min} - L_{b_min}$; (b) $L_{c_min} - L_{b_max}$; (c) $L_{c_max} - L_{b_min}$; (d) $L_{c_max} - L_{b_max}$

The effective SERR variation on the brace and chord under different crack length combinations at the load level of 165kN is shown in Fig. 6-14. In this figure, the SERR surface is formed by interpolation among the discrete points (red points) obtained from each model. The spline interpolation method is used here and the sensitivity analysis on the interpolation method will be discussed in section 6.3.3. Fig. 6-14 (a) shows that the effective SERR on the brace is mainly influenced by L_b , whereas the influence from L_c is limited to the case when L_b is small. Fig. 6-14 (b) shows that the effective SERR on the chord is mainly influenced by L_c while influence from L_b is minimal. The variation of SERR is caused by several parameters such as the thickness of the composite wrap, friction at the interface, effective length on the crack tip for averaging the SERR values, et al. For instance, a larger crack length corresponds to thinner composite wrap and more significant friction effect. A thinner composite can lead to increased SERR values whereas more friction effect may lead to reduced SERR values. It should be noted that some crack length combinations doesn't exist actually but a certain crack growth relationship between L_b and L_c needs to be determined in the following steps.

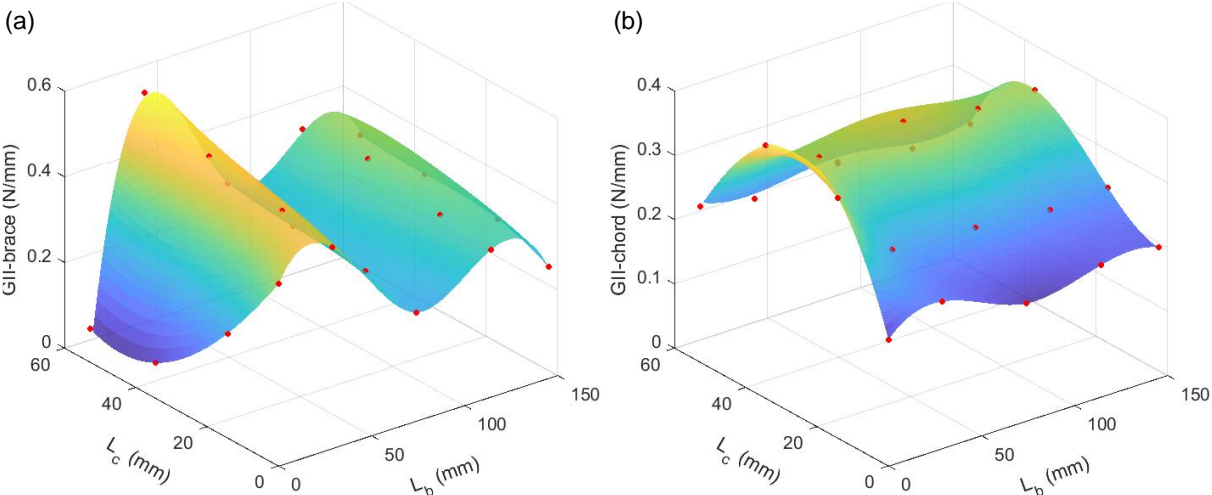


Fig. 6-14 Mode II SERR surface of the chord and brace for small scale X45 joint model at 165 kN (a) G_{II} on the brace; (b) G_{II} on the chord

Step 4: Selection of FCG curves and prediction of L_b and L_c

After obtaining the SERR surface, the next step is to predict the crack growth on the brace and chord in an algorithm with an iterative procedure as shown in Fig. 6-7. The FCG curve needs to be determined based on characterisation results in Chapter 3 and interpolated according to the roughness measurement results on the surface of the steel tubes. One typical FCG curve interpolation result is illustrated in Fig. 6-15, where Fig. 6-15 (a) shows the basic Paris curves and Fig. 6-15 (b) shows the total life FCG curves used for small scale joints with high roughness level (F3 series). In the basic Paris curves, the exponent C parameter is obtained by substituting the measured roughness parameter S_q into Eq. (3-15) based on the FEA results shown in Fig. 3-26. In the total life FCG curves, the fracture toughness G_c is obtained by substituting S_q into Eq. (3-12) based on the FEA results shown in Fig.3-17. The SERR threshold G_{th} is assumed to be

a portion of G_c . The portion of G_{th} and the curvature exponent D_1 and D_2 parameters will be calibrated by comparing the simulated stiffness degradation of the joint with the test results. A sensitivity analysis on these two parameters, G_{th} and D_1/D_2 , is conducted in section 6.3.3.

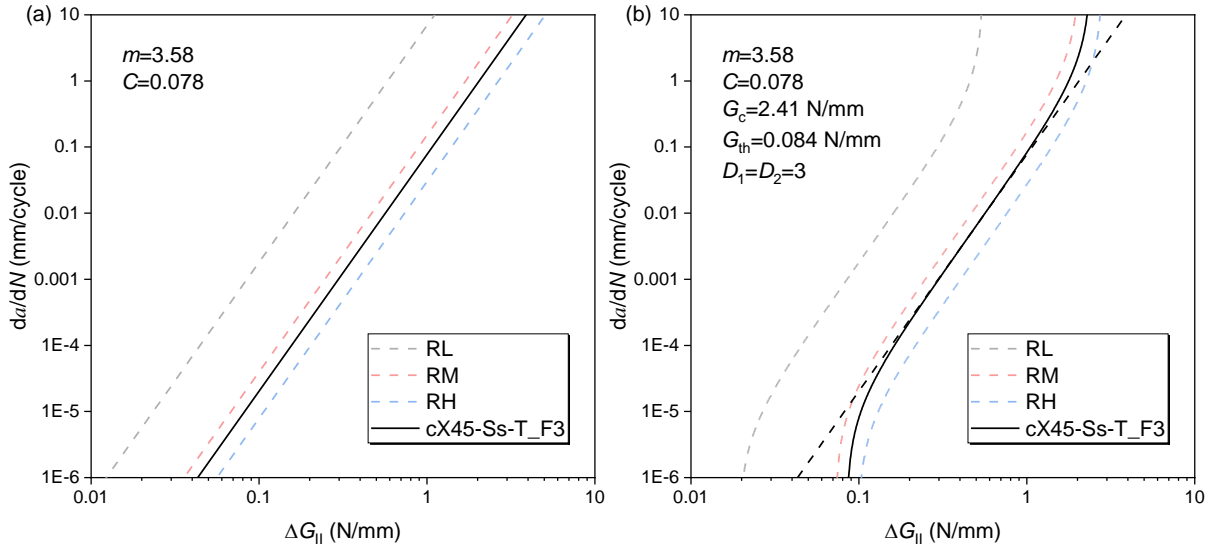


Fig. 6-15 Extrapolation of FCG curves between different roughness series (a) Paris curves; (b) total life FCG curves

An arbitrary relationship between L_b and L_c is assumed in the beginning of the iterative procedure as shown in Fig. 6-16 (a). The number of cycles needed for crack growth on the brace and chord is calculated respectively by numerically integrating the FCG equation (either Eq. 3-12 or Eq. 3-14), based on the SERR values corresponding to each point on the assumed relationship. The numerical integration of the basic Paris equation and total life FCG equation is shown below:

$$N_i = \sum_0^i \Delta N_i = \sum_0^i \frac{\Delta a}{C(\Delta G_{II,i})^m} \tag{6-2}$$

$$N_i = \sum_0^i \Delta N_i = \sum_0^i \frac{\Delta a \left[1 - \left(\frac{\Delta G_{II,i}}{G_c} \right)^{D_1} \right]}{C(\Delta G_{II,i})^m \left[1 - \left(\frac{G_{th}}{\Delta G_{II,i}} \right)^{D_2} \right]} \tag{6-3}$$

where N_i represents the number of cycles needed for crack growth on the chord or brace to the i th discrete point in the L_b vs. L_c curve. It is obtained by summing ΔN_i , the number of cycles needed for crack growth within a unit crack length Δa (1 mm in this case), from 0 mm to the current crack length. $\Delta G_{II,i}$ represents the SERR values on the chord or brace at the corresponding crack length. A new relationship between L_b and L_c is obtained based on the cycle calculation. The whole procedure is iterated until the relationship between L_b and L_c is stabilised.

The example of stabilised relationship between L_b and L_c is plotted together with the SERR surfaces of the brace and chord in Fig. 6-16 (b). This figure can clearly show the competing of crack growth on the brace and chord driven by the SERR values. In the beginning, where L_b and L_c are near 0 mm, G_{II} on the brace is higher, thus leading to dominated crack growth on the brace. The crack growth on the chord becomes dominated as the G_{II} on the chord increases and G_{II} on the brace decreases around $L_b \approx 110$ mm and $L_c \approx 30$ mm. After that crack growth on the brace becomes faster again due to variation of the SERR.

Based on the obtained relationship between L_b and L_c , the stiffness degradation of the joint can be calculated. The modelling results will be shown in the next section.

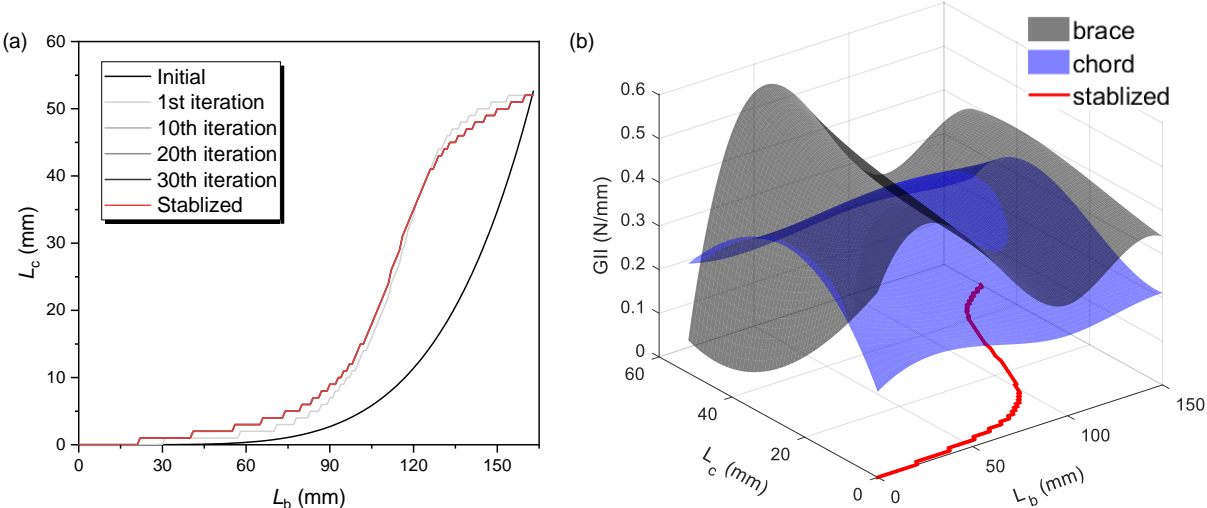


Fig. 6-16 Iteration of relationship between L_b and L_c (a) iteration procedure; (b) the stabilized relationship plotted with SERR surface

6.4.2 Model calibration based on joint experiments

The test matrix for calibrating the FE model is shown in Table 6-3. A total of 4 series are included, namely (a) small scale joints with high roughness under 10-110 kN, (b) small scale joints with high roughness under 15-165 kN, (c) small scale joints with low roughness under 15-165 kN, and (d) middle scale joints with high roughness under 30-330 kN. The average roughness of the surface of steel tubes for each series of the specimens are listed in this table.

Table 6-3 Test matrix for model calibration

Geometry	Scale	S_q (μm)	Load range (kN)	series
X45	Small scale	16.78	10-110	(a)
		10.98	15-165	(b)
	Middle scale	10.98	15-165	(c)
		22.07	30-330	(d)

In this section, calibrated results with the optimised combination of the modelling parameters (underlined in Table 6-5) are shown. Sensitivity studies for each parameter will be discussed in the next section.

6.3.2.1 Crack propagation

Based on the average measured roughness in Table 6-3, the FCG curves are interpolated for each specimen series and the results are shown in Fig. 6-17.

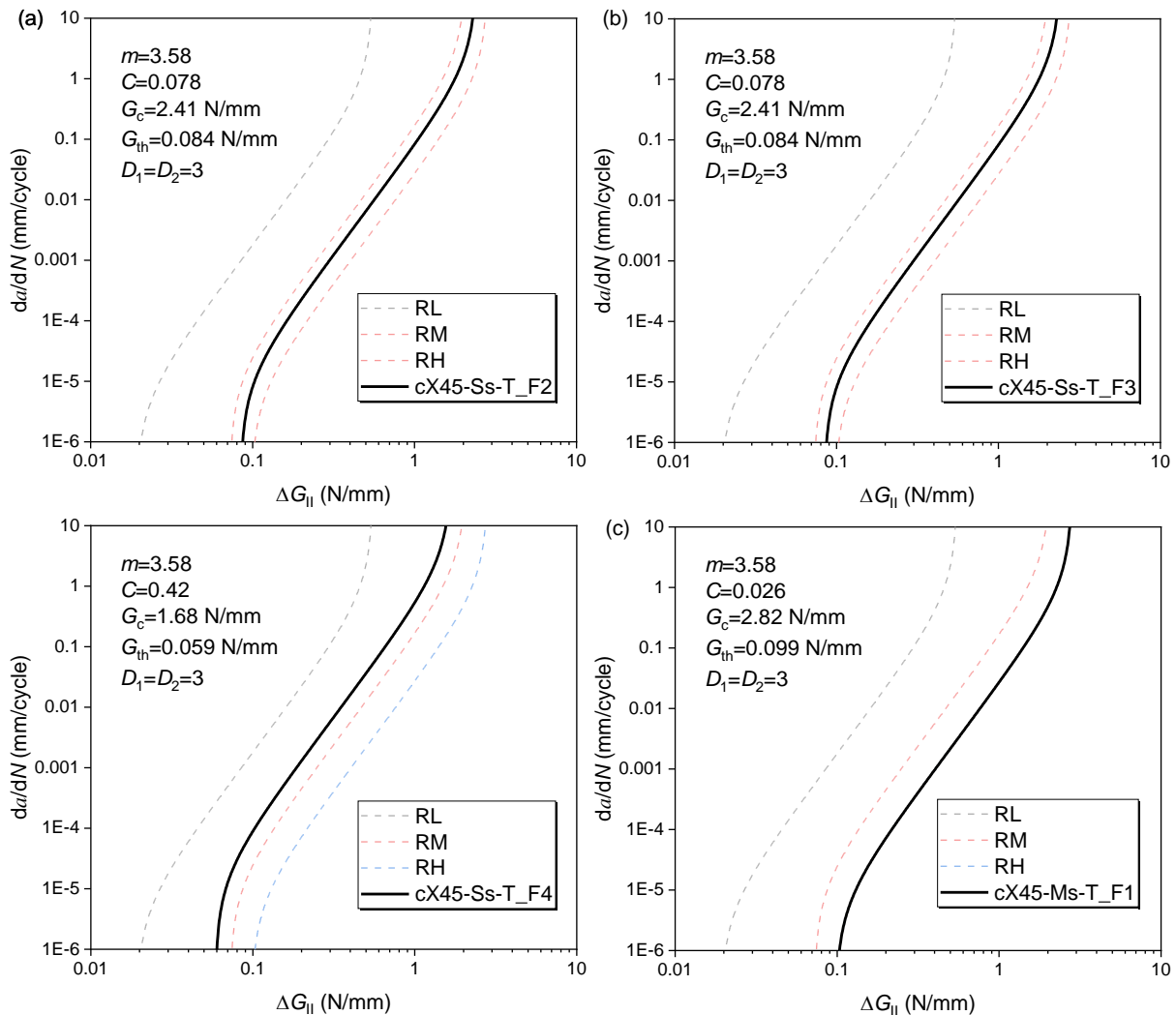


Fig. 6-17 Obtaining total fatigue life model parameters for different roughness series (a) small scale joints high roughness; (b) small scale joint low roughness; (c) middle scale joints

SERR surfaces on the brace and chord for each series are shown in Fig. 6-18. It shows that the variation trends of SERR under different geometries and load levels are generally the same on the brace and chord respectively, but the magnitudes vary for each case. Since the load level influences the crack patterns on the chord and braces, as well as the contraction of the composite wrap, the SERR values in case (b) do not increase proportionally as the load increases compared to case (a), although all materials are in elastic stage. The stabilised relationships between L_b and L_c are also shown in the same figure. It can be seen that under relatively low load level (case a and d), crack at the interface mainly grows on the brace, whereas crack on the chord remains undeveloped (L_b for the middle scale joints only grows until 150 mm). On the contrary, cracks on the chord and brace grows simultaneously under relatively higher load levels (case b

and c). It should be noted that the roughness level will not influence the SERR distribution at the interface if the load level keeps the same. So Fig. 6-18 (b) and (c) are totally the same.

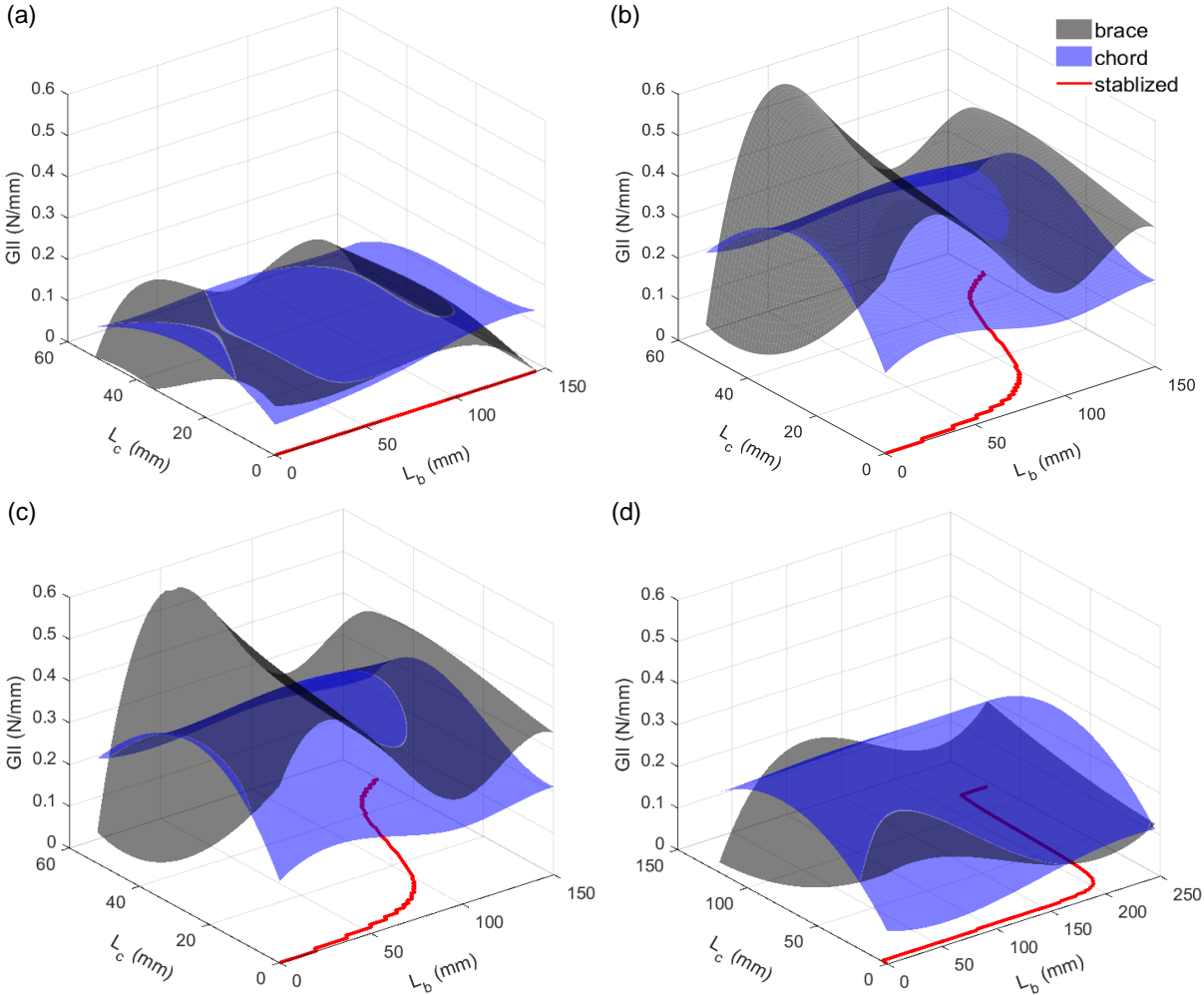


Fig. 6-18 SERR surface and stabilized relationship between L_b and L_c (a) small scale joints with high roughness under 10-110kN; (b) small scale joints with high roughness under 15-165kN; (c) small scale joints with low roughness under 15-165kN; (d) middle scale joints with high roughness under 30-330kN;

Crack growths on the braces of each series of specimens modelled by the FE model are plotted against the test results in Fig. 6-19, which are obtained by DIC analysis in Chapter 5. The figure shows that the FEA results overlap well with the test results for most of the cases, especially at the early loading stages. However, cracks grew with different rates on the top and bottom braces during the tests as discussed in Chapter 5 and also shown in Fig. 6-19 (b), where the FEA results deviate significantly from the test results after 35,000 cycles. This difference may be caused by different interface conditions, such as roughness, defects et al. in different braces, which cannot be considered in the FE model. Test results of middle scale joints were not obtained due to the relatively low load levels thus limited crack growth and scattered strain variations as shown in Fig. 5-25.

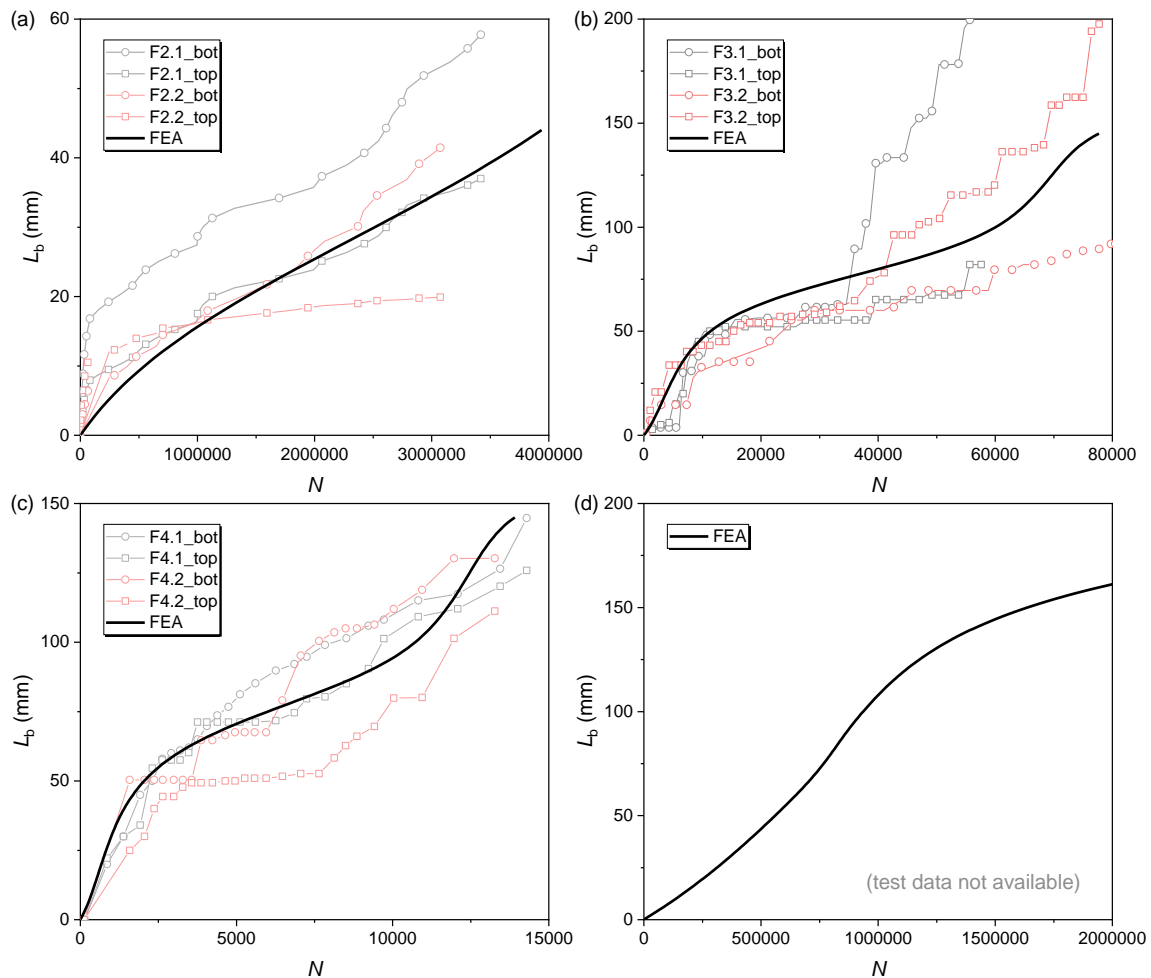


Fig. 6-19 Comparison of crack growth on the brace between test results and FEA (a) small scale joints with high roughness under 10-110kN; (b) small scale joints with high roughness under 15-165kN; (c) small scale joints with low roughness under 15-165kN; (d) middle scale joints with high roughness under 30-330kN;

6.3.2.2 Stiffness degradation

Stiffness degradations of each series of specimens obtained by FE model are plotted against the test results in Fig. 6-20. The comparison shows that the FEA results generally match well with the test results. A more quantitative comparison between the FEA and average test results is conducted in terms of fatigue lives under different failure criteria, namely 10%, 20% and 40% of stiffness degradation, in Table 6-4. It shows that the FEA results can well reproduce the test results with the error (in linear scale) less than 20% and can be as small as -0.04% for small scale joints with high roughness except for case (a), whose error is around -35%. This is because that one of the tested specimen in case (a) has not reached the failure criterion of 10%. The number of cycles is extrapolated based on the stiffness degradation rate. However, the simulated fatigue life of small scale joints with low roughness underestimates the test results under the failure criterion of 10% and overestimates the test results under failure criterion of 20% and 40% with the errors more than 30%. This difference can also be reflected by the deviation of the

stiffness degradation curves in Fig. 6-20 (c). It should be noted that the variation of the stiffness degradation can be influenced by the surface conditions of the steel tubes, thickness of the composite wrap and possibly the temperature variation during the fatigue test, et al.. Meanwhile, the stiffness degradation trend obtained by FEA is driven by the SERR variation shown in Fig. 6-18, which cannot take the such influential factors into account. When expressed in the logarithmic space, the errors are much better and within only 5% for all of the cases.

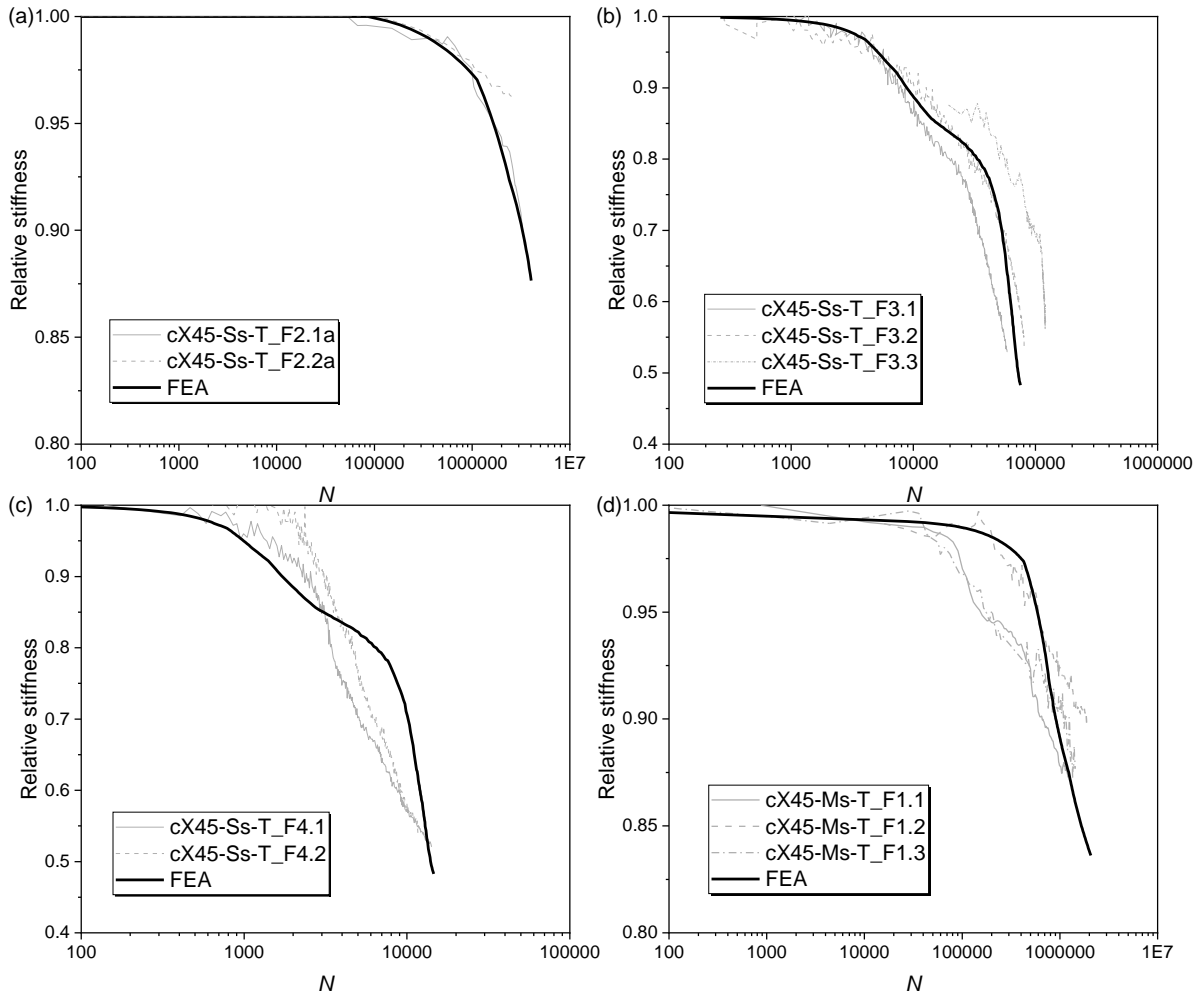


Fig. 6-20 Comparison of stiffness degradation between test results and FEA (a) small scale joints with high roughness under 10-110kN; (b) small scale joints with high roughness under 15-165kN; (c) small scale joints with low roughness under 15-165kN; (d) middle scale joints with high roughness under 30-330kN;

Table 6-4 Difference between the experimental and numerical fatigue life

Failure criterion	Case	Average experimental fatigue life (cycles)	Numerical fatigue life (cycles)	Error (linear scale)	Error (logarithmic scale)
10%	(a)	4920571	3167876	-35.62%	-2.86%

10%	(b)	8515	8512	-0.04%	0.00%
	(c)	2690	1700	-36.81%	-5.81%
	(d)	1214768	906221	-25.40%	-2.09%
20%	(b)	34280	31174	-9.06%	-0.91%
	(c)	3923	5836	48.76%	4.80%
40%	(b)	78756	62352	-20.83%	-2.07%
	(c)	8689	11829	36.14%	3.40%

More detailed comparison between FEA results against test results in terms of fatigue lives are conducted by taking every 1% stiffness degradation (from 1% to 40% for high load level, from 1% to 10% for low load level) as failure criterions shown in Fig. 6-21. The figure shows that the relative error of the two in the logarithmic space is within 20% for all the cases. The coefficient of determinations expressed in Eq. (6-4) are higher than 0.8 except for the case of small scale joints with low roughness level, where the stiffness degradation trends from test and FEA results are different as mentioned above.

$$R^2 = 1 - \frac{\sum_i (y_i - f_i)^2}{\sum_i (y_i - \bar{y})^2} \quad (6-4)$$

where y_i is the test results, \bar{y} is the average value of the test results and f_i is the modelling results.

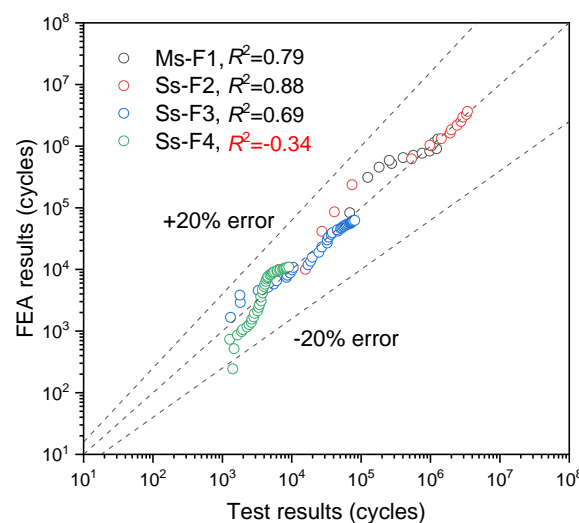


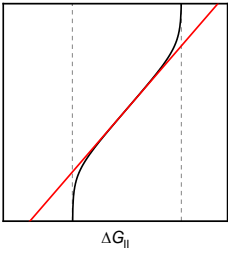
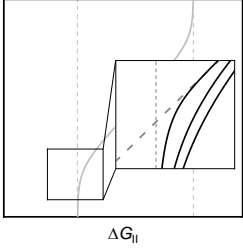
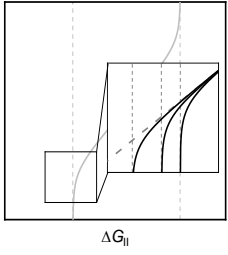
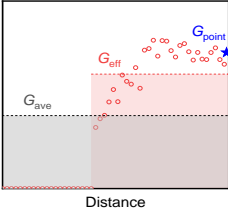
Fig. 6-21 Comparison of fatigue lives under different failure criterion between test and FEA results

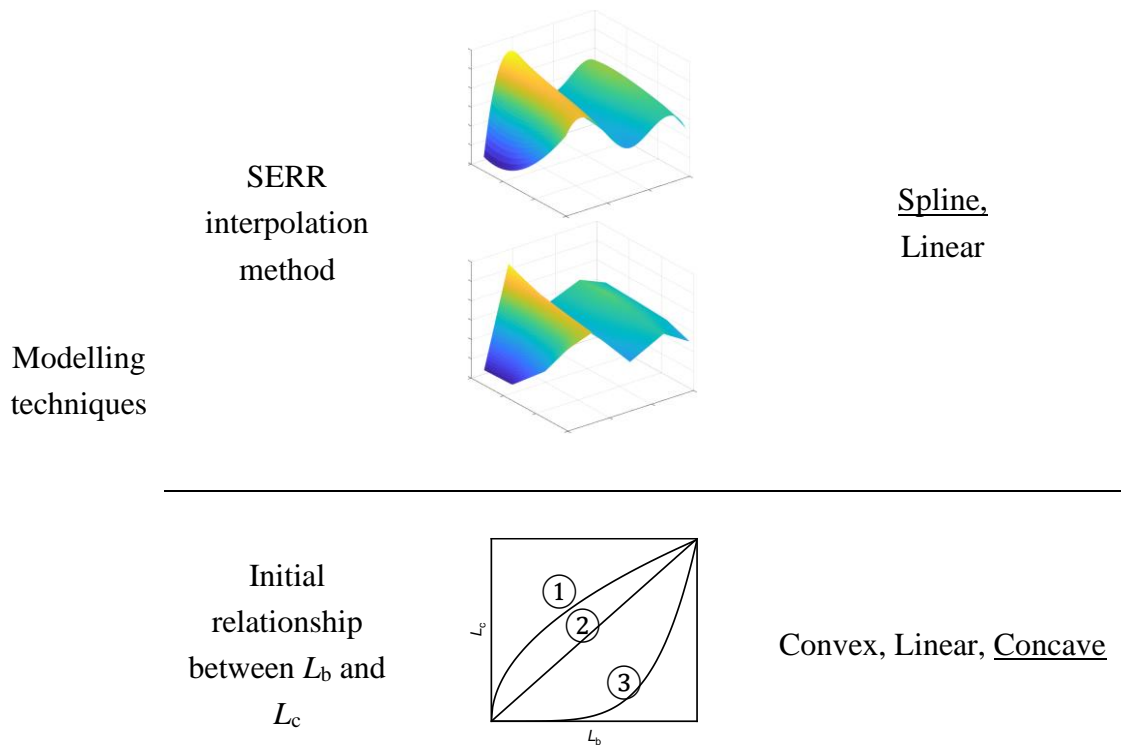
6.4.3 Sensitivity analysis on modelling parameters

While FEA results match well with the test results based on the optimised combination of parameters, each parameter can have significant or insignificant influence of the modelling results. Sensitivity analysis on each key modelling parameter is conducted in this section to investigate its influence and rationalize the choice of the optimised value.

Investigated parameters are divided into two categories, namely the input FCG parameters and the modelling techniques, with the definitions and ranges of each parameter shown in Table 6-5.

Table 6-5 Parameter matrix for sensitivity analysis

Type	Parameter	Sketch	Value
	FCG model		Paris curve, <u>Total life FCG</u>
Input FCG parameters	Curvature exponent, <i>D</i>		<u>3</u> , 5, 7
	Threshold SERR, <i>G_{th}</i>		1% <i>G_c</i> , <u>3% <i>G_c</i></u> , 5% <i>G_c</i>
Modelling techniques	Equivalent SERR		<i>G_{ave}</i> , <u><i>G_{eff}</i></u> , <i>G_{point}</i>



Note: the reference values adopted in 6.3.2 are underlined

6.3.3.1 Influence of FCG model

While the basic power function model (Paris curve) fits well with the results of 4ENF test, it has the limitation of considering the threshold behaviour of the fatigue crack growth curves. A total life FCG model was proposed in the end of Chapter 3. The comparison between these two models is shown in this section. Modelling results of small scale joints with high roughness level but under different load levels are compared. Fig. 6-22 shows the Paris curve and the best tuned FCG model together with the SERR ranges experienced by the joint under two different load levels according to the SERR surfaces. It shows that the SERR range is between 0.2-0.5 N/mm under 15-165kN, where two FCG models overlap with each other. Whereas the SERR range is around G_{th} , between 0.075-0.15N/mm, under 10-110kN, where the Paris curve is above the total life FCG model.

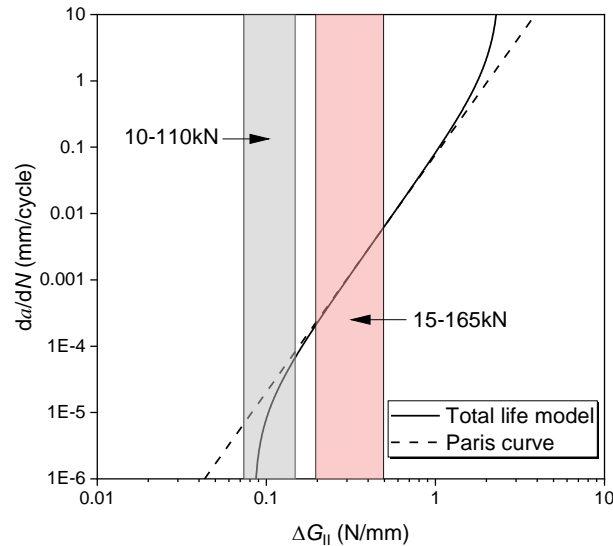


Fig. 6-22 Comparison of SERR range under 10-110kN and 15-165kN for small scale joints

Fig. 6-23 shows the modelling and test results of the joint under 15-165kN. The difference of modelling results, namely the crack growth and stiffness degradation, based on the Paris curve and total life FCG model, is insignificant. Both results match well with the test results due to the fact that two FCG models overlap in this SERR range. However, modelling results based on these two models are significantly different under 10-110kN as shown in Fig. 6-24. The crack growth and stiffness degradation is overestimated thus shorter fatigue life is obtained by using the Paris curves, while modelling results based on the total life FCG model match well with the test results. This is due to the fact that the Paris curve is above the total life FCG model around the relatively low SERR range thus the crack growth rates are overestimated.

Considering the fact that using Paris curves may overestimate the crack growth when the SERR level is near the threshold, the total life FCG model is adopted in the following analysis.

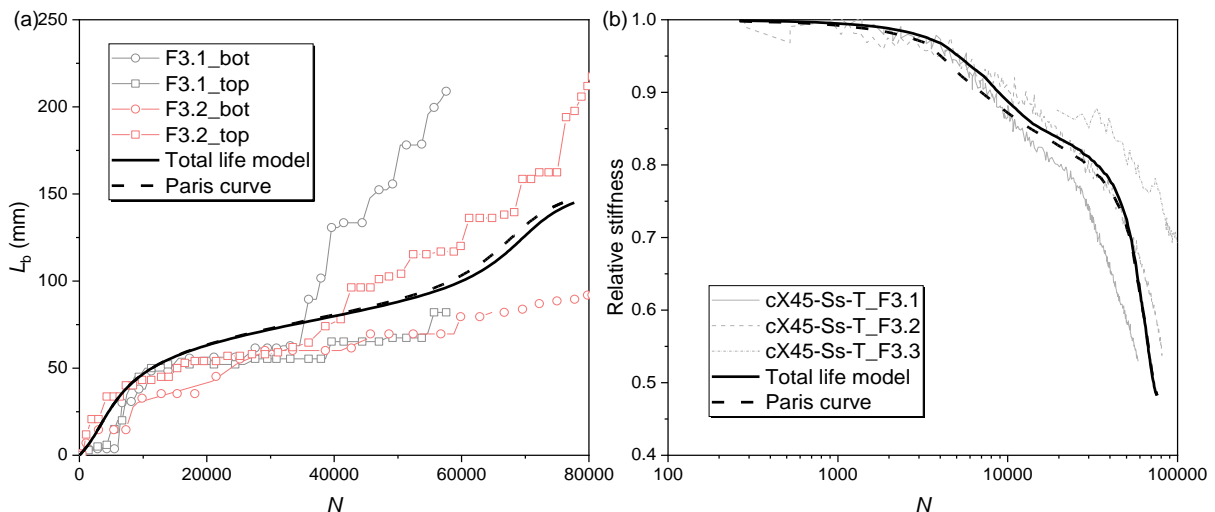


Fig. 6-23 Comparison between modelling results by total life model and Paris curves on small scale joints under 15-165kN (a) crack growth; (b) stiffness degradation

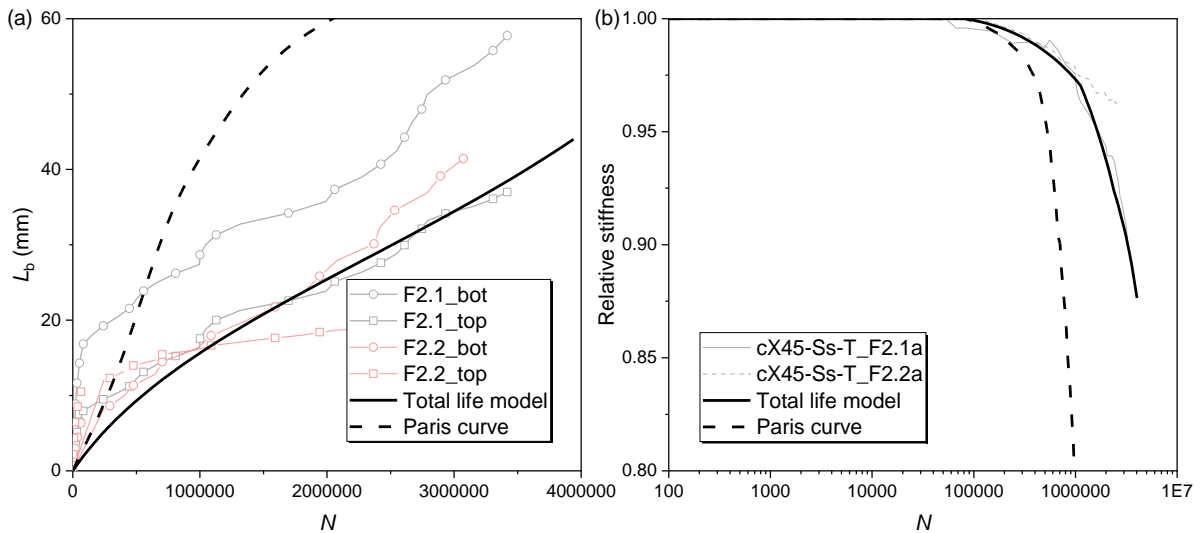


Fig. 6-24 Comparison between modelling results by total life model and Paris curves on small scale joints under 10-110kN (a) crack growth; (b) stiffness degradation

6.3.3.2 Influence of curvature exponent D and SERR threshold

It has been shown from the previous section that the total life FCG model can well reproduce the test results in terms of crack growth and stiffness degradation for the case where SERR range is near the threshold G_{th} . However, the matching quality still depends on the curvature of the FCG curve in the subcritical region, which is determined by the curvature exponent D and threshold ratio G_{th}/G_c . As shown in Fig. 6-25 (a), the total life FCG model becomes closer to the power function, leading to higher crack growth rates, in the threshold region as D increases. Meanwhile, as shown in Fig. 6-25 (b), the total life FCG model becomes further away from the power function, leading to lower crack growth rates, in the threshold region as G_{th} increases. A sensitivity study is conducted in this section to find the optimal combination of these two parameters, which can help reproduce test results for all the cases.

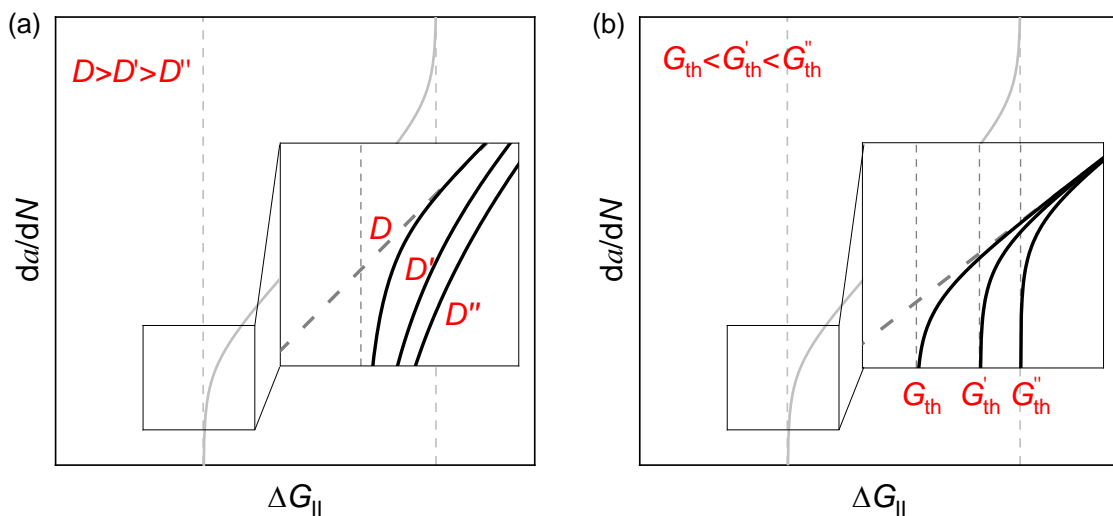


Fig. 6-25 Influence of (a) curvature exponent D and (b) threshold G_{th} on the shape of total life FCG model

It has been confirmed from Chapter 3 that the curvature exponent D above 3 can lead to the same fitting quality for the ENF test data as that based on the power function. Meanwhile, the threshold ratio can be 1%-9% according to the literature and limited by the current test data. D values of 3, 5, 7 in combination with the threshold ratios of 1%, 3%, 5% are adopted to investigate their influence on the modelling results of stiffness degradation of the joint. The optimal combination of these two should lead to relatively good matching quality for all the 4 test cases. The matching quality of the modelling results with the test data is evaluated by the coefficient of determination, R^2 , which is obtained by comparing the fatigue lives using different failure criteria as shown in Eq.(6-4) and Fig. 6-21.

The R^2 values for all the 4 test cases using different combinations of D and G_{th}/G_c are shown in Fig. 6-26 (a). R^2 values below 0 are shown as equal to 0. It can be seen that the matching quality for the Ss-F3 series (small scale joints with high roughness under 15-165kN) and Ms-F1 series (middle scale joints with high roughness under 30-330kN) is always above 0.7 even 0.9 regardless of the combination of the two parameters. This is due to the fact that the SERR values experienced by these two joint during the test are in the range where the total life FCG model overlaps with the power function. The curvature of the total life FCG model near the threshold will not influence the crack growth rate in that region. On the contrary, the matching quality for the Ss-F4 series (small scale joints with low roughness under 15-165kN) is always bad (below 0) due to the different variation trends between the test data and modelling results as discussed in section 6.3.2.2. The only test case which is rather sensitive to the D and G_{th}/G_c values is the Ss-F2 series (small scale joints with high roughness under 10-110kN), who experienced the SERR range between 0.075-0.15N/mm during the test as shown in Fig. 6-22. Any deviation of the ratio G_{th}/G_c away from (higher or lower than) 3% can lead to R^2 below 0. Meanwhile, the matching quality may deteriorate as the D value increases from 3 to 7.

In order to evaluate the overall matching quality for all the test cases, an equivalent R^2 , which is the geometric mean value for 3 test cases (Ss-F4 series is excluded considering the mismatch of stiffness degradation trend) expressed in Eq. (6-5) is adopted:

$$R_{eq}^2 = \sqrt[3]{R_1^2 R_2^2 R_3^2} \quad (6-5)$$

where R_1^2, R_2^2, R_3^2 are the coefficients of determination for Ss-F2, Ss-F4 and Ms-F1 series, respectively. As shown in Fig. 6-26 (b), the combination of $D=3$ and $G_{th}/G_c=3\%$ gives the best matching quality ($R_{eq}^2 > 0.75$) for all the test cases, which will be adopted for the remaining analysis. A small deviation of G_{th}/G_c , e.g. 3.2% or 2.8%, may produce better overall fitting quality but will not be further studied in the current study.

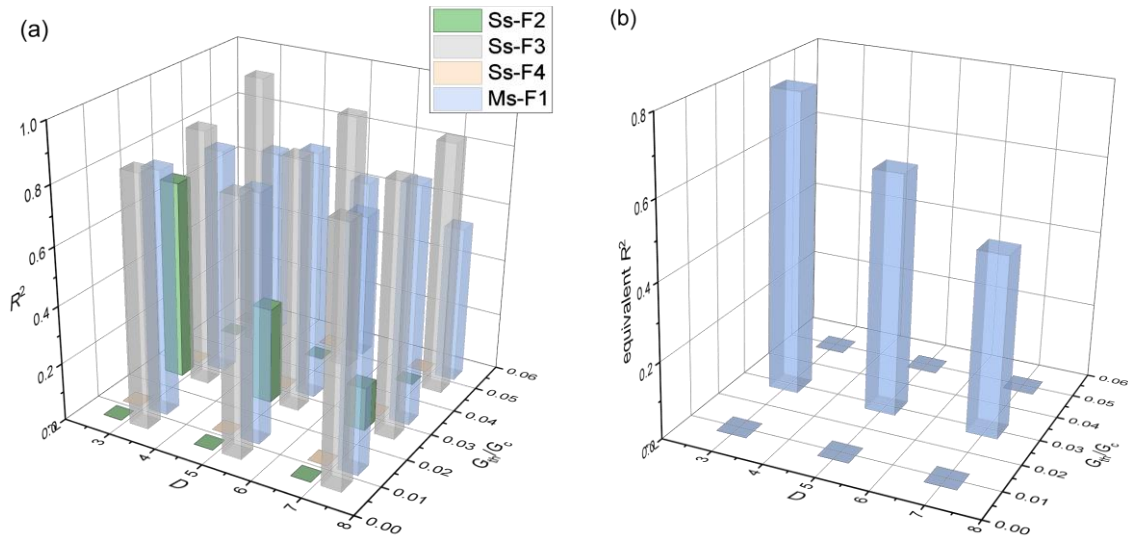


Fig. 6-26 Coefficient of determination (R^2) versus threshold ratio and curvature exponent D
 (a) R^2 of each case; (b) equivalent R^2 of all cases

6.3.3.3 Influence of equivalent SERR defining method

As the driving mechanism for crack growth at the interface, it is crucial to choose appropriate SERR values at the crack tip. Whereas the SERR distribution along the crack tip is influenced by the crack shapes, which are simply created to be the same as those in monotonic failure process and simplified as semi-circles on the chord. Some unrealistic values may arise at certain locations of the crack tip. Different equivalent SERR defining methods are proposed and compared in this section. The three equivalent SERR defining methods are shown in Fig. 6-27: 1) point SERR G_{II_point} , which is the SERR value at the location where the crack length is defined; 2) effective SERR G_{II_eff} , which is the average value of SERR over the region where SERR values are above G_{th} ; 3) average SERR G_{II_ave} , which is the average value of SERR over the entire length of crack tip. For SERR distributions above G_{th} along the entire crack tip, e.g. when L_b is large enough, G_{II_eff} equals to G_{II_ave} .

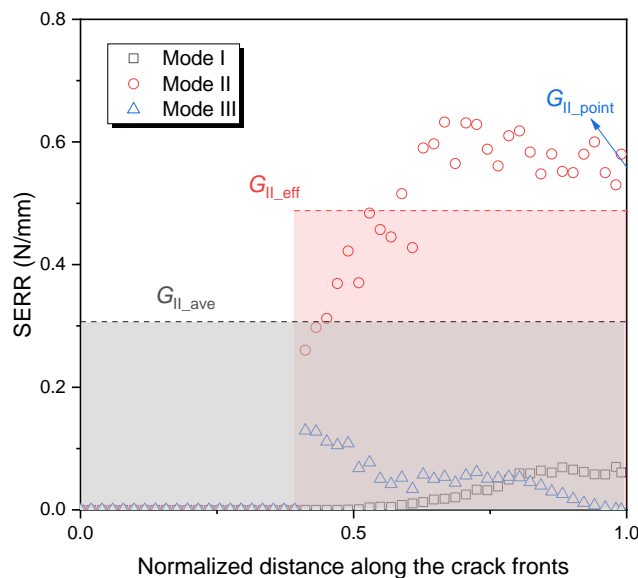
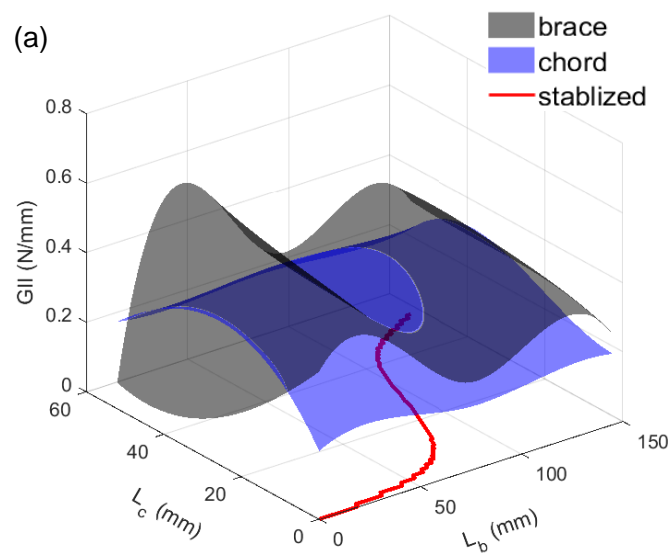


Fig. 6-27 Different equivalent methods for SERR on the brace

SERR surfaces obtained according to the three different methods for small scale joints under 15-165kN are shown in Fig. 6-28. It can be seen from Fig. 6-28 (b) that G_{II_ave} on the brace is smaller than G_{II_eff} when L_b is small, where the SERR values are not evenly distributed along the entire crack tip. On the contrary, the point SERR G_{II_point} is usually above the other two average values, thus leading to generally highest SERR surfaces both on the chord and brace as shown in Fig. 6-28 (c). Meanwhile, some zero values may arise when crack initiates on the chord and brace, namely when L_b or L_c is near zero.

Crack growth on the brace and stiffness degradation modelling based on three different equivalent SERR defining methods are compared with test results in Fig. 6-29. When adopting G_{II_ave} , crack predominantly grows on the chord due to very low SERR values when crack initiates on the brace as illustrated in Fig. 6-28 (b). This leads to too much longer crack initiation life (with limited stiffness degradation at the initial stage as shown in Fig. 6-30 (b)), and abrupt stiffness drop at later stage. When adopting G_{II_point} , on the contrary, crack predominately grows on the brace due to very low SERR values when crack initiates on the chord as illustrated in Fig. 6-28 (c). The higher point SERR values on the brace lead to more rapid crack growth thus early stiffness degradation as shown in Fig. 6-30 (b).

In general, the effective SERR method can well reproduce the crack growth on the brace and stiffness degradation as test results. It not only works well for the case of small scale joints with high roughness under 15-16kN, but also leads to good match with test results for other cases as shown in 6.4.2. The effective SERR method is adopted for the remaining analysis.



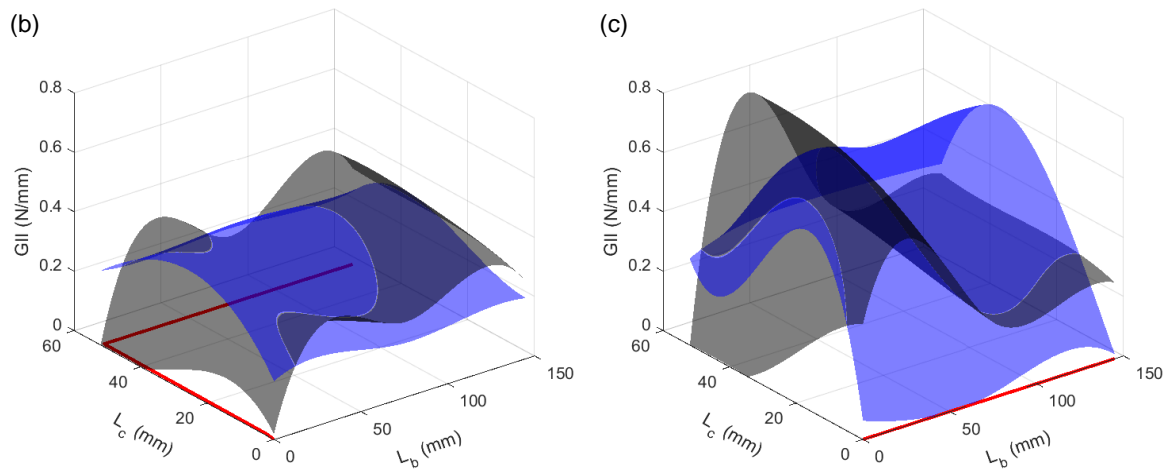


Fig. 6-28 SERR surface and stabilized relationship between L_b and L_c based on (a) effective SERR G_{II_eff} ; (b) average SERR G_{II_ave} ; (c) point SERR G_{II_point}

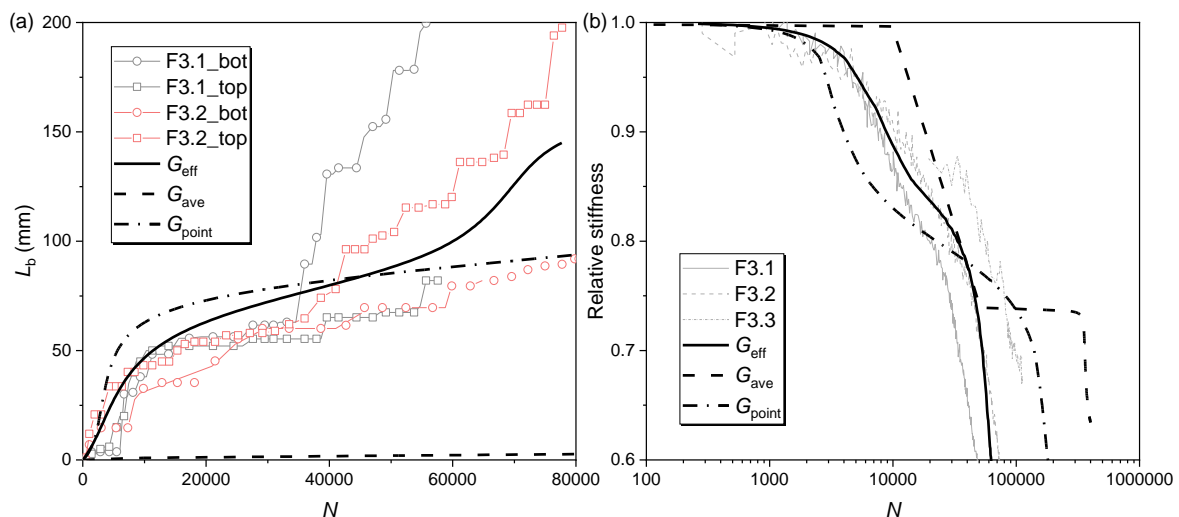


Fig. 6-29 Comparison of different SERR equivalent methods on (a) crack growth; (b) stiffness degradation

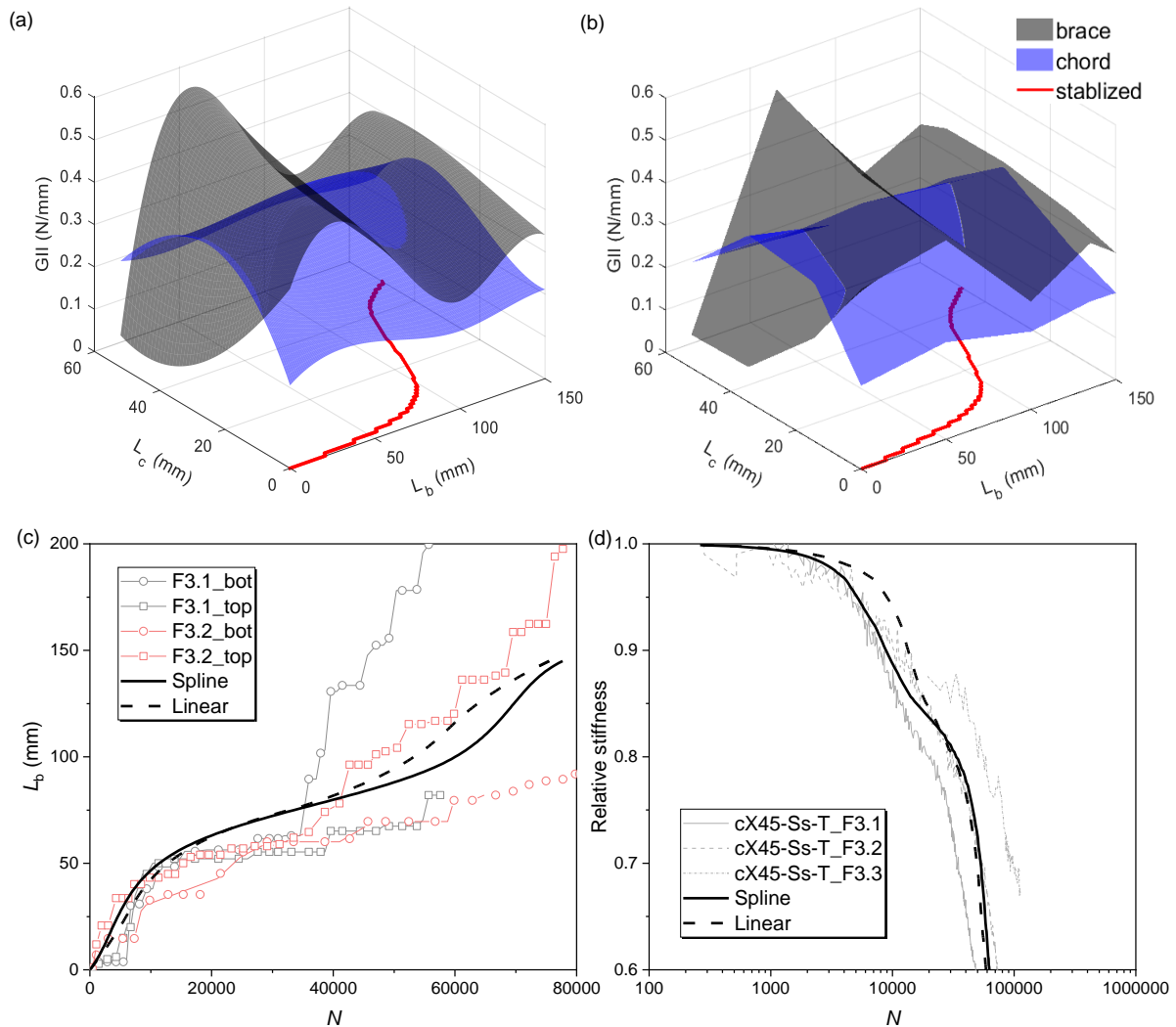
6.3.3.4 Influence of interpolation method for the SERR surface

As introduced in 6.4.1, the SERR surfaces are obtained by interpolating specific SERR values obtained from FE models in the model matrix (Fig. 6-12). The interpolating method may play an important role in determining the modelling results. Two commonly used methods, linear interpolation and cubic spline interpolation, are compared.

SERR surfaces obtained based on these two methods are shown in Fig. 6-30 (a) and (b). While smooth surfaces are obtained based on the spline method, surfaces obtained based on linear interpolation exhibit sharp edges. It shows that the stabilized relationships between L_b and L_c (the red curves) are almost identical. Modelling crack growth and stiffness degradation based on these two interpolation methods are shown in Fig. 6-30 (a) and (d). It shows that both methods match well with the test results, but the linear interpolation method slightly

underestimates crack growth and stiffness degradation in the early stage, and overestimates the crack growth and stiffness degradation at the later stages. This may be due to the fact that the linear interpolated surface underestimates the SERR values around the peak of the surface and overestimates the SERR values around the valley of the surface as shown in Fig. 6-30 (e).

Considering similar results obtained by these two interpolation methods, possible underestimation and overestimation of SERR based on linear interpolation method, and good match between modelling results and test results based on the spline method for other cases, the spline interpolation method is adopted for the remaining analysis.



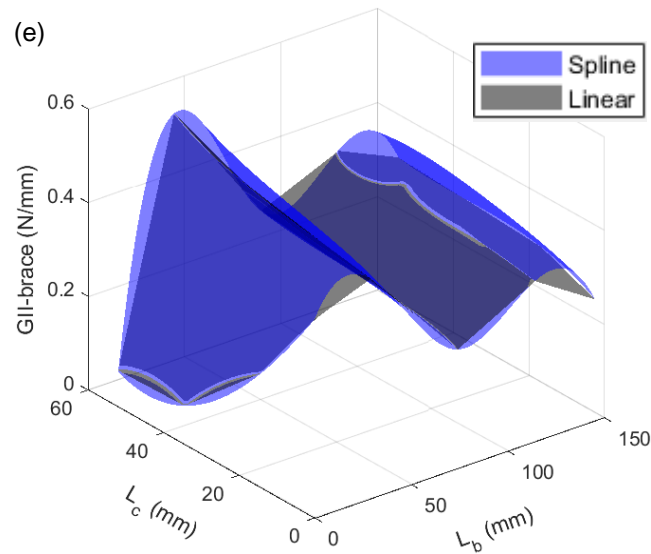
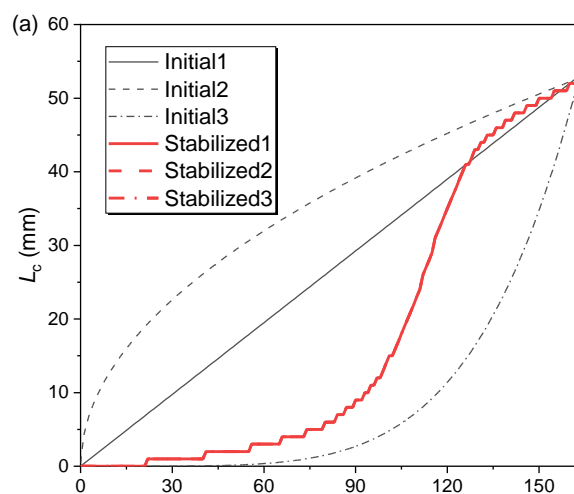


Fig. 6-30 Comparison of different interpolation methods of SERR surface (a) spline method; (b) linear method; (c) comparison of crack growth; (d) comparison of stiffness degradation; (e) comparison of SERR surfaces

6.3.3.5 Influence of initial relationship between L_b and L_c

Another modelling technique which may influence the results is the initial relationship between L_b and L_c . As shown in Fig. 6-31 (a), three arbitrary but representative initial relationships, namely linear, convex and concave shapes, are applied for modelling the fatigue debonding behaviour of small scale joints with high roughness under 15-165kN. The results show that the stabilized relationship, crack growth, as well as the stiffness degradation modelled by different initial relationships are identical to each other, indicating that the initial relationship between L_b and L_c will not influence the modelling results. The linear relationship is adopted for the remaining analysis for simplicity.



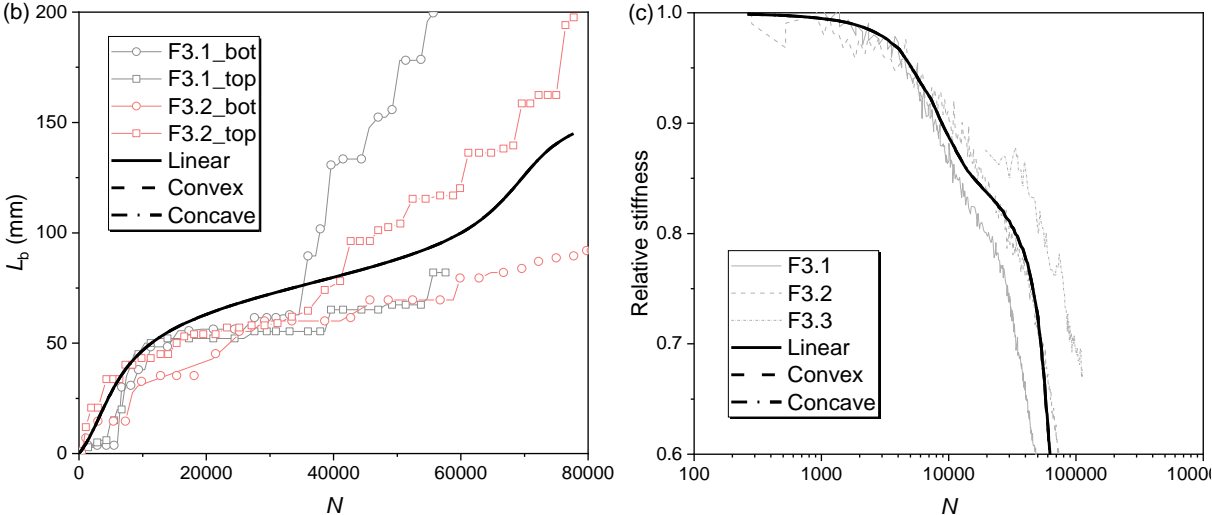


Fig. 6-31 Sensitivity study on the initial relationship between L_b and L_c (a) initial and stabilized relationship; (b) crack growth based on different initial relationships; (c) stiffness degradation based on different initial relationships

6.5 Probabilistic analysis

It has been shown in Chapter 5 that results of the cyclic tests, including stiffness degradation and crack propagation, are quiet scattering and cannot be well reproduced by the deterministic analysis. The scatter mainly comes from several factors, such as the random surface roughness of the steel tubes and fatigue crack growth properties at the bonded composite-to-steel interface. Variation of other factors such as the geometry of the specimen, material properties and some environmental effects may also contribute to this phenomenon. The study presented in this thesis is first of such kind and chooses the most critical factors, surface roughness and FCG properties, as the starting point. Other influencing factors are excluded and can be investigated in the future. A probabilistic analysis is conducted in this section to explain and reproduce the scattering test results. Explanation for each considered probabilistic parameter is discussed, followed by a Monte Carlo simulation.

6.5.1 Parameters of probabilistic distribution

- Surface roughness of steel tubes

In the deterministic analysis, the mean value of S_q for each roughness level is substituted into Eq. (3-9) and Eq. (3-13) for interpolation of fracture toughness G_c and C parameter of FCG curves. For Monte Carlo simulation, probabilistic roughness parameters are used and their distributions are determined as follows. Histogram of measurement results at different locations on the specimen as shown in Table 5-4, of each roughness series (high and low roughness level of small scale joints, high roughness level of medium scale joints) are shown in Fig. 6-32. 4 different distributions are considered here, including normal distribution, extreme value distribution, lognormal distribution and Weibull distribution. The Anderson-Darling test [177]

is used to assess the goodness-of-fit for each distribution on the measurement results. According to the Anderson-Darling test, the p -value is a critical value to do the assessment. A significance level of 5% is used in this analysis. When p -value is greater than 0.05, the results of distribution fit are considered undeniable.

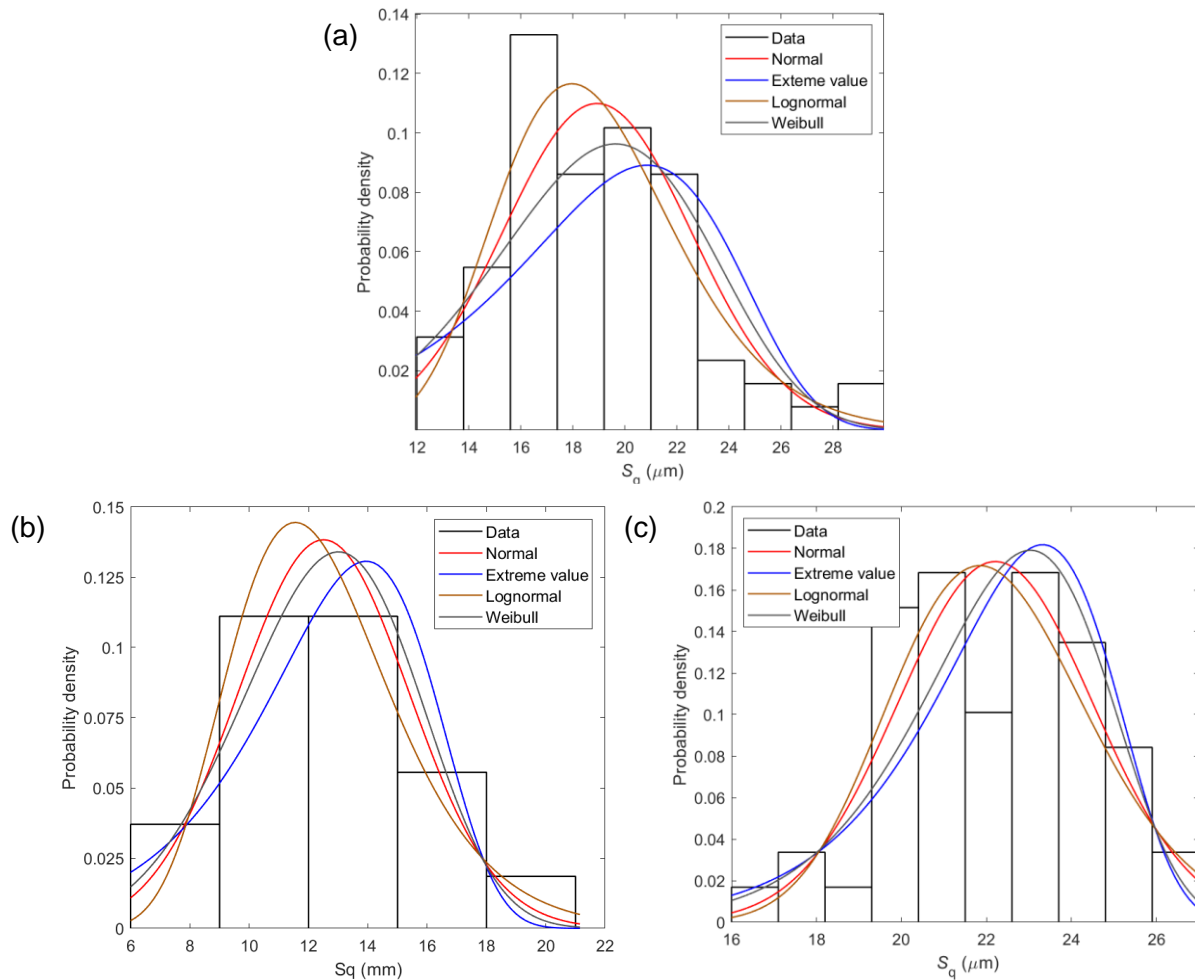


Fig. 6-32 Probabilistic distribution of surface roughness measurement results for different series of specimens (a) small-scale high roughness level; (b) small-scale low roughness level; (c) middle-scale

p -values of Anderson-Darling test for each series of roughness measurement are shown in Table 6-6. It can be seen that except for the small scale joints with high roughness level, all 4 different distributions are applicable for fitting the roughness distribution, with the p -values significantly greater than 5%. However, for the small scale joints with high roughness, only the result of lognormal distribution is undeniable. The lognormal distribution is adopted for all the roughness levels.

Table 6-6 p -value of Anderson-Darling test for each distribution

Series	Normal	Extreme value	Lognormal	Weibull
Ss-HR	0.0444	0.0005	0.6890	0.0006
Ss-LR	0.3923	0.2466	0.2436	0.4499
Ms-HR	0.2559	0.1504	0.1498	0.2498

The statistical parameters on linear scale (μ_N and σ_N) and lognormal scale (μ_L and σ_L) for different roughness series are listed in Table 6-7, which will be used for the Monte Carlo simulation in the next section.

Table 6-7 Statistical parameters for different roughness series

Series	μ_N	σ_N	μ_L	σ_L
Ss-HR	16.78	3.66	2.80	0.21
Ss-LR	10.98	2.88	2.50	0.23
Ms-HR	22.07	2.30	3.10	0.11

- *FCG curve parameter – C*

The FCG properties, namely the C parameter, may vary at different locations of the bonded composite-to-steel interface due to varied surface conditions, fracture modes and so on, even though the nominal surface roughness parameter is fixed. Not only a probabilistic S_q parameter but also a probabilistic C parameter should be used when conducting interpolation in section 6.3.2.1 according to Eq. (3-13). Statistical analysis of the FCG curves is conducted firstly in this section, assuming that the C parameter follows the lognormal distribution considering the bi-logarithmic relationship of FCG curve and taking reference from literature [178,179]. A deterministic m value is used during the whole analysis.

The statistical analysis of fatigue crack propagation data follows the recommendation of ASTM E739-91 [180]. In this method, the FCG relationship $da/dN=C(\Delta G)^m$ is linearized as $Y=C^*+m^*X$, where $Y=\text{Log}(da/dN)$, $X=\text{Log}(\Delta G)$, $C^*=\text{Log}(C)$ and $m^*=m$. The fatigue crack growth data Y is assumed to pertain to a random sample and there are no run-outs or suspended tests for the entire range of X . The crack growth rate da/dN follows the lognormal distribution and the variance of the distribution is constant. The maximum likelihood estimators of C^* and m^* are as follows:

$$C^* = \bar{Y} - m^* \bar{X} \quad (6-6)$$

$$m^* = \frac{\sum_{i=1}^k (X_i - \bar{X})(Y_i - \bar{Y})}{\sum_{i=1}^k (X_i - \bar{X})^2} \quad (6-7)$$

where \hat{C}^* and \hat{m}^* are the estimator of C^* and m^* , \bar{X} and \bar{Y} are the average values of X and Y , and k is the total number of readings during the test. The recommended expression for estimating the standard deviation of the normal distribution for Y is

$$\sigma = \sqrt{\frac{\sum_{i=1}^k (Y_i - \hat{Y}_i)^2}{k-2}} \tag{6-8}$$

where $\hat{Y}_i = \hat{C}^* + \hat{m}^* X_i$. Thus, $\hat{\sigma}$ can also be taken as the standard deviation of C^* when $m^*=m$ is constant. The corresponding mean value and standard deviation of C values can be derived as

$$\mu_C = 10^{C^*} \tag{6-9}$$

$$\sigma_C = \sqrt{10^{2C^* + \sigma^2} \cdot (10^{\sigma^2} - 1)} \tag{6-10}$$

The coefficient of variation for the C parameter can be calculated by $CoV = \sigma_C / \mu_C$.

The procedure is conducted for 4ENF test data of three different roughness levels. The obtained CoVs are summarised in Table 6-8. The CoVs of different roughness series are assumed to be constant and the average value is used in the Monte Carlo simulation.

Table 6-8 CoV of C value for different roughness series

Series	CoV (%)
RL	36.07
RM	73.37
RH	35.94
average	48.46

One example of 1000 generated probabilistic FCG curves is plotted together with the test results for high roughness series in Fig. 6-33. In this figure, the light grey curves represent probabilistic FCG curves considering the variability of surface roughness, while the dark grey curves represent probabilistic FCG curves with the mean value of surface roughness where only the variability of C parameter (with $CoV=35.94\%$) is considered. It can be seen that dark grey probabilistic FCG curves can well reproduce the scattering level of the test results, and the scattering level can be larger when the variability of surface roughness is considered.

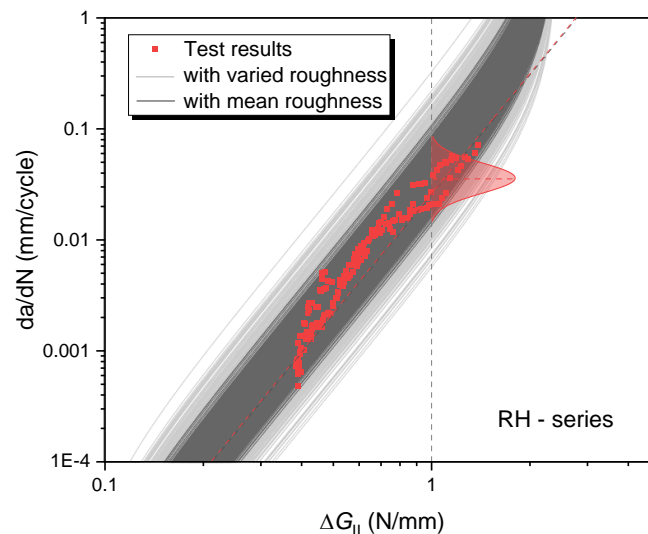


Fig. 6-33 Probabilistic FCG curves with test results

6.5.2 Monte Carlo simulation

6.5.2.1 Methodology

In the Monte Carlo simulation, the surface roughness (S_q) and crack growth property (C) are considered as the probabilistic, instead of deterministic, inputs. A random S_q value is generated following the distribution discussed in the previous section for each series of specimen. The mean value of C parameter is determined by substituting the random S_q value into Eq. (3-16). Subsequently, random C values are generated by taking different CoVs in Table 6-8. These random C parameters are substituted into Eq. (6-2) or Eq. (6-3), with each unit crack increment (1 mm) assigned with a unique C value, until that a full crack growth curve is obtained by the numerical integration. The integration procedure is repeated for multiple, e.g. 1000, times, thus probabilistic crack growth curves are obtained. By using a unique C value for each crack increment, this method assumes that the surface roughness of the steel tube is not constant along the entire crack growth path but can be a random value at any location of the steel surface. This assumption avoids the situation that the crack growth property along the whole path is represented by an extreme value, which is not realistic and may result in a too conservative or non-conservative prediction. The comparison between the modelling strategy of using a constant C value and varied C values along the crack growth path will be discussed in Chapter 7.

One example of the post-processing of the probabilistic analysis is illustrated in Fig. 6-34 for small scale joints with high roughness series loaded under the load range of 15-165kN. The probabilistic crack growth curves are shown in Step 1, followed by Step 2, where the probabilistic resulting stiffness degradation curves are obtained. By taking a certain stiffness-based failure criterion, e.g. 40% stiffness degradation in for instance, the distribution of fatigue lives of the joint is obtained in Step 3. The Anderson-Darling test is conducted by adopting different distributions. It is shown that the lognormal distribution shows the best fit, with the p -value being 0.7463, above 0.05. Finally in Step 4, the cumulative distribution function (CDF) is obtained, based on which fatigue lives corresponding to certain cumulative probabilities (or corresponding survival probabilities) can be obtained.

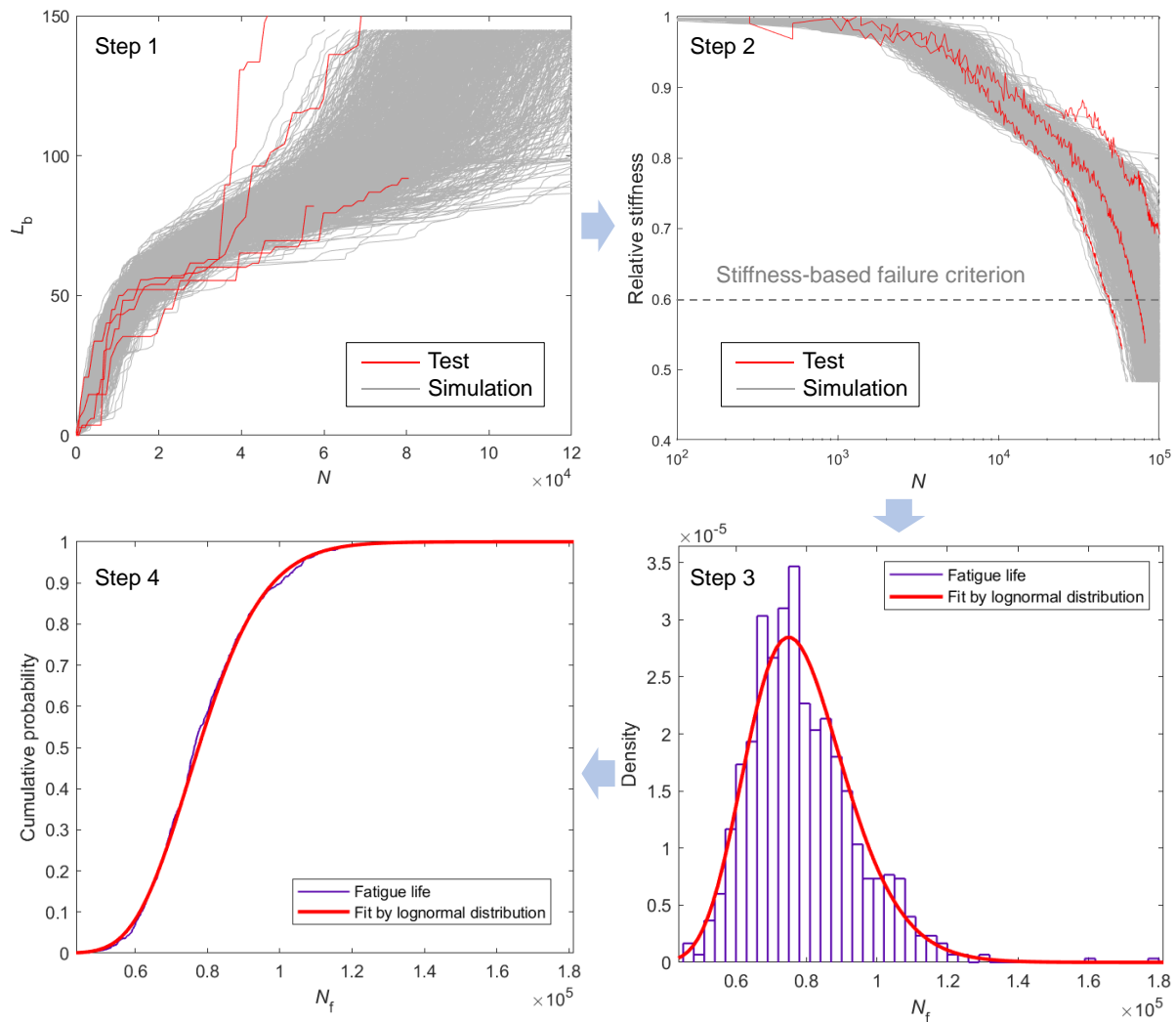


Fig. 6-34 Steps for analysing Monte Carlo simulation results

Table 6-9 p -value of Anderson-Darling test for each distribution

Distribution types	Normal	Extreme value	Lognormal	Weibull
p -value	0.0005	0.0005	0.7463	0.0005

A sensitivity study on the number of samples (number of simulations for crack growth) for the Monte Carlo simulation is conducted. The variation of mean value and standard deviation of the fatigue lives corresponding to a certain failure criterion versus the number of samples is shown in Fig. 6-35. It can be seen that these two values stabilize after reaching 1000 times of simulation. For the following analysis, 1000 samples are used considering the computing accuracy and efficiency.

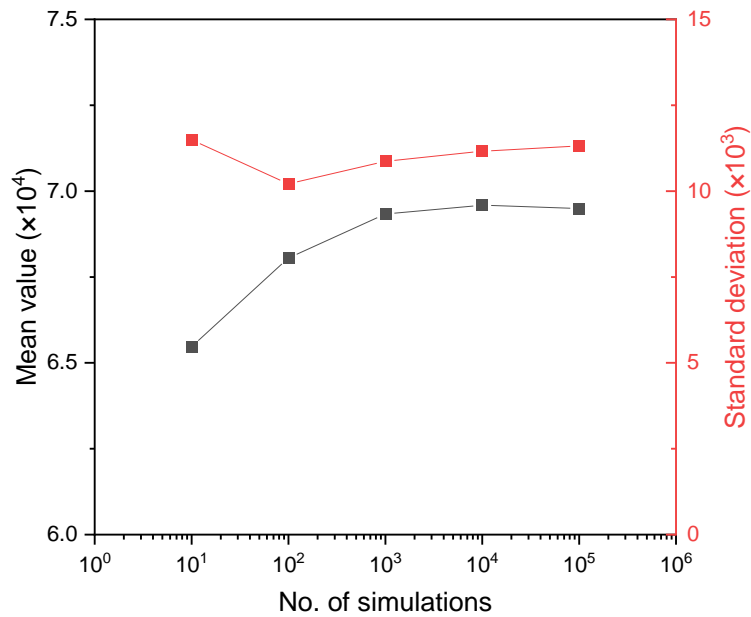


Fig. 6-35 Sensitivity of the modelling results (mean value and standard deviation) on the number of simulations

6.5.2.2 Simulation results

The results of Monte Carlo simulation for other 3 cases, including the probabilistic crack growth and stiffness degradation, are shown in Fig. 6-36 to Fig. 6-38. Together with Fig. 6-34, it can be seen that probabilistic results from Monte Carlo simulation can well reproduce the scattering level of the test results by taking into account the randomness of surface roughness, S_q , and C parameter. Specifically, the test results are within the predicted scattering bands. This is due to the fact that the number of test results is so limited (only up to 4 results) compared to the simulation results (1000 results). One individual test result is just a special case with a unique combination of surface roughness distribution on the steel tube and C parameter of the FCG curve. Although the stiffness variation trend for case (c) shown in Fig. 6-37 (b) still cannot reflect the test results very well, the Monte Carlo simulation generally explain the scattering test results by taking the randomness of S_q and C into account.

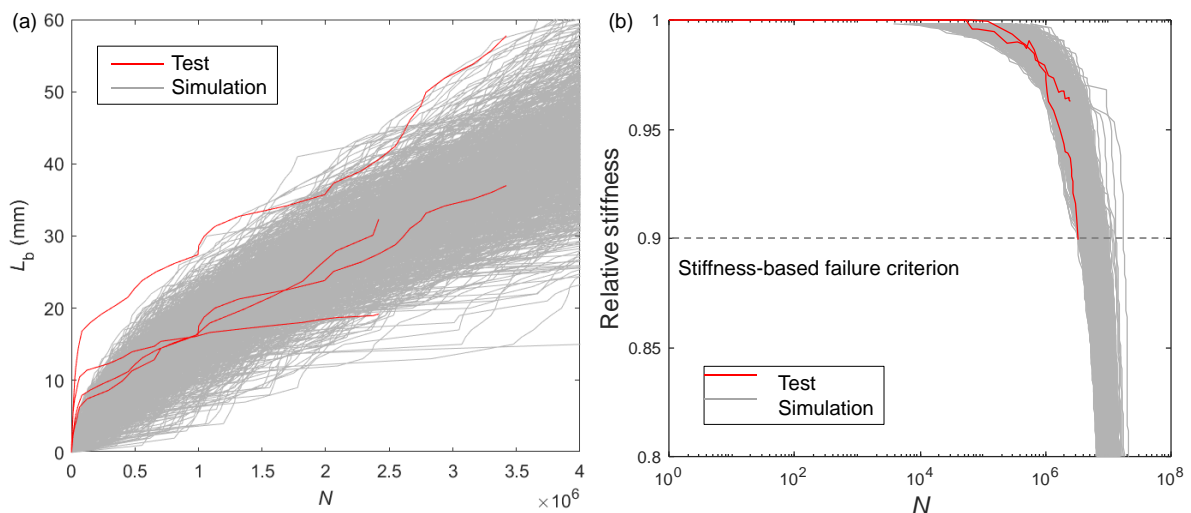


Fig. 6-36 Monte Carlo simulation on small scale joints with high roughness under 10-110 kN
 (a) crack growth; (b) stiffness degradation

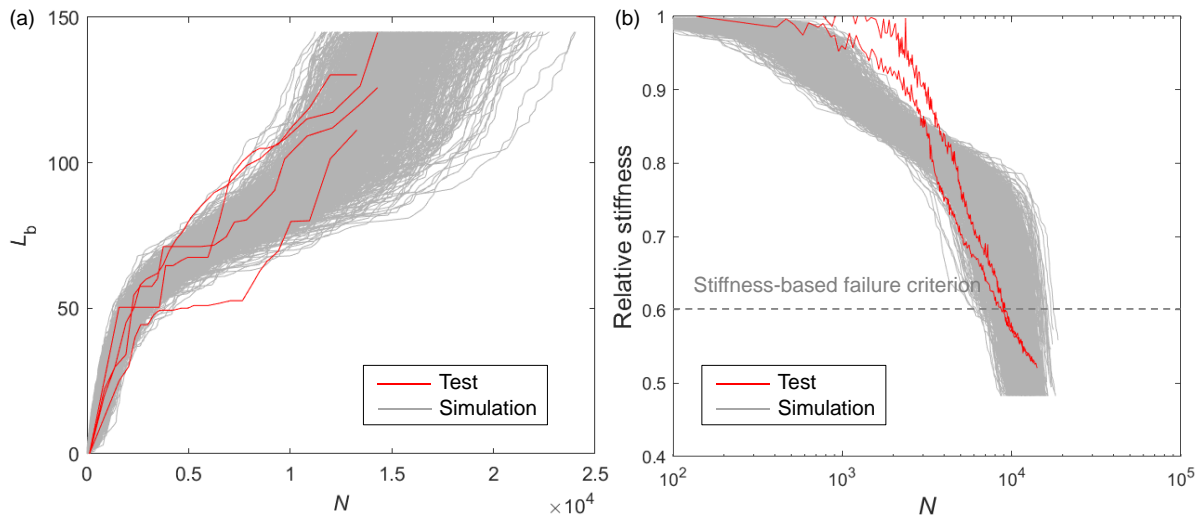


Fig. 6-37 Monte Carlo simulation on small scale joints with low roughness (a) crack growth; (b) stiffness degradation

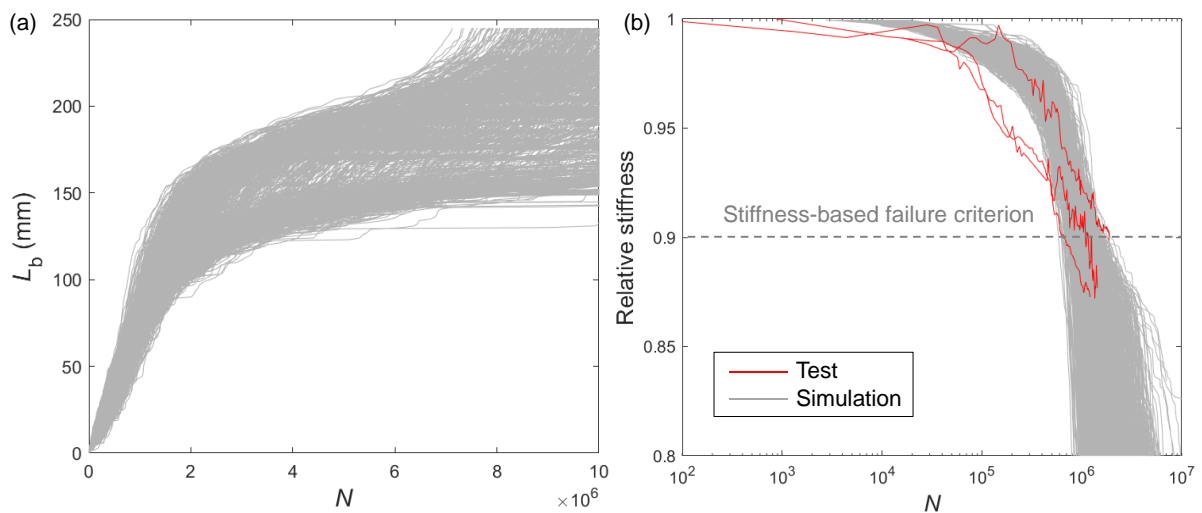


Fig. 6-38 Monte Carlo simulation on medium scale joints (a) crack growth; (b) stiffness degradation

A quantitative comparison of statistic values, including the mean value and standard deviation, between the test results and simulation results are shown in Table 6-10. It can be seen that the difference between the mean values of test results and simulation results (prediction errors) are within an acceptable range, namely the absolute values are within 10% for most of the cases except for case (c), where the simulated variation trend of stiffness degradation deviates from the test results. The prediction error of mean values in the deterministic analysis and probabilistic analysis are further compared in Table 6-11. It can be seen that except for case (c) (in grey colour), the prediction errors in the probabilistic analysis are reduced by 5-20% (in green colour) compared to those in the deterministic analysis. This shows that the mean value of the cloud of data from the probabilistic analysis can better reproduce the test results statistically when taking the randomness of S_q and C into account.

Talking about the standard deviation, the standard deviations of the test results are comparable and in the same magnitude with those of the simulation results for most of the cases under

different failure criteria. The standard deviation of the test results for some cases are even larger possibly because that the number of test results is so limited (up to 4). More tests need to be conducted in the future to better characterise the scattering level experimentally.

Table 6-10 Comparison between the experimental and numerical fatigue life

Failure criterion	Case	Experiment		Simulation		Error of mean value
		Mean value (cycles)	Standard deviation (cycles)	Mean value (cycles)	Standard deviation (cycles)	
10%	(a)	4920571	2031370	5772390	1265547	17.31%
	(b)	8515	4645	7963	1475	-6.48%
	(c)	2691	387	1475	278	-45.18%
	(d)	1214768	624134	1164660	261569	-4.12%
20%	(b)	34280	18595	33108	6538	-3.42%
	(c)	3923	754	6090	1281	55.24%
40%	(b)	78756	35368	71953	11972	-8.64%
	(c)	8689	236	13054	2117	50.24%

Table 6-11 Comparison between the error of mean values in the deterministic and probabilistic analysis

Failure criterion	Case	Deterministic analysis, Er_d	Probabilistic analysis, Er_p	Variation $ Er_p - Er_d $
10%	(a)	-35.62%	17.31%	-18.31%
	(b)	-0.04%	-6.48%	6.45%
	(c)	-36.81%	-45.18%	8.36%
	(d)	-25.40%	-4.12%	-21.27%
20%	(b)	-9.06%	-3.42%	-5.64%
	(c)	48.76%	55.24%	6.47%
40%	(b)	-20.83%	-9%	-12.19%
	(c)	36.14%	50%	14.1%

After knowing the fatigue life distributions under different criteria, the cumulative distribution function (CDF) can be obtained for different cases shown in Fig. 6-39. The fatigue lives corresponding to certain cumulative probabilities (or corresponding survival probabilities) can be obtained. For example, the fatigue life of small scale joint with high roughness loaded under 10-110kN corresponding to 90% cumulative probability (or 10% reliability) is 7.5 million cycles, as indicated in Fig. 6-39 (a). Meanwhile, it is found out from Fig. 6-39 (b) and (c) that under higher stiffness degradation tolerance, namely higher allowable stiffness degradation, the fatigue life of the joint can be much higher. For example, the fatigue life of small scale joints with high roughness loaded under 15-165kN corresponding to 90% cumulative probability

increases from around 40,000 cycles to more than 80,000 cycles when the stiffness-based failure criterion becomes more tolerant from 20% to 40%.

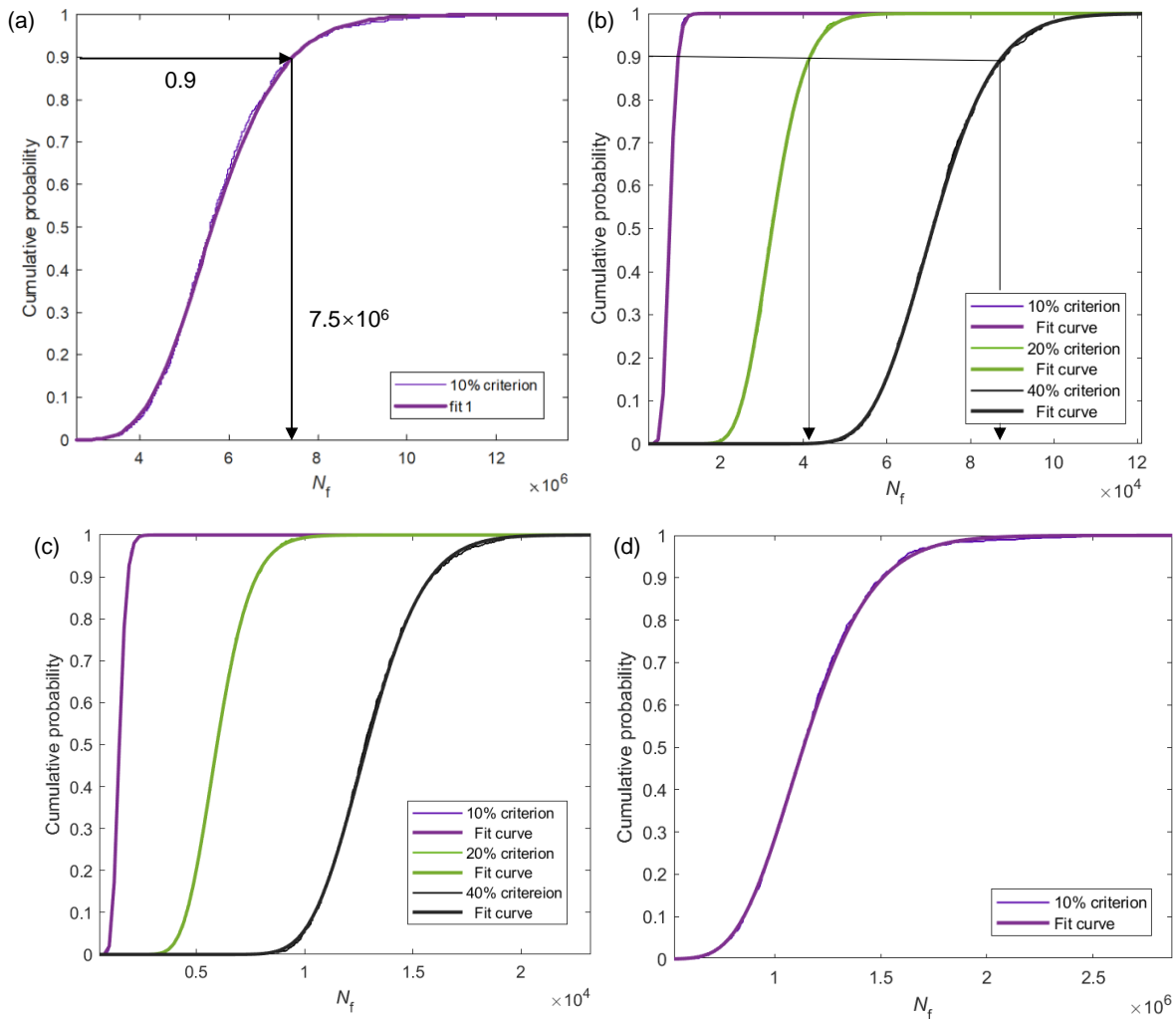


Fig. 6-39 Cumulative distribution function (CDF) under different failure criteria (a) small scale joints high roughness; (b) small scale joint low roughness; (c) middle scale joints

6.6 Conclusions

This chapter establishes the numerical methodology to simulate the fatigue crack propagation at the interface and stiffness degradation of the wrapped composite joints with complex geometry. The FE model is built and validated against the static test results in terms of force-displacement responses and surface strain on the composite wrap, and against the fatigue test results in terms of crack propagation and stiffness degradation. The modelling parameters are calibrated through a sensitivity analysis. In order to reproduce and explain the scattering fatigue test results, a probabilistic analysis based on the Monte Carlo simulation is conducted considering the randomness of surface roughness and FCG parameters. The following conclusions can be drawn from this chapter:

- The FE model where VCCT in combination with friction is utilised to simulate the fracture behaviour at the composite-to-steel interface can well reproduce the force-displacement responses and surface strain distributions on the composite wrap obtained from the static tests. The fracture toughness is calibrated based on the modelling results as to be 1.02N/mm for mode I and 1.34N/mm for mode II. The friction coefficient between composite and steel is measured by the tribometer and found to be 0.5.
- The fatigue behaviour prediction model adopts the stationary crack method, where the debonding crack patterns are assumed to be the same as those in the static debonding process. The SERR values are extracted at the crack tips and the number of cycles needed is calculated based on the FCG curves through an automatic iterative procedure, where the interaction between crack growth on the chord and braces can be considered. The calibrated FE model can well replicate the crack growth and stiffness degradation behaviour of the joint with different surface roughness, at different scales and under different load levels, with the prediction error of stiffness-controlled fatigue lives within 30% in the linear scale and within 10% in the logarithmic scale.
- The modelling parameters are calibrated through a sensitivity study. Among these parameters, it is found out that the total life FCG model can fit not only the test results for joint loaded under higher load level (around 50% of the static resistance), but also those under lower load level (around 30% of the static resistance) by taking into account the threshold behaviour of crack growth at relatively low SERR levels. The curvature exponent, D , of FCG model is calibrated to be 3 and the SERR threshold, G_{th} , to be 3% of the fracture toughness. The effective SERR at the crack tips, G_{eff} , is found to be the most appropriate crack growth driving force. The interpolation method for the SERR values outside the model matrix, and the initially assumed relationship between the crack length on the chord and braces have no influence on the modelling results.
- A probabilistic analysis is conducted to explain and reproduce the scattering test results under cyclic loading by taking into account the randomness of the surface roughness of the steel tubes and FCG C parameter. The surface roughness is measured at different locations of the joint and are found to follow the lognormal distribution. The coefficient of variance (CoV) of C parameter reflects the scattering level of the FCG curve and is found to be 48.46%.
- The probabilistic analysis can better reproduce the test results statistically (with the prediction error of the mean value within 20%) compared to the deterministic analysis, and shows comparable scattering level. Fatigue life distributions of the joints under different stiffness-based failure criteria are obtained, which are found to be lognormal distribution as well. The cumulative distribution functions are established accordingly and can be used to determine the fatigue life of the joint with a certain survival probability. The probabilistic $S-N$ curves can be obtained numerically based on the analysis.

Chapter VII

ASSESSMENT ON THE FAILURE CRITERION OF CHS X-45 JOINTS UNDER CYCLIC LOADING

7.1 Introduction

In order to construct the $S-N$ curves of the wrapped composite joints, one critical issue is to determine the failure criterion of the joint under cyclic loading. The stable crack propagation, thus stable stiffness degradation, of the wrapped composite joints makes it possible to carry out the damage tolerance design. It means that the wrapped composite joints can be designed in such a way that the joint can still sustain its original ultimate resistance after experiencing a certain stiffness degradation. In that sense, the failure criterion under fatigue loading can be defined based on the critical residual stiffness, below which the residual resistance of joint drops significantly. By finding out the critical residual stiffness, the corresponding critical crack length can be taken as the minimum required wrapping length with respect to fatigue design.

In this chapter, pre-cracks monitored by DIC after the fatigue tests are embedded in the FE model. In this way the FE model is further validated against the static tests after cyclic loading. The validated FE model is then monotonically loaded with different pre-crack lengths embedded in the composite-to-brace interface. The relationship between the residual resistance, as well as the residual stiffness, of the joint and the crack length is established, such that the critical stiffness reduction corresponding to a significant resistance reduction can be determined.

The failure criterion is proposed for the small scale and medium scale X-45 joint using the same method, based on which the design $S-N$ curves of these two series of specimens are constructed for the test results and numerical results, respectively. The $S-N$ curves can be used for preliminary design of the wrapped composite joints with the same geometries.

7.2 Model validation

Being validated against the static test on intact joint in Chapter 6, the FE model is further validated based on the static tests after cyclic loading to prove its capacity for simulating the residual resistance of the joint with embedded pre-cracks. The small scale X-45 joint with high roughness is selected since the static tests were carried out after cyclic loading, and the crack growth on the brace is obtained through DIC monitoring.

In the FE model, an asymmetric pre-crack pattern after the cyclic tests, namely 200 mm on one brace and 75 mm on the other one according to DIC results shown in Fig.5-13 of Chapter 5, is embedded at the composite-to-steel interface. The lengths of two pre-cracks on each side of the chord are determined proportionally based on the predicted relationship between L_b and L_c shown in Fig.6-18 in Chapter 6. The FE model with pre-cracks is shown in Fig. 7-1. Two types of interaction properties, as being used in Chapter 6, are used in this simulation as well. For the first type, the LEFM-based VCCT technique is utilized in combination with semi-calibrated fracture toughness as shown in Table 6-1, to simulate the debonding behaviour at the interface. For the second type, the damage-mechanics-based CZM technique used in Ref. [140] is utilised. Other modelling parameters such as the boundary conditions, materials and mesh topology is the same as used in the intact model in Chapter 6.

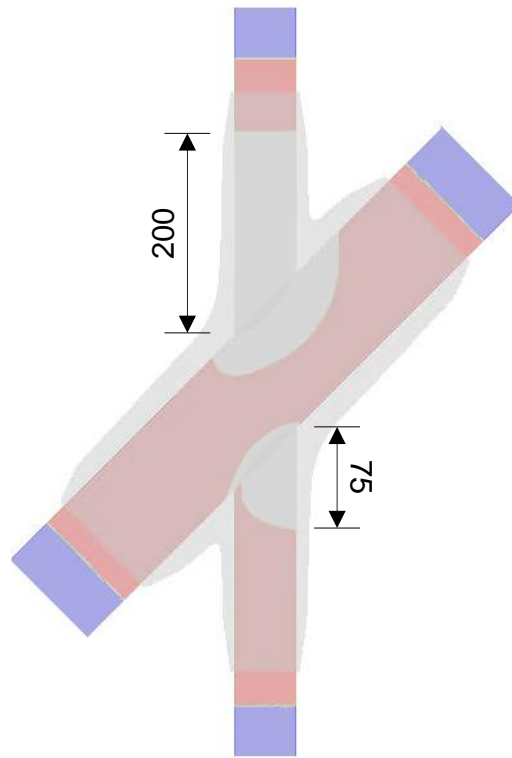


Fig. 7-1 FE model with asymmetric crack pattern on the top and bottom sides

Force displacement curves of the test results, as well as the FEA results based on VCCT and CZM are compared in Fig. 7-2. The figure shows that FEA results based on both VCCT and CZM overlap well with test results of specimen cX45-Ss-T_SF3.2. The reason can be explained by the failure modes shown in Fig. 7-3. Debonding happens at the composite-to-steel interface in the brace with longer crack length, i.e. shorter remaining bond length, until that the composite wrap fractures abruptly near the end of the wrap, leading to sudden drop of the force. The brittle failure of the composite wrap, happening before the nonlinear damage accumulates at the interface, leads to similar resistance of the two FE models, as well as the test result of specimen cX45-Ss-T_SF3.2 as shown in Table 7-1. The difference between the FE models and the specimen is within 5%. However, residual resistance of specimen cX45-Ss-T_SF3.1 is over 25% higher than the other one and shows more nonlinearity before the final failure. This is possibly due to the limited material failure of the joint as observed in Fig. 7-3. Damage at the interface has more chance to accumulate until full debonding happens towards the end of the composite wrap. The FE model generally provides a conservative prediction.

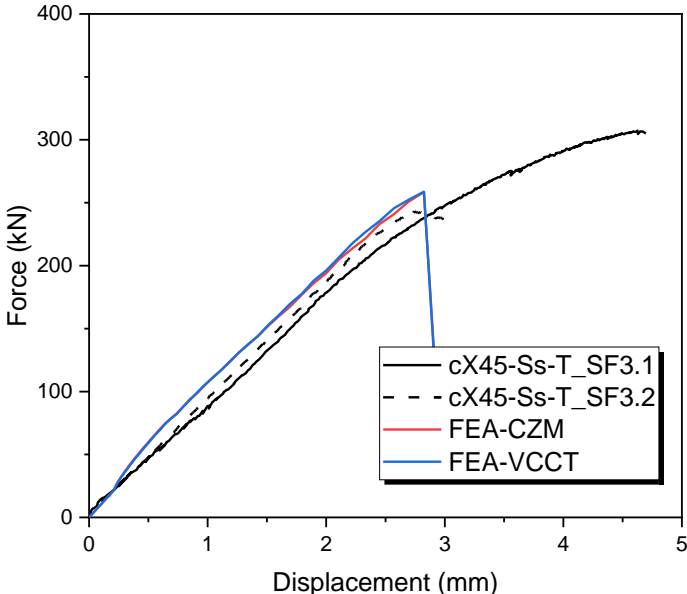


Fig. 7-2 Validation of FE model with asymmetric crack pattern via force-displacement responses

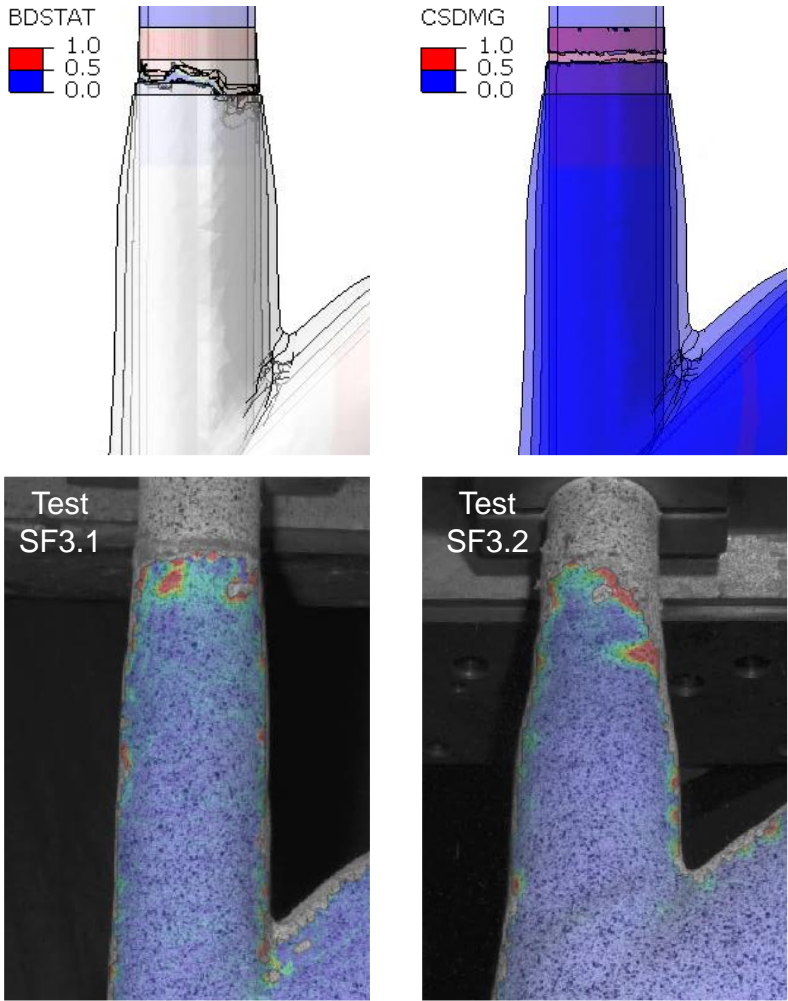


Fig. 7-3 Comparison of failure modes in VCCT-based, CZM-based FE model and test results in DIC (after peak load)

Table 7-1 Comparison of ultimate resistance between test results and FE model

Specimens	Test – SF3.1	Test – SF3.2	FEA- CZM	FEA- VCCT
Ultimate resistance (kN)	307	243	258	259

Now that CZM and VCCT-based FE model give similar results on the residual resistance of the joint, CZM technique is chosen for the following simulation to 1) capture possible nonlinear behaviour at the interface; 2) keep consistence with the ultimate resistance prediction in Ref. [140].

After being validated, the FE model is then utilized to establish the relationship between the residual resistance of the joint and the crack length on the brace. Considering the limitation of the FE model to simulate the asymmetric debonding process during monotonic loading and for simplification, symmetric crack patterns will be adopted in the following analysis. To verify the validation of this strategy, another FE model with symmetric crack pattern is created as shown in Fig. 7-4 (b), the crack length on both sides being the same with the longer crack length of the asymmetric model. Meanwhile, it is shown in Chapter 6 that the relationship between L_b and L_c may be different under different load levels, it is necessary to investigate the influence of debonding crack on the chord on the residual resistance of the joint. The third model is created, where the debonding crack on the chord is zero as shown in Fig. 7-4 (c).

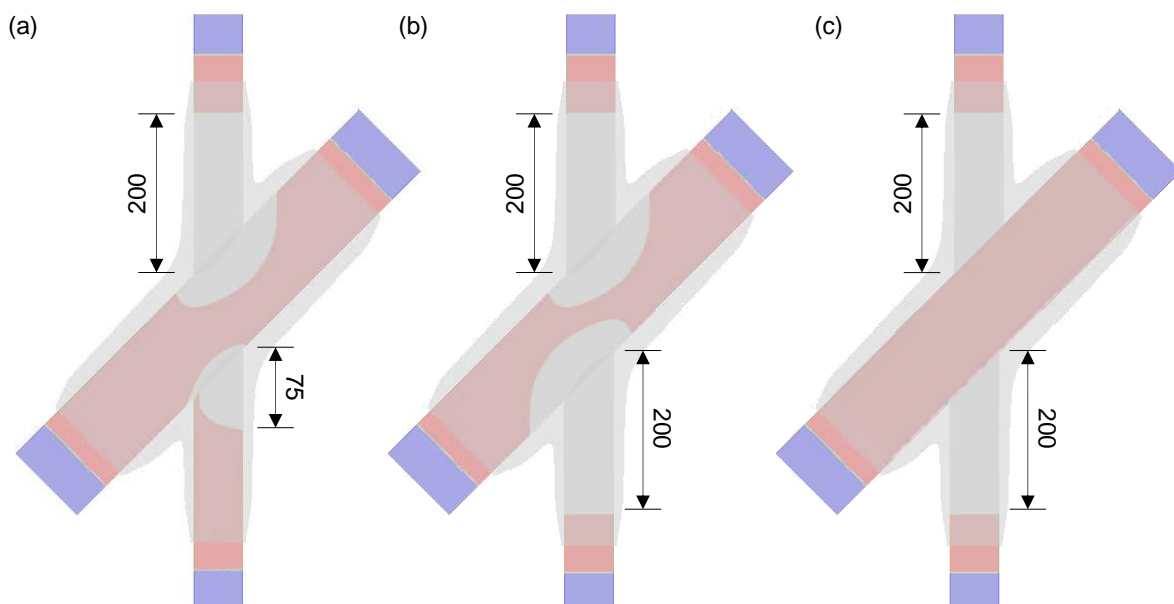


Fig. 7-4 Three different simulated debonding patterns (a) asymmetric pattern; (b) symmetric pattern; (c) no debonding on the chord

Force-displacement responses of the three FE models, namely the FE model with asymmetric crack pattern, the one with symmetric crack pattern and the third one with zero debonding on the chord, are compared in Fig. 7-5. It can be seen that although the initial stiffness are rather different due to different embedded crack length, the ultimate resistances are all around 260 kN with the difference less than 5%. The results prove that the resistance of the joint is determined by the shorter remaining bond length on the brace, where the composite wrap fractures. The debonding pattern on the chord will not influence the ultimate resistance. It is not necessary to keep the crack length on the chord strictly following the relationship between L_b and L_c obtained in Chapter 6. The obtained relationship between the residual resistance of the joint and the crack length on the brace is applicable for the joint loaded under different force levels. However, debonding crack on the chord will still roughly follow the relationship during the following failure criterion determination analysis.

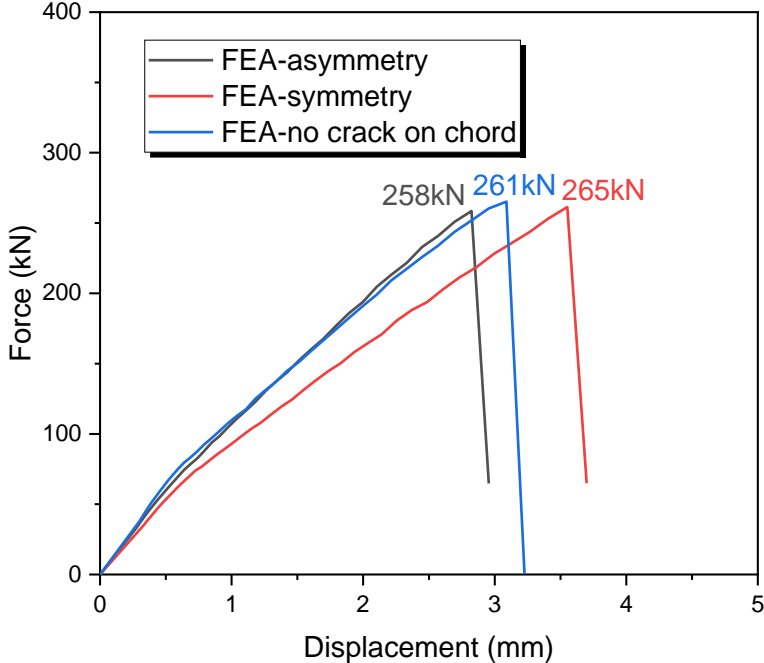


Fig. 7-5 Influence of debonding pattern on the simulated residual resistance of Ss-X45 joint

7.3 Failure criterion determination

7.3.1 Small scale X-45 joints

Crack patterns for small scale X-45 joints for failure criterion determination analysis are shown in Fig. 7-6. Crack lengths on the brace and chord increase gradually from model by model, following the predicted relationship between L_b and L_c obtained in Chapter 6. Monotonic load is applied on these pre-cracked FE models based on the CZM described above. The ultimate resistance and the initial stiffness of the models are extracted, plotted against the crack length on the brace in Fig. 7-7. The results show that the decrease of ultimate resistance of the joint with crack length within 135 mm is insignificant, namely within 5%, compared to the intact model. Beyond 135 mm the ultimate resistance drops a lot. The 5% resistance reduction,

corresponds to crack growth of $2.25d=135$ mm (d is the diameter of the brace), and stiffness degradation around 40% (residual stiffness of 60%). The stiffness degradation is more straightforward to obtain and can be adopted as the failure criterion for the small scale joint under cyclic loading. To justify the 5% resistance reduction failure criterion, another failure criterion defined in [181] for a similar type of structures, bridge decks and slab bridges made of composite materials, is taken for comparison. According to [181], the result of post-fatigue static tests on the composite decks should be within two standard deviations of the mean value of the static resistance achieved in the static tests. The coefficient of variation (CoV) of the static resistance of the wrapped composite joints considering debonding failure is obtained from [140] and is found to be 13%. Thus, the allowable resistance reduction according to this failure criterion is 26%, which is far above the 5% reduction criterion. This means that the 5% reduction criterion is a fairly strict criterion and can help achieve a reliable design of the wrapped composite joints.

Taking the 5% resistance reduction as the failure criterion, the corresponding remaining bond length, around $4.5d - 2.25d = 2.25d = 135$ mm, can be deemed as the effective bond length for this type of joint.

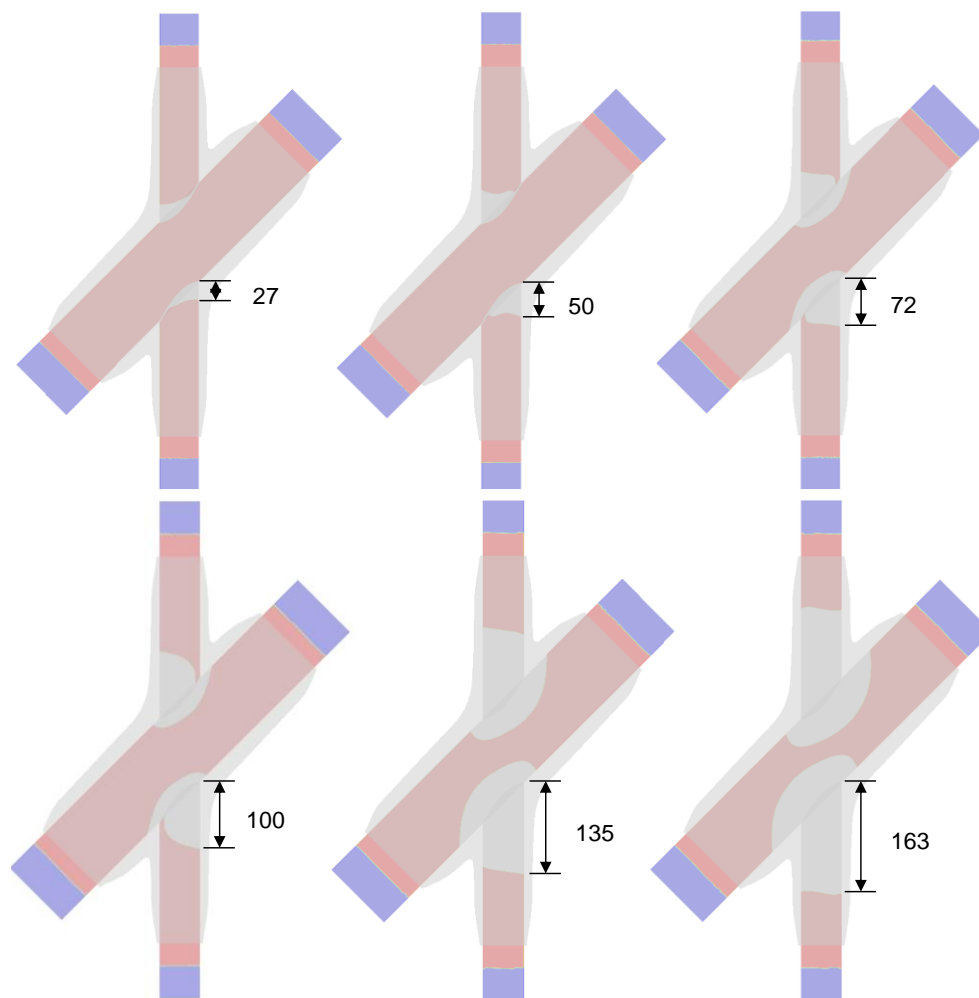


Fig. 7-6 Debonding crack patterns for residual resistance analysis for small scale joint

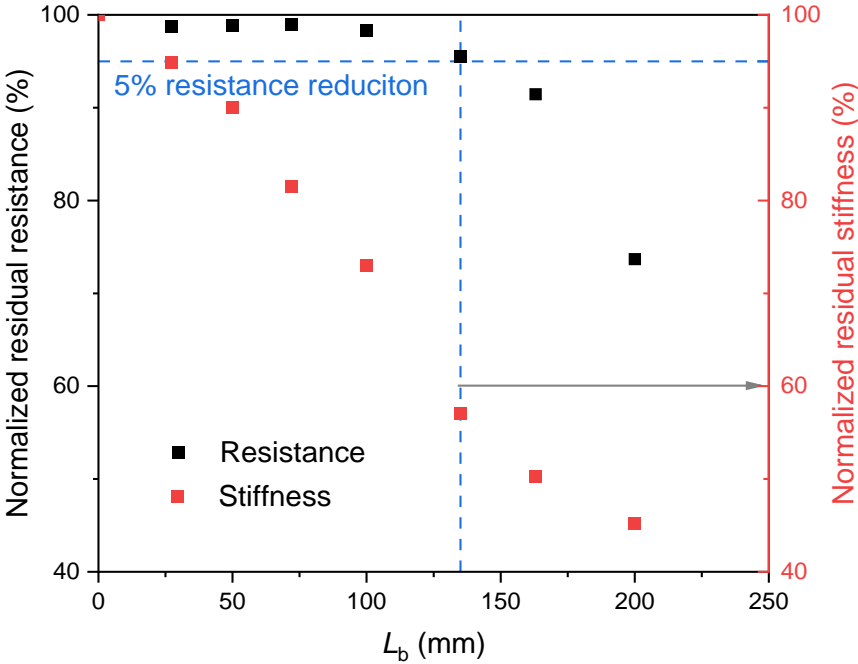


Fig. 7-7 Residual resistance of the joint versus debonding length on the brace for small scale joint

7.3.2 Medium scale X-45 joints

The same analysis is conducted on the medium scale X-45 joints. Crack patterns are shown in Fig. 7-8. In the series of FE models, debonding crack is only considered to increase on the brace, while crack on the chord remains zero. This is due to the fact that debonding on the chord during the cyclic loading is insignificant according to the Chapter 6.

The ultimate resistance of the joint versus crack length on the brace is shown in Fig. 7-9. It can be seen that for medium scale joints, the ultimate resistance reduction remains within 5% until crack length of 250 mm, approximately 1.5 times diameter (d) of the brace. The remaining bond length, namely the effective bond length, is $3d$, taking the 5% resistance reduction as the failure criterion. Correspondingly, the stiffness degradation is around 33%, with the residual stiffness being 67%. The effective bond length of the medium scale joint ($3d$) is relatively larger than that of small scale joint ($2.25d$). This might be due to the relatively smaller wrapping thickness of the medium scale joints, which is around 2 times of the thickness of the tube. On the contrary, the wrapping thickness of the small scale joints is around 5 times of the thickness of the tube. A larger bond area, corresponding to a larger relative bond length, is needed to maintain the original ultimate resistance.

It should be noted that the failure criteria determined here are only applicable for the joints with the investigated geometry and dimensions in the current study. A more general criterion applicable for different joint angles, wrapping thickness and diameter ratios between the chord and brace should be developed in the future.

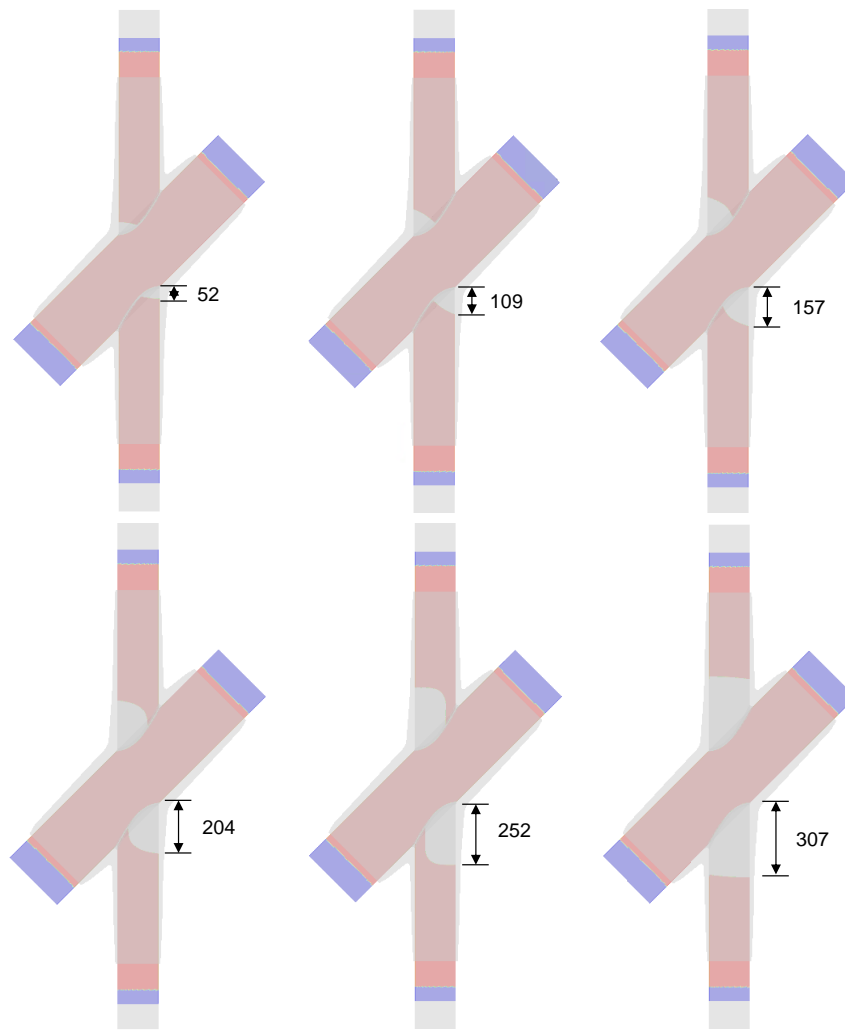


Fig. 7-8 Debonding crack patterns for residual resistance analysis for medium scale joint

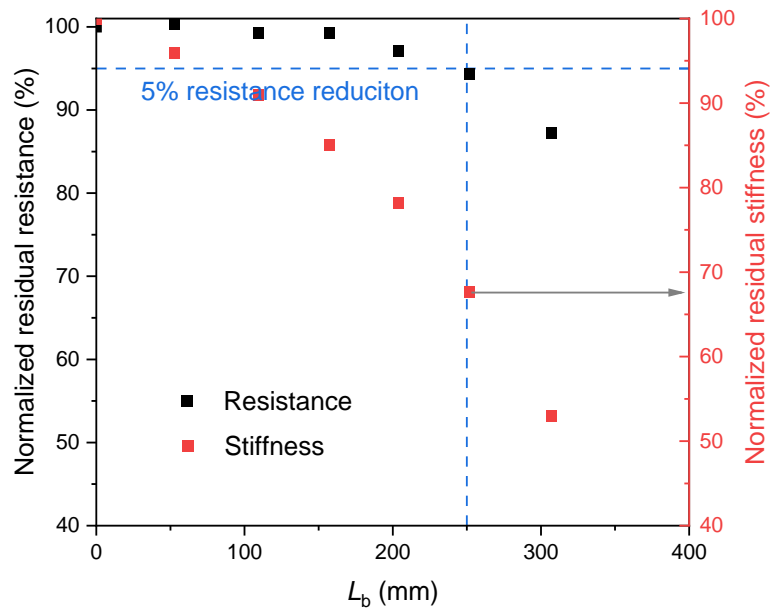


Fig. 7-9 Residual resistance of the joint versus debonding length on the brace for medium scale joint

7.4 S-N curve

7.4.1 Small scale X-45 joints

Taking the 5% resistance reduction criterion, namely the 40% allowable stiffness degradation, the fatigue lives of the wrapped composite joints can be calculated under different load levels. The obtained test results by adopting the failure criterion have already shown in Chapter 5 and are shown again here in Fig. 7-10 together with other existing design curves.

Again, the wrapped composite joint exhibits much better fatigue performance than the welded joints, especially at the high-cycle range. The negative inverse slope of the two regression curves is around 13.5, which is much higher than that of welded tubular joints ($m=3$ or 4). The fatigue performance of the joint can even better than the non-welded steel members (B1 curve) beyond $1E7$ cycles. It should be noted that the fatigue lives of the joint under 10-110kN ($\Delta\sigma_{norm}=141$ MPa) are obtained by extrapolation of the stiffness degradation curves considering the debonding failure mode. In reality the fatigue life may be controlled by the fracture of steel members at the high-cycle range.

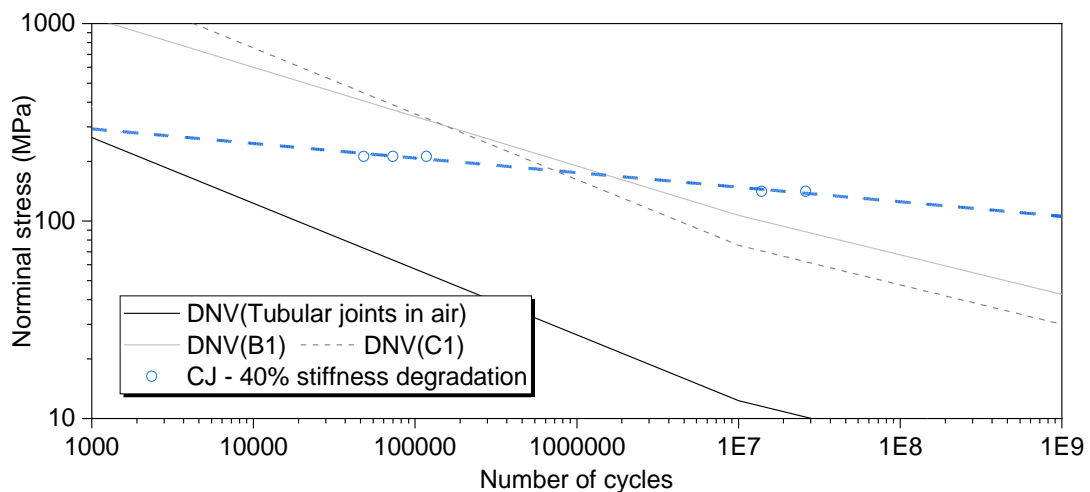


Fig. 7-10 Comparison between test results taking different failure criteria and existing design curves

The mean and characteristic $S-N$ curves of the joints obtained based on the test results and Monte Carlo simulation are compared in this section.

According to DNVGL-RP-C203 [19], a basic design $S-N$ curve is shown in Eq. (7-1):

$$\log N = \log \bar{a} - m \log \Delta\sigma \quad (7-1)$$

where $\log \bar{a}$ is the intercept of the $\log N$ -axis by $S-N$ curve. The calculation of $\log \bar{a}$ is shown in Eq. (7-2):

$$\log \bar{a} = \log a - c S_{\log N} \quad (7-2)$$

where $\log a$ is the intercept of mean $S-N$ curve with the $\log N$ -axis. $S_{\log N}$ is the standard deviation of $\log N$. c is the factor whose value depends on the number of fatigue test data.

The design $S-N$ curve should provide a 97.7% probability of survival and be estimated with at least 75% confidence. In such situation, c equals to 2 when plenty amount of test data is available but needs to be increased when the test data is limited to account for the statistical uncertainty. The mean and characteristic $S-N$ curves based on the test data and simulation results are compared in Fig. 7-11. The fatigue strength at $1E7$ cycles is also shown in the figure for comparison reason. In Fig. 7-11 (a), $c=3.36$ for the test data (taken from Table F-3 in DNVGL-RP-C203) since there is only 4 data points and $c=2$ for the simulation results. It can be seen that the mean $S-N$ curves from test and simulation overlap with each other, with the fatigue strength at $1E7$ cycles being 145 MPa and 148 MPa, respectively. However, the band between the two characteristic $S-N$ curves from the test data is wider than that from the simulation results, although the test data points are within the simulation bands. The fatigue strength at $1E7$ cycles corresponding to the lower bound of the simulated $S-N$ curve (144 MPa) is 6% higher than that of the test $S-N$ curve (136 MPa). The reason could be that an increased c factor is used for the test results due to the limited amount of data points. To eliminate this influence, $c=2$ is also applied for the test results and the comparison is made again in Fig. 7-11 (b). The band between the upper and lower bounds of the test $S-N$ curve becomes narrower but is still wider than the simulation band. The reasons could be that 1) the standard deviation of $\log N$ of the test data is too large due to the limited number of data points; 2) the considered number of probabilistic input parameters for the Monte Carlo simulation is limited. More parameters such as the probabilistic material properties and probabilistic thickness of the composite wrap can be considered in the future; 3) the coefficient of variation for the C parameter of FCG curve is small due to limited number of tested specimens. More 4ENF tests need to be conducted in the future to improve the prediction reliability. 4) the simulation assumes that the surface roughness, as a result the C parameter, varies along the crack growth path. This strategy may “smoothen” the variability of the predicted results since each predicted crack growth curve actually reflect the “averaged” value of multiple C values. Further discussion on this topic with respect to the methodology of Monte Carlo simulation will be expanded in the next section.

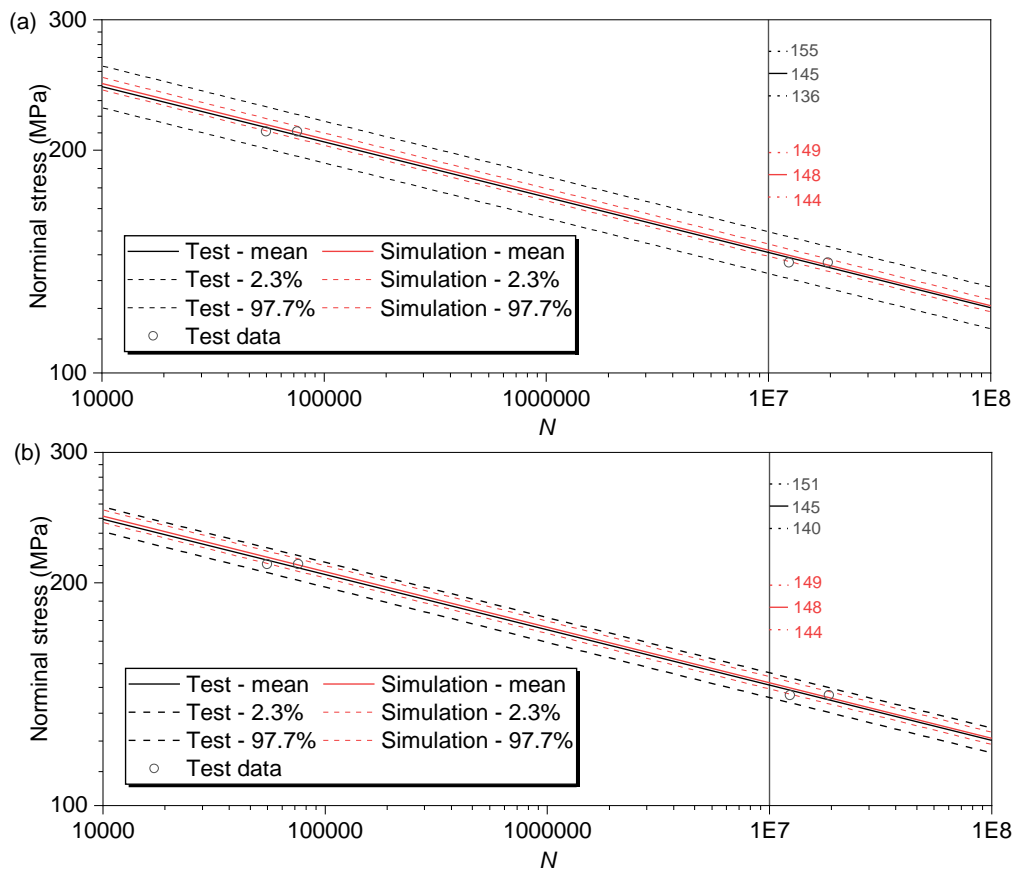


Fig. 7-11 Comparison between test results and simulated results (a) test results with mean \pm 3.3 SD upper and lower bounds; (b) test results with mean \pm 2 SD upper and lower bounds

To ensure a reasonably conservative design, the lower bound (97.7%) of the test results estimated with 75% confidence can be adopted as the design $S-N$ curve, which is expressed in Eq. (7-3):

$$\log N = 35.58 - 13.39 \log \Delta \sigma \quad (7-3)$$

The design $S-N$ curve is plotted together with the B1 curve from DNV in Fig. 7-12. It shows that the design $S-N$ curve of the wrapped composite joint can be used below 2.5×10^6 considering the debonding failure at the composite-to-steel interface, beyond which the fracture of steel members may take place and the B1 curve can be adopted.

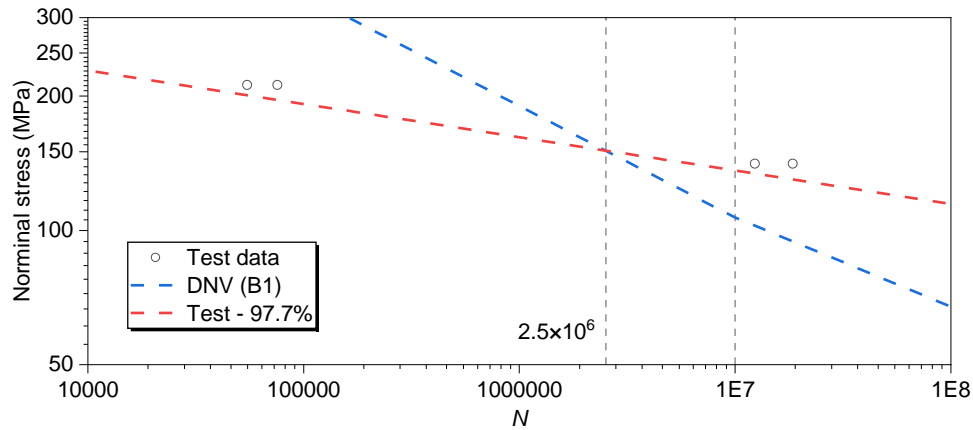


Fig. 7-12 Design *S-N* curve for small scale X-45 wrapped composite joint

7.4.2 Medium scale X-45 joints

Since the medium scale joint tests were only conducted at one load level, which is not enough to establish the *S-N* curve, the simulation results based on multiple load levels are used here to construct the *S-N* curve. It has been proved from the previous section that the simulation results can well predict the mean *S-N* curve, although the predicted scattering level of the results need to be improved in the future. The mean *S-N* curve, together with the upper and lower bounds is plotted in Fig. 7-13 and compared with existing design curves. The lower bound (97.7%) can be adopted as the design *S-N* curve and is expressed as:

$$\log N = 25.31 - 10.83 \log \Delta\sigma \tag{7-4}$$

The design *S-N* curve is again well above those of welded joints, with the fatigue strength at 1E7 cycles being 49 MPa. But it should be noted that after 1E8 cycles, the fracture of steel members instead of the debonding failure at the joint, may take place and control the fatigue design. It can also be seen that the inverse slope 10.83 is comparable to that of small scale joints. This proves that the slope of *S-N* curves is limitedly dependent on joint scale, thus can be used for determination of damage equivalent loads in the future design.

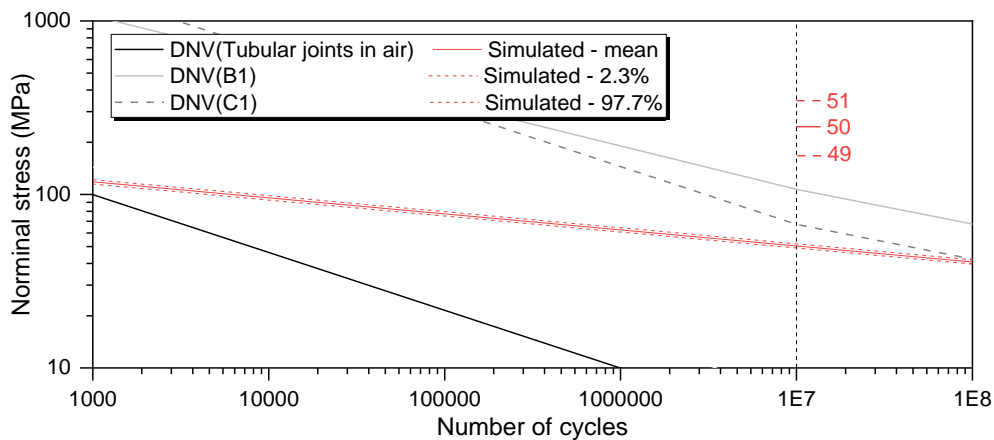


Fig. 7-13 Comparison between predicted *S-N* curves of medium scale joints with existing curves

7.4.3 Discussion on design S-N curves

This section shows the Monte Carlo simulation results of adopting another strategy, that is to assume a constant surface roughness, as a result a constant C parameter, along the entire crack growth path. The variability of the parameters is considered among different predictions. The simulation results are shown in Fig. 7-14, which is equivalent to Fig. 6-34 in Chapter 6 but using a different modelling strategy.

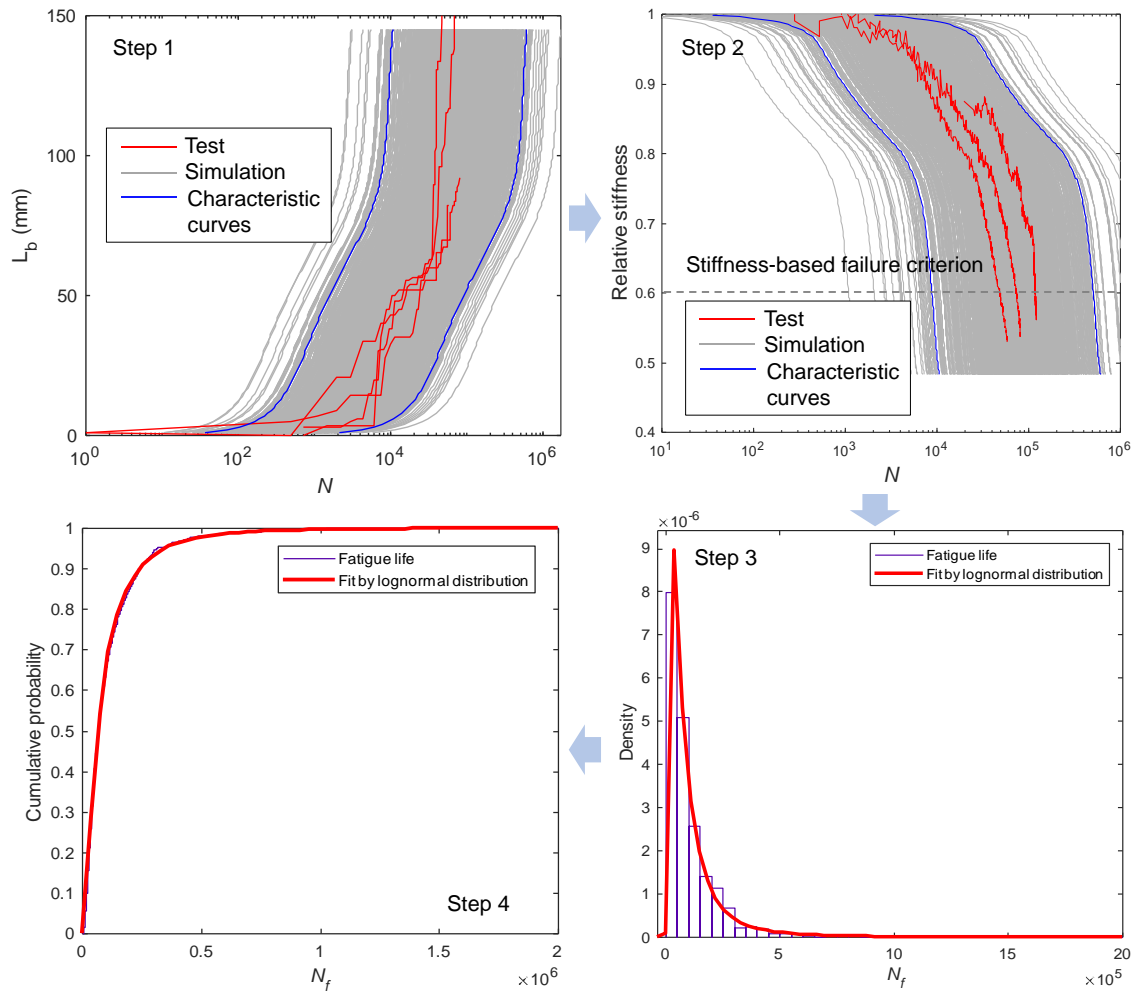


Fig. 7-14 Monte Carlo simulation results by assuming a constant C value along the entire crack growth path

The results show that predicted crack growth and stiffness degradation curves sweep much wider bands than those of test results and also those of simulation results in Fig. 6-34. Taking 40% stiffness degradation as the failure criterion, quiet dispersed distribution of fatigue lives of the joint is obtained as shown in Fig. 7-14, Step 3. The COV of fatigue lives can be as high as 137%, while the varied C strategy only lead to COV=12%. This is due to the fact that some extreme values may be used to represent the surface roughness, thus extreme C parameters, of the entire crack growth path. For instance, the characteristic crack growth and stiffness degradation curves (blue curves) in Fig. 7-14 correspond to characteristic C parameter of 0.0099 with the survival probability of 2.3% and 0.57 with the survival probability of 97.7%,

respectively. Both the characteristic C values are far below or above the mean value of 0.078. These extreme values may lead to very conservative or non-conservative predictions, which are unrealistic.

The comparison is made between the test results and the simulation results in Fig. 7-15. In Fig. 7-15 (a), the characteristic $S-N$ curves based on the test results are estimated with 75% confidence, with the c factor in Eq. (7-2) being 3.3. Whereas in Fig. 7-15 (b), the characteristic $S-N$ curves based on the test results are estimated with 95% confidence, with the c factor equalling to 7.1. The increased estimation confidence leads to much wider band between the characteristic curves and the design can be more conservative when the lower bound is used. It can be seen that the slope of the predicted $S-N$ curve is similar to that of the test results, with the negative inverse slope being 12.7 (the same value for the test results is 13.5). The fatigue strength at $1E7$ cycles is 143 MPa, which is very close to that of the test results, 145 MPa. However, the simulated lower bound of the $S-N$ curve is much lower than that of the test results estimated with 75% confidence, as shown in Fig. 7-15 (a). The fatigue strength at $1E7$ cycles is 122 MPa, which is 10% lower than that of the test results, 136 MPa. When constructing the characteristic $S-N$ curves with 95% confidence as shown in Fig. 7-15 (b), the simulated results and test results becomes closer, with the fatigue strengths at $1E7$ cycles being 127 MPa and 122 MPa, respectively.

The results mean that the simulation results by using the constant C value strategy may lead to much higher scattering level of fatigue lives. Therefore, the design $S-N$ curve, i.e. the lower bound corresponding to 97.7% survival probability, can be as conservative as that obtained from the 4 test data points estimated with 95% confidence. Considering that the test results are already very conservative due to the limited number of data points, adopting the simulated design $S-N$ curve can lead to quiet uneconomic structure design.

In practice, one can choose between the two simulation strategies (varied C strategy or constant C strategy) to achieve different design reliabilities. In the constant C strategy, since the lower bound of the simulation results are lower than that from the test results as shown in Fig. 7-15, the simulated lower bound can be used as the design $S-N$ curve and the expression is provided as in Eq. (7-5):

$$\log N = 33.43 - 12.67 \log \Delta \sigma \quad (7-5)$$

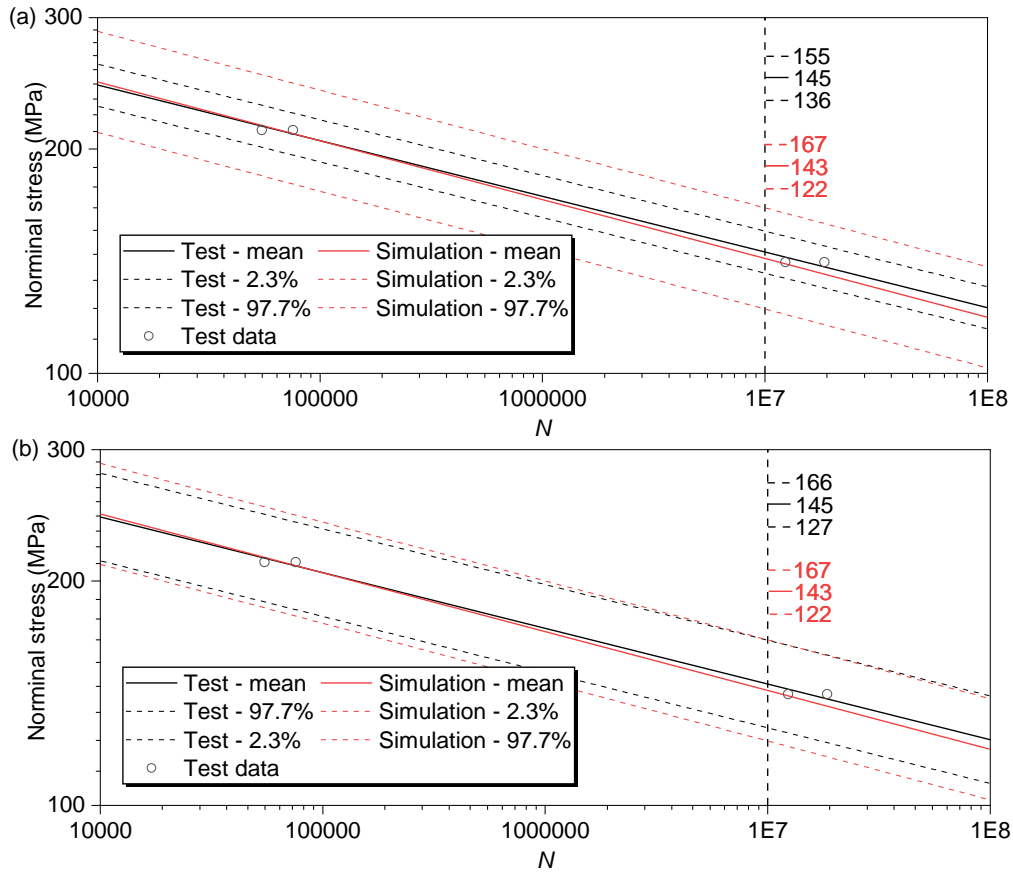


Fig. 7-15 Comparison between test results and simulated results (a) test results with mean ± 3.3 SD upper and lower bounds; (b) test results with mean ± 7.1 SD upper and lower bounds

The design $S-N$ curve can also be obtained for the medium scale joints based on the constant C simulation strategy and the expression is given in Eq. (7-6):

$$\log N = 31.86 - 11.21 \log \Delta\sigma \quad (7-6)$$

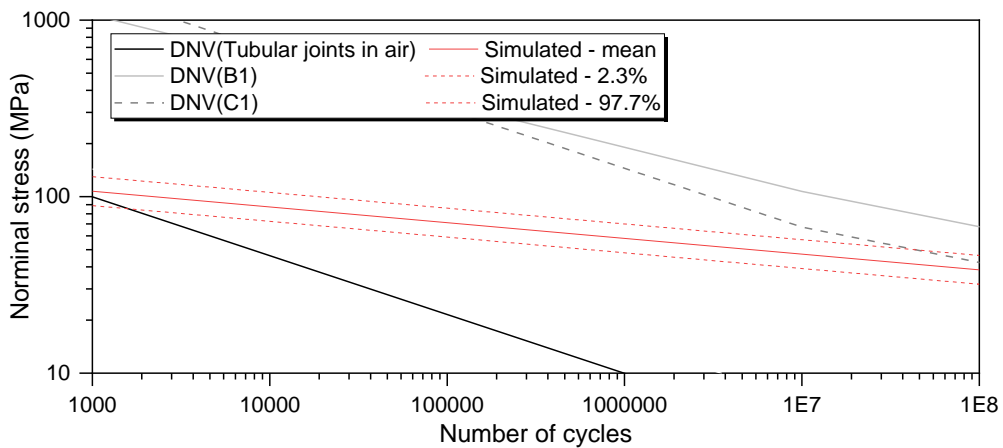


Fig. 7-16 $S-N$ curves of medium scale joints obtained based on the constant C simulation strategy

At the current stage, the expression of Eq. (7-3), shown in Fig. 7-12, for small scale joints, and the expression of Eq. (7-4), shown in Fig. 7-13, for medium scale joints can be adopted as the design $S-N$ curves considering its reasonable design reliability and economy.

7.5 Conclusions

In this chapter, the failure criterion of the wrapped composite joint under cyclic loading is determined to construct the design $S-N$ curves. The FE model of the joint is further validated against the post-fatigue static test results. Pre-cracks of different lengths are embedded at the composite-to-steel interface in the FE model to find the relationship between the residual resistance and the crack length on the brace, based on which the failure criterion of the joint under fatigue loading is determined. By using the failure criterion, the design $S-N$ curves of the joint are constructed based on the test results and numerical results, respectively. The probabilistic analysis with varied and constant C parameter along the entire crack path are compared. The following conclusions can be drawn from this chapter:

- Both the VCCT-based and CZM-based FE models with asymmetric crack patterns obtained from DIC can well predict, with the error within 5%, the ultimate resistance of joints during the post-fatigue static tests, where the failure mode is fracture of composite wrap near the end. It is found out that the residual resistance of the joint is controlled by the brace with longer crack, namely with shorter remaining bonded area. Crack development on the chord does not influence the resistance of the joint.
- Taking 5% resistance reduction as the failure criterion, which is more rigorous than the mean-minus-two-standard-deviation criterion for post-fatigue static resistance in literature, the allowable stiffness degradation is 40% for small-scale joints and 33% for medium-scale joints. The allowable crack growth on the brace is $2.25 d$ for small scale joint and $1.5 d$ for medium scale joint. The corresponding effective bond lengths for the these two scales of joint are $2.25 d$ and $3 d$, respectively. The effective bond length of the medium scale joint is longer than that of small scale joint due to the fact that the medium scale joint has relatively thinner composite wrap thus larger bonded area is needed to maintain the original resistance.
- The numerically predicted mean $S-N$ curve overlaps well with that obtained by the test results. However, by adopting the simulation strategy of varying C parameter along the crack path, the predicted design $S-N$ curve with 97.7% survival probability is 6% higher than that of the test results, representing a less conservative design. This is due to the fact that the number of test data points is limited and due to the limited input probabilistic parameters and varied C parameter modelling strategy of Monte Carlo simulation. In this situation, the lower bound of the test results can be adopted as the design $S-N$ curve.
- By fixing the C parameter along the entire crack growth path, the predicted design $S-N$ curve with 97.7% survival probability is comparable with that of the lower bound of the

test results estimated with 95% confidence. However, this may lead to very conservative design of the wrapped composite joints.

In the future, more reliable predicted design $S-N$ curves need to be obtained. To achieve that more probabilistic parameters can be considered in the Monte Carlo simulation and more interface tests need to be conducted to better characterise the COV of C parameter.

Chapter VIII

CONCLUSIONS AND RECOMMENDATIONS

8.1 Conclusions

In this dissertation, fatigue debonding resistance of the CHS wrapped composite X-joints is investigated experimentally through 18 interface coupon, 6 axial splice joint, 15 small scale X-joint, 3 medium scale X-joint specimens and numerically through finite element models. The fatigue debonding behaviour at the composite-to-steel interface is studied at the coupon level (1-D), splice joint level (2-D) and complex X-joint level (3-D), respectively. Experimental results of fatigue crack growth properties obtained at the composite-to-steel interface at the coupon level serve as the basis for predicting crack growth at the joint level. The crack growth retardation phenomenon is found and explained by cyclic tests on the joint level with a simple geometry, i.e. the axial splice joints (A-joints). Tensile cyclic tests are conducted on the wrapped composite X-joints with different steel surface roughness at small scale (with brace diameter of 60.3 mm) and medium scale (with brace diameter of 168 mm). A numerical script is developed where the crack growth is predicted based on fracture mechanics, and the interaction between debonding on the chord and brace members is considered to predict the crack growth and stiffness degradation of the X-joint. The crack growth prediction is validated against the experimental results and then used for a probabilistic analysis to explain and quantify the scattering of the results. The failure criteria of the wrapped composite X-joint under cyclic loads is established, which is the base of the design $S-N$ curves. In summary, the fatigue debonding behaviour of wrapped composite joint is quantified and the numerical prediction method is established on the small-scale and medium-scale X-joint under tensile cyclic loading. It serves as the first step towards predicting the fatigue debonding behaviour of joints with more complex geometries, at different scales and under different loading conditions.

The following are the most important conclusions:

- Displacement controlled cyclic 4ENF tests exhibit stable crack propagation and are suitable to characterize the fatigue crack growth properties at the composite-to-steel bi-material interface. With limited fiber bridging at the interface during the cyclic tests, surface roughness of the steel plate plays the most important role on the interface properties. Increased surface roughness leads to significantly increased fatigue resistance of the bonded joint. The slope of the Paris curves, m , is mildly dependent, up to 20%, on the surface roughness. However, the intercept C parameter decreases one order of magnitude from low to medium and another order of magnitude from medium to high roughness levels. The friction at the composite-to-steel interface of 4ENF specimen has very big influence on results, which leads to up to 58% higher calculated fracture toughness and 74% lower C parameter of the Paris curve using the extended global method. This research provides a methodology for considering the friction effect when determining the SERR values through the virtual crack closure technique (VCCT). That is to incorporate the friction behaviour at the composite-to-steel interface in the FE model.

- The fatigue crack growth retardation, thus stiffness degradation stabilization, is found in tensile cyclic tests on the axial splice joints. The retardation phenomenon is due to the friction effect at the cracked interface, where normal compressive stresses exist due to confinement caused by contraction of the composite wrap. When incorporating friction at the composite-to-steel interface, the SERR values obtained by the FE model using VCCT decreases as the crack grows. Prediction based on the reduced SERR values using the LEFM approach explains the retarded crack growth and stabilized stiffness degradation during the cyclic tests. The LEFM approach is enhanced in this way for the non-linear crack growth analysis. Validated with a simple joint geometry, the FE model can be used to make prediction on a more complex joint, e.g. X-joint.
- The wrapped composite X-joints exhibit gradual stiffness degradation of up to 40% with debonding, mainly mode II debonding, at the composite-to-steel interface. 70% increase of the steel surface roughness leads to 8-120 times decrease of stiffness degradation rate, thus substantially extended fatigue life of the joint. The proposed *S-N* curves shows that even with the most rigorous damage tolerance where allowable stiffness degradation is only 10%, wrapped composite joints with lower roughness still show better fatigue performance compared to welded joints. After 20% stiffness degradation, the small scale wrapped composite joints tested in the lab still sustains the load equivalent to the yield resistance of the steel brace. The medium scale joints maintain a desirable stiffness degradation trend and exhibits superior fatigue performance compared to welded joints. The above analysis demonstrates the potential of high fatigue resistance of wrapped composite joints to be scaled up for full-scale applications, for example, in the case of support towers for offshore wind turbines.
- A methodology for predicting crack growth and stiffness degradation of bonded joint with a complex geometry, e.g. the wrapped composite joints, is established. In this method, the crack patterns are predefined and the number of cycles needed for a critical length is predicted. Using the total life fatigue crack growth model and calibrated modelling parameters, the FE model in combination with a numerical script predicts well the crack growth and stiffness degradation of the joints with different surface roughness, at different scales and under different load levels. The methodology considers debonding crack on the chord and braces.
- A probabilistic analysis based on a Monte Carlo simulation considering the variability of surface roughness and fatigue crack growth properties can well explain and reproduce the scattering test results statistically. The fatigue life with a certain survival probability is obtained in the analysis.
- The stable crack growth behaviour of the wrapped composite joint makes it possible to conduct the damage tolerance design. The failure criterion of the joint depends on a critical stiffness degradation, below which the ultimate resistance of the joint drops significantly. The critical stiffness degradation is determined as to be 40% for small-scale joints and 33% for medium scale joints, respectively.

- The design $S-N$ curves of the wrapped composite X-joint are constructed experimentally and numerically. The numerical results considering varied C parameters along the crack growth path gives less conservative design curves than experimental results estimated with 75% confidence. This is due to limited test data points and varied C parameters along the crack path in the Monte Carlo simulation. When adopting a constant C value along the entire crack growth path, however, the numerically obtained design curve becomes much more conservative and is comparable with that of the test results estimated with 95% confidence. In practice, one can choose between these two simulation strategies to achieve different design reliabilities.

8.2 Recommendations

As the first exploration on the fatigue behaviour of wrapped composite joints, the present work has limitations and opens new research questions for future studies:

- At the interface level, the fatigue crack growth properties are studied in the linearly proportional part of the Paris curve. However, the SERR values at the crack tip may reach levels close to the threshold region of the fatigue crack growth curve when the joint is subjected to low load ranges. More cyclic tests should be done using the 4ENF test configuration to obtain the threshold SERR values, G_{th} .
- There might be other mechanisms besides friction at the interface which lead to crack growth retardation phenomena during the debonding process. One of the possible mechanisms is fibre bridging. Current study utilises friction behaviour as the modification on linear elastic fracture mechanics when predicting crack growth. Damage-mechanics-based approach, such as cyclic cohesive zone model, should be investigated to analyse quality of a such prediction.
- At the joint level, the uniplanar X-joint is studied assuming that it could represents the multi-planar K-K joints. Cyclic load tests on an actual K-K joints should be performed to investigate validity of the assumption for the fatigue performance.
- The study only focused on the debonding behaviour of the joints under cyclic loads. However, material damage and fracture may occur when the composite wrap is optimised in the future, which should ideally be the optimal failure modes. The numerical FE model should also incorporate the material degradation under cyclic loads.
- The wrapped composite joints will be applied in a harsh marine environment in the future, where the moisture, sea water, high or low temperatures may lead to mechanical degradation of the joints. The influence of environmental aging on the fatigue performance of the joint needs to be investigated.

REFERENCE

- [1] REPowerEU Plan. Brussels, Belgium: 2022. <https://doi.org/https://eur-lex.europa.eu/legal-content/EN/TXT/?uri=COM%3A2022%3A230%3AFIN&qid=1653033742483>.
- [2] Sesto E, Lipman NH. Wind energy in Europe. 2022. <https://doi.org/https://windeurope.org/intelligence-platform/product/wind-energy-in-europe-2022-statistics-and-the-outlook-for-2023-2027/>.
- [3] Kallehave D, Byrne BW, LeBlanc Thilsted C, Mikkelsen KK. Optimization of monopiles for offshore wind turbines. *Philos Trans R Soc A Math Phys Eng Sci* 2015;373:296–8. <https://doi.org/10.1098/RSTA.2014.0100>.
- [4] Rodrigues S, Restrepo C, Katsouris G, Pinto RT, Soleimanzadeh M, Bosman P, et al. A Multi-Objective Optimization Framework for Offshore Wind Farm Layouts and Electric Infrastructures. *Energies* 2016, Vol 9, Page 216 2016;9:216. <https://doi.org/10.3390/EN9030216>.
- [5] Pavlovic M, Bogers P, Veljkovic M. Method for Making a Virgin Joint Between Two Separate Structural Hollow Sections, and Such a Virgin Joint. 17/052, 303, 2021.
- [6] He P, Pavlovic M. Feasibility of Wrapped FRP Circular Hollow Section Joints. 17th Int. Symp. Tubul. Struct., Singapore: 2020, p. 292–9. https://doi.org/10.3850/978-981-11-0745-0_043-cd.
- [7] Zhang J, Fowai I, Sun K. A glance at offshore wind turbine foundation structures. *Brodogradnja* 2016;67:101–13. <https://doi.org/10.21278/brod67207>.
- [8] Chew KH, Ng EYK, Tai K, Muskulus M, Zwick D. Offshore wind turbine jacket substructure: A comparison study between four-legged and three-legged designs. *J Ocean Wind Energy* 2014;1:74–81.
- [9] offshoreWind.biz. Germany: ThyssenKrupp Mannex to Market Innovative Offshore Foundation ‘Hexabase’ 2012. <https://www.offshorewind.biz/2012/03/15/germany-thyssenkrupp-mannex-to-market-innovative-offshore-foundation-hexabase/>.
- [10] Chen IW, Wong BL, Lin YH, Chau SW, Huang HH. Design and analysis of jacket substructures for offshore wind turbines. *Energies* 2016;9:264. <https://doi.org/10.3390/en9040264>.
- [11] Stolpe M, Sandal K. Structural optimization with several discrete design variables per part by outer approximation. *Struct Multidiscip Optim* 2018;57:2061–73. <https://doi.org/10.1007/s00158-018-1941-3>.
- [12] Zhao XL, Herion S, Packer J a, Puthli RS, Sedlacek G, Wardenier J, et al. Design guide for circular and rectangular hollow section welded joints under fatigue loading. vol. 8. TÜV, Köln; 2001.

- [13] Wardenier J, Packer JA, Zhao X-L, van der Vegte G. Hollow sections in structural applications. Geneva, Switzerland: CIDECT; 2010.
- [14] Haagenzen PJ. Fatigue of tubular joints and fatigue improvement methods. *Prog Struct Eng Mater* 1997;1:96–106. <https://doi.org/10.1002/pse.2260010115>.
- [15] Schijve J. Fatigue of structures and materials. 2nd Editio. Springer Science and Business Media B.V.; 2009. <https://doi.org/10.1007/978-1-4020-6808-9>.
- [16] Tong L, Xu G, Zhao X-L, Yan Y. Fatigue tests and design of CFRP-strengthened CHS gap K-joints. *Thin-Walled Struct* 2021;163:107694. <https://doi.org/10.1016/j.tws.2021.107694>.
- [17] European Committee for Standardisation. Eurocode 3: Design of steel structures — Part 1-9: Fatigue. Brussels, Belgium: British Standard Institution; 2005.
- [18] Zhao X-L, Packer JA, International Institute of Welding. Fatigue design procedure for welded hollow section joints : IIW Document XIII-1804-99 and IIW Document XV-1035-99 : recommendations of IIW Subcommittee XV-E. n.d.
- [19] DNV GL. DNVGL-RP-C203: Fatigue design of offshore steel structures. 2016.
- [20] Hobbacher AF. IIW Collection Recommendations for Fatigue Design of Welded Joints and Components. 2nd Editio. 3; 2016.
- [21] Health and Safety Executive. Background to new fatigue guidance for steel joints and connections in offshore structures. 1999.
- [22] Haagenzen PJ. Fatigue strength improvement methods. In: Macdonald K, editor. *Fract. Fatigue Welded Joints Struct*. 1st ed., Philadelphia, USA: Woodhead Publishing Limited; 2011, p. 297–329. <https://doi.org/10.1533/9780857092502.2.297>.
- [23] Chew KH, Tai K, Ng EYK, Muskulus M. Analytical gradient-based optimization of offshore wind turbine substructures under fatigue and extreme loads. *Mar Struct* 2016;47:23–41. <https://doi.org/10.1016/j.marstruc.2016.03.002>.
- [24] Iqbal M, Karuppanan S, Perumal V, Ovinis M, Rasul A. Rehabilitation Techniques for Offshore Tubular Joints. *J Mar Sci Eng* 2023;11. <https://doi.org/10.3390/jmse11020461>.
- [25] Haldimann-Sturm SC, Nussbaumer A. Fatigue design of cast steel nodes in tubular bridge structures. *Int J Fatigue* 2008;30:528–37. <https://doi.org/10.1016/j.ijfatigue.2007.03.007>.
- [26] Zhao XL, Zhang L. State-of-the-art review on FRP strengthened steel structures. *Eng Struct* 2007;29:1808–23. <https://doi.org/10.1016/j.engstruct.2006.10.006>.
- [27] Teng JG, Yu T, Fernando D. Strengthening of steel structures with fiber-reinforced polymer composites. *J Constr Steel Res* 2012;78:131–43. <https://doi.org/10.1016/J.JCSR.2012.06.011>.
- [28] Jiao H, Zhao XL. CFRP strengthened butt-welded very high strength (VHS) circular steel tubes. *Thin-Walled Struct* 2004;42:963–78.

- <https://doi.org/10.1016/j.tws.2004.03.003>.
- [29] Haedir J, Bambach MR, Zhao XL, Grzebieta RH. Strength of circular hollow sections (CHS) tubular beams externally reinforced by carbon FRP sheets in pure bending. *Thin-Walled Struct* 2009;47:1136–47. <https://doi.org/10.1016/j.tws.2008.10.017>.
- [30] Lesani M, Bahaari MR, Shokrieh MM. Numerical investigation of FRP-strengthened tubular T-joints under axial compressive loads. *Compos Struct* 2013;100:71–8. <https://doi.org/10.1016/j.compstruct.2012.12.020>.
- [31] Lesani M, Bahaari MR, Shokrieh MM. Experimental investigation of FRP-strengthened tubular T-joints under axial compressive loads. *Constr Build Mater* 2014;53:243–52. <https://doi.org/10.1016/j.conbuildmat.2013.11.097>.
- [32] Lesani M, Bahaari MR, Shokrieh MM. FRP wrapping for the rehabilitation of Circular Hollow Section (CHS) tubular steel connections. *Thin-Walled Struct* 2015;90:216–34. <https://doi.org/10.1016/j.tws.2014.12.013>.
- [33] Fu Y, Tong L, He L, Zhao XL. Experimental and numerical investigation on behavior of CFRP-strengthened circular hollow section gap K-joints. *Thin-Walled Struct* 2016;102:80–97. <https://doi.org/10.1016/J.TWS.2016.01.020>.
- [34] Sadat Hosseini A, Bahaari MR, Lesani M. Parametric Study of FRP Strengthening on Stress Concentration Factors in an Offshore Tubular T-Joint Subjected to In-Plane and Out-of-Plane Bending Moments. *Int J Steel Struct* 2019;19:1755–66. <https://doi.org/10.1007/s13296-019-00244-0>.
- [35] Nassiraei H, Reza doost P. Stress concentration factors in tubular T / Y-joints strengthened with FRP subjected to compressive load in offshore structures. *Int J Fatigue* 2020;140:105719. <https://doi.org/10.1016/j.ijfatigue.2020.105719>.
- [36] Nassiraei H, Reza doost P. SCFs in tubular X-connections retro fitted with FRP under in-plane bending load. *Compos Struct* 2021;274:114314. <https://doi.org/10.1016/j.compstruct.2021.114314>.
- [37] Nassiraei H, Reza doost P. Probabilistic analysis of the SCFs in tubular T / Y-joints reinforced with FRP under axial , in-plane bending , and out-of-plane bending loads. *Structures* 2022;35:1078–97. <https://doi.org/10.1016/j.istruc.2021.06.029>.
- [38] Zavvar E, Sadat A, Lotfollahi-yaghin MA. Stress concentration factors in steel tubular KT-connections with FRP-Wrapping under bending moments. *Structures* 2021;33:4743–65. <https://doi.org/10.1016/j.istruc.2021.06.100>.
- [39] Zavvar E, Henneberg J, Soares CG. Stress concentration factors in FRP-reinforced tubular DKT joints under axial loads. *Mar Struct* 2023;90:103429. <https://doi.org/10.1016/j.marstruc.2023.103429>.
- [40] Tong L, Xu G, Zhao XL, Zhou H, Xu F. Experimental and theoretical studies on reducing hot spot stress on CHS gap K-joints with CFRP strengthening. *Eng Struct* 2019;201:109827. <https://doi.org/10.1016/J.ENGSTRUCT.2019.109827>.

REFERENCE

- [41] Xu G, Tong L, Zhao X-L, Zhou H, Xu F. Numerical analysis and formulae for SCF reduction coefficients of CFRP-strengthened CHS gap K-joints. *Eng Struct* 2020;210:110369. <https://doi.org/10.1016/j.engstruct.2020.110369>.
- [42] Nadauld JD, Pantelides CP, Asce M. Rehabilitation of Cracked Aluminum Connections with GFRP Composites for Fatigue Stresses. *J Compos Constr* 2007;11:328–35. [https://doi.org/10.1061/\(ASCE\)1090-0268\(2007\)11:3\(328\)](https://doi.org/10.1061/(ASCE)1090-0268(2007)11:3(328)).
- [43] Xiao ZG, Zhao XL. Cfrp repaired welded thin-walled cross-beam connections subject to in-plane fatigue loading. 2012;12:195–211. <https://doi.org/10.1142/S0219455412004653>.
- [44] González-Velázquez JL. *A Practical Approach to Fracture Mechanics*. Amsterdam, Netherlands: Elsevier; 2020.
- [45] Williams ML. The stresses around a fault or crack in dissimilar media. *Bull Seismol Soc Am* 1959;49:199–204. <https://doi.org/10.1785/BSSA0490020199>.
- [46] Alderliesten RC, Schijve J, van der Zwaag S. Application of the energy release rate approach for delamination growth in Glare. *Eng Fract Mech* 2006;73:697–709. <https://doi.org/10.1016/J.ENGFRACTMECH.2005.10.006>.
- [47] Irwin, G. R.; Krafft, J. M.; Paris, P. C. ; Wells AA. *Basic Aspects of Crack Growth and Fracture*. NRL Rep 1967;6598:9–10.
- [48] Williams JG. On the calculation of energy release rates for cracked laminates. *Int J Fract* 1988 362 1988;36:101–19. <https://doi.org/10.1007/BF00017790>.
- [49] Shahverdi M, Vassilopoulos AP, Keller T. Mixed-Mode I/II fracture behavior of asymmetric adhesively-bonded pultruded composite joints. *Eng Fract Mech* 2014;115:43–59. <https://doi.org/10.1016/J.ENGFRACTMECH.2013.11.014>.
- [50] Krueger R. The virtual crack closure technique for modeling interlaminar failure and delamination in advanced composite materials. *Numer. Model. Fail. Adv. Compos. Mater.*, Elsevier Ltd.; 2015, p. 3–53. <https://doi.org/10.1016/B978-0-08-100332-9.00001-3>.
- [51] Shivakumar K, Chen H, Abali F, Le D, Davis C. A total fatigue life model for mode I delaminated composite laminates. *Int J Fatigue* 2006;28:33–42. <https://doi.org/10.1016/J.IJFATIGUE.2005.04.006>.
- [52] Paris P, Erdogan F. A Critical Analysis of Crack Propagation Laws. *J Basic Eng* 1963;85:528–33.
- [53] Rans C, Alderliesten R, Benedictus R. Misinterpreting the results: How similitude can improve our understanding of fatigue delamination growth. *Compos Sci Technol* 2011;71:230–8. <https://doi.org/10.1016/j.compscitech.2010.11.010>.
- [54] Blanco N, Gamstedt EK, Asp LE, Costa J. Mixed-mode delamination growth in carbon-fibre composite laminates under cyclic loading. *Int J Solids Struct* 2004;41:4219–35. <https://doi.org/10.1016/J.IJSOLSTR.2004.02.040>.

- [55] Allegri G, Wisnom MR. A non-linear damage evolution model for mode II fatigue delamination onset and growth. *Int J Fatigue* 2012;43:226–34. <https://doi.org/10.1016/j.ijfatigue.2012.03.016>.
- [56] Al-Khudairi O, Hadavinia H, Waggott A, Lewis E, Little C. Characterising mode I/mode II fatigue delamination growth in unidirectional fibre reinforced polymer laminates. *Mater Des* 2015;66:93–102. <https://doi.org/10.1016/J.MATDES.2014.10.038>.
- [57] Martin RH, Murri GB. Characterization of Mode I and Mode II Delamination Growth and Thresholds in AS4/PEEK Composites. 1990.
- [58] Shahverdi M, Vassilopoulos AP, Keller T. A total fatigue life model for the prediction of the R-ratio effects on fatigue crack growth of adhesively-bonded pultruded GFRP DCB joints. *Compos Part A Appl Sci Manuf* 2012;43:1783–90. <https://doi.org/10.1016/j.compositesa.2012.05.004>.
- [59] Leal AJS, Campilho RDSG. Numerical evaluation of the ENF and 4ENF tests for the shear toughness estimation of adhesive joints. *Compos Struct* 2018;202:333–43. <https://doi.org/10.1016/J.COMPSTRUCT.2018.01.107>.
- [60] ASTM D7905. Standard test method for determination of the mode II interlaminar fracture toughness of unidirectional fiber-reinforced polymer matrix composites. *ASTM* 2014:1–18. https://doi.org/10.1520/D7905_D7905M-19E01.
- [61] Carlsson LA, Gillespie JW, Pipes RB. On the Analysis and Design of the End Notched Flexure (ENF) Specimen for Mode II Testing. *J Compos Mater* 1986;20:594–604. <https://doi.org/10.1177/002199838602000606>.
- [62] Wang J, Qiao P. Novel beam analysis of end notched flexure specimen for mode-II fracture. *Eng Fract Mech* 2004;71:219–31. [https://doi.org/10.1016/S0013-7944\(03\)00096-1](https://doi.org/10.1016/S0013-7944(03)00096-1).
- [63] Shindo Y, Sato T, Narita F, Sanada K. Mode II interlaminar fracture and damage evaluation of GFRP woven laminates at cryogenic temperatures using the 4ENF specimen. *J Compos Mater* 2008;42:1089–101. <https://doi.org/10.1177/0021998308090451>.
- [64] Sun X, Davidson BD. Numerical evaluation of the effects of friction and geometric nonlinearities on the energy release rate in three- and four-point bend end-notched flexure tests. *Eng Fract Mech* 2006;73:1343–61. <https://doi.org/10.1016/J.ENGFRACTMECH.2005.11.007>.
- [65] Wang W, De Freitas ST, Poulis JA, Zarouchas D. A review of experimental and theoretical fracture characterization of bi-material bonded joints. *Compos Part B Eng* 2021;206:108537. <https://doi.org/10.1016/j.compositesb.2020.108537>.
- [66] Jiang Z, Fang Z, Wan S, Xie K. Mode-II fracture behavior evaluation for adhesively bonded pultruded GFRP/steel joint using four-point bending test. *Thin-Walled Struct* 2021;167:108130. <https://doi.org/10.1016/J.TWS.2021.108130>.

- [67] Ouyang Z, Li G. Nonlinear interface shear fracture of end notched flexure specimens. *Int J Solids Struct* 2009;46:2659–68. <https://doi.org/10.1016/J.IJSOLSTR.2009.02.011>.
- [68] Bienias J, Dadej K. Fatigue delamination growth of carbon and glass reinforced fiber metal laminates in fracture mode II. *Int J Fatigue* 2020;130:105267. <https://doi.org/10.1016/J.IJFATIGUE.2019.105267>.
- [69] Adamos L, Tsokanas P, Loutas T. An experimental study of the interfacial fracture behavior of Titanium/CFRP adhesive joints under mode I and mode II fatigue. *Int J Fatigue* 2020;136:105586. <https://doi.org/10.1016/j.ijfatigue.2020.105586>.
- [70] Hwang JH, Jin CK, Lee MS, Choi SW, Kang CG. Effect of surface roughness on the bonding strength and spring-back of a CFRP/CR980 hybrid composite. *Metals (Basel)* 2018;8:1–12. <https://doi.org/10.3390/met8090716>.
- [71] Moreira Arouche M, Teixeira de Freitas S, de Barros S. On the influence of glass fiber mat on the mixed-mode fracture of composite-to-metal bonded joints. *Compos Struct* 2021;256:113109. <https://doi.org/10.1016/J.COMPSTRUCT.2020.113109>.
- [72] Kumar P, Shinde PS, Bhoyar G. Fracture Toughness and Shear Strength of the Bonded Interface Between an Aluminium Alloy Skin and a FRP Patch. *J Inst Eng Ser C* 2019;100:779–89. <https://doi.org/10.1007/s40032-018-0467-1>.
- [73] Silva MAG, Biscaia H, Ribeiro P. On factors affecting CFRP-steel bonded joints. *Constr Build Mater* 2019;226:360–75. <https://doi.org/10.1016/j.conbuildmat.2019.06.220>.
- [74] Azari S, Papini M, Spelt JK. Effect of Surface Roughness on the Performance of Adhesive Joints Under Static and Cyclic Loading. *J Adhes* 2010;86:742–64. <https://doi.org/10.1080/00218464.2010.482430>.
- [75] Shikimoto K, Ishida S, Jinnouchi W, Ogawa Y, Akebono H, Sugeta A. Effect of laser patterning preprocessing on fatigue strength of adhesive bonded joints using thin steel plate. *Mater Trans* 2020;61:469–74. <https://doi.org/10.2320/matertrans.Z-M2019870>.
- [76] Manoli A, Ghadge R, Kumar P. Effect of surface roughness on the fatigue strength of E-glass composite single lap joint bonded with modified graphene oxide-epoxy adhesive. *Mater Phys Mech* 2023;51:65–80. https://doi.org/10.18149/MPM.5122023_7.
- [77] Carrera B. Effects of Surface Condition on the Fatigue Behavior of CFRP-to-Steel Joints. Virginia Polytechnic Institute and State University, 2022.
- [78] He X. A review of finite element analysis of adhesively bonded joints. *Int J Adhes Adhes* 2011;31:248–64. <https://doi.org/10.1016/j.ijadhadh.2011.01.006>.
- [79] Parashar A, Mertiny P. Adhesively bonded composite tubular joints: Review. *Int J Adhes Adhes* 2012;38:58–68. <https://doi.org/10.1016/j.ijadhadh.2012.05.004>.
- [80] Abdel Wahab MM. Fatigue in Adhesively Bonded Joints: A Review. *ISRN Mater Sci* 2012;2012:1–25. <https://doi.org/10.5402/2012/746308>.
- [81] Oskay C. Multiscale modeling of the response and life prediction of composite materials. Elsevier Ltd.; 2015. <https://doi.org/10.1016/B978-0-08-100332-9.00013-X>.

- [82] Ashcroft IA, Mubashar A. Fatigue. In: Robert D. Adams, editor. *Adhes. Bond. Sci. Technol. Appl. Second Edi*, Elsevier; 2021, p. 317–66. <https://doi.org/10.1016/B978-0-12-819954-1.00006-X>.
- [83] Jen YM, Ko CW. Evaluation of fatigue life of adhesively bonded aluminum single-lap joints using interfacial parameters. *Int J Fatigue* 2010;32:330–40. <https://doi.org/10.1016/j.ijfatigue.2009.07.001>.
- [84] Bernasconi A, Beretta S, Moroni F, Pironi A. Local stress analysis of the fatigue behaviour of adhesively bonded thick composite laminates. *J Adhes* 2010;86:480–500. <https://doi.org/10.1080/00218464.2010.484300>.
- [85] Azari S, Papini M, Spelt JK. Effect of adhesive thickness on fatigue and fracture of toughened epoxy joints - Part I: Experiments. *Eng Fract Mech* 2011;78:153–62. <https://doi.org/10.1016/j.engfracmech.2010.06.025>.
- [86] Azari S, Papini M, Spelt JK. Effect of adhesive thickness on fatigue and fracture of toughened epoxy joints - Part II: Analysis and finite element modeling. *Eng Fract Mech* 2011;78:138–52. <https://doi.org/10.1016/j.engfracmech.2010.07.006>.
- [87] Ishii K, Imanaka M, Nakayama H, Kodama H. Evaluation of the fatigue strength of adhesively bonded CFRP/metal single and single-step double-lap joints. *Compos Sci Technol* 1999;59:1675–83. [https://doi.org/10.1016/S0266-3538\(99\)00028-7](https://doi.org/10.1016/S0266-3538(99)00028-7).
- [88] Ke L, Zhu F, Chen Z, Feng Z, Zhou J, Li Y. Fatigue failure mechanisms and probabilistic S-N curves for CFRP–steel adhesively bonded joints. *Int J Fatigue* 2023;168:107470. <https://doi.org/10.1016/J.IJFATIGUE.2022.107470>.
- [89] Colombi P, Fava G. Fatigue behaviour of tensile steel/CFRP joints. *Compos Struct* 2012;94:2407–17. <https://doi.org/10.1016/J.COMPSTRUCT.2012.03.001>.
- [90] Bocciarelli M, Colombi P, Fava G, Poggi C. Fatigue performance of tensile steel members strengthened with CFRP plates. *Compos Struct* 2009;87:334–43. <https://doi.org/10.1016/j.compstruct.2008.02.004>.
- [91] Doroudi Y, Fernando D, Nguyen VT, Torres JP. Experimental Study on CFRP-to-Steel Bonded Interfaces under Quasi-Static Cyclic Loading. *J Compos Constr* 2019;23. [https://doi.org/10.1061/\(asce\)cc.1943-5614.0000945](https://doi.org/10.1061/(asce)cc.1943-5614.0000945).
- [92] Zhang Z, Shang JK, Lawrence F V. A Backface Strain Technique for Detecting Fatigue Crack Initiation in Adhesive Joints. *J Adhes* 1995;49:23–36. <https://doi.org/10.1080/00218469508009975>.
- [93] Dillard D.A. LR. A Stress Singularity Approach for the Prediction of Fatigue Crack Initiation in Adhesive Bonds. Part 1: Theory. *J Adhes* 2006;70. <https://doi.org/https://doi.org/10.1080/00218469908010490>.
- [94] Shenoy V, Ashcroft IA, Critchlow GW, Crocombe AD. Unified methodology for the prediction of the fatigue behaviour of adhesively bonded joints. *Int J Fatigue* 2010;32:1278–88. <https://doi.org/10.1016/j.ijfatigue.2010.01.013>.

- [95] Graner Solana A, Crocombe AD, Ashcroft IA. Fatigue life and backface strain predictions in adhesively bonded joints. *Int J Adhes Adhes* 2010;30:36–42. <https://doi.org/10.1016/j.ijadhadh.2009.08.001>.
- [96] Hilmy I, Wahab MMA, Ashcroft IA, Crocombe AD. A finite element analysis of scarf joint for controlling the triaxiality function in adhesive bonding. *Key Eng Mater* 2008;385–387:17–20. <https://doi.org/10.4028/www.scientific.net/kem.385-387.17>.
- [97] Quaresimin M, Ricotta M. Life prediction of bonded joints in composite materials. *Int J Fatigue* 2006;28:1166–76. <https://doi.org/10.1016/j.ijfatigue.2006.02.005>.
- [98] Yang JN, Jones DL, Yang SH, Meskini A. A Stiffness Degradation Model for Graphite/Epoxy Laminates. *J Compos Mater* 1990;24:753–69. <https://doi.org/10.1177/002199839002400705>.
- [99] Philippidis TP, Vassilopoulos AP. Fatigue design allowables for GRP laminates based on stiffness degradation measurements. *Compos Sci Technol* 2000;60:2819–28. [https://doi.org/10.1016/S0266-3538\(00\)00150-0](https://doi.org/10.1016/S0266-3538(00)00150-0).
- [100] Iwashita K, Wu Z, Ishikawa T, Hamaguchi Y, Suzuki T. Bonding and debonding behavior of FRP sheets under fatigue loading. *Adv Compos Mater* 2007;16:31–44. <https://doi.org/10.1163/156855107779755291>.
- [101] Min X, Zhang J, Wang C, Song S, Yang D. Experimental investigation of fatigue debonding growth in FRP - Concrete interface. *Materials (Basel)* 2020;13:1–18. <https://doi.org/10.3390/ma13061459>.
- [102] Senthilkumar M, Sreekanth T, Reddy SM. Nondestructive health monitoring techniques for composite materials: A review: <https://doi.org/10.1177/0967391120921701> 2020;29:528–40. <https://doi.org/10.1177/0967391120921701>.
- [103] Duchene P, Chaki S, Ayadi A, Krawczak P. A review of non-destructive techniques used for mechanical damage assessment in polymer composites. *J Mater Sci* 2018 5311 2018;53:7915–38. <https://doi.org/10.1007/S10853-018-2045-6>.
- [104] Ghiassi B, Verstryngge E, Lourenço PB, Oliveira D V. Characterization of debonding in FRP-strengthened masonry using the acoustic emission technique. *Eng Struct* 2014;66:24–34. <https://doi.org/10.1016/j.engstruct.2014.01.050>.
- [105] Pohoryles DA, Melo J, Rossetto T, Fabian M, McCague C, Stavrianaki K, et al. Use of DIC and AE for Monitoring Effective Strain and Debonding in FRP and FRCM-Retrofitted RC Beams. *J Compos Constr* 2017;21:04016057. [https://doi.org/10.1061/\(ASCE\)CC.1943-5614.0000715](https://doi.org/10.1061/(ASCE)CC.1943-5614.0000715).
- [106] Li J, Lu Y, Lee YF. Debonding detection in CFRP-reinforced steel structures using anti-symmetrical guided waves. *Compos Struct* 2020;253:112813. <https://doi.org/10.1016/J.COMPSTRUCT.2020.112813>.
- [107] Yelve NP, Mitra M, Mujumdar PM. Detection of delamination in composite laminates using Lamb wave based nonlinear method. *Compos Struct* 2017;159:257–66.

- <https://doi.org/10.1016/J.COMPSTRUCT.2016.09.073>.
- [108] Mustapha S, Ye L. Propagation behaviour of guided waves in tapered sandwich structures and debonding identification using time reversal. *Wave Motion* 2015;57:154–70. <https://doi.org/10.1016/J.WAVEMOTI.2015.03.010>.
- [109] Ghosh KK, Karbhari VM. A critical review of infrared thermography as a method for non-destructive evaluation of FRP rehabilitated structures. *Int J Mater Prod Technol* 2006;25:241–66. <https://doi.org/10.1504/IJMPT.2006.008882>.
- [110] Ghosh KK, Karbhari VM. Use of infrared thermography for quantitative non-destructive evaluation in FRP strengthened bridge systems. *Mater Struct* 2010 44:169–85. <https://doi.org/10.1617/S11527-010-9617-5>.
- [111] Owen RDB. Portable linear accelerators for X-ray and electron-beam applications in civil engineering. *NDT E Int* 1998;31:401–9. [https://doi.org/10.1016/S0963-8695\(98\)00042-5](https://doi.org/10.1016/S0963-8695(98)00042-5).
- [112] Lakshmi Aparna M, Chaitanya G, Srinivas K, Rao JA. Fatigue Testing of Continuous GFRP Composites Using Digital Image Correlation (DIC) Technique a Review. *Mater Today Proc* 2015;2:3125–31. <https://doi.org/10.1016/J.MATPR.2015.07.275>.
- [113] Ghiassi B, Xavier J, Oliveira D V., Lourenço PB. Application of digital image correlation in investigating the bond between FRP and masonry. *Compos Struct* 2013;106:340–9. <https://doi.org/10.1016/J.COMPSTRUCT.2013.06.024>.
- [114] Zhang P, Lei D, Ren Q, He J, Shen H, Yang Z. Experimental and numerical investigation of debonding process of the FRP plate-concrete interface. *Constr Build Mater* 2020;235:117457. <https://doi.org/10.1016/J.CONBUILDMAT.2019.117457>.
- [115] Ali-Ahmad M, Subramaniam K, Ghosn M. Experimental Investigation and Fracture Analysis of Debonding between Concrete and FRP Sheets. *J Eng Mech* 2006;132:914–23. [https://doi.org/10.1061/\(ASCE\)0733-9399\(2006\)132:9\(914\)](https://doi.org/10.1061/(ASCE)0733-9399(2006)132:9(914)).
- [116] Wang HT, Wu G, Pang YY, Shi JW, Zakari HM. Experimental study on the bond behavior between CFRP plates and steel substrates under fatigue loading. *Compos Part B Eng* 2019;176:107266. <https://doi.org/10.1016/j.compositesb.2019.107266>.
- [117] Zheng B, Dawood M. Debonding of Carbon Fiber–Reinforced Polymer Patches from Cracked Steel Elements under Fatigue Loading. *J Compos Constr* 2016;20:04016038. [https://doi.org/10.1061/\(ASCE\)CC.1943-5614.0000694](https://doi.org/10.1061/(ASCE)CC.1943-5614.0000694).
- [118] Szebényi G, Hliva V. Detection of Delamination in Polymer Composites by Digital Image Correlation—Experimental Test. *Polymers (Basel)* 2019;11:523. <https://doi.org/10.3390/polym11030523>.
- [119] Ajmal OZ. The use of digital image correlation to monitor delaminations in composite structures. 2018.
- [120] Feng W, He P, Pavlovic M. Combined DIC and FEA method for analysing debonding crack propagation in fatigue experiments on wrapped composite joints. *Compos Struct*

- 2022;297:115977. <https://doi.org/10.1016/J.COMPSTRUCT.2022.115977>.
- [121] Pascoe JA, Alderliesten RC, Benedictus R. Methods for the prediction of fatigue delamination growth in composites and adhesive bonds - A critical review. *Eng Fract Mech* 2013;112–113:72–96. <https://doi.org/10.1016/j.engfracmech.2013.10.003>.
- [122] Ratwani MM, Kan HP. Compression Fatigue Analysis of Fiber Composites. *J Aircr* 1981;18:458–62.
- [123] Poursartip A, Chinatambi N. Fatigue damage development in notched (02/±45) s laminates. *Compos Mater Fatigue Fract* 1989;2:45–65.
- [124] Pirondi A, Giuliese G, Moroni F, Bernasconi A, Jamil A. Comparative study of cohesive zone and virtual crack closure techniques for three-dimensional fatigue debonding. *J Adhes* 2014;90:457–81. <https://doi.org/10.1080/00218464.2013.859616>.
- [125] Martulli LM, Bernasconi A. An efficient and versatile use of the VCCT for composites delamination growth under fatigue loadings in 3D numerical analysis: the Sequential Static Fatigue algorithm. *Int J Fatigue* 2023;170:107493. <https://doi.org/10.1016/J.IJFATIGUE.2022.107493>.
- [126] Latifi M, Van Der Meer FP, Sluys LJ. A level set model for simulating fatigue-driven delamination in composites. *Int J Fatigue* 2015;80:434–42. <https://doi.org/10.1016/j.ijfatigue.2015.07.003>.
- [127] Latifi M, van der Meer FP, Sluys LJ. Fatigue modeling in composites with the thick level set interface method. *Compos Part A Appl Sci Manuf* 2017;101:72–80. <https://doi.org/10.1016/j.compositesa.2017.05.035>.
- [128] Hallett SR, Harper PW. Modelling delamination with cohesive interface elements. *Numer. Model. Fail. Adv. Compos. Mater.*, Elsevier Ltd.; 2015, p. 55–72. <https://doi.org/10.1016/B978-0-08-100332-9.00002-5>.
- [129] Harper PW, Hallett SR. A fatigue degradation law for cohesive interface elements – Development and application to composite materials. *Int J Fatigue* 2010;32:1774–87. <https://doi.org/10.1016/j.ijfatigue.2010.04.006>.
- [130] Moura MFSF De, Silva LFM, Marques AT, Ferna M V. Composite bonded joints under mode I fatigue loading. *Int J Adhes Adhes* 2011;31:280–5. <https://doi.org/10.1016/j.ijadhadh.2010.10.003>.
- [131] Rocha AVM, Akhavan-Safar A, Carbas R, Marques EAS, Goyal R, El-zein M, et al. Numerical analysis of mixed-mode fatigue crack growth of adhesive joints using CZM. *Theor Appl Fract Mech* 2020;106:102493. <https://doi.org/10.1016/J.TAFMEC.2020.102493>.
- [132] Doroudi Y, Fernando D, Zhou H, Nguyen VT, Ghafoori E. Fatigue behavior of FRP-to-steel bonded interface: An experimental study with a damage plasticity model. *Int J Fatigue* 2020;139:105785. <https://doi.org/10.1016/j.ijfatigue.2020.105785>.
- [133] Khoramishad H, Crocombe AD, Katnam KB, Ashcroft IA. Fatigue damage modelling

- of adhesively bonded joints under variable amplitude loading using a cohesive zone model. *Eng Fract Mech* 2011;78:3212–25. <https://doi.org/10.1016/j.engfracmech.2011.09.008>.
- [134] Choi Y-H, Kim H-G. Development of a Cohesive Zone Model for Fatigue Crack Growth. *Multiscale Sci Eng* 2020;2:42–53. <https://doi.org/10.1007/s42493-020-00034-5>.
- [135] Liao M, Yang QX. A probabilistic model for fatigue crack growth. *Eng Fract Mech* 1992;43:651–5. [https://doi.org/10.1016/0013-7944\(92\)90206-T](https://doi.org/10.1016/0013-7944(92)90206-T).
- [136] Bogdanov S, Mikheevskiy S, Glinka G. Probabilistic analysis of the fatigue crack growth based on the application of the Monte-Carlo method to unigrow model. *Mater Perform Charact* 2014;3:214–31. <https://doi.org/10.1520/MPC20130066>.
- [137] Sanches RF, De Jesus AMP, Correia JAFO, Da Silva ALL, Fernandes AA. A probabilistic fatigue approach for riveted joints using Monte Carlo simulation. *J Constr Steel Res* 2015;110:149–62. <https://doi.org/10.1016/j.jcsr.2015.02.019>.
- [138] He W, Liu J, Xie D. Probabilistic life assessment on fatigue crack growth in mixed-mode by coupling of Kriging model and finite element analysis. *Eng Fract Mech* 2015;139:56–77. <https://doi.org/10.1016/J.ENGFRACMECH.2015.03.040>.
- [139] Reddy K, Karthik Reddy Lyathakula F-G, Yuan F-G, Reddy Lyathakula K. Probabilistic fatigue life prediction for adhesively bonded joints via surrogate model. *Proc. Sensors Smart Struct. Technol. Civil, Mech. Aerosp. Syst.*, vol. 11591, SPIE; 2021, p. 152–62. <https://doi.org/10.1117/12.2585281>.
- [140] He P. Debonding Resistance of CHS Wrapped Composite X-Joints. Delft University of Technology, 2023. <https://doi.org/https://doi.org/10.4233/uuid:3ad94ee9-07fd-47f9-a766-843a91830534>.
- [141] BS EN 10002-1:2001 / ISO 6892-1. Metallic materials - Tensile testing - Part 1: Method of test at room temperature. *Dtsch Norm* 2009:68.
- [142] BS EN ISO. 527-1:2019 Plastics. Determination of tensile properties. General principles 2019.
- [143] ISO. 14126 Fibre-reinforced plastic composites - Determination of compressive properties in the in-plane direction. *Iso* 2001;2001:1–25.
- [144] International Organization for Standardization. ISO 14129:1997, Fibre-reinforced plastic composites - Determination of the in-plane shear stress/shear strain response, including the in-plane shear modulus and strength, by the plus or minus 45 degree tension test method 2007.
- [145] ISO 25178-2:2021(en), Geometrical product specifications (GPS) — Surface texture: Areal — Part 2: Terms, definitions and surface texture parameters n.d. <https://www.iso.org/obp/ui/#iso:std:iso:25178:-2:ed-2:v1:en> (accessed February 14, 2023).
- [146] Blau PJ. Friction science and technology: From concepts to applications, second edition.

- 2008.
- [147] Arouche MM, Wang W, Teixeira de Freitas S, de Barros S. Strain-based methodology for mixed-mode I+II fracture: A new partitioning method for bi-material adhesively bonded joints. *J Adhes* 2019;95:385–404. <https://doi.org/10.1080/00218464.2019.1565756>.
- [148] Weikang Feng, Marcio Moreira Arouche MP. Fatigue crack growth characterization of composite-to-steel bonded interface using ENF and 4ENF tests. Submitted 2023;334:117963. <https://doi.org/10.1016/j.compstruct.2024.117963>.
- [149] Shahverdi M, Vassilopoulos AP, Keller T. Mixed-Mode I/II fracture behavior of asymmetric adhesively-bonded pultruded composite joints. *Eng Fract Mech* 2014;115:43–59. <https://doi.org/10.1016/j.engfracmech.2013.11.014>.
- [150] Fernando D. Bond behaviour and debonding failures in CFRP-strengthened steel members. The Hong Kong Polytechnic University, 2010.
- [151] Zhu M, Gorbatiikh L, Fonteyn S, Van Hemelrijck D, Pyl L, Carrella-Payan D, et al. Digital image correlation assisted characterization of Mode I fatigue delamination in composites. *Compos Struct* 2020;253:112746. <https://doi.org/10.1016/j.compstruct.2020.112746>.
- [152] van Dam JPB, Abrahams ST, Yilmaz A, Gonzalez-Garcia Y, Terryn H, Mol JMC. Effect of surface roughness and chemistry on the adhesion and durability of a steel-epoxy adhesive interface. *Int J Adhes Adhes* 2020;96:102450. <https://doi.org/10.1016/j.ijadhadh.2019.102450>.
- [153] Tanaka K, Tanaka H. Stress-ratio effect on mode II propagation of interlaminar fatigue cracks in graphite/epoxy composites. *ASTM Spec Tech Publ* 1997;1285:126–42. <https://doi.org/10.1520/stp19925s>.
- [154] Ratcliffe JG, Johnston WM. Influence of mixed mode I-mode II loading on fatigue delamination growth characteristics of a graphite epoxy tape laminate. *Proc. Am. Soc. Compos. - 29th Tech. Conf. ASC 2014; 16th US-Japan Conf. Compos. Mater. ASTM-D30 Meet., 2014*.
- [155] Feng W, Pavlovic M, Koetsier M, Veljkovic M. Interfacial fatigue debonding retardation in wrapped composite joints: Experimental and numerical study. *Compos Struct* 2023;319:117146. <https://doi.org/10.1016/j.compstruct.2023.117146>.
- [156] Landry B, Laplante G, Leblanc LR. Environmental effects on mode II fatigue delamination growth in an aerospace grade carbon/epoxy composite. *Compos Part A Appl Sci Manuf* 2012;43:475–85. <https://doi.org/10.1016/j.compositesa.2011.11.015>.
- [157] Matsubara G, Ono H, Tanaka K. Mode II fatigue crack growth from delamination in unidirectional tape and satin-woven fabric laminates of high strength GFRP. *Int J Fatigue* 2006;28:1177–86. <https://doi.org/10.1016/j.ijfatigue.2006.02.006>.
- [158] Hojo M, Ando T, Tanaka M, Adachi T, Ochiai S, Endo Y. Modes I and II interlaminar

- fracture toughness and fatigue delamination of CF/epoxy laminates with self-same epoxy interleaf. *Int J Fatigue* 2006;28:1154–65. <https://doi.org/10.1016/J.IJFATIGUE.2006.02.004>.
- [159] Asp LE, Sjögren A, Greenhalgh ES. Delamination Growth and Thresholds in a Carbon/Epoxy Composite under Fatigue Loading. *J Compos Technol Res* 2001;23:55–68. <https://doi.org/10.1520/ctr10914j>.
- [160] Abaqus 6.14 Documentation n.d. <http://130.149.89.49:2080/v6.14/> (accessed September 22, 2021).
- [161] Feng W, Pavlovic M. Fatigue behaviour of non-welded wrapped composite joints for steel hollow sections in axial load experiments. *Eng Struct* 2021;249:113369. <https://doi.org/10.1016/J.ENGSTRUCT.2021.113369>.
- [162] Liu L, Wang X, Wu Z, Keller T. Tension-tension fatigue behavior of ductile adhesively-bonded FRP joints. *Compos Struct* 2021;268:113925. <https://doi.org/10.1016/J.COMPSTRUCT.2021.113925>.
- [163] Olivier G, Csillag F, Tromp E, Pavlović M. Static, fatigue and creep performance of blind-bolted connectors in shear experiments on steel-FRP joints. *Eng Struct* 2021;230:111713. <https://doi.org/10.1016/j.engstruct.2020.111713>.
- [164] Anderson WE, McEvily AJ. Discussion: “A Critical Analysis of Crack Propagation Laws” (Paris, P., and Erdogan, F., 1963, *ASME J. Basic Eng.*, 85, pp. 528–533). *J Basic Eng* 1963;85:533–533. <https://doi.org/10.1115/1.3656901>.
- [165] Khan R. Fiber bridging in composite laminates: A literature review. *Compos Struct* 2019;229. <https://doi.org/10.1016/j.compstruct.2019.111418>.
- [166] Abaqus Unified FEA - SIMULIA™ by Dassault Systèmes® n.d. <https://www.3ds.com/products-services/simulia/products/abaqus/> (accessed May 12, 2022).
- [167] Farmand-Ashtiani E, Cugnoni J, Botsis J. Effects of large scale bridging in load controlled fatigue delamination of unidirectional carbon-epoxy specimens. *Compos Sci Technol* 2016;137:52–9. <https://doi.org/10.1016/J.COMPSCITECH.2016.10.022>.
- [168] Yao L, Sun Y, Guo L, Zhao M, Jia L, Alderliesten RC, et al. A modified Paris relation for fatigue delamination with fibre bridging in composite laminates. *Compos Struct* 2017;176:556–64. <https://doi.org/10.1016/J.COMPSTRUCT.2017.05.070>.
- [169] Liu C, Gong Y, Gong Y, Li W, Liu Z, Hu N. Mode II fatigue delamination behaviour of composite multidirectional laminates and the stress ratio effect. *Eng Fract Mech* 2022;264:108321. <https://doi.org/10.1016/J.ENGFRACTMECH.2022.108321>.
- [170] Zhang Y, Vassilopoulos AP, Keller T. Stiffness degradation and fatigue life prediction of adhesively-bonded joints for fiber-reinforced polymer composites. *Int J Fatigue* 2008;30:1813–20. <https://doi.org/10.1016/j.ijfatigue.2008.02.007>.
- [171] Feng W, He P, Pavlovic M. Combined DIC and FEA method for analysing debonding

- crack propagation in fatigue experiments on wrapped composite joints. *Compos Struct* 2022;115977. <https://doi.org/10.1016/J.COMPSTRUCT.2022.115977>.
- [172] He P, Pavlovic M. Failure modes of bonded wrapped composite joints for steel circular hollow sections in ultimate load experiments. *Eng Struct* 2022;254:113799. <https://doi.org/10.1016/j.engstruct.2021.113799>.
- [173] Arya C. Eurocode 3: Design of steel structures. *Des Struct Elem* 2015;3:395–453. <https://doi.org/10.1201/b18121-19>.
- [174] Egilsson S. *Fatigue of Wrapped Composite Joints*. Delft University of Technology, 2023.
- [175] Takeda T, Miura M, Shindo Y, Narita F. Fatigue delamination growth in woven glass / epoxy composite laminates under mixed-mode II / III loading conditions at cryogenic temperatures. *Cryogenics (Guildf)* 2013;58:55–61. <https://doi.org/10.1016/j.cryogenics.2013.10.001>.
- [176] Miura M, Shindo Y, Narita F, Watanabe S, Suzuki M. Mode III fatigue delamination growth of glass fiber reinforced polymer woven laminates at cryogenic temperatures. *Cryogenics (Guildf)* 2009;49:407–12. <https://doi.org/10.1016/J.CRYOGENICS.2009.05.004>.
- [177] Statistics M. *Asymptotic Theory of Certain " Goodness of Fit " Criteria Based on Stochastic Processes* Author (s): T . W . Anderson and D . A . Darling Published by : Institute of Mathematical Statistics Stable URL : <https://www.jstor.org/stable/2236446> REFERENCES Lin 1952;23:193–212.
- [178] Correia JAFO, De Jesus AMP, Calçada R, Pedrosa B, Rebelo C, Da Silva LS, et al. Statistical analysis of fatigue crack propagation data of materials from ancient portuguese metallic bridges. *Frat Ed Integrita Strutt* 2017;11:136–46. <https://doi.org/10.3221/IGF-ESIS.42.15>.
- [179] Wu W, Kolstein H, Veljkovic M. Fatigue resistance of rib-to-deck welded joint in OSDs, analyzed by fracture mechanics. *J Constr Steel Res* 2019;162:105700. <https://doi.org/10.1016/j.jcsr.2019.105700>.
- [180] Practice S. *Standard Practice for Statistical Analysis of Linear or Linearized Stress-Life* (. *Stat Anal Fatigue Data* 2009;91:129-129–9. <https://doi.org/10.1520/stp29332s>.
- [181] CEN/TS 19101: 2022. *Design of Fibre-Polymer Composite Structures*. European Committee for Standardization (CEN). 2021.

ACKNOWLEDGEMENTS

When I received the admission letter for this PhD position in 2018, I began to anticipate this unknown journey. Now, as this magical journey draws to a close, countless memories flood my mind. At this moment, I want to express my sincerest gratitude to my friends and colleagues who have helped me along the way.

Firstly, I would like to express my gratitude to my promotor Prof. Milan Veljkovic and my co-promotor Dr. Marko Pavlovic for giving me the opportunity to pursue a PhD degree. Dr. Pavlovic, it has been a great honour to have you as such a respected supervisor, amiable friend, and role model in academia during my PhD study. I still remember the online interview you conducted with me on November 2, 2018; the fascinating topics discussed and your insightful questions marked the beginning of our unforgettable mentor-student relationship. Looking back over the past five years, the various challenges encountered in my PhD journey often left me feeling lost. Marko, it was your on-site guidance during my experiments, your meticulous attention to detail in the finite element models, and your thorough revisions during my journal paper writing that helped me overcome numerous obstacles and successfully complete my PhD. Your patient explanations and innovative thinking during each progress meeting always left me feeling like our discussions were never enough. I also would like to thank you for providing me with opportunities to participate in academic conferences and summer school, which expanded my academic horizons and enhanced my social skills. Additionally, I want to express my gratitude for your psychological support during my PhD study. In 2020, the pandemic combined with the challenges encountered in the project left me feeling extremely anxious and demoralized, to the point where I entertained thoughts of dropping out. It was your patient guidance and positive encouragement that gave me the courage to continue. The time spent working with you will undoubtedly be a treasure in my life for years to come.

Prof. Veljkovic, every quarterly meeting with you feels like a breath of fresh air. Your oversight of the macro direction of my PhD project during each meeting has been crucial in ensuring the successful completion of my study. I am always impressed by your attention to detail, which helped shape my scientific perspective and improve my critical thinking skills. I am also very grateful for your organization of team meetings during the pandemic, where you showed genuine concern for the physical and mental well-being of each of us. I will always remember your blessings to us during each Chinese New Year. Thank you, Milan!

I would also like to express my gratitude to my supervisors during my master's study, Prof. Wei Wang and Dr. Cheng Fang from Tongji University. It was you who provided me with the enlightenment in scientific research. I sincerely thank Prof. Bert Sluys, Prof. Dilum Fernando, Prof. Elyas Ghafoori, Dr. Xiaoli Jiang, and Dr. Jose Sena-Cruz from my doctoral committee for providing valuable feedback and suggestions for my doctoral thesis. Additionally, I want to

ACKNOWLEDGEMENTS

thank the China Scholarship Council (CSC) for funding my study in TU Delft. Special thanks to Tree Composites B.V. and Verstedden B.V. for producing experimental specimens.

The completion of my PhD project would not have been possible without the help of many colleagues. I sincerely thank all my colleagues from the WrapNode project. Pei He, I will always remember our ‘Peikang’ team. I cannot imagine the challenges I would have faced when I first arrived in the Netherlands without your help. Your excellent work has laid a solid foundation for the smooth progression of my project, the twin project of yours. Jincheng Yang, every discussion with you about fracture mechanics and finite element modelling has been truly inspiring. The establishment of the prediction method for crack growth in wrapped composite joints would not have been possible without your help. I would also express my sincere gratitude to Mathieu Koetsier and Marcio Moreira Arouche for helping me conduct experiments and collaborate on writing journal papers, Sigurdur Egilsson for developing the numerical algorithm, Tjeu Peeters for organising research activities and Siyuan Hou for conducting ENF/4ENF tests. I would also like to express my gratitude to colleagues from Tress Composites, Maxim Segeren, Mees Wolters, Tim Kapteijn, Vasilis Mylonopoulos, Clement Waltener, et al. I really learnt a lot from you during every team meeting we had. The success of the experiments relies on the assistance of other colleagues in Stevin Lab II. Thank you Peter de Vries for providing guidance and advice for my experiments. Many thanks to Giorgos Stamoulis for helping me in utilizing DIC, the advanced technology, to achieve excellent experimental results. Thank you Fred Schilperoort for helping me realizing different loading conditions for my experiments. Special thanks are given to Dr. Alessandro Cabboi for introducing me to tribology, the entirely new field for me. Kees van Beek, John Hermsen and Louis den Breejen, I will never forget your effort for providing advice and assistance for my experiments.

During my PhD journey, it’s my privilege to work with many outstanding colleagues within our SCS group and ES department. Thank you Weijian Wu and Fei Yang for providing me with support in my daily life when I first arrived in the Netherlands. Appreciation is owed to Haohui Xin, Rui Yan, Lu Cheng, and Angeliki Christoforidou for providing guidance and inspiration for my PhD project. Zhanchong Shi, Da Xiang and Ding Liao, the daily discussions and travels with you enriched my life. I would also like to express my sincere gratitude to all my (former) officemates Shuang Qiu, Xiuli Wang, Tao Yang, Tjeu Peeters and Abishek Baskar. Your presence fills this two-person office with laughter and joy. Many thanks should be given to Yufei Zhang, Rong Liu, Xiaoling Liu, Olena Karpenko, Trayana Tankova, Florentia Kavoura, Martin Paul Nijgh, Abhijith, Kamath, David Malschaert and Hagar El Bamby. Having you all around has made my PhD life colourful and more motivated. Finally, I would also like to extend my gratitude to our secretary Claire de Bruin for the assistance provided during my PhD study.

My sincere gratitude should be given to all lovely friends I met in the Netherlands Yitao Huang, Yubao Zhou, Hao Cheng, Ze Chang, Zhi Wan, Yuxuan Feng, Li Wang, Yuanchen Zeng, Yi Zheng, Fanxiang Xu, Shichen Liu, Ruipeng Liu, et al and Hexiao Zhang on the other side of the earth. Chatting, traveling, cooking, and playing board games together with you are

indispensable and wonderful memories of my PhD journey. Special thanks are given to Shisong Ren for sharing research tips and life insights with me. Zhaohang Zhang and Tan Zhang, I feel so lucky to have you in the Netherlands. Travelling, dining together with you and meeting friends in Leiden really made my PhD life joyful.

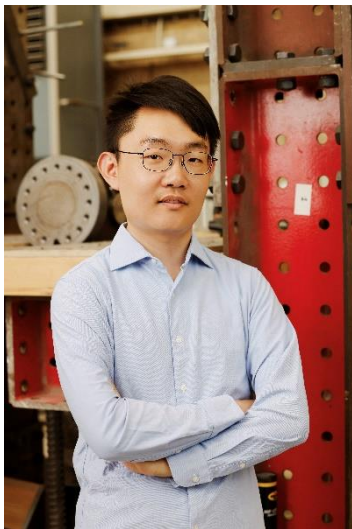
Last but not least, my deepest gratitude goes to my family members in China. Thank you for nurturing me and providing me with such a precious learning opportunity through your unconditional support. Thank you for countless video chats in our daily lives, which have given me the courage and strength to move forward.

Weikang Feng



Delft, Feb. 2024

CURRICULUM VITAE



Weikang FENG

05-04-1994 Born in Zaozhuang, China

Sep.2012 – Jun. 2016 Bachelor of Engineering in Civil Engineering

Tongji University, China

Sep.2016 – Jun. 2019 Master of Engineering in Architectural and Civil Engineering

Tongji University, China

Oct.2019 – Present PhD. in Steel and Composite Structures

Delft University of Technology, the Netherlands

LIST OF PUBLICATIONS

JOURNAL ARTICLES:

- [1] **Weikang Feng**, Marcio Moreira Arouche, Marko Pavlovic*. Fatigue crack growth characterization of composite-to-steel bonded interface using ENF and 4ENF tests. *Composite Structures* 2024;334:117963.
- [2] **Weikang Feng**, Marcio Moreira Arouche, Marko Pavlovic*. Influence of surface roughness on the mode II fracture toughness and fatigue resistance of bonded composite-to-steel joints. *Construction and Building Materials* 2023; 411:134358
- [3] **Weikang Feng**, Marko Pavlovic*, Mathieu Koetsier, Milan Veljkovic. Interfacial fatigue debonding retardation in wrapped composite joints : experimental and numerical study. *Composite Structures* 2023;319:117146.
- [4] **Weikang Feng**, Pei He, Marko Pavlovic*. Combined DIC and FEA method for analysing debonding crack propagation in fatigue experiments on wrapped composite joints. *Composite Structures* 2022:115977.
- [5] **Weikang Feng**, Marko Pavlovic*. Fatigue behaviour of non-welded wrapped composite joints for steel hollow sections in axial load experiments. *Engineering Structures* 2021;249:113369.
- [6] Pei He, **Weikang Feng**, Marko Pavlovic*. Influence of steel yielding and resin toughness on debonding of wrapped composite joints. *Composite Structures* 2023;312:116862.

CONFERENCE PROCEEDINGS:

- [1] **Weikang Feng**, Marcio Moreira Arouche, Marko Pavlovic. Influence of surface roughness on the mode II fatigue resistance of the bonded composite-to-steel interface. 11th International Conference on Fiber-Reinforced Polymer (FRP) Composites in Civil Engineering. Rio de Janeiro, Brazil, 2023
- [2] **Weikang Feng**, Pei He, Mathieu Koetsier, Marko Pavlovic. DIC-based monitoring on debonding crack propagation in wrapped composite joints. 20th European Conference on Composite Materials: Composites Meet Sustainability. Lausanne, Switzerland, 2022
- [3] Marcio Moreira Arouche, **Weikang Feng**, Paraskevi Karatsi, Tim Kapteijn, Marko Pavlovic. Effect of salt water ageing on the degradation of steel-composite bonded interfaces. 10th Eurosteel conference. Amsterdam, Netherland, 2023